Development of efficient permeation barriers based on hot-wire CVD grown silicon-nitride multilayers for organic devices deposited on flexible substrates

Subimal Majee

THÈSE

Présentée en vue d'obtenir le grade de

DOCTEUR DE L'ÉCOLE POLYTECHNIQUE

Spécialité "Physique et Science des Matériaux"

par

SUBIMAL MAJEE

subimal.majee@polytechnique.edu

DEVELOPMENT OF EFFICIENT PERMEATION BARRIERS BASED ON HOT-WIRE CVD GROWN SILICON-NITRIDE MULTILAYERS FOR ORGANIC DEVICES DEPOSITED ON FLEXIBLE SUBSTRATES

Thèse soutenue le 10 Septembre 2014 devant le jury compose de :

Prof. Laurence VIGNAU	Institut Polytechnique de Bordeaux	Reviewer
Prof. Dr. Ruud SCHROPP	Eindhoven University of Technology	Reviewer
Dr. Alain MADEC	Air Liquide	Examiner
Prof. Pedro ALPUIM	INL, Portugal	Examiner (President)
Prof. Yvan BONNASSIEUX	Ecole Polytechnique	Director of thesis
Dr. Jean-Eric BOURÉE	Ecole Polytechnique	Invited

Summary in English

Efficient gas-diffusion (permeation) barriers are needed for organic optoelectronic devices because the presence of moisture or oxygen can cause strong degradation. In order for these devices to operate continuously during a long term, so to be commercialized, a reliable flexible thin film encapsulation is required, which is a major challenge. Very low water vapor transmission rates of the order of 10^{-5} g/m^2.day are required. To reach this goal two ways have been adopted: on one hand fabricating SiN$_x$:H / SiN$_x$:H multilayer barriers separated by a specific Ar plasma treatment, on the other hand fabricating the conventional inorganic/organic hybrid multilayer moisture barriers.

We have chosen hot-wire chemical vapor deposition (HW-CVD) as the main technique for depositing the inorganic layers and a large part of our efforts has been devoted to the complete study of the parameters controlling the plasma treatment: the energy of the ions impinging the inorganic surfaces was crucial. Several analytical (morphological, structural, optical, electrical) techniques have been necessary to assess qualitatively and quantitatively the different layers composing the moisture barriers. A physical interpretation of the plasma process treatment has been given, based on the interface atomic rearrangements induced by the low energy ions (< 40 eV). For each way of encapsulation, we have obtained very low water vapor transmission rates (4 to 7×10^{-5} g/m^2.day). Combining above two encapsulation methods, we have achieved extremely low WVTR rate (6×10^{-6} g/m^2.day), which seems sufficient for the utilization of organic electronic devices.

Résumé en français

Les dispositifs optoélectroniques à base de matériaux organiques nécessitent la réalisation de couches barrière de perméation car l'oxygène et l'humidité dégradent fortement ces dispositifs. Afin d'augmenter leur durée de vie et ainsi les rendre commercialement attractifs, des couches d'encapsulation sont nécessaires, ceci représente un défi majeur surtout dans le cadre des substrats flexibles comme les plastiques. Des faibles valeurs du taux de perméation sont exigées, typiquement de l'ordre de 10^{-5} g/m^2.jour dans le cadre de l'eau. Deux voies ont été étudiées, dans le cadre de cette thèse, pour atteindre cet objectif: d'une part en fabriquant des barrières multicouches à base de nitrure de silicium amorphe, chaque couche étant séparée de la suivante par un traitement plasma d'argon, d'autre part en fabriquant des barrières hybrides alternant des couches inorganiques avec des couches organiques.

Nous avons choisi la technique de dépôt chimique en phase vapeur par filament chaud (HW-CVD) pour le dépôt des couches inorganiques et nos efforts ont porté sur l'étude approfondie des paramètres contrôlant le plasma. Il ressort que l'énergie des ions impactant la surface a été le paramètre déterminant. Diverses techniques d'analyse ont été nécessaires pour évaluer précisément la qualité des couches constituant les barrières de perméation. Une interprétation physique du procédé plasma a été proposée, basée sur le réarrangement atomique induit à chaque interface par les ions de faible énergie (< 40 eV). Pour chacune des voies choisies, des très faibles taux de perméation (4 à 7×10^{-5} g/m^2.jour) ont été atteints. Avec la combinaison de ces deux méthodes d'encapsulation, nous avons atteint une valeur de WVTR extrêmement faible (6×10^{-6} g/m^2.jour), ce qui semble suffisant pour l'utilisation dans des dispositifs organiques.

ACKNOWLEDGEMENTS

CONTENTS

LIST OF TABLES

LIST OF FIGURES

pressure. Reprinted from [174] with permission from 2002 Elsevier.

versus time for two 50 nm thick SiN$_x$:H single-layers separated by Ar plasma surface treatment for different RF power densities. (b) Zoom of the first region of conductances. (c) Evolution of the "lag-time" versus the Ar plasma power density of the SiN$_x$:H films. (d) Evolution of WVTR values versus the Ar plasma power density of the SiN$_x$:H films.

NOMENCLATURE

OPV	Organic Photovoltaic
OLED	Organic light-emitting diode
ITO	Indium tin oxide
WVTR	Water vapor transmission rate
OTR	Oxygen transmission rate
PVD	Physical vapor deposition
PE-CVD	Plasma enhanced chemical vapor deposition
HW-CVD	Hot wire chemical vapor deposition
ALD	Atomic layer deposition
Cat-CVD	Catalytic chemical vapor deposition
i-CVD	Initiated chemical vapor deposition
MDECR	Matrix Distributed Electron Cyclotron Resonance
PET	Polyethylene terephthalate
$SiN_x{:}H$	Amorphous silicon nitride
PMMA	Poly (methyl methacrylate)
$d_{f\text{-}s}$	Filament to substrate distance
T_{sub}	Substrate temperature
T_f	Filament temperature
AFM	Atomic force microscopy
XRD	X-ray diffraction
XRR	X-ray reflectometry
XPS	X-ray photoelectron spectroscopy
GD-OES	Glow discharge optical emission spectroscopy
FTIR	Fourier Transform Infrared Spectroscopy
UV-visible SE	Ultraviolet-visible spectroscopic ellipsometry
D	Diffusion coefficient
P	Permeation coefficient
S	Solubility coefficient
δ_{Ca}	Density of calcium
ρ_{Ca}	Thin film calcium volume resistivity

TCF	Temperature Correction Factor
TCR	Temperature Coefficient of Resistance
λ_{mfp}	Mean free path
p_g	Working gas pressure
E_w	Work function
T	Transmittance
R	Reflectance
n	Refractive index
T_g	Glass transition temperature
d_f	Single layer thickness
D_H	Hydrogen dilution
r_d	Deposition rate
I_{fil}	Filament current
F	Flow rate
d_c	Critical thickness
d_{th}	Threshold thickness
BIF	Barrier improvement factor
n_0	Plasma electron density
T_e	Electron temperature
f_i	Ionization probability
V_{Bias}	Bias voltage
P_{RF}	RF power
I_{ion}	Ion current
P_w	Power density
F_i	Ion flux
E_T	Energy transfer
E_d	Displacement threshold energy
$R_{av.}$	Average roughness
r	Radius of curvature
Y	Young's modulus
S_{eff}	Effective absorption cross-section

CHAPTER 1
INTRODUCTION

1.1 ORGANIC OPTO-ELECTRONIC DEVICES

The global energy requirement is increasing very rapidly and it is expected to double within the next 50 years due to the overall growth of the world population as well as due to the improvement in the quality of life that makes a demand on energy. Although, a large proportion (about 65-70%) of the present consumption of energy throughout the globe is dependent largely on the carbon based fossil fuels (such as oil, coal or natural gas) [1, 2], the global amount of these fossil fuels is running out very drastically. The usage of fossil fuels is held responsible for the increased molecular concentration of carbon dioxide in the earth's atmosphere. Over the past decades, due to the global awareness of the limited availability of carbon based fuels [3], the global warming [4] and increased fuel price around the world [2], the production of environment friendly, low cost renewable energy technologies is drawing intensive attention of the scientific society. In 2012, by example, the cumulative wind-power installed capacity in the world was 282 GW, whereas the photovoltaic installed capacity and solar thermal installed capacity were 102 GW and 274 GW, respectively. Photovoltaic (PV) are one of the major fastest growing alternative energy production technologies that directly convert daylight into electricity [2, 5]. There are several advantages that focus attention on it such as its ready availability, easy portability and lower production cost compared to fuel based energy technologies [2]. The PV technology has a significant potential as a renewable energy technology and just to give an idea of its potential, according to Hermann *et al*. [6] and Grossiord *et al*. [2], the total annual solar energy incident on the earth surface is estimated to be 63×10^{15} W, which is around thousand times greater than total energy requirement of the world population (i.e. about 15×10^{12} W) and this requirement is also growing very drastically every year.

The majority (about 87%: multi-Silicon~48%, mono-Silicon~38% and ribbon Silicon~1%) of the PV technology that is commercially available is based on crystalline Silicon (c-Si) according to the market share survey in 2011. The market share is growing at about 40% each year over the past decade even though it is limited by the high semiconductor batch production costs, limited availability of solar-grade Silicon material and their higher geographical location dependent installation price as compared to the conventional grid power supply. To ensure sustainable growth for PV, efforts have been devoted to the manufacture of alternative low-cost thin film solar cells and this field is now an attractive field of research [2, 7-9]. According to 2011 survey, about 13% of the

total market share of PV technology is based on thin film solar cells (a-Silicon~5%, CdTe~7% and $Cu(InGa)Se_2$~1%).

The recent advancement of Organic Photovoltaic (OPV) devices opens a new pathway to circumvent the problems of Si-based PV technology [2]. This approach is based on solar cells fabricated from organic materials, conjugated polymers and small molecules. Compared with inorganic counterparts, organic and conjugated semiconducting materials are interesting due to several reasons:

- Lightweight, low consumption of materials (very thin films ~ 100 - 200 nm thick), flexible shape, versatile materials synthesis and low cost for large scale industrial production.
- Continuous tunability of material energy levels and gap via molecular design and synthesis through the pioneering work of Heeger *et al*. on conductivity in the conjugated polymer polyacetylene (PA) [10].
- Integrability into products such as textiles (clothing), flexible packaging systems and lightweight consumer goods [2, 11].

While sustainable electricity generation is one part of the global energy problem, the other part constitutes maximal utilization of the generated electricity. With the increase of renewable energy technologies, there is a drastic need to create novel methodologies to reduce the electronic energy load and increase energy conservation. A small percentage of the consumed energy is utilized to produce illumination and the rest is wasted as heat, thus making the traditional sources of light energy inefficient. Fluorescent lamps are about four times more energy efficient, yet a significant amount of energy is still wasted [12]. Over the past few decades there was no significant improvement on the energy efficiency of conventional lighting sources and as a matter of fact, the development of new lighting technologies such as Light Emitting Diodes (LEDs) is desired and is being pursued relentlessly.

Organic light-emitting diodes (OLEDs) can be made from two broad types of materials: small molecules like the ones made for the first time by Tang and Van Slyke in 1987 in Kodak [13] and polymer materials whose electroluminescence was discovered by researchers at the University of Cambridge in 1990 [14]. During the past two decades, OLEDs have emerged rapidly due to their promising applications in flat-panel displays by replacing cathode ray tubes (CRTs) or liquid crystal displays (LCDs) [15]. They offer the convenience of flexibility and light weight coupled with wide viewing angle, high contrast and full color capability. OLEDs are energy efficient, deliver roll to roll

manufacturing capability with potential for large area color displays [15]. Some examples of flexible organic optoelectronic devices are shown in Fig. 1.1.

<center>(a)   (b)   (c)</center>
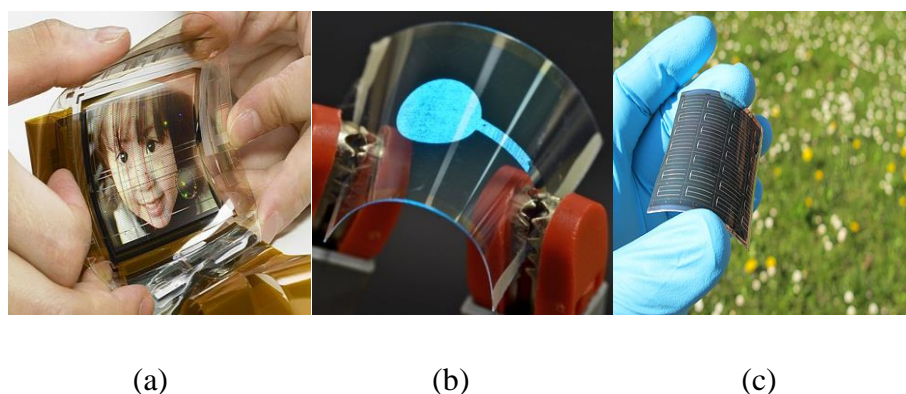
Fig. 1.1: (a) A color flexible OLED from Sony lab [16], (b) A flexible OLED device from LPICM, Ecole Polytechnique, France, (c) A flexible solar cell from EMPA [17].

1.2 CHALLENGES OF ORGANIC OPTO-ELECTRONIC DEVICES

In spite of the promising advantages of the organic electronic devices, there are some challenges that should be overcome before their wide spread industrial application. The organic opto-electronic devices usually consist of a substrate and an active layer sandwiched between a transparent anode (with high work function) and a low work function metal cathode, as shown in Fig. 1.2. The device structure is completed with some form of encapsulation above the cathode. If the substrate is permeable, as is the case with most flexible plastic materials, then an additional permeation barrier below the device layers is also necessary [18].

In these devices, the active layers exposed to the atmosphere, deteriorate rapidly and lead to the whole device failure. Efficiencies up to 8% have been reported for conjugated polymer [19], while efficiencies up to 8 to 10% [20, 21] have been reported for small molecule based photovoltaic devices respectively. Conjugated polymers are known to be unstable in air [22] and susceptible to photo-degradation induced by oxygen and moisture [23]. By example, Poly (p-phenylene vinylene) (PPV) and its derivatives are very sensitive to atmosphere. In this case, the oxygen atoms are bonded to vinyl bonds and break the conjugation and lead to the formation of carbonyl groups [23, 24]. As shown by spectroscopic ellipsometry results, during the simultaneous exposure to air and light, the thickness of the active layer increases, while its refractive index and optical absorption coefficient drastically decrease which leads to the PPV degradation [25]. In spite of the fact that the degradation

effect is significantly decreased when conjugated polymers are mixed with fullerenes [26], PPV based solar cells usually do not operate for more than a few hours in air [27].

Along with the degradation of the active layers, the metals used as cathode are highly reactive with oxygen and water vapor, and thus, oxidize very rapidly, resulting in the formation of insulating oxide barriers and making the injection and collection of charge carriers less efficient. This results in reduced device performance and efficiency. Exposure to moisture and oxygen in the environment may also lead to the formation of non-emissive areas in the OLEDs, known as dark spots, reducing their light output and lifetimes [28]. Various mechanisms of the dark spots have been reported. Crystallization of the organic material by Joule heating and local decomposition of the ITO/organic interface has been reported as the possible origins of dark spots [29, 30]. The cathode delamination is also a primary factor in the growth of the dark spots [31].
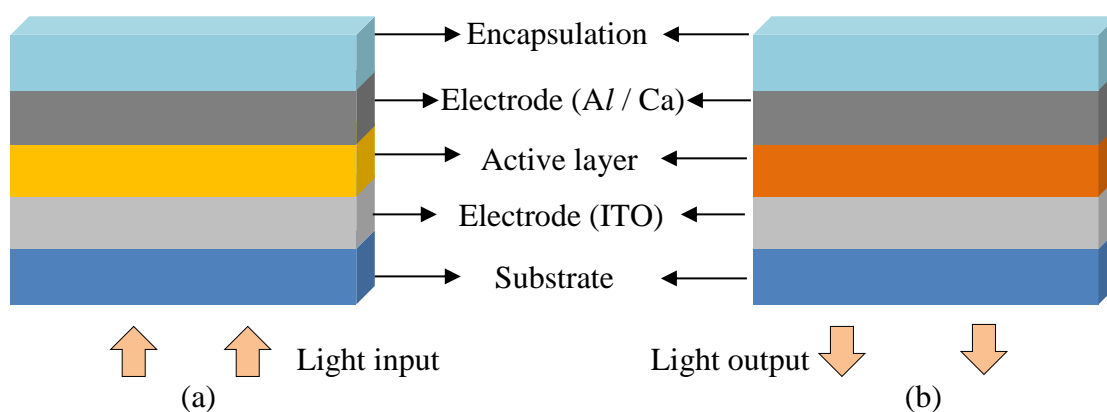
Fig. 1.2: Schematic diagram (not to scale) of: (a) Organic solar cell device and (b) Organic light emitting diode device.

Therefore, to achieve a wide spread commercial use of flexible organic devices; there are still some challenges to be overcome. Whereas, the major research in this field is based on developing stable organic active materials, this thesis addresses the other part of the problem which being making encapsulation barrier to protect the active layers and electrodes from the direct exposure to the environment. The thesis also discusses the choice of substrate.

1.2.1 Encapsulation barrier:

Most high-performance semiconducting organic compounds show degraded performance when exposed to environmental moisture. So encapsulation barrier is required. There is a wide range of

permeation barrier requirements for different devices and applications as seen in Fig. 1.3. For the normal food packaging technologies, the encapsulation barrier requirement is not as stringent as the electronic devices and a single polymer film is sufficient to provide the required efficient packaging. Generally, devices such as OLEDs that use chemically reactive electrodes have the highest sensitivity to moisture, and degradation is observed at the organic layer/ electrode interface [32-34]. The extensively used terms to define the permeability of water vapor and oxygen are water vapor transmission rate (WVTR) and oxygen transmission rate (OTR). WVTR is defined as the amount of water molecules diffusing through a unit area of the barrier film per unit time under conditions of the test and expressed as g/ m^2.day. OTR is defined as the volume of oxygen diffusing through a unit area of the barrier film per unit time under conditions of the test and expressed as cm^3/ m^2.day. The most widely quoted value for required WVTR for an OLED lifetime of >10 000 h is 1×10^{-6} g/ m^2.day. This value was originally estimated by calculating the amount of water and oxygen needed to degrade the reactive cathode [18, 34]. Other experimental methods also confirmed this value to be a reasonable estimate [35]. The required OTR for similar lifetimes have been reported to be 10^{-5} to 10^{-3} cm^3/ m^2.day [18, 36-38].

Moisture causes a degradation of both the active absorber material and the transparent front electrode for the organic photovoltaic devices [39]. Organic solar cells also need to be protected against ultraviolet light. Therefore the key parameters for an effective encapsulation of flexible organic solar cells are [40]:

- Water and oxygen resistant permeation barrier.
- High optical transmission in the visible region.
- UV stability and (depending on the absorber material) UV absorption or reflection.
- Mechanical stability against bending and local mechanical impacts like scratches or hail.
- Thermal stability in a temperature range between -40 °C and +85 °C according to IEC-61646 [41].

The permeation barrier requirements for organic solar cells are determined mainly by the solar cell absorber material that is used. A water vapor transmission rate of 10^{-6} g/ m^2.day and an oxygen transmission rate below 10^{-3} cm^3/ m^2.day were previously reported to avoid degradation of organic solar cells [42]. However, recent studies have shown that for organic solar cells WVTR in the range of 10^{-4} to 10^{-3} g/m².day is quite sufficient to achieve lifetimes of several thousands of hours in operation [43, 44]. These studies have also proved that the requirements for OPV cells are not as stringent as those of the OLED devices.
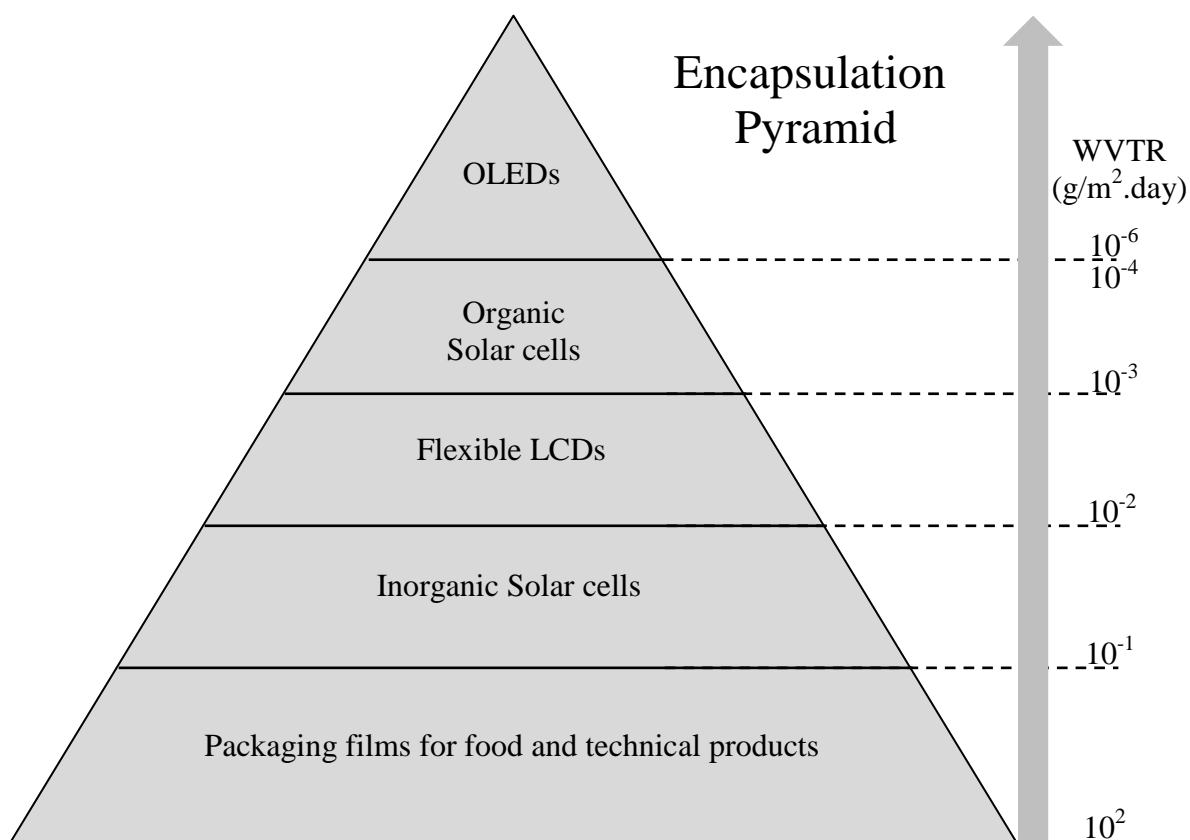
Fig. 1.3: WVTR requirements for common flexible applications including sensitive electronic devices [18, 32, 34, 43, 44].

1.2.2 Flexible substrate:

There are several considerations regarding substrate selection for organic devices including Young modulus, UV stability, dimensional stability, compatibility with process chemicals, moisture uptake and cost. The leading candidates as substrate materials for organic electronic devices are polymers, metal foils and ultrathin glass. Thin glass and metal foils both provide the same effective barrier layers, although a flexible top barrier is still required [18]. The polymeric substrates   are considered better substrates due to their flexibility, lightweight and transparency. But the major disadvantage of polymeric substrates is that they are permeable to water vapor and oxygen and thus require an additional barrier layer. The other vital aspect is the processing temperature required by the subsequent barrier layers, which is generally high, and which the polymeric substrates must be compatible with. In the endeavor to solve the latter problem the growth temperature for different inorganic thin film has been reduced [45] and the thermal stability of the polymer substrates has been improved [46].

1.3 MEASUREMENT OF PERMEATION RATES:

Permeation of oxygen and water vapor is usually measured with standard equipment from Mocon [47] and Brugger [48]. The two types of equipment have a measurement range starting at 0.0005 g/ m^2.day and 0.005 g/ m^2.day respectively [49]. The permeated species are detected by a coulometric sensor and electrolysis, respectively for the two instruments form Mocon and Brugger. However, none of the commercially available systems based on these techniques meet the sensitivity requirements for the low permeation rates required by OLEDs [18]. Therefore new techniques have been developed. One approach is the Calcium corrosion test, where an opaque metal such as Calcium is oxidized by the reaction with oxygen and moisture and becomes transparent and insulating. Measuring the optical transparency, the electrical conductivity or using mass spectrometry, the permeation rate is assessed [43, 44, 49-62]. Reported effective transmission rate sensitivity for water vapor through barrier films using the Ca-test are as low as 10^{-6} g/ m^2.day [54, 58, 60-62] and 10^{-7} g/ m^2.day [56, 59]. Although, the calcium test has the advantage of discriminating between bulk permeation and defect based permeation, it does not discriminate between oxygen and water vapor permeation. Permeation techniques using an ultra-high vacuum have been used to obtain OTR (oxygen transmission rate) measurements as low as 1×10^{-6} cm^3/ m^2.day by a residual gas analyzer. But the same technique for water vapor is very difficult due to the longer pumping times [18, 49].

To measure reliable water transmission rate, the other approach that is used is known as the tritium transmission rate (TTR) measurement using a radioactive HTO (hydrogen-tritium-oxygen) tracer method [49, 63-65]. HTO is the source of tritium that can diffuse through the films either as molecular HTO or possibly as tritium atoms. The detection limit of WVTR is below ~1×10^{-6} g/ m^2.day.

1.4 ENCAPSULATION BARRIER TECHNOLOGY:

Before the development of organic electronic technology, most of the encapsulation barrier research was for sensitive food and medicinal packaging. As discussed above, the requirement for encapsulation barrier for those applications is not quite rigorous and requires a WVTR in the range between 1 - 40 g/ m^2.day. Thin monolithic polymeric films are quite sufficient for such applications. The basic research in the field of barrier technologies for food and medicines provide the basic concepts for developing ultra-high efficiency barrier technology required for the sensitive organic electronic devices. A number of methods currently exist for the encapsulation of organic electronics, including the hermetic sealing of devices fabricated on glass substrates using a metal or glass lid. While these structures can protect organic devices from water vapor and oxygen effectively, such

packaging architectures are not amenable to flexible applications where the devices are based on flexible polymer substrates, which is a major thrust area for future organic electronics. Hence, instead of rigid encapsulation, thin film encapsulation is attractive because of its flexibility and light weight. However, there exist several constraints on the development and utilization of thin film encapsulation. The desirable characteristics for the permeation barrier films are their high density, limited defects, good adhesion, thermal stability and uniform thickness. Moreover high electrical resistivity, high transparency and low residual stress properties are needed for these materials. Additionally, they must be deposited at low temperatures in order to be compatible with the plastic substrates [40]. Throughout the past few decades, the development of highly efficient barrier layers for organic electronic devices has been one of the major research areas and most of the research was based on developing either single-layer thin films or multi-layer or alternating layer thin films to provide the aspired barrier performance.

1.4.1 Single-layer thin film barrier:

Single-layer thin film encapsulation technology is probably the most popular barrier process because it reduces the production complexity and the manufacturing costs. Several technologies currently exists for the development of encapsulating single-layer thin films, such as physical vapor deposition (PVD), plasma enhanced chemical vapor deposition (PE-CVD), atomic layer deposition (ALD) and hot wire chemical vapor deposition (HW-CVD). In spite of their lucrative production advantages, very thin single layers of transparent materials such as silica, silicon nitride or alumina, often used as barrier layers, contain extensive pinholes through which water molecules can diffuse up to the organic device surface and thus deteriorate the device performance [35, 66-68]. The development of defects, pin holes or micro-voids occurs due to the poor cleaning process of the substrate, the processing conditions and the lowering of the substrate temperature to be compatible with the underlying polymeric substrate. The surface mobility of precursors during deposition goes down with substrate temperature; higher porosity and a higher density of pinholes are expected in low temperature thin films compared to the high temperature ones [69]. An arbitrary classification based on three different types of defects in single-layer thin films as shown in Fig. 1.4, their respective contributions depend on the size of the permeant molecules (usually 0.2 - 0.3 nm in size), and the number and size of each class of defect; (a) unhindered transport through 'macro-defects' (> 100 nm), (b) hindered transport through 'nano-defects' (1 - 10 nm), and (c) hindered transport through the amorphous lattice of the film (interstice < 1 nm) [70]. Copious amount of research has been focused on minimizing the number and size of defects in a single layer coating.
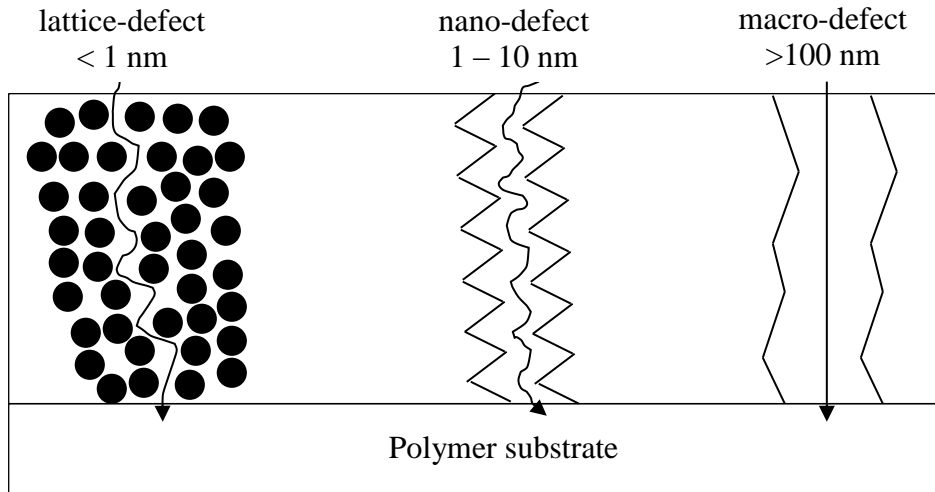
Fig. 1. 4: A schematic diagram showing the different gas transport pathways through different types of defects inside single-layer thin film [70].

The leading barrier technology in the industries is based on development of thin films using the PE-CVD method. Most of the barrier films are based on bulk oxides, nitrides or oxynitrides. Although all these materials offer barrier encapsulation properties compared to the bare substrates, their performance is mainly limited by the large defect densities. Commonly used silicon oxide or silicon nitride deposited by PE-CVD systems, show a WVTR of 0.01 g/ m^2.day, which is several orders of magnitude greater than the targeted requirements [71-74].

Compared to the existing technologies, ALD has shown remarkable achievement towards making thin film barrier technology. Several researchers have shown promising single-layer encapsulation by ALD grown Aluminum Oxide (Al$_2$O$_3$), due to their conformal deposition, low defect density and ability to be deposited at low substrate temperature [75-77]. The effective WVTR value measured for ALD grown 25 nm of Al$_2$O$_3$ is 1.7×10^{-5} g/m^2.day [52], which is sufficient for the longer lifetimes for both OPV and OLED devices. Recently, Yang *et al*. has reported that Al$_2$O$_3$ grown by ALD has a WVTR value of 8.7×10^{-6} g/m^2.day [78]. This value is the best barrier value for a single layer film within the best of our knowledge. Other than using Al$_2$O$_3$, Seo *et al*. reported a WVTR of 6×10^{-4} g/m^2.day using ALD grown TiO$_2$ films [79]. Although ALD grown films shows promise of good barrier performance, the processing method is quite slow (~1 nm/min) compared to the other CVD methods (PE-CVD, HW-CVD) and the number of materials that can be deposited using ALD is limited.

Some researchers used HW-CVD method to deposit single layer films on plastic substrates. This technique offers many advantages compared to conventional PE-CVD method, like low substrate damage (due to absence of ion bombardments) during processing, low hydrogen content (or high density) of the deposited material and conformal step coverage [60-62, 69, 80-86]. HW-CVD also allows faster growth rate compared to ALD method. Heya et al. has reported HW-CVD grown SiN_x single-layer coating of a polyethylene terephthalate (PET) substrate at 100 °C and they obtained a WVTR of 0.01 g/m^2.day [85]. Kim et al. demonstrated high density SiN_x passivation layer deposited by catalyzer-enhanced CVD method at a substrate temperature of 50 °C and achieved a WVTR of (2-6) $\times$ 10^{-3} g/m^2.day [87]. The SiN_x films with thickness of 50 nm were prepared by HW-CVD method on the cyclic olefin copolymer (COC) and the PET substrates. MOCON and Ca degradation test measurement resulted in a WVTR value of 0.02 g/m^2.day for PET and 0.006 g/m^2.day for COC after SiN_x deposition [88]. Hiroshi Nakayama et al. have developed a single layer of amorphous SiCN grown by organic Cat-CVD (Catalytic CVD) method with a thickness of 100 nm and they have measured the permeation value less than 1 mg/m^2.day. This value changed from 5 $\times$ 10^{-1} g/m^2.day to 1 $\times$ 10^{-3} g/m^2.day, corresponding to the W-filament temperature increase from 100 °C to 1200 °C [89].

1.4.2 Multilayer thin film encapsulation

As the limited performance of single-layer thin film encapsulation is mainly due to their high defect densities, the number of defects must be reduced or the effect of defects must be minimized [40]. Multilayer or alternating layers of thin films are widely used to minimize the propagation of defects or pinholes from one single-layer to the next single-layer film and thus improving the overall barrier performance of the structure [18, 35, 90-92]. The propagation of defects are interrupted using either a multi-layer structure of the same inorganic thin-film or alternating-layer structure of two different inorganic thin films or hybrid layer structure of inorganic / organic thin films. The idea is to hinder the propagation of pinholes and create a tortuous diffusion pathway for the diffusing permeant molecules through the barrier, as shown in Fig. 1.5.
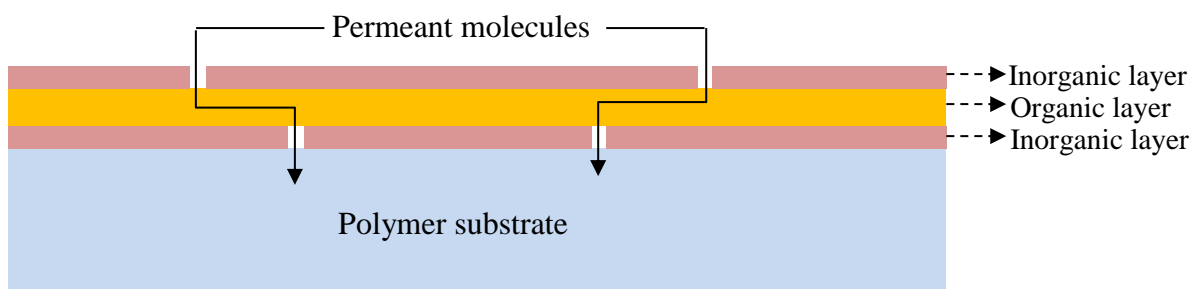
Fig. 1.5: Schematic diagram of multilayer or alternating layer barrier structure. The intermediate layer is either inorganic thin film (several nm) or organic thin layer (several nm to μm).

The most effective commercialization of encapsulating barrier technology is based on making hybrid layer structure consisting of two hard inorganic thin films separated by a soft organic layer. The organic layer hinders the propagation of defects and makes the diffusion path more circuitous, while absorbing the stress induced inside the inorganic layers and thus making the whole structure more flexible. The Barix^{TM} encapsulation coating from Vitex Inc. has reported an estimated effective WVTR equivalent to 2×10^{-6} g/m^2.day at ambient conditions measured using Ca corrosion tests [38]. This geometry uses several dyads (pair of organic and inorganic layer) of PVD grown AlO$_x$ and UV curable acrylate monomers which can be deposited in a roll-to-roll process in vacuum. General Electric has developed a graded barrier layer by PE-CVD [93, 94], consisting of an organosilicon (SiO$_x$C$_y$) and inorganic SiO$_x$N$_y$ alternating layers deposited by PE-CVD. The reported effective WVTRs for various graded films range from 5×10^{-6} g/m^2.day to 5×10^{-5} g/m^2.day. Recently, Tera Barrier Films has developed an alternating layer structure consisting of inorganic oxide layers and intermediate nanoparticle sealing layer to fill-up the pinholes inside the inorganic layers by the nanoparticles. The reported barrier performance for this structure is 10^{-6} g/m^2.day [95]. Akedo *et al*. have demonstrated an OLED device lifetime of >1000 h at 85 °C using monolithic thin film encapsulation consisting of PE-CVD SiN$_x$ / plasma-polymerized CN$_x$:H multilayer stack [96]. T.-N. Chen *et al*. reported that the effective WVTR of their combined SiO$_x$ / SiN$_x$ / parylene barrier structure on polycarbonate substrates was found to be 2.5×10^{-7} g/m^2.day at 25 °C and 45 % RH [91]. These values are to the best of our knowledge the lowest effective WVTR measurements reported. Chwang *et al*. reported the lifetime for encapsulated phosphorescent OLEDs (PHOLEDs) fabricated on glass and barrier coated plastic substrate as 3700 h and 2500 h respectively at ambient condition [92]. This encapsulation consists of 4-5 pairs of alternating Al$_2$O$_3$ and polyacrylate. Lungenshmied et al. used alternating SiO$_x$ and organosilicon deposited by PE-CVD on the PEN substrate [97]. Yoshida *et al*. used a UV curable resin / SiON layer pairs as a moisture barrier film to achieve the desired OLED barrier performance [98]. Seo *et al*. has demonstrated ALD grown nanolaminate layer structure comprising of Al$_2$O$_3$ / ZrO$_2$ with WVTR of 2×10^{-4} g/m^2.day [99]. The

same group has shown extremely bendable hybrid encapsulation layer consisting of ALD grown Al_2O_3 and plasma polymerized layers with effective WVTR of 10^{-4} g/m^2.day even after 10 000 times of bending [100]. Multilayer dyads composed of silica nano-particle embedded hybrid nano-composite (S-H) and ALD grown MgO has demonstrated excellent barrier properties with WVTR of 4.33×10^{-6} g/m^2.day [101]. Ogawa *et al*. has prepared Cat-CVD grown SiN_x / SiO_xN_y stacked films to protect OLEDs and they succeeded in maintaining the initial intensity over 1000 h under 60 °C and 90% RH, which is equivalent to 50 000 h in normal temperature and humidity conditions [84]. The improvement of the barrier properties is due to the blocking of propagation of pinholes from the underlying SiN_x layer by the less dense and flexible SiO_xN_y layer. Recently, Spee *et al*. has reported a hybrid layer structure consisting of SiN_x and PGMA layers, where the inorganic thin film was deposited inside a HW-CVD reactor and the organic layer was deposited inside an initiated CVD (iCVD) reactor. Their reported WVTR was 5×10^{-6} g/m^2.day which was sufficient for the longer lifetimes for OLED devices [69].

1.5 OBJECTIVE AND ORGANIZATION OF DISSERTATION:

The reliability issues of the organic electronic devices must the solved in order for their wide spread commercialization. As discussed above, the thin film technology is the most promising encapsulation method due to its light weight, flexibility and low cost roll to roll production. Hence, the primary objective of this present work is developing ultra-high barrier encapsulation structure using the thin film technology to be incorporated in real organic electronic devices.

In this work silicon nitride (SiN_x:H) thin films have been chosen as an effective inorganic barrier material. The benefit of SiN_x:H films over other oxide materials is that it does not require reactive oxygen atoms in the deposition process, which could react in an undesirable manner with the underlying polymer substrates. The advantage of SiN_x:H over other metal nitrides is that it is more transparent and also that gaseous precursors for plasma-based deposition are more readily available, e.g., in the form of silanes [102]. The present research work is divided into two separate parts consisting of two different barrier technology methods.

The major part of the present work is based on a unique process of formation of barrier method consisting of deposition of multilayer stack of SiN_x:H single-layers deposited on Polyethylene terephthalate (PET) substrates, each single-layer being surface-treated by low energy Argon plasma treatment. We have chosen Hot Wire Chemical Vapor Deposition (HW-CVD) method to deposit the SiN_x:H films because of the lower hydrogen content inside the film and its higher density compared

to the conventional material obtained by plasma assisted CVD techniques and it's faster growth rate compared to ALD method. The idea behind the use of the Argon plasma surface treatment between two successive SiN_x:H single-layers is to hinder the propagation of the pinholes from one single-layer to the other. The ionic bombardment by low energy Argon ions on the surface of the SiN_x:H thin films makes an atomic relocation at the interface and a smoothing of the surface, which impedes the diffusion of permeant molecules throughout the whole layer thickness.

The second part of the thesis deals with the development of the conventional alternating layer structure containing inorganic / organic / inorganic thin layers. The first portion of this work consists of the alternating layer stacks composed of Matrix Distributed Electron Cyclotron Resonance (MDECR)-PECVD grown SiN_x:H films separated by a spin-coated PMMA [Poly (methyl methacrylate)] polymer layer. The use of MDECR-PECVD technology for deposition of optical thin films offers several advantages over conventional radio frequency capacitive-coupled PECVD, such as faster growth rates, superior control of the deposition process, relatively low ion bombardment energy and the possibility to use lower substrate temperatures [103-105]. The PMMA polymer is chosen because it is widely used and inexpensive. Next the alternating layer stacks composed of HW-CVD grown SiN_x:H films separated by a spin-coated PMMA polymer layer is presented in order to compare the barrier properties with the MDECR PE-CVD grown samples.

The barrier layers have been characterized using different characterization methods which includes the structural, morphological, optical and mechanical characterizations. Utilizing the electrical Ca corrosion method to quantify ultra-low permeation through these films is discussed. Finally, permeation mechanism through these films is demonstrated and discussed.

After the general introduction (chapter 1), chapter 2 consists of brief descriptions of the film deposition techniques as well as all the characterization methods used in this thesis. The growth mechanisms and characteristics of the HW-CVD grown SiN_x:H films are discussed in Chapter 3. Chapter 4 describes the main part of this thesis, i.e. the barrier properties of the Argon plasma treated SiN_x:H films and their simple physical interpretation deduced from the experimental study of permeation barrier versus several parameters. The conventional inorganic / organic hybrid layer barrier structures and their properties are introduced in Chapter 5. Chapter 6 consists of combination of two separate encapsulation methods and application of barriers on OLED devices. Finally all the studies discussed throughout this thesis are summarized in Chapter 7.

CHAPTER 2

EXPERIMENTAL TECHNIQUES

This chapter is devoted to the experimental techniques used in this study. Firstly, the film deposition techniques and plasma treatment technique are described. Next, the characterization techniques (morphological, structural, optical, electrical and mechanical) are described. Finally, the specific technical points are summarized.

2.1 BARRIER FILM DEPOSITION SYSTEMS

The amorphous silicon nitride (SiN_x:H) thin films studied throughout this thesis as a permeation barrier layer, have been deposited using Hot Wire Chemical Vapor Deposition (HW-CVD) system for the most part. The argon plasma treatment between each successive SiN_x:H single-layer films to reduce the water molecule permeability, which is the main objective of this thesis, is carried out inside a glow discharge radio frequency plasma enhanced chemical vapor deposition system. In the organic- inorganic hybrid structure which is another part of this thesis, the organic polymer film is grown by widely used spin coating technique. A minor part of this thesis is devoted to the development of inorganic-organic hybrid structure, where the inorganic (SiN_x:H) layer is deposited by Matrix Distributed Electron Cyclotron Resonance Plasma Enhanced Chemical Vapor Deposition (MDECR-PECVD) system in order to compare the barrier properties with HW-CVD grown samples.

The sequence of HW-CVD film deposition and the argon plasma treatment is carried out in a twin chamber CVD system situated inside a clean-room located at International Iberian Nanotechnology Laboratory, Braga, Portugal, under the supervision of Prof. Alpuim. The twin chamber CVD system is described first. This is followed by descriptions of MDECR-PECVD system situated at LPICM, Ecole Polytechnique, France under the supervision of Dr. Bulkin. The organic layers are deposited by spin-coating system which is described after that.

2.1.1 Twin chamber CVD system

The twin chamber CVD system consisting of both HW-CVD and PE-CVD reactors are shown in Fig. 2.1 (a) and the pictures of the HW-CVD reactor and PE-CVD reactor are shown in Fig. 2.1 (b) and (c) respectively. This is an ultra-high vacuum CVD system. The system is equipped with cold-cathode Penning gauges for measuring the base pressure inside each of the three chambers (including

the load-lock) and Baratron capacitive gauges to measure the working pressure in each deposition chamber. The chambers are pumped independently by two dedicated systems consisting of one turbo-molecular and one rotary pump for each chamber.

<center>(a)   (b)   (c)</center>
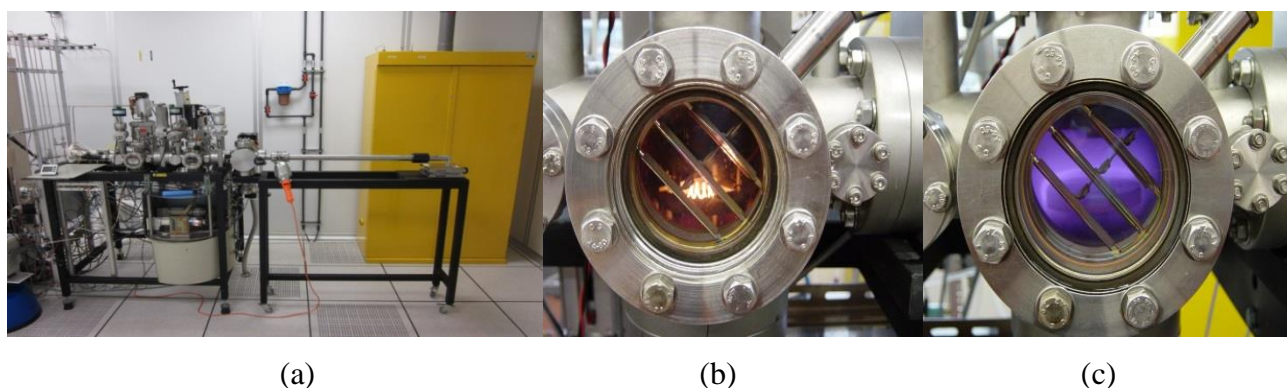
Fig. 2.1: (a) The twin chamber (HW-CVD and PE-CVD) CVD system at International Iberian Nanotechnology Laboratory, Braga, Portugal. (b) The HW-CVD chamber showing the glowing filament. (c) The PE-CVD chamber showing the glow discharge.

2.1.1.1 HW-CVD chamber

Fig. 2.2 shows the schematic diagram of the inner vessel in the HW-CVD chamber. The process gas lines connect to a manifold where the gases are mixed previously to their injection in the chamber using a feed-through through the reactor wall. A filament is mounted to an electrode at the bottom of the chamber and it is electrically connected to a current supply. For the study in this thesis, the filament is a single-coil shaped tantalum (Ta) filament with 0.5 mm of diameter and 15 cm of length. The filament acts as a catalyst, providing thereby the surface for heterogeneous pyrolytic decomposition of the reactant gases into radicals, which are the precursors for the thin film growth.

The substrates are mounted in a sample holder which is able to accommodate samples with dimensions up to 3.3×3.3 cm^2. The sample holder is introduced into the load-lock which is then pumped down to a pressure of $\sim 5 \times 10^{-6}$ Torr and is then transferred into the reaction chamber, without breaking the vacuum, with the help of a magnetic arm. The sample holder is then remotely clamped (using a motion feed-through) to the heated sample holder support that stays on the top side of the HW-CVD chamber. The substrate faces down, at a fixed distance from the filament so that any powder that could fall from the system moving parts during load and unload or from the shutter will not reach the sample surface. In order to reduce the radiation damage to the plastic substrates from the glowing filament a large distance (d_{f-s}) of 7.5 cm was established between filament and substrate holder. The substrate temperature (T_s) is fixed at 100 °C in order stay near the glass transition

<center>15</center>

temperature of the plastic substrates. The substrate temperature is measured with a thermocouple embedded in the stainless steel substrate-holder, close to the substrate. During the filament heating time, a shutter is moved to the closed position in order to protect the substrate from the spurious species emitted from the filament.

The reactor is equipped with eight lines of different process gases. The source gases are mixed in a manifold and injected in the chamber through the side wall. The flow rates are controlled by mass flow controllers.

The three chambers (HW-CVD, PE-CVD and load-lock) are separated by gate valves. This gate valve system allows transferring the samples from chamber to chamber with the help of a magnetic transfer arm that stays parked in the load lock during depositions. In this way any sequence of SiN_x:H depositions and argon treatments can be performed without ever breaking the vacuum.

The deposition of thin films was performed in several steps as discussed below:

i)   The substrate is fixed inside the substrate holder and then is loaded into the load lock which is then pumped down to ~5×10^{-6} Torr before the substrate holder is transferred into the HW-CVD chamber using the magnetic arm.

ii)   The substrate holder is resistively heated to the substrate deposition temperature (T_s) by the embedded resistor in the sample holder support, connected to a thyristor and controlled by a Eurotherm controller. The temperature reading for the feedback allowing the system to operate in closed loop control mode is provided by a thermocouple also embedded in the substrate holder support.

iii)   Filaments are degassed under hydrogen atmosphere for several minutes at a very high temperature corresponding to a certain filament current value to obtain desired filament temperature (T_f) (2000 °C). The shutter is kept closed in this step to protect the substrate.

iv)   A mixture of source gases is injected when T_s actual reading was identical to the set point and stable. The shutter remains closed.

v)   The shutter is opened to start the deposition at a stabilized substrate temperature (T_s).

vi)   At the end of the deposition, the shutter is closed and gas flow is stopped. The filament is slowly turned off and the heating of the substrate is also turned off.

There are several parameters which are varied in order to obtain optimized growth condition for SiN_x:H deposition. The details of growth mechanism and the growth optimization parameters and process are discussed in chapter 3.
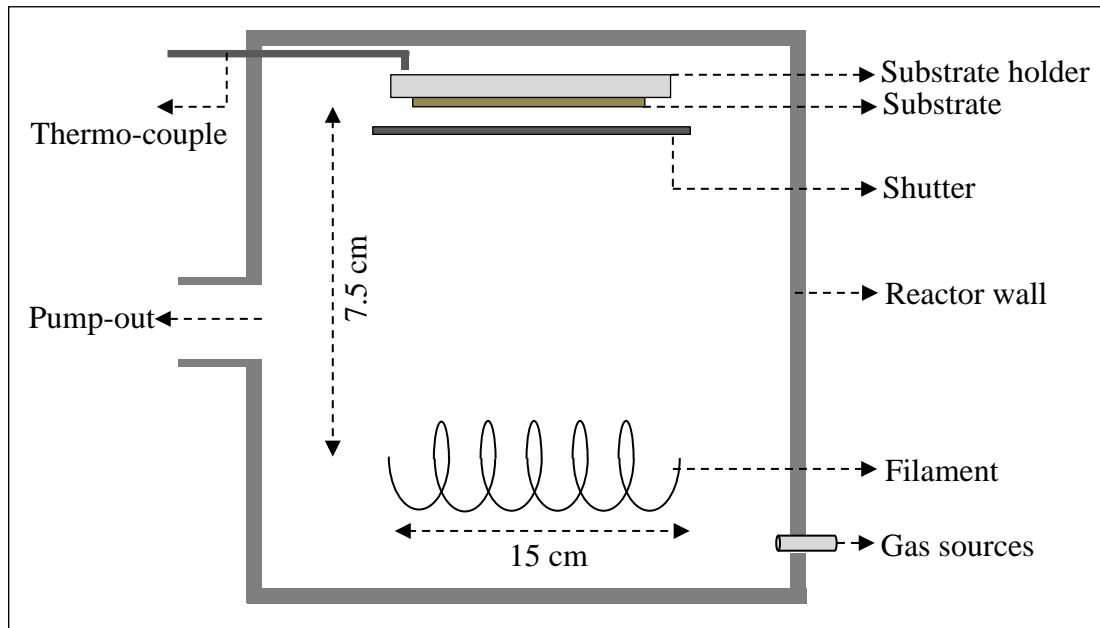
Fig. 2.2: Schematic diagram (not to scale) of the HW-CVD chamber.

2.1.1.2 RF PE-CVD chamber

The sequence of SiN_x:H deposition and the argon plasma surface treatment is carried out by moving the sample between chambers inside the twin chamber CVD system. After the deposition of SiN_x:H thin film inside the HW-CVD chamber, the sample is transferred to the PE-CVD chamber through the gate-valve without breaking the vacuum.

The reactor is part of a twin chamber system and is described above. Fig. 2.3 shows the schematic diagram of the inner vessel. It is similar to the HW-CVD reactor except that the filament electrode is replaced here by the RF electrode (anode) which is a stainless steel disc situated inside and at the bottom of the chamber. The substrate holder support is used as the top electrode (cathode) and is grounded to earth. The bottom electrode is connected through an electrical feed-through to the external RF circuit (see figure) consisting of a 13.56 MHz RF generator, a matching box consisting of variable capacitances and inductances and an attenuator to allow the 500 W RF power supply to be operated at about its midrange for better stability and control. The dimensions of the electrodes are 20 cm^2 and the adjustable inter-electrode distance used is 2.5 cm. The self-bias voltage that develops at the electrode is measured by the control electronics and is part of the matching box self-tuning control circuit. The same sample holder used for the HW-CVD chamber is used for the PE-CVD chamber. The sample holder is clamped to the top electrode of the reactor and connected to an independent electrical heating circuit similar to the one used for the HW-CVD chamber. The

substrate temperature (T_s) is fixed at 100 °C in order to be compatible with the work on plastic substrates. The substrate temperature is measured with a thermocouple embedded in a stainless steel substrate-holder, close to the substrate. Electrical measurements are performed with a 2-channel 60 MHz Digital Oscilloscope Agilent in order to measure the voltage drops at different points in the RF circuit (see schematic circuit drawing).

There are several parameters which are varied for the surface plasma treatment method. The details of parameters and their respective effects on the overall permeation barrier properties are discussed in Chapter 4.
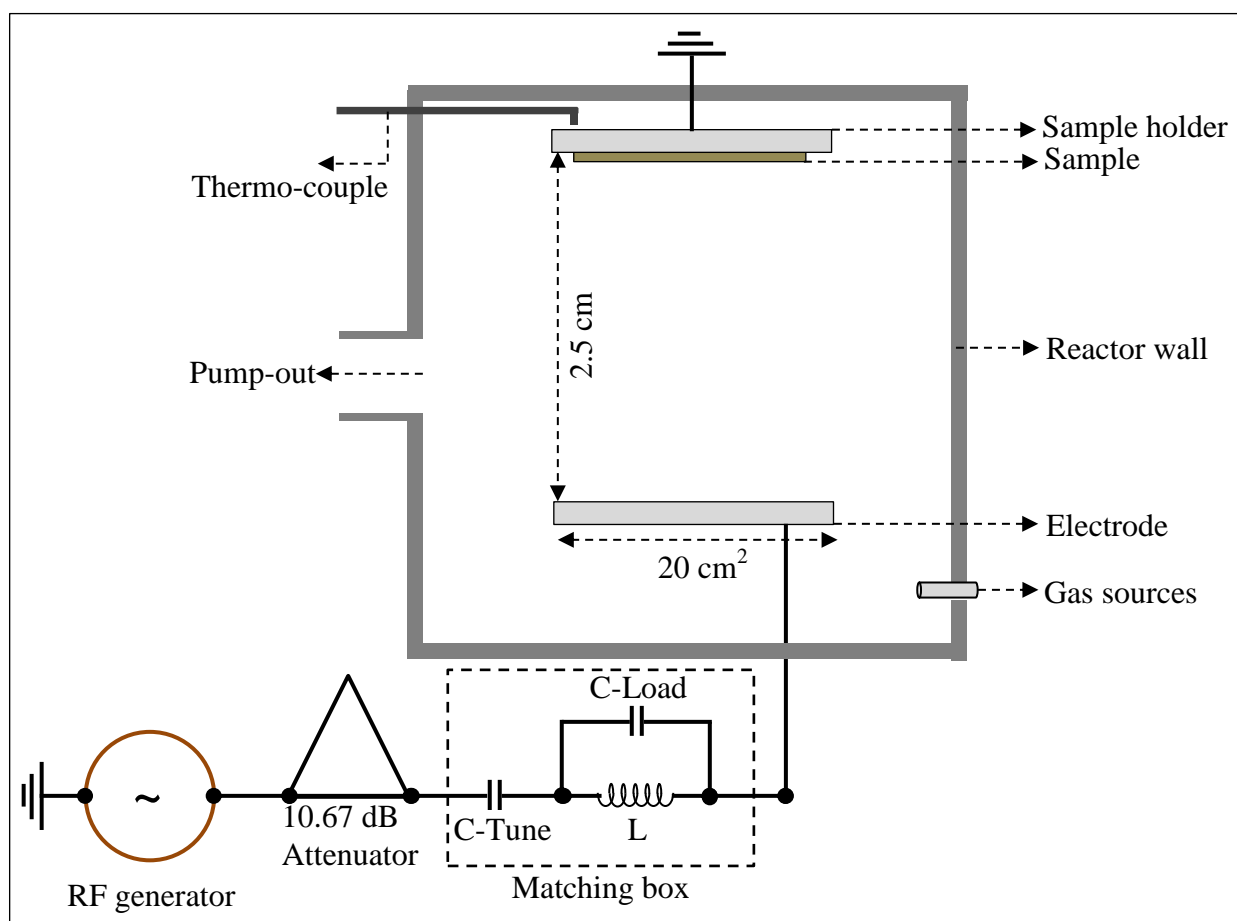
Fig. 2.3: Schematic diagram (not to scale) of the PE-CVD reactor for the argon treatment.

2.1.2 Matrix Distributed Electron Cyclotron Resonance PECVD (MDECR-PECVD)

The MDECR-PECVD Venus system available at LPICM, Ecole Polytechnique is used in a short part of this thesis for the development of inorganic SiN$_x$:H thin film to fabricate inorganic / organic / inorganic hybrid structure. The dedicated MDECR-PECVD system is a high density plasma CVD system and allows faster growth rates, superior control of the deposition process, relatively low ion

bombardment energy and the possibility to use lower substrate temperatures as compared to the conventional capacitive-coupled PE-CVD system [103].

The reactor is composed of a 50 litre cylindrical vacuum chamber and a turbo-molecular pump as shown in Fig. 2.4 (a) and (b). The reactor is equipped with two 2.45 GHz magnetron generators to supply the microwave power. The microwave power is fed into the reactor using flexible coaxial cables to a set of 16 microwave antennas. The antennas are integrated with a $SmCo_5$ permanent magnet and arranged in 4×4 matrix configuration. The antenna to the substrate holder distance is approximately 12 cm and the substrate holder (22 cm diameter) is kept horizontally inside the reactor chamber. A gas distribution ring injects the precursor gases uniformly onto the substrate area [104].

The detailed microwave antenna matrix configurations and the deposition procedure and mechanism were already discussed extensively in a previous dedicated thesis [105] and previous publications [103, 104]. In this present thesis, the amorphous SiN_x:H thin film as a permeation barrier layer was deposited utilizing the previous optimized deposition conditions. The SiN_x:H films are deposited on cleaned PET substrates at room temperature and low pressure (2 mTorr) in the MDECR-PECVD reactor with 1000 W microwave power with a deposition rate of ~6 Å/s. The precursor gases SiH_4 and N_2 are injected into the reactor through the gas distribution rings with gas flow rates of 10 sccm and 80 sccm respectively.

(a)

Microwave Connections

Impedance Matching unit

Microwave antenna & magnets

Injection of oxidants

ECR region

12 cm

Gas sources
Substrate holder

Substrate

22 cm

Pump out

(b)
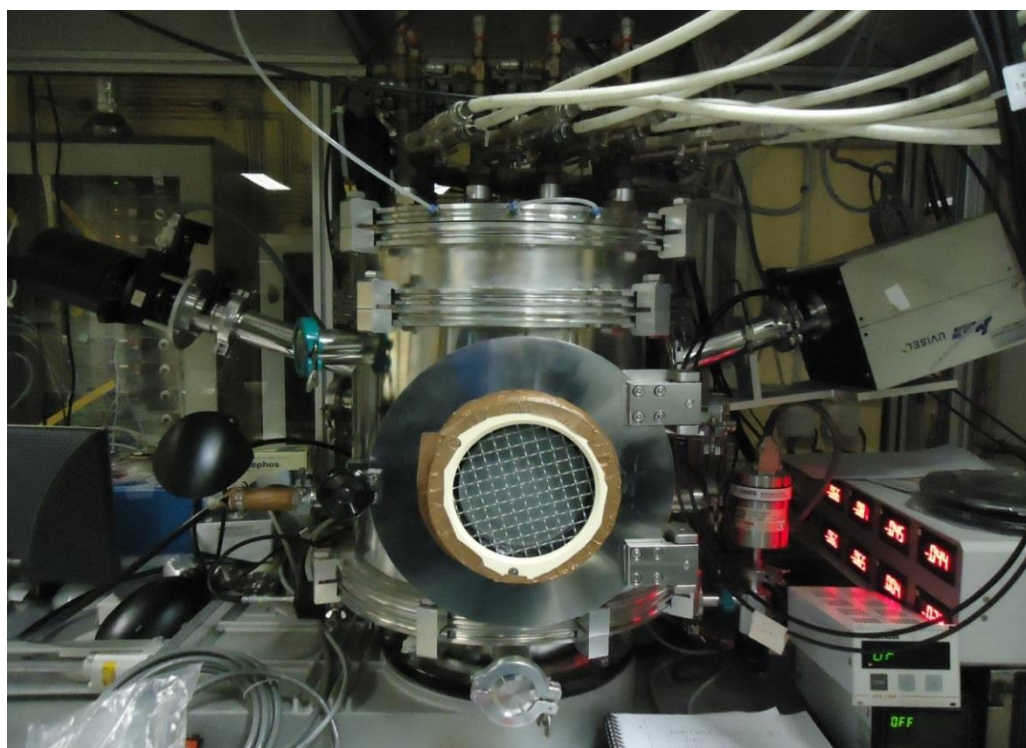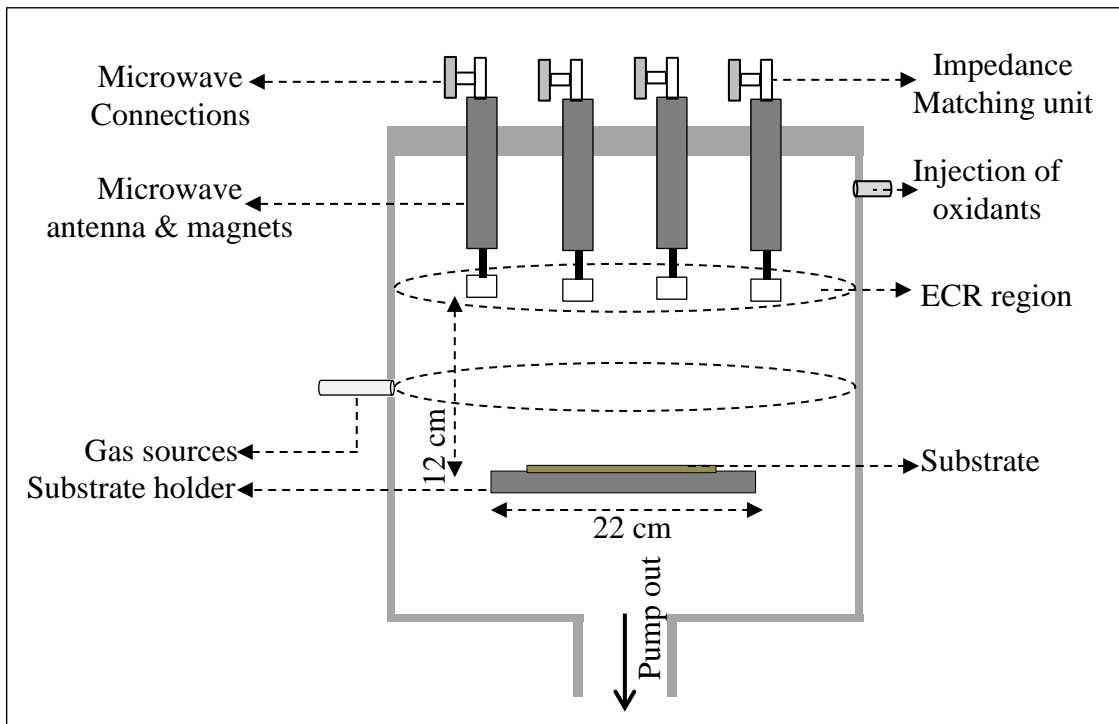
Fig. 2.4: (a) The MDECR-PECVD Venus system at LPICM, Ecole Polytechnique. (b) Schematic diagram (not to scale) of the deposition reactor.

2.1.3 Spin coating

Spin coating is a widely used technique for the deposition of thin films. A typical process involves depositing drop of material solution onto the middle of the substrate and spinning the sample with different spinning parameters followed by a drying process. Due to the centripetal acceleration, the solution spreads over the entire substrate growing a thin layer of the material. The film thickness on the substrate depends on the solution density and the speed of the rotation.

The typical spin-coater system consists of a rotating plate (chuck) on top of a rotator. The entire system is covered by a glass cover to avoid the spreading of the solution outside the system. The chuck is integrated with a needle-hole creating small vacuum to stabilize the substrate while spinning. The rotation speed, acceleration and time are controlled by an outside electronic system.
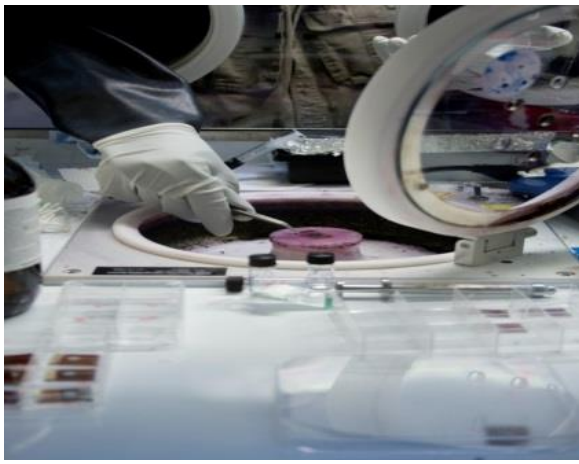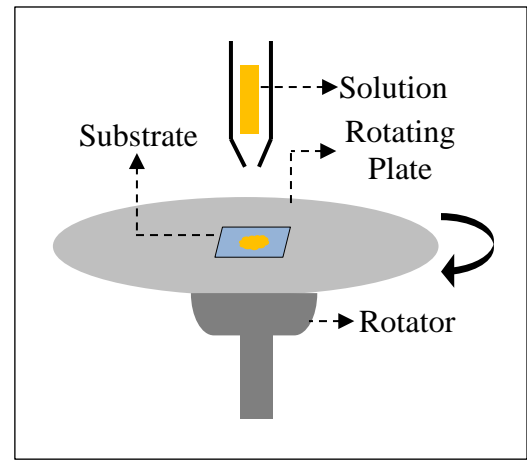
<div align="center">(a)   (b)</div>

Fig. 2.5: (a) The spin-coating system inside the glove-box at LPICM, Ecole Polytechnique. (b) Schematic diagram (not to scale) of the operation of the system.

In order to develop alternating hard-soft inorganic / organic like structure, polymer layers are deposited by spin-coating technique inside the glove-box between two inorganic layers. The commercially available PMMA [Poly (methyl methacrylate)] (from Sigma Aldrich) is dissolved in chloroform (5 wt. %) and the solution is spin-coated on the already grown SiN_x:H film at different speeds followed by an annealing treatment at 100 °C for 30 min. The optimization of the rotation speed with the variation of the film thickness and characterization of the film are discussed in chapter 5.

2.2 MORPHOLOGICAL CHARACTERIZATION

2.2.1 Profilometry

Before evaluating the exact optical constants using the spectroscopic ellipsometer, the film thickness is estimated using a profilometer with the precision of ≈100 Å and with a force of 10 mg. For the study in this thesis, Dektak 150 profilometer is used to evaluate the film thickness deposited either on crystalline silicon or glass substrate. At least ten thickness measurements are taken on the film along the centerline of the substrate to see the homogeneity of the film thickness.

2.2.2　Atomic force microscopy (AFM)

The morphological analysis such as roughness of the barrier films is carried out using the atomic force microscopy (AFM) technique. A small and sharp nanometer size probe, usually made of silicon or silicon nitride, mounted on a flexible cantilever moves on the sample surface under van der Waals

interaction force effect, which is controlled to be constant by keeping the distance between the probe and the sample surface constant. The scan along the x and y axes and the control of the distance between the probe and the sample surface along the z axis are generally performed by using piezoelectric scanners. The cantilever deflection is detected using a laser spot reflected from the cantilever onto photodiodes.

The measurements are performed using tapping mode of AFM (Integrated Dynamics Engineering) at a certain frequency for different sizes of the acquisition zones. The tapping mode allows one to carry out non-destructive measurements without influence of adsorbed layers. The change in frequency induced by van der Waals interaction force is detected in order to control the distance between the probe and the film surface.

2.3 STRUCTURAL CHARACTERIZATION

2.3.1   X-ray diffraction (XRD)

X-ray diffraction (XRD) is an instrumental technique that allows determining the crystalline and amorphous phases of materials. When an incident X-ray beam interacts with the planes of atoms inside the material, part of the beam is transmitted, part is absorbed by the material, part is refracted and scattered, and part is diffracted. By applying the Bragg's law of diffraction, we can measure the distances between the planes of the atoms that constitute the material. Bragg's Law is $n'\lambda=2d\,sin\theta$, where the integer n' is the order of the diffracted beam, λ is the wavelength of the incident X-ray beam, d is the distance between adjacent planes of atoms (the d-spacings), and θ is the angle of incidence of the X-ray beam to the surface. The characteristic set of d-spacings and their intensity generated in a typical X-ray scan provide a unique "fingerprint" of the phases present in the sample. When properly interpreted, by comparison with standard reference patterns and measurements, this "fingerprint" allows for identification of the material. Presence of an amorphous material in the sample can be determined by occurrence of specific wide halo on diffraction pattern. XRD patterns shown in this thesis were obtained from measurements performed at room temperature with the K_α line of Cu radiation with λ of 1.54 Å issued from an electrical generator (40 kV, 45 mA).

2.3.2   X-ray reflectometry (XRR)

The as deposited and argon plasma treated thin films have been characterized using X-ray reflectometry method in order to obtain the precise film thickness, the mass density of the films and surface roughness. This study involves irradiation of a parallel and monochromatic beam of X-ray on

the film surface and study the variation of reflected beam intensity with the variation of the angle of incidence (θ), measured as usual in X-ray scattering, to the surface and not to the normal to the surface.

In the X-ray field, where the scattering by all the electrons of the solid is important and far from any absorption, the refractive index (n) of material is less than the refractive index in vacuum and slightly less than 1. When the X-ray beam is incident on a flat surface with an angle equal to or less than the critical angle of total reflection (θ_c), generally 1° maximum, total reflection occurs. This is the reason why the surface under analysis should be as flat as possible. The refractive index (n) of the material is given by the following relationship [106]:

$$n = 1 - \delta - i\beta \tag{2.1}$$

$$\delta = \left(\frac{r_e\lambda^2}{2\pi}\right) N_0 \rho \sum_i x_i(Z_i + f_i') / \sum_i x_i M_i \tag{2.2}$$

$$\beta = \left(\frac{r_e\lambda^2}{2\pi}\right) N_0 \rho \sum_i x_i(Z_i + f_i'') / \sum_i x_i M_i \tag{2.3}$$

r_e: Classical radius of an electron (2.818×10^{-15} m)

N_0: Avogadro number

λ: X-ray wavelength

ρ: Density (g/cm^3)

Z_i: Atomic number of the i-th atom

M_i: Atomic weight of the i-th atom

x_i: Atomic ratio (molar ratio) of the i-th atom

f_i', f_i'': Atomic scattering factors of the i-th atom

The value of the parameter δ is very small and ranging from 10^{-5} to 10^{-6} for X-rays with wavelength approximately 1 Å. The critical angle (θ_c) for total reflection is given by the following formula:

$$\theta_c = \sqrt{2\delta} \tag{2.4}$$

The density of the surface film can be deduced by measuring the critical angle for total reflection. At a given wavelength, for $\theta > \theta_c$, the reflected intensity depends on the density profile of the interface and decreases rapidly while oscillating. These oscillations, called Kiessig fringes, result from the interference phenomenon between the waves reflected by the various optical surfaces (air-film and film-substrate). Their angular positions are dependent on the thickness of the film. The contrast of the fringes depends on the relative intensity of the two waves, that is to say the respective indices of the two materials. The period of oscillation depends on the optical path difference between

the two waves, allowing deducing the thickness of the film.

X-ray reflectometry (XRR) analyses are carried out on SiN_x:H thin-film deposited on crystalline silicon wafer using a home-made diffractometer under the supervision of Dr. R. Cortes (LPMC, Ecole Polytechnique). XRR intensities are recorded over each reciprocal space (*q*) where *q= 4πsinθ/λ*, and the angular range starting below the critical angle up to 2° with a step size of 0.01° and using $CuK_α$ radiation. The data obtained from the XRR measurements are analyzed using the Parratt32 software package based on Parratt formalism [107].

2.3.3   X-ray photoelectron spectroscopy (XPS)

X-ray photoelectron spectroscopy (XPS) is an important and extensively used characterization technique to analyze the surface of films. The method is based on the irradiation of X-ray on the solids and ejection of electrons due to the photoelectric effect. The electrons carries the information regarding chemical oxidation states, electronic structure and atomic composition of the solid being analyzed. The energy distribution of electrons depends on the energy of the X-ray, the binding energy and work function of the material. Each chemical element being characterized by a single spectrum, this method allows analyzing precisely the chemical nature of a given material.

For the XPS measurements in this study, Kratos Axis Ultra DLD spectrometer set up situated at IRAMIS, CEA Saclay, France, is used. A monochromatic Al $K_α$ X-ray source is used with energy of 1486.7 eV with a charge compensation system. Photoelectron data are collected at take-off angle of 90°. Survey spectra are taken at analyzer pass energy of 160 eV and high resolution spectra at pass energy of 40 eV or 20 eV. The analysis chamber has a base pressure of 10^{-10} mbar. The spectrums are calibrated using a known binding energy, in our case carbon, C1s at 285 eV. The spectrometer is coupled with Eclipse (VG scientific) data acquisition software to analyze the data.

2.3.4   Glow Discharge Optical Emission Spectroscopy (GD-OES)

Glow discharge optical emission spectroscopy is a useful technique recently advancing to analyze the thin films in more easier and faster way. While it can detect almost all the elements; the detection limit being down to ppm range. The atomic concentration of elements can be evaluated throughout the depth profile from 10 nm to 100 μm thickness.

The basic principle of glow discharge is based creating plasma inside very low pressure gas (typically argon) by high electric field applied across two electrodes. As shown in Fig. 2.6, there are

several zones throughout the discharge region and the negative glow (high charge density space) as well as the cathode dark region (low charge density space) is of particular interest. Electrons travelling from one electrode to the other collide with the gas atoms forming positive ions. These ions attracted by the negative potential gain sufficient energy to impinge on the sample surface kept at the cathode to knock atoms off the film surface. The sputtered atoms are excited by collisions with more energetic electrons inside the plasma. When these excited atoms are de-excited, they emit photons with characteristic wavelength. Recording the signal of these wavelengths, the atomic concentrations of each type of atoms are evaluated [108, 109].

The relative signal intensity of different elements inside the SiN_x:H thin films deposited on crystalline silicon wafers throughout their depth are evaluated using GD-Profiler 2 at Horiba Scientific (Longjumeau, France). The standard argon plasma is used to study the depth profile. In our experiments, the operating conditions are: argon pressure of 650 Pa and 30 W RF power. When Ar atoms are looked for in the films, Neon gas has been used as a plasma source.
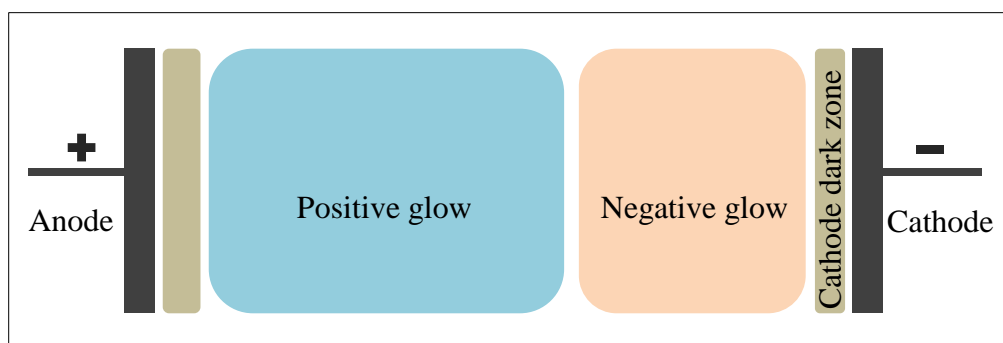
Fig. 2.6: Schematic diagram and basic principle of the glow discharge chamber.

2.3.5 Fourier Transform Infrared Spectroscopy

Fourier Transform Infrared Spectroscopy (FTIR) is a non-destructive, widely used technique to assess the information regarding the chemical composition and atomic bonding in thin films. When a thin film is exposed to the IR radiation, the sample molecules selectively absorb radiation of specific wavelength. This absorption gives rise to the change in dipole moment or in other words charge imbalance of the sample molecules. As a result, the vibrational energy levels of sample molecules transfer from ground state to the excited energy state, leading to specific absorption peaks in the IR-spectrum. The FTIR measurements used in this thesis are carried out using a Bruker Equinox 55 spectrometer with wave number range: 370-25000 cm^{-1} and resolution better than 0.5 cm^{-1}. The instrument has a variable temperature cell: 80K – 400K. The instrument is purged with dry nitrogen

before the measurement in order to get rid of the absorption peaks corresponding to water or CO_2. The absorption signal due to the substrate is subtracted from the measured data during the analysis.

2.4 OPTICAL CHARACTERIZATION

2.4.1 UV-visible spectroscopic ellipsometry (UV-visible SE)

UV-visible spectroscopic ellipsometry, which is a non-destructive and non-contact optical technique, is a useful method for assessing the thickness and optical constants of barrier films during and after deposition [110, 111]. UV-visible spectroscopic ellipsometry measures the change in polarization state of a light beam after its reflection from the film surface. If a linearly polarized light beam is incident with an angle φ as defined to the normal to the surface, on a film (refractive index n), the reflected beam will be elliptically polarized. At each wavelength of the incident beam, the change in polarization is represented by two parameters: amplitude ratio (ψ) and phase difference (Δ). These two parameters are related to the complex Fresnel reflection coefficients r_s and r_p through the following relation:

$$\rho = \frac{r_p}{r_s} = \frac{E_p^r/E_p^i}{E_s^r/E_s^i} = tan\psi e^{i\Delta} \qquad (2.5)$$

where E_p and E_s the parallel and perpendicular components of the E vector parallel to the plane of incidence and perpendicular to the plane of incidence, defining the planes of polarization for the waves. The superscripts i and r corresponds to the incident and reflected beams.

Spectroscopic ellipsometry measurements are carried out by using a phase modulated [112] UV-visible spectroscopic ellipsometer, UVISEL (Jovin-Yvon), in the photon energy ranging from 1.5 to 5.0 eV. The UV-visible beam is emitted from Xenon lamp and passes through a linear polarizer then a photo-elastic modulator (50 kHz). After reflection on the sample surface, it traverses through a second polarizer (placed as an analyzer) and is focused at the entrance slit of a monochromator and photomultiplier.

In the case of a phase-modulated ellipsometer, the measured parameters are I_s and I_c, which are related to ψ and Δ according to: $I_s = sin\ 2\psi\ sin\ \Delta$ and $I_c = sin\ 2\psi\ cos\ \Delta$. In order to analyze ψ and Δ, or I_s and I_c data, a model, based on the Abelès matrix approach [113], specific dispersion relation and the Bruggeman Effective Medium Approximation [114] is used. For developing the structure of the model, the DeltaPsi II software package supplied by the ellipsometer manufacturer is used.

Due to large anisotropy of polyethylene terephthalate (PET) substrate, the optical modeling of the barrier films deposited on PET substrates is quite impossible. To evaluate the optical constants of thin films deposited on PET substrates, single-wavelength polarimetric study under Fourier plane is used to deduce the refractive index [115]. However, the measurement procedure and optical modeling for the PET substrate are also impossible due to local anisotropy and the study is out of the scope of the aim of the present thesis. For that reason, all the optical constants used throughout this thesis are deduced from spectroscopic ellipsometer study on thin films deposited on crystalline silicon wafer substrates with a substrate thickness of 510 μm. The optical constants of crystalline silicon are quite well defined.

2.4.2 Integrating sphere

The integrating spheres are used for applications such as highly reflective and anti-reflective coatings, color correction coatings, band-pass characteristics of UV, visible and near infra-red (NIR) filters. It is based on homogeneous distribution of multiple radiations by means of multiple Lambertian reflections. The reflection and transmission measurements of the permeation barrier thin films are performed using Perkin Elmer Integrating Sphere (LAMBDA 950). This instrument is useful for performance of wavelengths up to 3300 nm and based on InGaAs photo-detector with UV/vis resolution of ≤ 0.05 nm and NIR resolution of ≤ 0.20 nm. The reflectance (R) and transmittance (T) of the permeation barrier deposited on PET substrates are measured using this set-up to check the compatibility of the barrier films for their utilization as a window layer for organic optoelectronic devices.

2.5 PERMEATION BARRIER CHARACTERIZATION

The purpose of permeation barrier films is to limit the exposure of organic electronics to water vapor and oxygen. Thus controlled permeation rate through the barrier films is necessary. Measuring and quantifying ultra-low permeation rates of water vapor ($\sim 10^{-6}$ g/m^2.day) and oxygen with high reliability and accuracy is one of the main challenges of characterizing encapsulation films [37, 43, 44, 50-60]. The permeation rates of oxygen and water vapor across the barrier layers are characterized in terms of the oxygen transmission rate (OTR) and the water vapor transmission rate (WVTR). Typically, commercial systems are useful for analyzing most single-layer and some of multilayer films but are not sensitive enough to detect the ultra-low permeation rates of advanced encapsulation materials. Common coulometric permeation measurements tools are limited to a sensitivity of 5×10^{-4} g/m^2.day [47] for water vapor and the tritium test provides a higher sensitivity,

but requires radioactive substances and large experimental efforts [49, 63-65]. Building an organic device such as an OLED or OPV represents an involved test procedure with many experimental parameters, which are difficult to control. Thus, a simple and precise evaluation is essential for the development of ultra-high barrier encapsulations [57].

The Ca corrosion test is a widely known method for measuring ultra-low permeation rate barrier films [56, 57, 59]. Calcium is a conducting and opaque metal which becomes non-conducting and transparent after oxidation [51]. It rapidly oxidizes in air due to the highly negative Gibbs free energy ($G°_{rxn}$) of formation of Ca oxides making it very sensitive for detecting the presence of oxygen and water vapor. Since the oxide is a dielectric and transparent, both of them are possible to monitor the consumption of Ca by either measuring the change in electrical conductance or in optical transparency [57]. Hence, the measurement of Ca conductance or transparency changes versus time provides an indirect method to determine the oxidation and corrosion rates of Ca. In recent years several groups of experts from academic, public-private research and development labs, implemented Ca test. According to a recent publication by Reese *et al.* [56, 59], Table 2.1 comprises all the implementations of Ca based permeation measurement tests.

References	Method	Range (g/m^2.day)	Features
Nisato *et al.* [37]	Optical Ca Test	5×10^{-5} to 1 (21 °C/50% RH) 4×10^{-7} (85 °C/50% RH)	➤ Can see pinholes/defects in barrier. ➤ High sensitivity. ➤ Edge seal limited ➤ Not commercially available
Kumar *et al.* [50]	Optical Ca Test	10^{-2} (50 °C/95% RH)	➤ Temperature dependent measurement ➤ Poor sensitivity ➤ Edge seal limited ➤ Not commercially available
Paetzold *et al.* [51]	Electrical Ca Test	$<5 \times 10^{-5}$ (38 °C/90% RH)	➤ High sensitivity ➤ Quantitative for uniform films or films with many defects close to one another. ➤ Parallel *in situ* measurements possible. ➤ Not commercially available
Carcia *et al.* [52]	Optical Ca Test	$< 10^{-5}$ (38 °C/85% RH)	➤ High sensitivity ➤ Edge seal limited ➤ Thickness and temperature dependence of permeation measurement ➤ Not commercially available
Choi *et al.* [54]	Electrical Ca Test	$<10^{-6}$ to 10 (20 °C/60% RH)	➤ High sensitivity. ➤ Quantitative for uniform films or films with many defects close to one another. ➤ Parallel *in situ* measurements possible. ➤ Edge seal limited ➤ Not commercially available
Leo *et al.* [57]	Electrical Ca Test	10^{-5} to 15 (30 °C/24% RH)	➤ High sensitivity ➤ Well discrimination between electrical and optical measurements ➤ Parallel *in situ* measurements possible ➤ Result is independent of the variations of

			electrode material and thickness of the Ca layer
			➢ Not commercially available
Song *et al.* [58]	Electrical Ca Test	10^{-6} to 10 (20 °C/50% RH)	➢ High sensitivity
			➢ Bending force is taken into account for flexible Ca test
			➢ Degradation from the edge seal permeation is negligible.
			➢ Evaluation of flexibility of the barrier is possible
			➢ Not commercially available
Cros *et al.* [44]	Optical Ca Test	1×10^{-5} (38 °C/90% RH)	➢ High sensitivity
			➢ Use of mass spectrometer detection and isotope labeling
			➢ Not commercially available
Reese *et al.* [56, 59]	Electrical Ca Test	10^{-7} to 10 (20°C/ Ambient) 10^{-6} to 10 (85°C/85% RH)	➢ High sensitivity
			➢ Gives quantitative average WVTR for all film types, including defect dominated with defects well separated
			➢ Parallel *in situ* measurements possible
			➢ Redundancy in each measurement
			➢ Edge seal failure detection
			➢ Not commercially available
This work [60-62]	Electrical Ca Test	10^{-6} to 10 (Room temperature/ambient)	➢ High sensitivity
			➢ Redundancy in each measurement
			➢ Edge seal failure detection
			➢ Not commercially available
			➢ Low capital investment

Table 2.1: List of previous works on calcium degradation tests.

In this work we used Ca corrosion tests with electrical analysis instead of optical analysis (measurement of optical transmittance change) because the electrical analysis can be performed in a highly parallel and automated manner with higher sensitivity. Metallic calcium is a good electrical conductor while CaO and Ca(OH)$_2$ are insulating materials. Thus the WVTR is assessed by measuring the evolution of the conductance of a thin encapsulated calcium layer during the degradation process.

2.5.1 Calcium corrosion method

The calcium permeation test is based on the following reactions of metallic calcium with water and oxygen. There are multiple potential pathways, all of which are thermodynamically favorable [56]. These are

$Ca + 1/2 \ O_2 \rightarrow CaO$ $\qquad\qquad\qquad\qquad\qquad N = 1/2$

$Ca + H_2O(g) \rightarrow CaO + H_2$ $\qquad\qquad\qquad\qquad\qquad N = 1$

$CaO + H_2O(g) \rightarrow Ca(OH)_2$ $\qquad\qquad\qquad\qquad\qquad N = 1$

$Ca + 2H_2O(g) \rightarrow Ca(OH)_2 + H_2$ $\qquad\qquad\qquad\qquad\qquad N = 2$

where N indicates the reaction ratio. It has been determined using isotopic labeling methods [53] that at room temperature, the kinetics of corrosion directly from oxygen are significantly slower than that via moisture. This leaves the complication as to whether or not the reaction ratio of calcium to water (N) is 1 or 2, or some intermediate level. Previous implementations of the Ca test assumed a reaction ratio of 2, with limited evidence to support this assumption [37]. According to Reese *et al.*, the gravimetric studies shows that the final product is completely $Ca(OH)_2$ and thus the value of N is equal to 2 [56]. In all testing conditions described above in Table 2.1, it is impossible to distinguish between the contribution from either water vapor or oxygen to the Ca corrosion. As the Ca degradation from oxygen is significantly slower than that via water vapor, in this thesis, we will utilize the term WVTR to denote the combined effects of water vapor and oxygen permeation.

2.5.2 Experimental method

To measure the water vapor transmission rate (WVTR) value, we use the electrical calcium degradation test method [51, 54, 56-60]. All flexible barrier coated substrates are cut to 2.2×2.2 cm^2 pieces, carefully cleaned and then transferred to a glove box system with active purification. The cleaning procedure is very important because the particle contaminations on the calcium sensor and in the encapsulation layers causes defects leading to localized oxidation giving erroneous values of effective WVTR. The cleaning process employed in this study consisted of three cleaning steps: soft detergent – deionized (DI) water – nitrogen blowing. The barrier coated substrates are degassed at 90 °C for about 3 hours inside the glove-box prior to the Ca deposition to get rid of integrated water molecules.

For the Ca degradation test, 100 nm Ca layer with an area of 1.13 cm^2 and aluminium contacts (150 nm) are deposited through shadow masks on the back side of the barrier coated substrates using thermal evaporator (see Fig. 2.7). Deposition rate and thickness are monitored using a calibrated quartz crystal microbalance near the substrate. A low deposition rate of 0.2 nm/s at a pressure $<10^{-6}$ mbar is chosen to get a really smooth layer. The Ca layer is then covered with a glass plate and the edges of which are sealed with epoxy resin (Nagase Chemtex Corp. XNR 5570). The resin is cured under UV-lamp (365 nm wavelength) inside the glove-box. The water permeation through the epoxy edge-seal is confirmed to be negligible by using a glass plate as a substrate as discussed later. Therefore, the Ca layer is on one side of the barrier film and the other side is exposed to the environment. Water vapor molecules after diffusing through the barrier coated polymer substrate react with the deposited calcium and thus reduce its conductivity. The change of conductance is measured using a four point probe technique of Solartron-Schlumberger 7060 Systems Voltmeter

(current is injected through the outer probes and the voltage is measured through the inner probes) and the data is recorded using a LABVIEW system. From the evolution of the conductivity value, the permeation rate is evaluated.
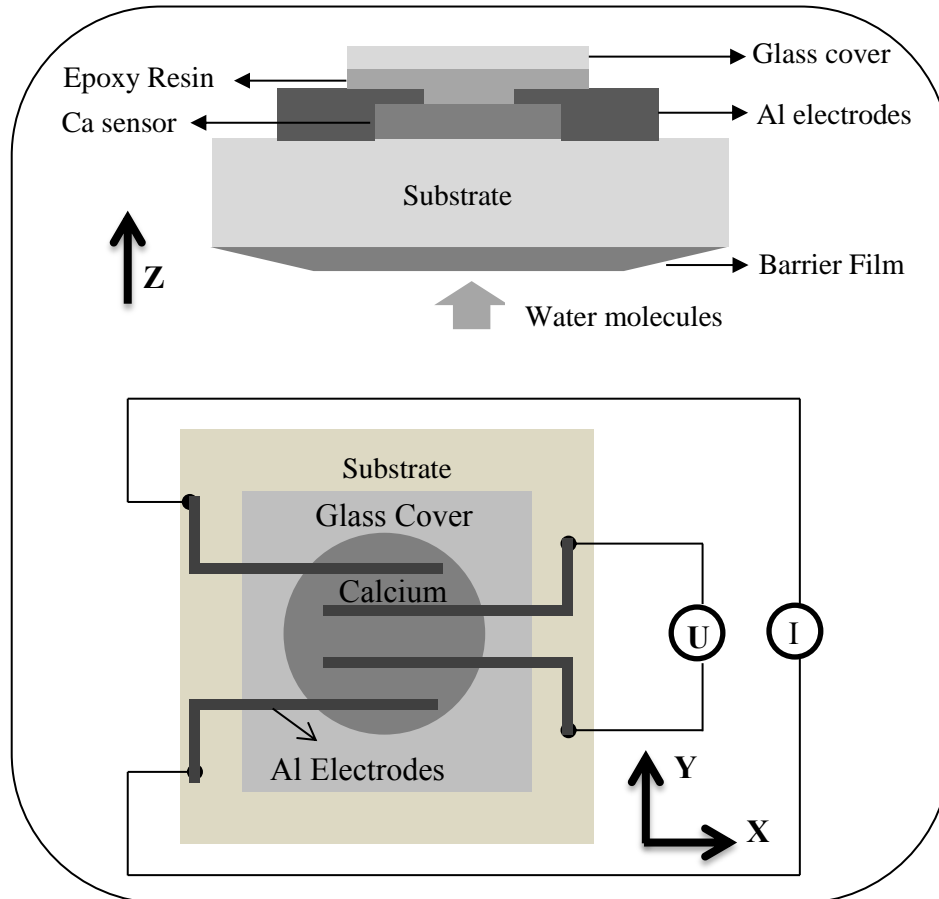
Fig. 2.7: Schematic diagram (not to scale) of the calcium degradation test set-up (a) side view, (b) top view.

2.5.3 Calculations

The water vapor permeation through a homogeneous film is usually defined as a combination of absorption of permeate into the film followed by diffusion of permeate. Therefore, if the diffusion coefficient (D) is assumed to be constant, the relationship between the diffusion coefficient (D), the permeation coefficient (P) and the solubility coefficient (S) simplifies to:

$$P = S.D \qquad (2.1)$$

The solubility and diffusion coefficients are intrinsic material properties and the water vapor permeation rates of barrier films are usually reported in the unit of g/m^2.day at given temperature and concentration (generally described in relative humidity: RH).
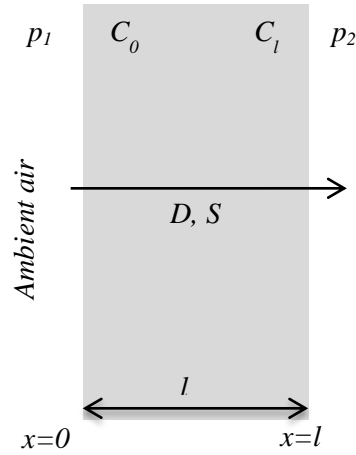
Fig. 2.8: Permeation of water vapor through a film. *C, p, l, D* and *S* indicate vapor concentration, vapor pressure, thickness of the film, and diffusion and solubility coefficients respectively.

The figure 2.8 shows the permeation model and if the film is initially free of the diffusing species, the initial and boundary conditions for the system can be expressed as [116]:

$$C \ (x, \ 0) = 0; \qquad (2.6a)$$

$$C \ (0, \ t) = C_0; \qquad (2.6b)$$

$$C \ (l, \ t) = C_l; \qquad (2.6c)$$

The permeation of water vapor can be described by Fick's first law of mass diffusion using the analogy to Fourier's law of heat conduction. The permeant flux *J* is proportional to the concentration as

$$J = -D \frac{\partial c}{\partial x} \qquad (2.7)$$

Where, *C* is the concentration of the diffusing species and *x* is the space co-ordinate measured normal to the section.

Once the mass balance of an element is taken into account, equation (2.7) can be used to derive the fundamental differential equation of diffusion:

$$\frac{\partial C}{\partial t} = D. \left(\frac{\partial^2 C}{\partial x^2}\right) \tag{2.8}$$

With the assumption of Henry's law which relates the concentration, C to the partial pressure, Δp through the linear relationship $C = S\Delta p$, the concentration in equation (2.7) can then be replaced using the solubility coefficient and partial pressure. Under steady state conditions, assuming diffusion and solubility coefficients to be independent of concentration, the permeation flux can be expressed as:

$$J = \frac{DS(p_2 - p_1)}{l} \tag{2.9}$$

If the upstream concentration, C_0, remains constant during the course of the diffusion process and the downstream concentration is negligible compared to the upstream pressure (that is $C_l \approx 0$), the solution of equation (2.8) subject to the boundary conditions of (2.6), by either Laplace transform or separation of variables is given below [117]:

$$C(x,t) = C_0 \left(1 - \frac{x}{l}\right) - \frac{2C_0}{\pi} \sum_{n=1}^{\infty} \frac{1}{n} \sin\left(\frac{n\pi x}{l}\right) e^{-Dn^2\pi^2 t/l^2} \tag{2.10}$$

Where C_0 is a fixed concentration on one side and l is the thickness of film. In general, the previous equations apply to diffusion through a single-layer film.

The mass flux J is obtained by differentiation with respect to distance in accordance with Fick's first law. The flux at the downstream surface ($x=l$) can be integrated over time to give the total mass (Q) transmitted through the layer per unit area [117]:

$$Q(t) = \int_{t'=0}^{t} J(x = l, t) dt' = \frac{DtC_0}{l} - \frac{lC_0}{6} - \frac{2lC_0}{\pi^2} \sum_{n=1}^{\infty} \frac{(-1)^n}{n^2} e^{-Dn^2\pi^2 t/l^2} \tag{2.11}$$

The water vapor mass transport rate (R_w) through the barrier film with area A_f is given by [56, 59],

$$R_w = \frac{Q(t)}{t}. A_f = WVTR. A_f \tag{2.12}$$

The mass consumption rate of calcium, R_{Ca}, can be calculated from the mass transport rate of water, R_w as,

$$R_{Ca} = R_w \left(\frac{M_{Ca}}{M_w}\right) \frac{1}{-N} \tag{2.13}$$

where M_{Ca} is the atomic mass of calcium, and M_w the molecular weight of water. Negative sign is used due to the exothermic reaction of Ca with water. For thin Ca layers relative to the diameter of

the Ca sensor (nm as compared to cm) one can ignore oxidation of the sides of the Ca sensor such that,

$$R_{Ca} = A_{Ca}\delta_{Ca}\frac{dh}{dt} \qquad (2.14)$$

Where h is the Ca thickness, A_{Ca} is the total Ca sensor area, and the density of Ca ($\delta_{Ca} = 1.55$ g/cm³). Combining equations (2.12)–(2.14) yields

$$WVTR = -N\delta_{Ca}\left(\frac{A_{Ca}}{A_f}\right)\left(\frac{M_w}{M_{Ca}}\right)\left(\frac{dh}{dt}\right) \qquad (2.15)$$

The resistivity of the Ca sensor is measured using a four point probe technique. So the multiplication of the effective width (w) by the length (l_{eff}) corresponds to the area inside the middle electrodes. Then the resistance (R) can be approximated by,

$$R = \frac{\rho_{Ca}l_{eff}}{wh} \qquad (2.16)$$

Where ρ_{Ca} is the thin film calcium volume resistivity and w is the line width. Combining Eq. (2.15) and (2.16) yields

$$WVTR = -N\delta_{Ca}\rho_{Ca}\left(\frac{l_{eff}}{w}\right)\left(\frac{A_{Ca}}{A_f}\right)\left(\frac{M_w}{M_{Ca}}\right)\left[\frac{d(1/R)}{dt}\right] = -N\delta_{Ca}\rho_{Ca}\left(\frac{l_{eff}}{w}\right)\left(\frac{A_{Ca}}{A_f}\right)\left(\frac{M_w}{M_{Ca}}\right)\left[\frac{dG}{dt}\right] \qquad (2.17)$$

Where $G = 1/R$ = conductance.

2.5.4 Calibration

The sheet resistance of the Ca sensor is measured with four point probe method. Due to the finite width (w) and $h<<s$ (where s is the probe spacing), there should be a correction factor. According to F.M.Smits [118],

$$R_{sheet} = 4.5324RF_1F_2 \qquad (2.18)$$

Where $F_1=F_1(h/s)$ is the thickness correction factor (≈ 1 for $h<<s$) and $F_2=F_2(d/s)$ is the finite width correction factor (≈ 0.95), d being the diameter of Ca sensor.

There is one more correction factor, Temperature Correction Factor (*TCF*). The sheet resistance should be normalized to the value it would be if measured at 23 °C. The *TCF* is calculated as follows:

$$TCF = [1 - TCR \times (T - 23)] \qquad (2.19)$$

Where T is the measured temperature in °C and *TCR* is the Temperature Coefficient of Resistance (for Ca= 0.0041 /°C).

Combining Eq. (2.18)-(2.19),

$$R = \frac{R_{sheet}}{4.5324 F_1 F_2 TCF} \qquad (2.20)$$

The bulk resistivity ρ_{Ca} deduced from equation (2.16), is 9×10^{-8} (Ω.m). This value is reasonable when compared to literature values for bulk resistivity. Paetzold *et* al. measured a value of $8.95 \pm 0.78 \times 10^{-8}$ (Ω.m) [51].

2.5.5 Result computation

Fig 2.9 shows a typical conductance evolution curve. The conductance evolution curve consists of three different zones:

(a) Lag time zone: Because the water molecules are obstructed by the solid (barrier and the substrate), the diffusion path is straight along the medium co-ordinate, and hence the true diffusion path length (l_c) is greater than or at least equal to the total length of the barrier coated substrate (l). The tortuosity factor, τ, is defined as the ratio of true molecular path length to the displacement of the molecular path along the medium co-ordinate [116].

$$\tau = \frac{l_c}{l} \qquad (2.21)$$

This region which is related to the tortuosity factor, τ, corresponds to the stable region of curve from the beginning of the measurement to the curvature where the curve tends to go down. The water molecules after passing through the barrier and then the substrate reach to the calcium sensor. This region shows the minimum time taken by the water molecules to diffuse through the whole thickness of the barrier to reach the calcium sensor.

(b) Degradation zone: Water molecules after penetrating through the barrier coated substrate reach the calcium sensor and react with it to form CaO or $Ca(OH)_2$ as discussed in 2.5.1. Gravimetric studies have determined that the stoichiometry of the final product is almost completely $Ca(OH)_2$ as discussed above. Because of the tortuosity of the barrier due to the statistical occurrences of pinholes and defects inside the barrier films (which contribute to the inhomogeneity of the

barrier), all the water molecules do not reach the Ca sensor at the same time and they contribute to the total evolution of the second region until all the Ca is oxidized. So this region corresponds to the degradation of the sensor from calcium metal into $Ca(OH)_2$.

(c) Saturated zone: This region corresponds to the state when all the metallic calcium is converted to $Ca(OH)_2$ and no more evolution is observed. In this state the conductance tends to become negligible.
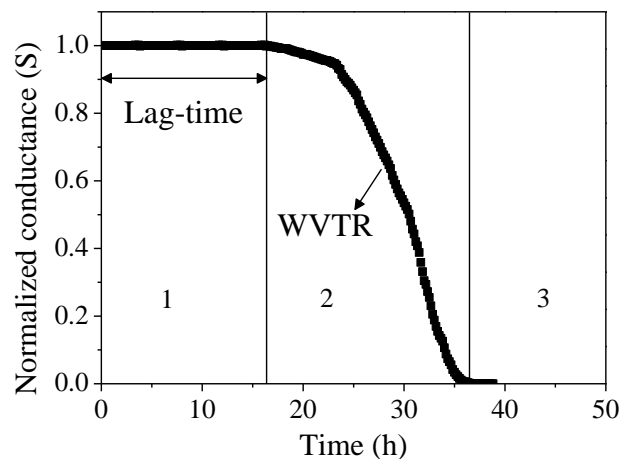
Fig. 2.9: Typical data of evolution of conductance of the calcium sensor with time, showing the three different zones.

The measurement of lag-time of the barrier is straight forward and is assessed from the first region of the conductance evolution. Computation of the slope of the second region of Ca degradation to measure the WVTR value from the raw data obtained from the conductance measurements of Ca sensor is a little tricky. In literature there are many methods to fit the evolution slope of conductance. Some of them based on the thermodynamic modeling considering the series resistance (Leo et al. [57]) and some based on the higher order polynomial fit of the inflection points (Reese et al. [56]). From most of the literatures it is clear that the slope of evolution to calculate the effective WVTR should be considered in the degradation region of above figure, as this is the region in which the metallic calcium after degradation converts to $Ca(OH)_2$. The main difficulty to find the slope is to determine a single slope for the entire degradation region, which is not the case for most of the evolutions. In this thesis, an average slope is considered to measure the effective WVTR taking into account all possible slopes in the degradation region by defining the beginning of decrease of conductance until the null conductance is reached.

2.5.6 Method sensitivity and reproducibility

All the samples are encapsulated with a glass cover on the topside (Fig 2.7). Glass is assumed to be a perfect barrier and water molecules only penetrate from the barrier side. However, permeation through the adhesive and along the interfaces between adhesive and glass cover or flexible substrate limits the sensitivity of the test. To define the background permeation, the electrical calcium test is performed for a glass substrate. Here the only sources of calcium degradation are diffusion through the adhesive layer. The test on glass substrate leads to a WVTR of $\sim 10^{-6}$ g/m^2.day after 10 000 h, which defines the sensitivity of the test.

The reproducibility is investigated by simultaneously measuring 20 uncoated flexible polyethylene terephthalate (PET) substrates. For this purpose we use commercial PET films from DuPont Teijin Films (Melinex ST 504 Film) of 175 μm thickness with one side planarized. It should be noted that the same commercial PET foils are used as substrates throughout this dissertation. The evolution of conductance of Ca sensor deposited on bare PET is shown in Fig. 2.10 with a lag time of ~1 h. The effective WVTR is averaged over 20 such measurements and the result is a WVTR of 0.17 ± 0.05 g/m^2.day with a standard deviation of 3.7%. This deviation may be caused by variations in the substrate cleaning process, the calcium conductivity or thickness and maybe inhomogeneity of the substrate itself.
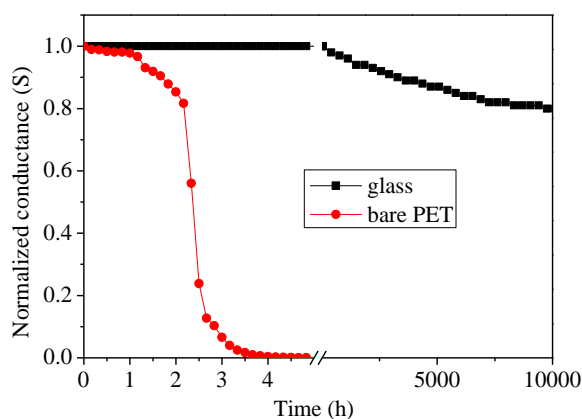
Fig. 2.10: Evolution of normalized conductance of the Ca sensor for glass substrate and bare PET substrate.

2.5.7 Technical drawbacks

Although the calcium degradation test set-up proved to be highly sensitive, the measurement is limited by several technical parameters. Deposition of epoxy resin on top of the calcium surface should be highly precise. A small air bubble inside the epoxy resin can create inhomogeneous

degradation of the calcium, which will lead to either reducing effective lag-time or erroneous effective WVTR value. To evaluate the homogeneity of the measurements, two different test set-ups were used, as seen from Fig. 2.11: (a) here the calcium top surface is completely covered by epoxy resin and (b) calcium top surface is partly covered by epoxy resin with some gas bubbles inside. However, the second method is not effective due to the impurity inside the glove-box system and the remaining water vapor and oxygen in the gas bubble react very rapidly with the sensor, leading very fast degradation and inhomogeneous oxidation; giving almost no effective lag-time and erroneous WVTR result (Fig. 2.12).
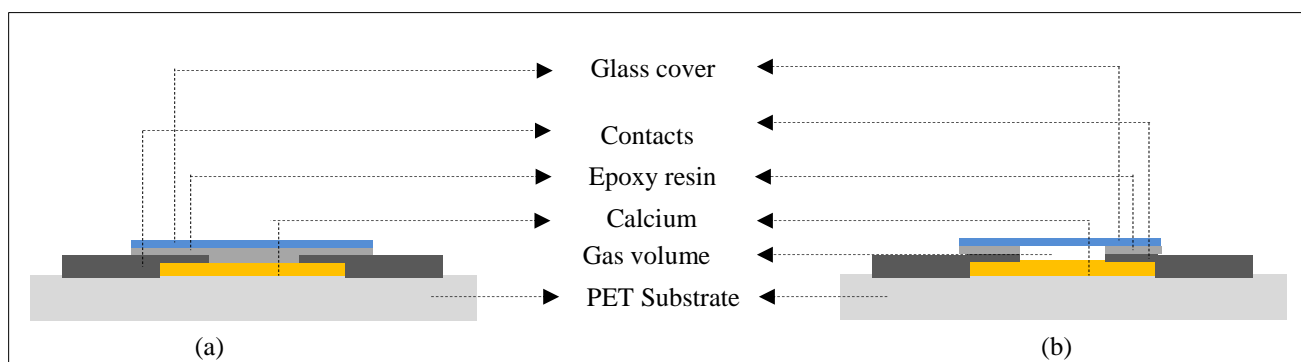
Fig. 2.11: Schematic diagram of calcium tests with: (a) Top side of the calcium is completely covered by glass plate and (b) Top side of the calcium is partly uncovered by gas volume.
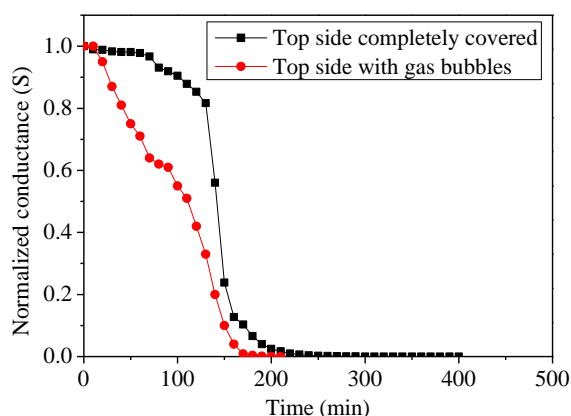
Fig. 2.12: Evolution of normalized conductance of Ca sensors deposited on bare PET substrates.

2.6 MECHANICAL CHARACTERIZATION

The actual purpose of the permeation barrier layers is to protect the sensitive devices based on plastic substrates for flexible applications. The brittle inorganic materials used as a permeation barrier film

for multilayer or hybrid layer structures have pinholes or defects which arise due to the processing conditions. However, the failure mechanics of the layers depends extensively on their mechanical properties and adhesion towards the underlying layer or the substrate.

The mechanical flexibility of the barrier coated substrates is characterized by bending the structure for several time cycles with a fixed radius of curvature (r). For the bending test, a home-made bending machine with a screw system (Fig. 2.13 (a)) is used and the sample is bent for different time cycles using an automated motor system. The bending of the sample gives rise to tensile strain inside the films, which in return forms channel cracks by the formation of interfacial delamination of two consecutive layers (Fig. 2.13 (b)) [119]. Ca degradation test is performed on such samples in order to verify the bending effect on the permeation barrier properties.
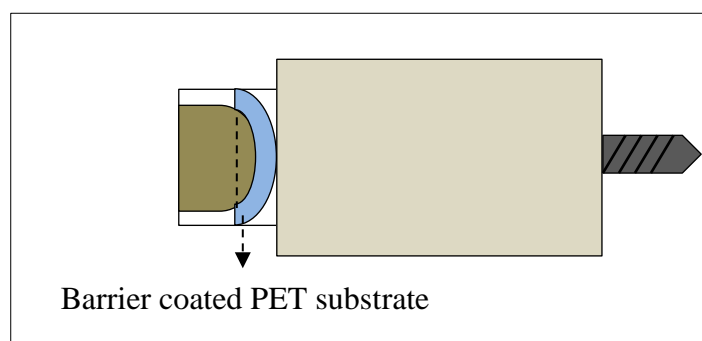
(a)
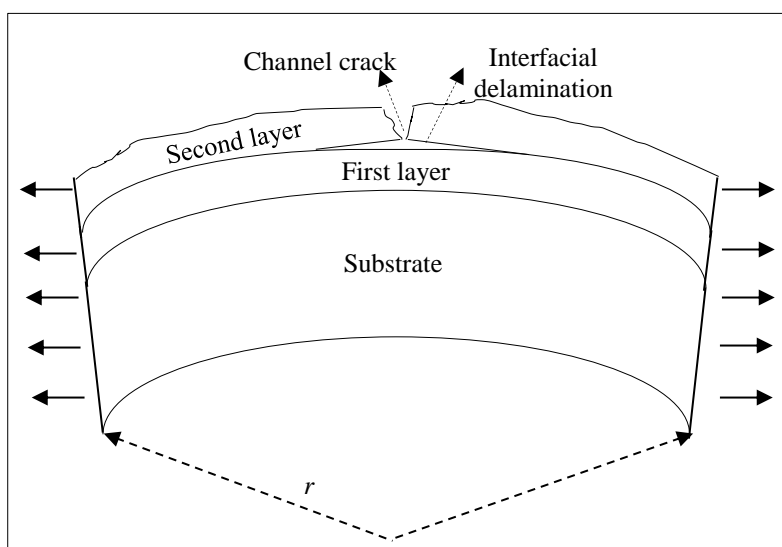
(b)

Fig. 2.13: (a) Schematic diagram (not to scale) for bending of barrier coated PET substrate inside two tracks with a fixed radius of curvature. (b) Schematic diagram of the channel cracking and formation of interfacial delamination.

2.7 SUMMARY OF CHAPTER 2

The deposition techniques as well as the characterization methods of the thin films to be used as a permeation barrier are discussed in this chapter. The specific technical points are summarized below:

i) The amorphous SiN$_x$:H thin films to be used as the inorganic layer for the barrier structures are deposited using HW-CVD and the plasma treatment is carried out in a RF-PECVD reactor. MDECR-PECVD is also used to deposit amorphous SiN$_x$:H thin films to be used as a barrier layer. The organic layer of PMMA to be used in fabricating alternating hybrid structure is deposited by spin-coating technique.

ii) The morphological characterizations of the deposited films are performed with the profilometry and atomic force microscopy (AFM) techniques. The structural and compositional analysis of the films are carried out using X-ray diffraction (XRD), X-ray reflectometry (XRR), X-ray photoelectron spectroscopy (XPS), glow discharge optical emission spectroscopy (GDOES) and Fourier Transform Infrared Spectroscopy (FTIR) techniques. The optical characterizations are done with UV-visible spectroscopic ellipsometry and integrating sphere methods.

iii) The permeation barrier properties are evaluated using the electrical calcium test method. The details of the test method as well as its theoretical background are discussed thoroughly in this chapter. The sensitivity and reproducibility of this test setup are introduced. Its technical drawbacks are also summarized.

iv) Finally, the mechanical characterizations of the films are carried out by bending the films for several cycles.

CHAPTER 3

PROPERTIES OF HW-CVD GROWN SILICON NITRIDE FILMS

3.1 INTRODUCTION

In this work silicon nitride (SiN_x:H) thin films have been used as an effective inorganic barrier material. SiN_x:H thin film is one of the most promising and widely used materials for barrier coating technology [120]. The benefit of SiN_x:H films over other oxide materials (SiO_x, Al_2O_3) deposited by other groups [71, 75-77,79] is that it does not require reactive oxygen atoms in the deposition process, which could react in an undesirable manner with the underlying flexible substrates. The advantage of silicon nitride over other metal nitrides is that it is more transparent and also that gaseous precursors for plasma-based deposition are more readily available, e.g., in the form of silanes (SiH_4) [102]. Although, the low temperature deposition process below 100 °C is required to be compatible with the flexible plastic substrate (PET), SiN_x:H films show low barrier properties as the deposition temperature decreases. However, the SiN_x:H films produced by HW-CVD method at low temperature are denser than those produced by PE-CVD method and therefore are suitable for the utilization as barrier films [120]. HW-CVD method is also advantageous compared to ALD technique, due to its higher deposition rate. SiN_x:H films particularly studied by the Japanese industry [121-124] are prepared with a gas mixture of SiH_4, NH_3 and H_2 using HW-CVD method. Osono *et al*. have reported low temperature deposition (below 80 °C) of SiN_x:H films using HW-CVD with very high deposition rate (110 nm/min) [125], thus allowing the possibility to grow high quality films on compatible plastic substrates. Alpuim *et al*. have succeeded to produce device quality SiN_x:H films with good dielectric properties at 100 °C with high density and high transparency [86]. A very high deposition rate (>7 nm/s) was achieved for device quality films by Verlaan *et al* [126].

This chapter is devoted to the properties of amorphous SiN_x:H films deposited by HW-CVD reactor on flexible PET substrates. The deposition temperature is fixed at 100 °C to be compatible with the glass transition temperature of the polymer substrates. First, the optimization of the film growth procedures is described in detail varying different deposition parameters. This is followed by the characterizations of the optimized SiN_x:H films by different analytical techniques. Finally the water vapor transmission rates of SiN_x:H films which qualify the quality of the permeation barriers for the

organic layers composing the different devices of interest (OLEDs and organic solar cells) are analysed.

3.2 HW-CVD PARAMETERS AND DEPOSITION CONDITIONS

There are several deposition parameters that affect the growth of SiN_x:H thin films deposited inside the HW-CVD chamber [127]. Some of the parameters are interdependent to each other as discussed below.

3.2.1 Choice of filament material

As a filament wire material, tungsten (W) was widely used throughout the last decades. This is cheap and the melting point (3422 °C) is very high. However, W wire reacts with the SiH_4 at filament temperature (T_f) up to 1850 °C, developing different phases of W-silicide (WSi_2 and W_5Si_3) [128] causing W contamination on deposited films, thus reducing the filament lifetime. It has been shown by Bourée *et al*. that for a high effective filament surface area ($S_f = 27$ cm^2), the W content inside the microcrystalline silicon films deposited by HW-CVD increases steadily from 5×10^{14} to 2×10^{18} atoms/cm^3 when the filament temperature T_f increases from 1500 to 1800 °C [129]. To avoid those contamination issues, it is required to maintain high T_f, and thus the possibility of depositing films at lower substrate temperature (T_s) using W wire is reduced. Since the year 2005, the W-filament has been replaced by the tantalum (Ta) wire. The melting point of Ta material is 3017 °C. It is less reactive with SiH_4 at lower temperature and the formation of Ta-silicide (Ta_5Si_3) takes place at a lower temperature (up to 1750 °C). Thus it is possible to use a low T_f inducing lower T_s, and there are lower contamination from the wire material [130] and improved wire lifetime. In this study, the filament used at INL, Braga is a single-coil shaped tantalum (Ta) filament with 0.5 mm of diameter and 15 cm of length.

3.2.2 Filament temperature (T_f)

Filament temperature T_f is an important parameter that affects T_s and the growth rate r_d. Filaments are heated by Joule effect using electrical connections and normally measured by using a one wavelength pyrometer. Due to radiation emitted from the filament, T_s increases depending on the distance between filament and substrates, thus creates limitations of low temperature film depositions. The filament acts as a catalyst, providing thereby the surface for heterogeneous thermal decomposition of the source gases into radical species, which are the precursors for the thin film growth [86]. The decomposition efficiencies of source gases increase with T_f. At a low T_f (less than

1750 °C for Ta filament) the filament material reacts with the source gases, while decreasing the wire lifetime. At a higher T_f some issues occur like elongation of filament which are limited if the Ta filament temperature does not exceed ~2000 °C. Therefore, the filament temperature should be in between those extreme temperature values. For the study used in this thesis, the Ta filament temperature is limited to around ~ 2000 °C.

3.2.3 Filament to substrate distance ($d_{f\text{-}s}$)

Along with the T_f; the filament to substrate distance ($d_{f\text{-}s}$) is also an important parameter affecting both T_s and r_d. With the increase of $d_{f\text{-}s}$, the T_s decreases due to the lower influence of filament radiation and r_d decreases monotonically as a function of $1/\ d_{f\text{-}s}$ [131]. The variation of $d_{f\text{-}s}$ also affects the number of collisions of the radical species travelling from the filament to the substrate for a given gas pressure (p_g) [132]. As stated by K. F. Feenstra *et al.*, the mean free path (λ_{mfp}) of the radicals must be smaller than the $d_{f\text{-}s}$ in order to obtain device quality films [133]. On the contrary, too many reactions between radicals are detrimental to the film qualities [134]. Therefore, $p_g.d_{f\text{-}s}$ product is a useful parameter which determines the film properties. For $p_g.d_{f\text{-}s}$ product value of approximately 6 Pa cm, optimal film properties are reported for the growth of amorphous silicon films [133]. In this present study, the $d_{f\text{-}s}$ is fixed to a value of 7.5 cm resulting in lower T_s of 100 °C.

3.2.4 Substrate temperature (T_s)

The diffusion length of the precursors depends largely on the T_s by the following relations [127]:
$$L_s = (2D_s\tau_s)^{1/2} \tag{3.1}$$
$$D_s = D_{s0}\exp(-E_s/k_BT_s) \tag{3.2}$$
where D_s, τ_s, D_{s0}, k_B and E_s are the surface diffusion coefficient, the residence time of the precursor on the surface, a constant, Boltzmann constant and the activation energy of thermal hopping of the precursor, respectively. T_s is affected by the radiation emitted from the heated filament as well as the conductive heat (Q_{fil}) transfer by species coming from the filament [133]. Thus T_s depends on $d_{f\text{-}s}$, T_f, filament surface area and amount of heat conducted by species coming out from the filament.

T_s also varies with the deposition time which limits the thin film thickness growth on flexible polymer substrates, which has a glass transition temperature (T_g) normally below 100 °C. With the increase of the deposition time, T_s increases monotonically up to a certain time and then it stabilizes [133]. This is also confirmed experimentally by Bourée *et al.* as shown in Fig. 3.1 [135]. In a recent

study by Alpuim *et al.*, device quality transparent SiN$_x$:H films have been grown at lower T_s (100 °C and 250 °C) [86].

In our system, samples are deposited at lower T_s (100 °C) in order to be compatible with the glass transition temperature of plastic substrates. The substrate temperature is measured by a thermocouple embedded near the substrate holder.
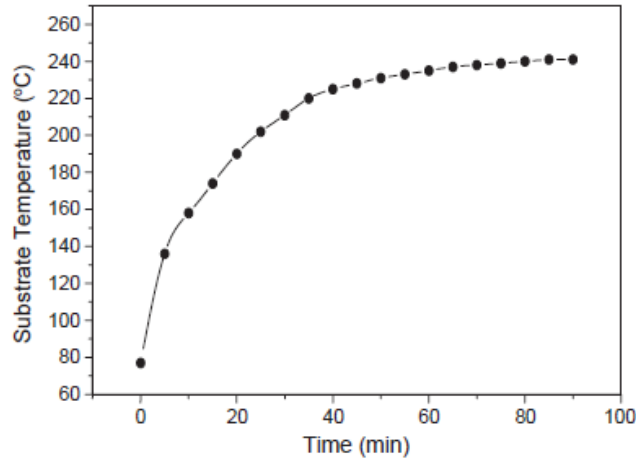
Fig. 3.1: Evolution of substrate temperature with deposition time. Reprinted from [135] with permission from 2006 Elsevier.

3.2.5 Working gas pressure (p_g)

The mean free path (λ_{mfp}) of radical species depends on the working gas pressure (p_g) inside the HW-CVD chamber. The product $p_g.d_{f-s}$ determines the number of collisions of the radicals travelling from the heated wire to the substrate. In a HW-CVD chamber, the working pressure is low to obtain a high SiH$_4$ dissociation efficiency. In a previous study by Alpuim *et al.*, amorphous SiN$_x$:H films have been deposited on glass substrates by HW-CVD chamber at p_g = 40 mTorr and d_{f-s} = 4.5 cm [86]. In order to keep the product $p_g.d_{f-s}$ almost constant in the present study, the working pressure is decreased to 25 mTorr ($\approx$3 Pa), while increasing the filament to substrate distance.

3.2.6 Source gases

Source gases play an important role in order to deposit high quality films. SiN$_x$:H film grown by HW-CVD was first reported by Matsumura using silane (SiH$_4$) as silicon source and explosive hydrazine (N$_2$H$_4$) as nitrogen source [80]. Yasui *et al.* have reported HW-CVD grown SiN$_x$:H film using SiH$_4$ and monomethylamine (NH$_2$CH$_3$) [136]. In 1992, Dupuie *et al.* [137] have prepared SiN$_x$:H films using SiH$_4$ and ammonia (NH$_3$) and in 1997, Okada and Matsumura also reported

various fundamental properties of Cat-CVD grown SiN_x:H films using SiH_4 and NH_3 [138]. In 1998, a group from NREL, Colorado has deposited a series of SiN_x:H films using SiH_4, NH_3, without and with H_2 addition at T_s ranging from 23 to 410 °C. They found a better step coverage of SiN_x:H films using the H_2 dilution [139]. This has been followed by a report from NREL in 2004, where they reported that H_2 addition enhances SiN_x:H film deposition significantly and high quality films at low T_s (< 350 °C) [140].

In the present study, SiN_x:H thin films are deposited inside a HW-CVD reactor using SiH_4, NH_3 diluted in H_2. The hydrogen dilution is defined by:

$$H_2 \; dilution \; (D_H) = \frac{F_{H_2}}{F_{H_2} + F_{SiH_4} + F_{NH_3}} \qquad\qquad (3.3)$$

Where, F stands for the respective flow rates.

3.3 GROWTH MECHANISMS

The source gases injected inside the vacuum chamber of HW-CVD reactor decompose into radicals by pyrolytic decomposition reactions of SiH_4, NH_3 and H_2 at the heated filament surface. The growth mechanism of SiN_x:H can be divided into three separate mechanics: dissociation of SiH_4, NH_3 and H_2 gases into radicals at the filament, gas phase reaction of the radicals with the source gases to produce precursor molecules and finally surface reactions to grow SiN_x:H thin films [127, 141].

3.3.1 Dissociation of source gases

The formation of radicals by the catalytic dissociation of the source gases is an essential step while developing the film growth. Radical formation has been studied extensively using various methods to undertake a systematic study of the growth mechanism inside HW-CVD chamber.

The nature and flux of radicals desorbed from a hot filament depend on the filament temperature and gas pressure in the reactor. In 1988, Doyle *et al*. have reported the SiH_4 decomposition probability (α) on a W surface and the main products from the surface were identified using mass spectroscopic technique as a function of T_f [142]. Under a low SiH_4 pressure (p_s) of 10 mTorr and $T_f > 1800$ °C, the reaction of SiH_4 with the heated filament leads to the formation of four H and one Si atom from the filament [142, 143]. This result was confirmed by Tange *et al*. by the use of mass spectroscopy techniques [144]. Nozaki *et al*. also reported the identification of Si, SiH and SiH_3 radicals using laser spectroscopic and mass spectroscopic techniques [145]. Using threshold ionization mass

spectroscopic technique, Zheng *et al.* [146] have found Si_2H_2 as the primary depositing radical accompanied by a few percent of Si atoms and lot of H atoms. Negligible SiH_n radical production was also observed for a temperature range of 1400 to 2400 °C and at p_s range of 0.01 to 3 Pa. In 2005, radical formation on different filament materials has been reported by Duan *et al.* [147] using laser-based single photon ionization technique. According to most of the authors, the decomposition of SiH_4 on a heated filament takes place by the following dissociation chain reactions: $SiH_4 \rightarrow SiH_3$ + H $\rightarrow SiH_2$ + 2H $\rightarrow$ SiH + 3H $\rightarrow$ Si + 4H, from the analogy to the dissociative adsorption of SiH_4 on the Si surface [148]. More generally, the dissociation reaction of SiH_4 on Ta filament surface is [149, 150]:

$$SiH_4 \rightarrow SiH_n^* + (4-n)H^* \; ; \; n \text{ being an integer between 0 and 3, } ^* \text{ indicates the radicals} \qquad (3.4)$$

In addition to the detection of radical species of SiH_4 dissociation, it is desired to identify the decomposition products of NH_3, another material gas for the fabrication of SiN_x:H films. The dissociation of NH_3 at the heated filament surface has been investigated by Umemoto *et al.* employing laser based spectroscopy and mass spectroscopy techniques. In 2003, they have detected NH and NH_2 radicals by the decomposition of NH_3 on W filament surface heated at 2000 K [151]. According to them, NH radicals are not primary products on heated catalyst surface, but are prepared in secondary reactions, such as: NH_2 + H $\rightarrow$ NH + H_2 and NH_2 + NH_2 $\rightarrow$ NH + NH_3. In 2011, Umemoto *et al.* [152] also detected NH radicals on heated Ru surface using laser spectroscopic method. In general, the decomposition of NH_3 on heated filament occurs due to the following reaction:

$$NH_3 \; \rightarrow \; NH_2^* + H^* \qquad (3.5)$$

The dissociation of H_2 on heated filament has been largely studied. Langmuir in 1912 has shown that molecular hydrogen was decomposed into atomic hydrogen on a tungsten filament heated at > 1900 K [153]. Then Umemoto *et al.* [154] have detected H radicals by using two-photon laser-induced fluorescence and vacuum ultraviolet absorption techniques. The hydrogen molecules are decomposed at the filament by the following reactions:

$$H_2 \; \rightarrow \; 2H^* \qquad (3.6)$$

Plotting ln [H] versus the inverse of T_f in the range of 1250 to 2200 K, Umemoto *et al.* could deduce the effective enthalpy for H atom formation ~ 2.47 eV. As the effective bond dissociation energy of a

gas-phase H_2 molecule is 4.74 eV, the Umemoto's experiment was the first proof of the catalytic action of a heated tungsten wire.

3.3.2 Gas phase reactions

The primary radical species emitting from the heater filament surface leads to the direct formation of thin film under very low p_g where the gas phase reactions could be ignored. Heintze *et al.* [155] have observed optimum film properties where $d_{f\text{-}s}$ equals to 1-2 mean free paths (λ_{mfp}). The number of collisions of species from the filament surface takes an important role in formation of precursors for film growth and can be easily controlled by changing the $p_g.d_{f\text{-}s}$ product. As p_g is increased, three secondary reactions of the primary dissociated species occur due to the abstraction reaction [134, 143]:

$$H^* + SiH_4 \rightarrow SiH_3^* + H_2 \tag{3.7}$$

$$H^* + NH_3 \rightarrow NH_2^* + H_2 \tag{3.8}$$

$$Si^* + SiH_4 \rightarrow HSiSiH_3^* \tag{3.9}$$

The SiH_3^* species is much less reactive with SiH_4 or H_2, so SiH_3^* species generated by reaction (2.7) becomes the primary source of Si deposition [143, 145]. Recombination reaction of H atoms may also occur in the gas phase reactions to produce H_2, which subsequently decomposes at the filament:

$$H^* + H^* + H_2 \rightarrow 2H_2 \tag{3.10}$$

The reactions between the radicals are less frequent and the products are less mobile on the growing surface. Electrons can also emit thermally from the heated filament and the current density follows the Richardson's law:

$$J_c = A_c T^2 \exp(-E_w/kT) \tag{3.11}$$

Where A_c is a constant and a function of the material (for tungsten A_c = 60 A/m^{2}K^2), E_w is the work function of the material (4.5 eV) and T is the emission temperature, T_f. Current density increases with increase of T_f. The emitted electrons charge negatively the insulating substrate, which grow films with inferior electrical properties [156]. However, in our study, the electrical properties of films are not taken in account, but only the barrier properties are studied.

3.3.3 Surface reactions

The film growth precursors are usually transferred by thermal diffusion to the substrate surface [157]. In our system, SiH_3^* and NH_2^* are the main precursors for the amorphous SiN_x:H deposition on the substrate which is kept at a lower temperature (100 °C). The amount of H-content in HW-CVD grown films (< 20 At. %) is low in comparison with the high H-content (>20 At. %) observed in PE-CVD grown films. The low H content is attributed to the high concentration of H atoms generated in the gas phase reactions. The high concentration of H atoms enhances the abstraction reaction of H atoms ($H + H \rightarrow H_2$ or $H + SiH \rightarrow Si + H_2$), inducing local heating [121].

3.4 DEPOSITION AND OPTIMIZATION OF FILM GROWTH

The SiN_x:H single layer films are deposited inside the HW-CVD reactor by the previously described deposition procedure (Chapter 2). The growth conditions are first optimized in order to reach the optimal growth conditions for the SiN_x:H single layers, namely leading to high transparency (T >80%) films with high density and good dielectric properties (refractive index, n of ~2 at 632.8 nm). The deposition procedures are performed at a fixed substrate temperature of 100 ºC in order to be compatible with the glass transition temperature (T_g) of the plastic substrates. The substrate temperature is measured with a thermocouple embedded in a stainless steel substrate-holder, close to the substrate. This means that, especially for the depositions made nominally at 100 °C, the surface temperature of the film is certainly higher than the substrate-holder temperature due to the heating from the hot filament [86, 135]. Whenever the substrate temperature read at the Eurotherm display exceeds the nominal deposition temperature by 10% (110 °C), the deposition is stopped. Thus the single-layer thickness (d_f) is limited in the range from 50 nm to 60 nm, which corresponds to a growth time of ~360 s.

In order to reach the optimal growth conditions for the SiN_x:H films, the working pressure is fixed at 25 mTorr and three parameters are changed: the hydrogen dilution, the R ratio (flow rate of ammonia / flow rate of silane) and the Ta filament current, I_{fil}. The flow rates of hydrogen and silane have been fixed at 54 sccm and 2 sccm respectively and flow rates of ammonia are varied in the range 2 to 8 sccm.

SiN_x:H films are optimized for their optical transmittance, refractive index and deposition rate, in this order. Highly transparent films in the visible region (transmittance >80%) are targeted which are simultaneously dense (n~2) and obtainable at a deposition rate, r_d, as high as possible. Highly transparent films are required for window layers in optoelectronic devices. A refractive index of ~2

means that the SiN$_x$:H films are dense and close to stoichiometry Si$_3$N$_4$ [158-162] (as opposed to porous films which have lower *n*, and Si-rich films which have higher *n* but are not fully transparent). A high r_d is important for economic reasons in general and in this case it also allows avoiding long exposure of the plastic substrate to the hot filament.

Fig. 3.2 shows optical transmission spectra of as-deposited SiN$_x$:H single-layers grown on c-Si wafers, acquired in the visible wavelength range from 250 to 750 nm. Two different parameters (I_{fil} and D_H) have been varied keeping the *R* ratio fixed at 2. All the samples reveal a transmittance above 60% for wavelengths larger than 500 nm. The film thickness (d_f) and the spectral refractive index, *n*, are obtained from the transmission spectra in the visible range applying the Minkov method [163] and adopting a classical Lorentz / Drude dielectric function for the dispersion behavior of the dielectric constant. The thickness of the single-layer film (d_f) and the refractive index (*n*), are also verified by fitting the measured data of the UVISEL HORIBA Jobin Yvon spectroscopic ellipsometer measurements using the DeltaPsi2 fitting software tool. The dispersion relation for the dielectric constant used in the parameterization from which the film's optical constants are obtained, is based on the classical Lorentz dielectric function:

$$\varepsilon(E) = \varepsilon_\infty + \frac{fE_0^2}{E_0^2 - E^2 + i\gamma_b E} \tag{3.12}$$

where ε_∞ is the high frequency dielectric constant, E_0, γ_b and *f* are, respectively, the resonance energy frequency, the line-width and the strength of the Lorentzian oscillator, related to the bound electrons.
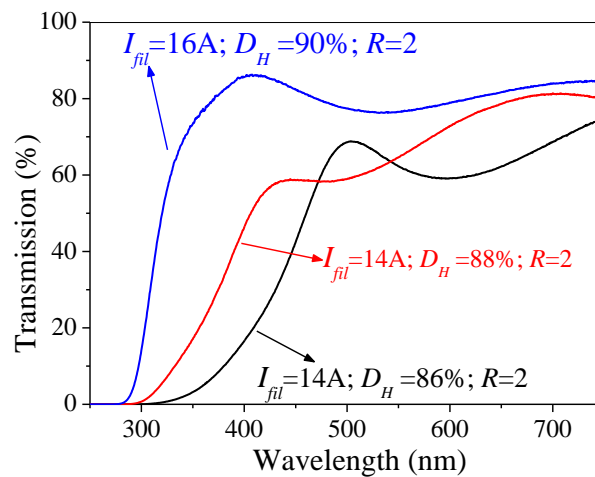
Fig. 3.2: Transmission spectra of some 50 nm thick SiN$_x$:H samples deposited at different deposition conditions.

Fig. 3.3 shows the refractive index (n) of the SiN$_x$:H single-layers as a function of ammonia-to-silane gas flow rate ratio (R), for different H$_2$ dilutions and filament currents (I_{fil}). Most of the films have n >2 which is attributed to a Si-rich composition of the films. The refractive index approaches to the stoichiometric value of 2 when R is increased from 2 to 3, when I_{fil} increases from 14 to 16 A, or when H$_2$ dilution increases from 86% (88% at $R = 3$) to 90%, keeping fixed all the other parameters.
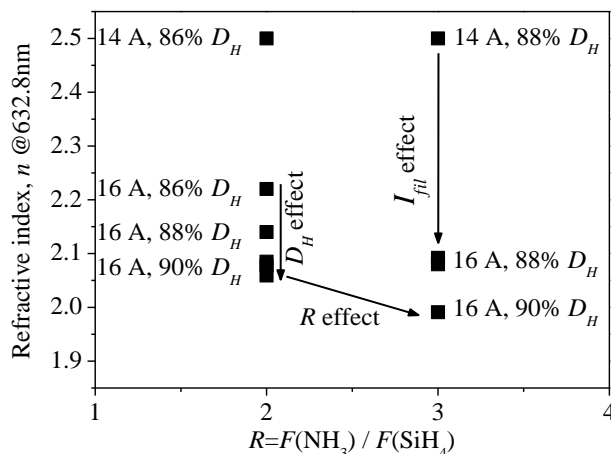
Fig. 3.3: Refractive index, n for the different single-layers of SiN$_x$:H, as a function of filament current (I_{fil}), NH$_3$ and SiH$_4$ gas flow rate ratio (R) and hydrogen dilution (D_H).

The above results are attributed to the effects of several mechanisms as discussed below:

- When R increases, keeping all the other parameters fixed the amount of ammonia inside the reactor increases and the decomposition probability of NH$_3$ on the heated filament increases as well. This effect increases the content of nitrogen and N/Si ratio inside the SiN$_x$:H films; reaching towards the stoichiometric value of refractive index (n~2) due to the increase of band gap and can be explained by the Kramers-Kronig dispersion relation [164].

- When I_{fil} increases, keeping all the other parameters fixed, the filament temperature increases as well. This gives rise to higher order dissociation of source gases into radicals and thus increasing the possibility of growing stoichiometric SiN$_x$:H films.

- When H$_2$ dilution increases, keeping all the other parameters fixed, there are large number of H* species to react with in the gas phase mechanism. Thus, the probability of abstraction reaction increases as well, giving rise to a lower concentration of hydrogen inside the films and better stoichiometry.

Fig.3.4 shows the effect of varying the same parameters that are varied in Fig. 3.3 on r_d. The information contained in the figure can be summarized by noting that r_d increases, as expected, when I_{fil} increases from 14 to 16 A, and decreases when H_2 dilution increases from 86% (88% at $R = 3$) to 90%, or when R increases from 2 to 3. The effect of H_2 dilution on r_d is explained by the surface etching of defective film tissue by atomic hydrogen while the R-effect is mainly due to the increase in gaseous fraction of the reactant gas (NH_3) with higher atomic bond energy. The dissociation probability of NH_3 is much smaller than that of SiH_4 for a given T_f and a given D_H.
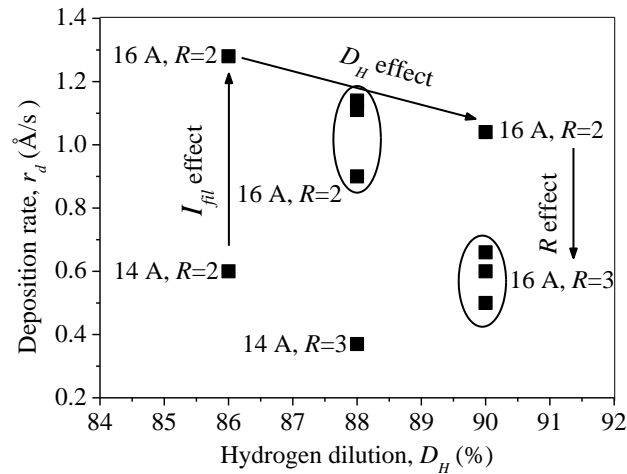
Fig. 3.4: Deposition rate, r_d for the different single-layers of SiN_x:H, as a function of filament current (I_{fil}), NH_3 and SiH_4 gas flow rate ratio (R) and hydrogen dilution (D_H).

Taking into consideration all the above results (Figs. 3.2, 3.3 and 3.4), single-layers of SiN_x:H thin films are obtained using the optimized conditions, namely 90% hydrogen dilution of silane and ammonia gaseous mixtures, Ta filament current of 16 A, corresponding to a filament temperature of 2000 ºC, and a flow rate ratio of NH_3 to SiH_4 (R) of 2, which give films with visible transmittance higher than 80%, $n{\sim}2$ at 632.8 nm and $r_d =1.1$ Å/s. Table 3.1 comprises all the optimized deposition conditions. It is to be noted here that compared to the previous work by Alpuim *et al*. [86], the substrate-to-filament distance has been increased to 7.5 cm, in order to avoid excessive heating of the PET substrates which have a maximum working temperature of ~110 ºC. Under these conditions it is found that lowering the working pressure from 40 mTorr to 25 mTorr and using H_2 dilution of the reactant gases yields more stoichiometric ($n{\sim}2$) and transparent ($> 80\%$) films than could be obtained by using the optimized deposition parameters for the conditions described in [86].

Parameters	Value
Maximum single-layer thickness (nm)	50-60
SiH_4 flow rate $F(SiH_4)$ (sccm)	2
NH_3 flow rate $F(NH_3)$ (sccm)	4
H_2 flow rate $F(H_2)$ (sccm)	54
H_2 dilution (D_H)	90%
Process gas pressure p_g (mTorr)	25
Nominal substrate temperature T_s (˚C)	100
Filament - substrate distance $d_{f\text{-}s}$ (cm)	7.5
Filament temperature T_f (˚C)	2000
Electric current supplied to the filament (A)	16
Total filament surface area (cm^2)	2.4

Table 3.1: Optimized deposition conditions for SiN_x:H thin films using HW-CVD

The optimized SiN_x:H thin films are characterized using different techniques. For the characterizations with ellipsometry, XRD and X-ray reflectometry analysis, the films are deposited on 510 μm thick c-Si wafers. For the optical transparency and morphological analysis and barrier property measurements, the SiN_x:H thin films are deposited on PET substrates. As mentioned earlier, in order to avoid damage of the PET substrates due to the radiation heating from the glowing filament, the single-layer film thickness is limited to 50-60 nm due to the increase of substrate temperature with deposition time and irradiation from the glowing filament. The detailed compositional analysis (FTIR, GD-OES and XPS measurements) of the films will be introduced in chapter 4, where the as deposited films will be compared with the low energy plasma treated films.

3.5 CHARACTERISTICS OF OPTIMIZED SILICON NITRIDE SINGLE-LAYER FILMS:

3.5.1 Optical characteristics

Fig. 3.5 shows the reflectance (R) and the transmittance (T) spectra of the bare PET substrate and SiN_x:H films deposited on PET substrate with the above mentioned optimized deposition conditions. The measurements are performed using Perkin Elmer Integrating Sphere apparatus both in transmission and reflection modes. The T and R curves indicates that the SiN_x:H layer is highly

transparent (> 80%) in the visible region, taking in to account the accuracy of the measurement (±1 %). It can also be seen from the spectrum that reflectance and transmittance of SiN$_x$:H layer together are around 100%, meaning that no absorption takes place in the layers and the films can perfectly be used as a window layer for organic optoelectronic devices. The slight absorption below 450 nm is due to the PET substrate itself.
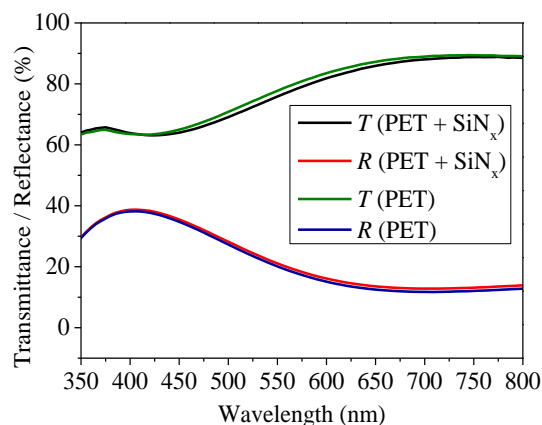
Fig. 3.5: Reflection and transmission spectra of SiN$_x$:H film on PET substrate. The reflectance (R) and transmittance (T) of the layer together is almost 100%, means no absorption inside the films.

From the fit of the spectroscopic ellipsometric measured data to the model (equation 3.12), in the visible region, the refractive index, n and the extinction coefficient, k, are obtained as shown in Fig. 3.6. The value of n at 632.8 nm is 2.01 which is close to the value 2.05 found in the literature for stoichiometric amorphous Si$_3$N$_4$ [158-162]. The value of k shows that the film is not absorbing in the visible region. The measured thickness of the single-layer is 50 ± 2 nm, which matches perfectly with the initial thickness measurements by profilometer and XRR method (discussed later).
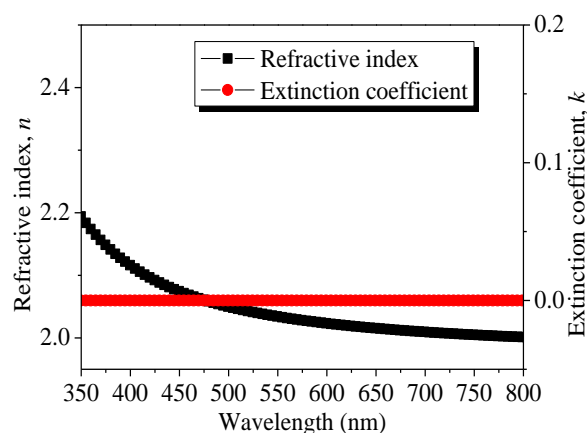
Fig. 3.6: Refractive index (n) and extinction coefficient (k), in the visible region, obtained from the ellipsometric measurement data for the single-layer of SiN$_x$:H (50 nm) on c-Si substrate.

3.5.2 Structural characteristics

The orientation and nature of the material are investigated using the XRD measurements. X-ray diffraction patterns of SiN$_x$:H single-layer films deposited on c-Si substrate and PET foils are shown in Fig. 3.7. The peaks in those figures correspond to the substrates themselves and there is no evidence of crystalline peaks corresponding to the SiN$_x$:H films. This suggests, as expected, that the SiN$_x$:H films deposited at low temperature (100 °C) are amorphous.
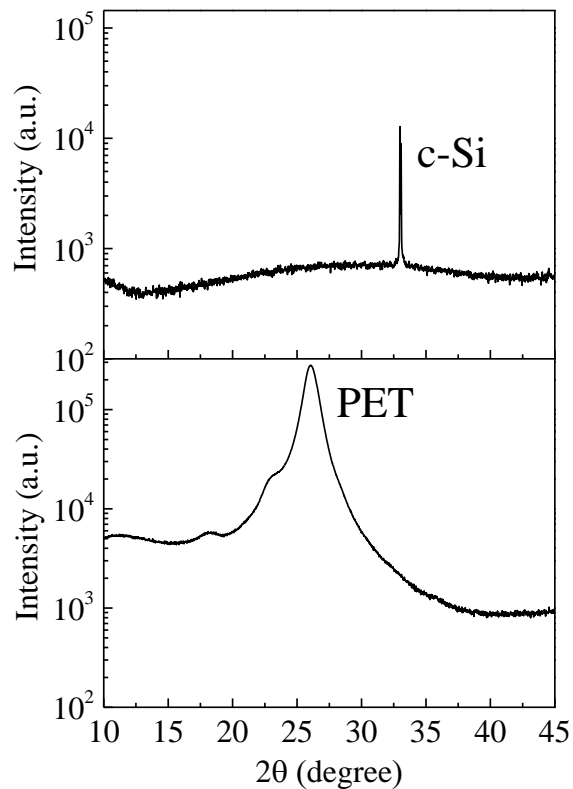
Fig. 3.7: X-ray diffraction patterns of SiN$_x$:H single-layer films (50 nm) deposited on c-Si substrate and on PET foil.

X-ray reflectometry (XRR) measurements are performed on 50 nm thick SiN$_x$:H single-layer film deposited on c-Si wafer. The analysis parameters are described previously in chapter 2. The precise film thickness, mass density of the film and surface roughness are measured. Fig. 3.8 shows the normalized reflected X-ray intensity with a critical angle position at 0.2 Å^{-1}. From the fitting of this measured data with Parratt model [107], the total film thickness is obtained very accurately from the fringes of the oscillation. The measured film thickness of the film matches perfectly with the initial thickness measurements by profilometer and ellipsometry (discussed above). The deposition rate is corrected accordingly. The mass density obtained from the fitted results is 2.83 ± 0.02 g/cm^3, which

is lower than that of stoichiometric Si_3N_4:H (3.1 g/cm^3) reported in literature [158]. It is to be noted here that compared to the previous work by Alpuim *et al*. [86] with mass density 2.56 g/cm^3, using H_2 dilution of the source gases and increasing the filament to substrate distance ($d_{f\text{-}s}$) in the present study, the mass density is higher. This is probably attributed to the effect of higher collisions of the radicals between the filament and the substrate and the abstraction reaction of atomic hydrogen during the surface reactions as discussed before in this chapter. The surface roughness of the film is 2 nm and is comparable to the AFM measurement (2.1 nm).
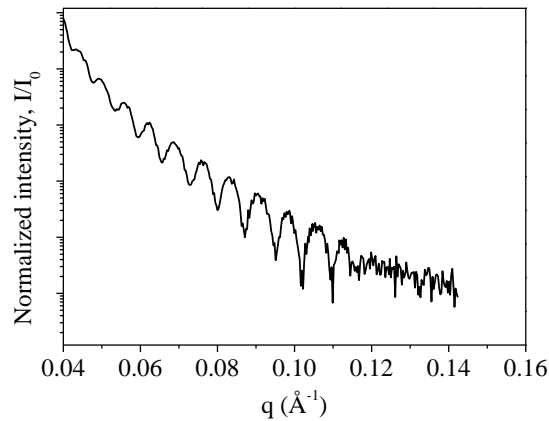
Fig. 3.8: X-ray reflectivity signal for the 50 nm thick SiN$_x$:H single-layer deposited on c-Si wafer.

3.5.3 Morphological characteristics

The average surface roughness of the single-layer SiN$_x$:H thin films is analysed using the tapping mode AFM technique. The single-layers are deposited on PET substrates at T_s =100 °C. It should be noted here that the initial roughness of the PET substrate depends considerably on the cleaning of dust particles by different solvents (possibly due to the wettability of PET towards those solvents). Several cleaning methods are undertaken in order to find an optimized method which gives rise to minimum initial roughness, as shown in Table 3.2. The minimum initial average roughness for PET foils before being exposed to HW-CVD process is 1.35 ± 0.06 nm which corresponds to a cleaning procedure of rinsing with DI water in an ultrasonic bath for 15 s. The average roughness of the bare PET substrate after exposure to the hot filament for the same time (400 s) as it takes for one single-layer (50 nm) deposition, but without film growth, is around 55 nm. The roughness of PET increases strongly when the PET foil is exposed to the Ta filament, probably due to the fact that the glass transition of PET at around 80 °C is somewhat overcome (100 °C) inducing a warping of the foil. This explains the high initial roughness of the SiN$_x$:H single-layer films deposited on PET substrates (discussed in next paragraph).

55

Cleaning method	0 s in ultrasonic	15 s in ultrasonic	60 s in ultrasonic	300 s in ultrasonic	600 s in ultrasonic
Deionized water	4.06 nm	1.35 nm	9 nm	9.45 nm	14.8 nm
Isopropyl alcohol	8.17 nm	2.16 nm	8.2 nm	9.89 nm	16 nm
Acetone	8.83 nm	3 nm	10.3 nm	10.56 nm	17.8 nm

Table 3.2: Initial average surface roughness of the bare PET substrates with different cleaning methods.

Three dimensional surface images of the single-layers with increasing thickness are shown in Fig. 3.9 and summarized in Fig. 3.10. Fig. 3.10 shows the decrease in average surface roughness from 55 nm to 23 nm when the PET substrate is covered by a SiNx:H layer of thickness at least equal to a critical thickness (d_c) of 50 nm. Critical thickness in this case is the maximum single-layer thickness which can be deposited in a single run inside the HW-CVD reactor without damaging the PET substrate and produces the maximum average surface roughness reduction. From this initial result of average roughness reduction, it is expected that the permeation of water vapor will be reduced maximum, when the substrate is coated with a layer thickness near its critical thickness value (50 nm).
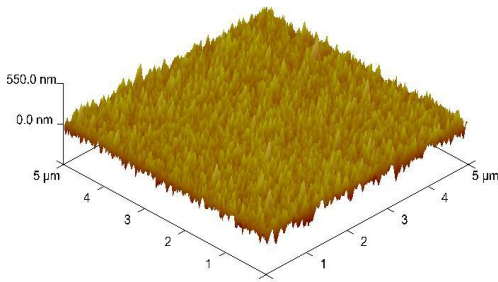
(a)
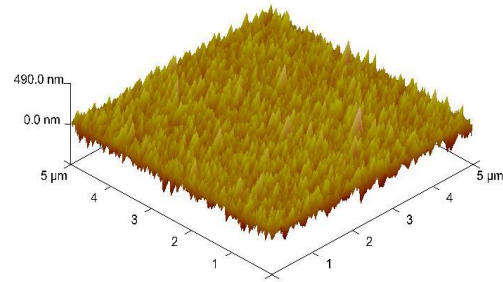
(b)
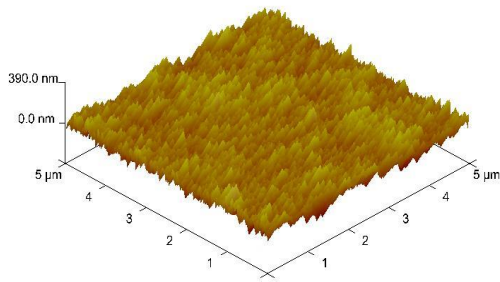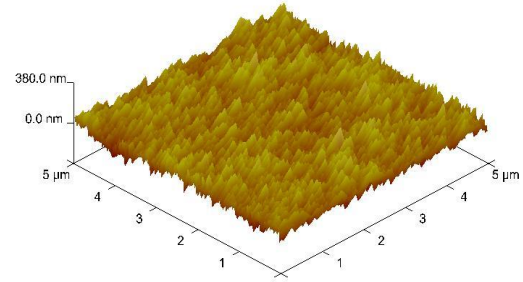
(c)   (d)
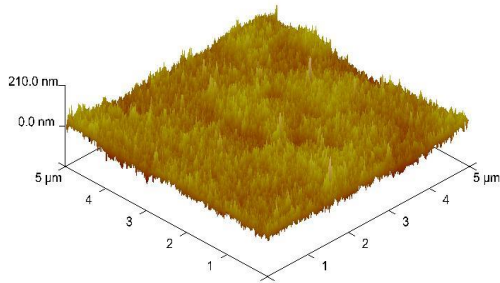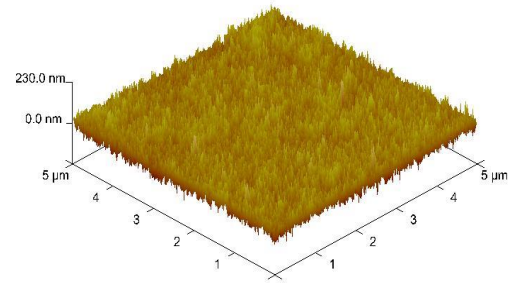
(e)   (f)

Fig. 3.9: Three dimensional AFM images of the surfaces of SiN$_x$:H single-layers deposited on PET substrates with increasing thickness: (a) 10 nm, (b) 20 nm, (c) 30 nm, (d) 40 nm, (e) 50 nm and (f) 60 nm. [To observe the effect, the sensitivity of the color scale is increased].
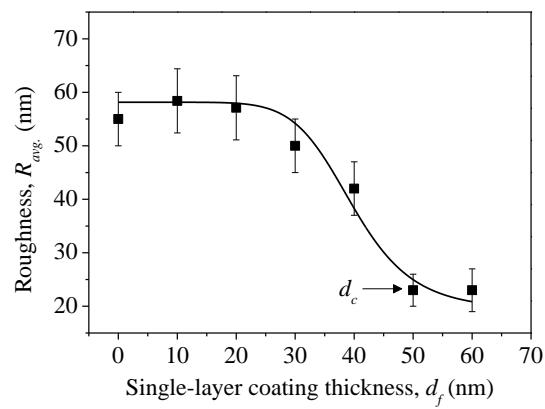
Fig. 3.10: Variation of average roughness of SiN$_x$:H single-layers coated on PET substrates with the coating thickness.

3.5.4 Barrier characteristics of single-layer films

The permeation barrier properties of the single-layer SiN_x:H films deposited on PET substrates are performed using the electrical calcium degradation test method at ambient atmospheric conditions. Figure 3.11 (a) shows the evolution of normalized conductance of Ca sensors, deposited on PET substrates whose back side has been coated with SiN_x:H single-layers with thickness ranging from 10 nm to 60 nm. Bare plastic is used as the reference for the calcium degradation test. With the increase of the SiN_x:H single-layer thickness (d_f), the minimum time taken by the water molecules to permeate through the whole barrier thickness including PET substrate ("lag-time"), is increased as can be seen in Fig. 3.11 (b). As seen in Fig. 3.11 (c), the barrier performance assessed by the decrease of the WVTR value also improves with the increase of SiN_x:H single-layer coating thickness (d_f). The WVTR of the single-layers depends strongly on the surface roughness of the films [165] and varies in a similar way with the average roughness variation as expected. The curve can be divided into three regions. The first one, from 0 to 20 nm, corresponds to the "threshold thickness (d_{th})" region, below which there is no barrier effect and over which ($d_f > d_{th}$, defining the second region) the permeation rate drops steeply until it stabilizes at a critical thickness (d_c) value (about 50 to 60 nm in this case, defining the third region). It should be noted that evolution of WVTR versus the single-layer thickness (Fig. 3.11 (c)) follows the same trend as the evolution of surface roughness versus thickness (Fig. 3.10). For $d_f > d_c$, no further significant decrease in WVTR is observed, the stabilized value being $\sim 1 \times 10^{-2}$ g/ m^2.day. From this first measurement, we define the critical thickness as the maximum single-layer thickness resulting in the maximum WVTR reduction.

It is worth mentioning that the critical thickness (d_c) for HW-CVD grown SiN_x:H single-layer thin films falls in the same range (50 to 100 nm) as reported by several authors [18, 68, 71, 166-168]. The d_c value depends considerably on the deposition method. The above results can be interpreted taking into account the gas permeation mechanism through the thin films, as described by H. Chatham [166]. In the second region of Fig. 3.11 (c), where permeation rate decreases with thickness, is dominated by the thermally activated diffusion of water vapor through the films. In this region the permeation rate varies inversely with the coating thickness (d_f) and the total permeation through the barrier coated polymer substrates can be expressed following a parallel type equation (3.13) [71, 169]:

$$\frac{d_{total}}{P_{total}} = \frac{d_f}{P_f} + \frac{d_s}{P_s} \qquad\qquad (3.13)$$

Where d_{total}, d_f and d_s are total thickness of the structure, coating thickness and substrate thickness respectively. P_{total}, P_f and P_s are overall permeability of the structure, permeability of the coating and permeability of the substrate respectively.

This is followed by the defect dominated permeation region, where the permeation rate is independent of the coating thickness (d_f). It should be noted that the samples are deposited on a face-down sample holder in the HW-CVD system. Therefore, the probability of defect formation due to the inner wall flakes is small. Takeda and co-workers [167, 170, 171] and Leterrier *et al*. [71] found that, with the increase of coating thickness, the compressive stresses are lowered. This indicates a stress relaxation process during the film growth which in turns results in the formation of nano-scopic defects. As discussed in chapter 1, the diffusion of water molecules is largely controlled by the nano-scopic defects and thus after the critical thickness no more barrier improvement is observed up to a definite range. Therefore, this proves that the permeation rate for single-layer barriers on polymer substrates generally changes by no more than one order of magnitude for the normal CVD deposited thin films and thus a single-layer barrier coating alone is not effective in reducing the overall barrier properties down to the required barrier for utilization of organic optoelectronic devices.

Based only on these WVTR results; it is expected that the stack of several SiN_x:H single-layers, each having a thickness equal to or greater than the critical thickness (d_c), will be very effective in reducing the overall WVTR value and thereby in improving the overall performance of the permeation barrier. This is due to the independence of structural defects during the subsequent deposited single-layers.
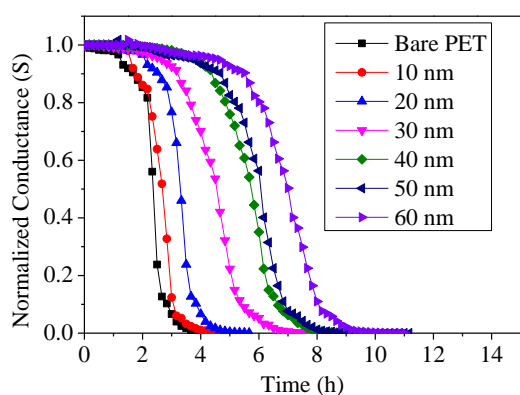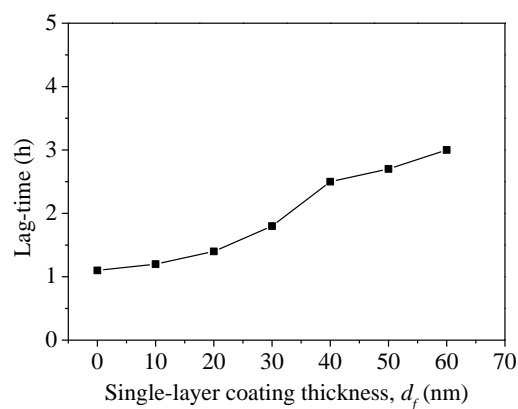
(a)   (b)
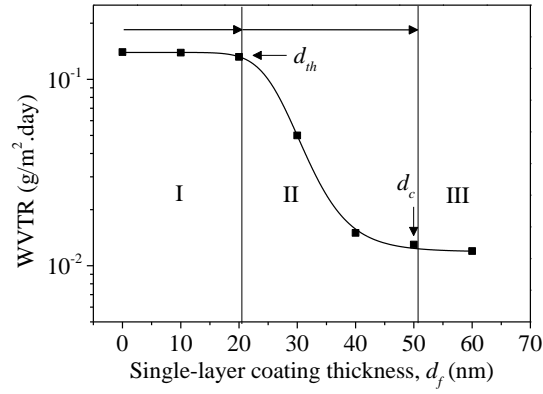
(c)

Fig. 3.11: (a) Evolution of normalized conductance of Ca sensor deposited on PET coated with single-layers of SiN$_x$:H thin films with different thicknesses. The uncoated PET is shown as reference. (b) Variation of "lag-time" with SiN$_x$:H single-layer coating thickness. (c) Effect of SiN$_x$:H single-layer coating thickness on WVTR values.

The barrier improvement factor (*BIF*) is another way to quantify the improvement of barrier properties using coatings. This quantity allows one to compare directly the barrier properties of different materials. *BIF* is defined by [166]:

$$BIF = \frac{WVTR \, (bare \, PET)}{WVTR(coated \, PET)} \qquad (3.14)$$

Fig. 3.12 shows the variation of the *BIF* with increasing SiN$_x$:H single-layer thickness. From the figure it is clear that, with increasing single-layer thickness, the barrier performance also improves and the *BIF* is 14 times higher for 50 nm single-layer thickness as compared to the bare PET substrate. The largest improvement occurs between 30 nm and 50 nm single-layers.
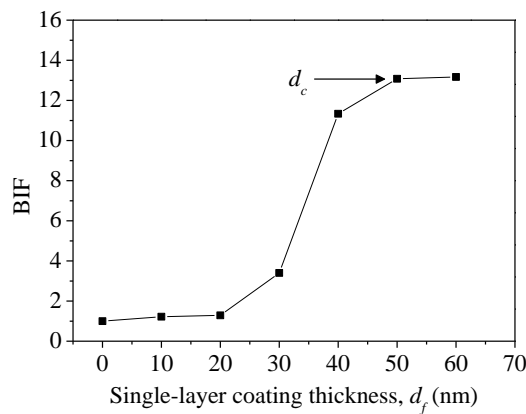
Fig. 3.12: Barrier improvement factor variation with SiN$_x$:H single-layer coating thickness.

3.6 MULTILAYER OF SiN$_x$:H FILMS

The improvement in barrier performance is limited mainly by pinholes or nanometer-to-micron sized structural defects, originating either from the surface roughness of the underlying layer or from the fact that depositing SiN$_x$:H layers at low temperature induce porosity. In order to improve the barrier properties, either the defect formation in the film needs to be avoided or the effect of defects needs to be minimized. Multilayers of inorganic thin films are quite effective in order to create a break of the channeling of defects from one layer to the next layer. In the following section of this chapter, the properties of the multilayer SiN$_x$:H thin films are investigated where the critical thickness (d_c) is taken to be a fixed parameter for the single-layer thickness. The multilayer structure is fabricated on PET substrates by making a stop between each successive single-layer deposition. During this stop, the shutter remains in closed position, while the sample is kept at the substrate temperature (T_s). The number of single-layers (each of thickness = 50 nm) is increased from 2 to 5 so that the total thickness ranges from 100 to 250 nm.

3.6.1 Morphological characteristics of multi-layer films

The surface topography of the multilayer films has been characterized by tapping mode AFM technique. Fig. 3.13 shows the surface topography of the SiN$_x$:H multilayers deposited on PET substrates. Due to high initial roughness of the heat treated PET foils (discussed above), the roughness is quite high for the samples. It can be observed from Fig. 3.14 that all the samples, in the range of thickness studied, have the effect of reducing the average surface roughness. The lowest average surface roughness of 15.5 nm is achieved for the stack of 5 SiN$_x$:H single-layers (5 layers $\times$ 50 nm/layer = 250 nm).

(a)

(b)

(c)   (d)
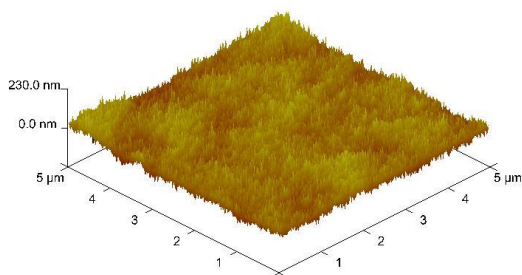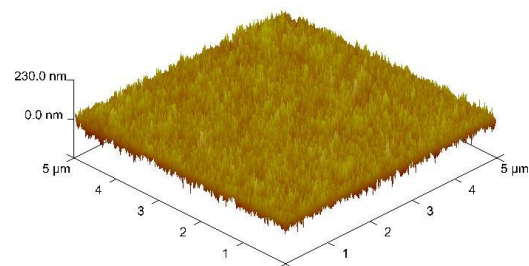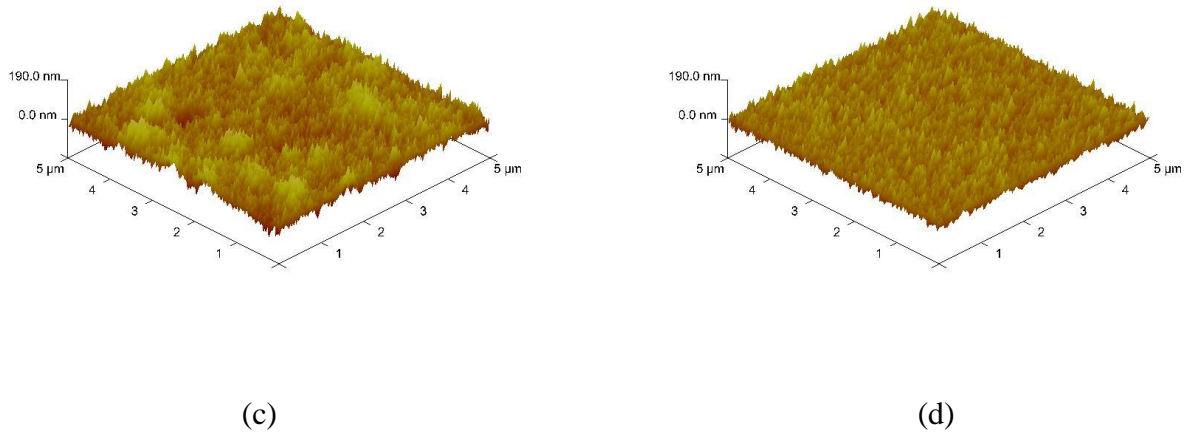
Fig. 3.13: Three dimensional AFM images of the surfaces of SiN$_x$:H multi-layers deposited on PET substrates with increasing thickness: (a) 50 nm + 50 nm, (b) 50 nm + 50 nm + 50 nm, (c) 50 nm + 50 nm + 50 nm + 50 nm, (d) 50 nm + 50 nm + 50 nm + 50 nm + 50 nm. [To observe the effect, the sensitivity of the color scale is increased].
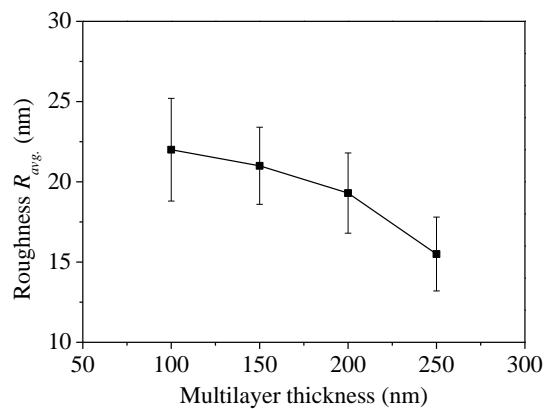
Fig. 3.14: Variation of average roughness of SiN$_x$:H multi-layers coated on PET substrates with the coating thickness.

3.6.2 Barrier characteristics of multi-layer films

The evolutions of normalized conductance of the Ca sensors deposited on such multi-barrier coated PET substrates are shown in Fig. 3.15 (a). Slight kinks are observable in the traces, which are probably due to the inhomogeneous oxidation of the calcium surface. One possible reason of this inhomogeneous oxidation is the in-homogeneities inside both the barrier layers and the PET substrate. When the number of SiN$_x$:H single layers increases, the number of interfaces between SiN$_x$:H films increases as well and there are possible breaks of the propagation of pinholes from one single-layer to the next single-layer. Due to that reason and to the increase in total thickness of the coating, the minimum time taken by the water molecules to reach the Ca sensor, which is at the

opposite side of the coated PET substrates ("lag-time"), increases with increasing number of stacked SiN$_x$:H single-layers as shown in Fig. 3.15 (b). A maximum lag-time of 14 hours has been achieved with 5 stacked SiN$_x$:H single-layers. The WVTR values have also decreased monotonically with increasing number of layers (see Fig. 3.15 (c)), reaching a minimum value of ~7.9 × 10^{-3} g/ (m^2.day). Fig. 3.15 (d) shows the variation of *BIF* with increasing number of SiN$_x$:H multi-layer thickness. When the single-layers of SiN$_x$:H are stacked, the BIF increases monotonically as compared to the bare PET substrates and reaches to the value of 21. This trend suggests that, if the number of layers is further increased, the barrier properties will improve. But the increased thickness will decrease the optical transparency and the mechanical flexibility of the whole structure. Thus a trade-off should be found.

The above observations are consistent as expected. The multilayer structures improve the barrier properties to some extent; however, the improvement is not sufficient in terms of the encapsulation requirements. There are two factors that affect the whole barrier mechanism for the multilayer structures. First of all, the surface quality of the individual inorganic films is quite critical in order to improve the permeation property. The interface roughness should be as small as possible in order to deposit the subsequent inorganic layer with higher structural quality. Secondly, the probability of the occurrence of pinholes or structural defects at the same lateral position in two subsequent thin films is not zero. This may facilitate the diffusion of water molecules in a faster way. In order to improve the overall barrier property, the film surface property should be modified. In the following chapter we will focus our efforts to modify the interface properties using impact of low energy ions.
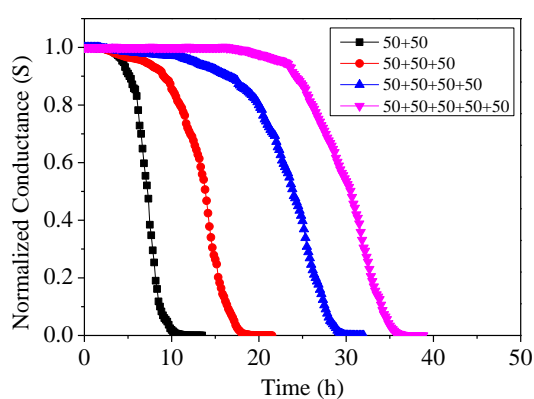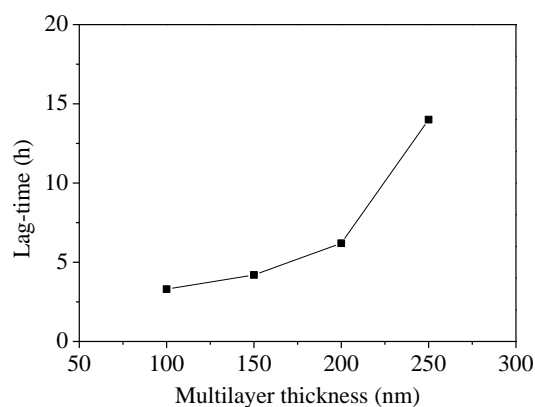
(a)   (b)
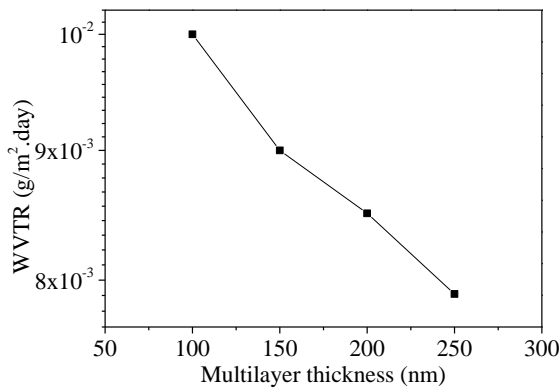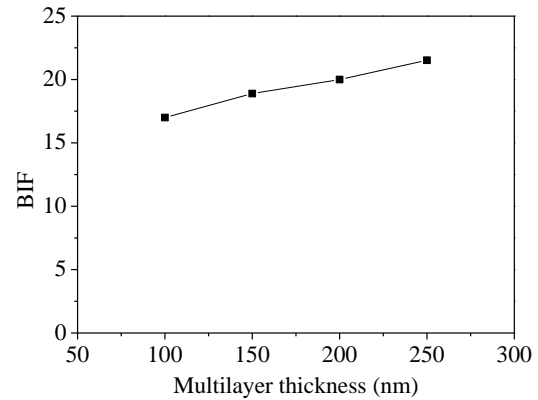
(c)	(d)

Fig. 3.15: (a) Evolution of normalized conductance of Ca sensor deposited on PET coated with multi-layers of SiN_x:H thin films with different thicknesses. (b) Variation of "lag-time" with SiN_x:H multi-layer coating thickness. (c) Effect of SiN_x:H multi-layer coating thickness on WVTR values. (d) Barrier improvement factor variation with SiN_x:H multi-layer coating thickness.

3.6 SUMMARY OF CHAPTER 3

i. In this chapter, using the HW-CVD technique, based on silane and ammonia gaseous mixtures diluted in hydrogen at a substrate temperature of 100 °C and after an optimization taking into account the different growth parameters, we have deposited device quality transparent and stoichiometric silicon nitride thin films which can be used as moisture barrier layers for encapsulation of flexible organic electronic devices.

ii. The optimized SiN_x:H thin films are characterized using different techniques. Transmission measurements suggest that the films are highly transparent in the visible region. The refractive index measurement indicates that the films are close to the stoichiometric Si_3N_4. The amorphous nature of the low temperature deposited films is evidenced by XRD analysis. The density measurements carried out by XRR method informs about the mass density value of the films.

iii. A critical thickness is defined from the initial roughness measurements by AFM and this value is confirmed by the permeation barrier measurements using the electrical calcium test. A tentative physical interpretation is given taking into account the gas permeation mechanism through films and model described previously by different authors.

iv. In order to improve the permeation barrier property, multilayers of SiN_x:H films are used to create a break in the propagation of defects throughout the whole structure. Although, the

multilayer structure improves the barrier property to some extent, however, the WVTR value is quite high to fulfil the requirement for the organic optoelectronic devices.

CHAPTER 4

SILICON NITRIDE MULTILAYER TREATED BY ARGON PLASMA

4.1 INTRODUCTION

The improvement of the barrier properties is mainly limited by the pinholes or defects that propagate from one single-layer to the other. The multilayer stack of SiN_x:H single-layers logically induces a barrier improvement compared to the single-layer films. However, the barrier properties (WVTR) of the multilayer stacks are several order of magnitude higher compared to the targeted values. As discussed in the previous chapter, this limited improvement is due to the non-zero probability of occurrence of pinholes or structural defects crossing subsequent SiN_x:H single-layers. Therefore, in the thesis, we looked for a technique which could drastically modify the surface structure of each single-layer films near the interface without modifying significantly the bulk layer structure, which is challenging. The conventional techniques to reduce the effect of pinhole or defect propagation are based on developing alternating hybrid layer structures, which could reduce the permeation rate substantially. This route seems interesting if we are able to deposit the organic layers as well as the inorganic layers in the same reactor, which is not our case. In this thesis, the effect of ion treatment on the single-layer surfaces on the overall permeation barrier properties has been studied. This unique encapsulation method is based on low energy ion bombardment on the thin film surface to create atomic displacements at the surface and then stacking the single-layer films one after the other to develop a multilayer structure.

The plasma treatment is a well-known industrial process used to deposit or to etch materials and to modify the film surface properties for various commercial purposes. The use of plasma surface treatment in corrosion resistant coating technology is already a well-established technique. Most of these treatment methods are based on plasma produced by corona or glow discharges. The basic aim of this chapter is to deal with the plasma treatment parameters in which the plasma active species interact only very superficially with the thin film material, i.e. with the first few atomic layers of the surface of the thin films. This interaction can lead to significant modifications of the film surfaces which could be beneficial for the diffusion barrier purposes. The idea of such plasma treatment is not to use highly energetic ions. It should neither damage the surface or the bulk layer of the films, nor

inject ions or atoms below the surface (ion implantation), nor remove material from the film (sputtering or etching) [172].

4.2 PLASMA TREATMENT PROCEDURE

In order to study the effects of plasma ion bombardment on the film surface, the ion bombardment parameters, such as, ion type, ion kinetic energy and ion flux (number of ions impinging per unit area of the electrode per unit time), need to be well controlled. In a plasma generator system, ions can have a considerable amount of kinetic energy compared to the neutrals because the ions can gain energy when they are accelerated inside the electric field produced in the plasma sheaths (as discussed later) between the two electrodes. Due to this reason, ions can induce film surface treatment or modify the film surface in comparison to the neutrals [172]. In the following we consider only cold (non-local thermodynamic equilibrium) plasmas where the energy of the electrons (T_e) is much higher than the energy of the ions.

Among the various types of plasma treatment methods, the radio frequency (RF) PE-CVD is widely used in laboratories. The details of the RF PE-CVD system are described in Chapter 2. It is a capacitive-coupled PE-CVD system, where the RF power is fed to the bottom electrode (anode) and top electrode (cathode) is used as a substrate holder. The plasma is produced between the two electrodes due to the inelastic collisions of electrons having energy above some threshold energy with the neutral species [172-175]. Plasma electron density n_0 and the electron temperature T_e are the fundamental properties of the plasma. In a typical low pressure capacitively-coupled RF PE-CVD cold plasma system, the plasma electrons having a non-Maxwellian (Druyvesteyn) energy distribution, defines the electron temperature, T_e [173]:

$$N(E) = \frac{An_0}{(kT_e)^{3/2}} \exp\left[-B\left(\frac{E}{kT_e}\right)^2\right] \qquad (4.1)$$

Where, A and B are constants depending on the energy distribution. The neutral species are ionized due to the collisions with the energetic electrons according to the convolution

$$N_i = \int n_0(E, T_e) f_i(E) dE \qquad (4.2)$$

Where, f_i is the ionization probability as shown schematically in Fig. 4.1.

The electrons have a higher mobility compared to the positive ions in an ionized gas, however inside the plasma where collective behavior of charged particles is dominant; a plasma sheath is created next to the electrodes due to quasi-neutrality conditions [173]. The plasma sheath acts as a diode and the electrodes acquire a self-bias voltage. The bias voltage is divided between the two electrodes and

inversely proportional to the electrode areas. Thus the smaller electrode acquires the larger bias voltage. The sheath voltage (roughly the bias voltage) accelerates the positive ions and the ions gain kinetic energies in order to bombard the sample. If the mean free path of the ions between two successive collisions is higher than the sheath thickness, then the mean ion energy is just: ion charge $\times$ V_{Bias}. If conversely the mean free path of ions is smaller than the space charge sheath then the mean ion energy is a fraction of that, say 0.4 [174, 176, 177]. At a typical low pressure region (say 50 mTorr), there are still significant ion collisions in the sheath. Therefore, a wide ion energy distribution occurs (Fig. 4.2), where the maximum energy E_{max} (i.e. the sheath voltage) is above the mean ion energy ($\bar{E}_{ion}$) [176, 177]. In a simple capacitive coupled PE-CVD system, V_{Bias} is proportional to the RF power and inversely proportional to the working pressure. The ion current and ion energy both vary with the input RF power (P_{RF}). The ion current increases with the square-root of both RF power and working pressure [173]. One useful approximate formula to calculate the ion current is $I_{ion} \approx P_{RF} / V_{Bias}$. In the rest of this chapter, the results are discussed in terms of power density ($P_w = P_{RF} /$ electrode area) and working pressure (p_g). However, it should be noted that the values of power density and working pressure only reflect the maximum ion energy (E_{max}) whereas the mean ion energy is 0.4 times of E_{max}. The ion flux, F_i, is defined as the total current falling on the electrode area [172, 173]

$$F_{ion} = \frac{I_{ion}}{eA_{electrode}} \quad \text{(ions/m}^2\text{.s)} \tag{4.3}$$

The ion fluence is an important parameter for the plasma treatment which can affect considerably for constant ion energy and defined as the product of the ion flux by treatment duration (t) [172, 173].

$Ion\ fluence = F_{ion} \times t\ \text{(ions.m}^{-2})$ \hfill (4.4)

The ion energy fluence is the other important parameter which is defined as the product of ion fluence by kinetic energy of each ions impinging on the cathode surface:

$Ion\ energy\ fluence = Ion\ fluence \times E_{max}\ \text{(eV/m}^2)$ \hfill (4.5)
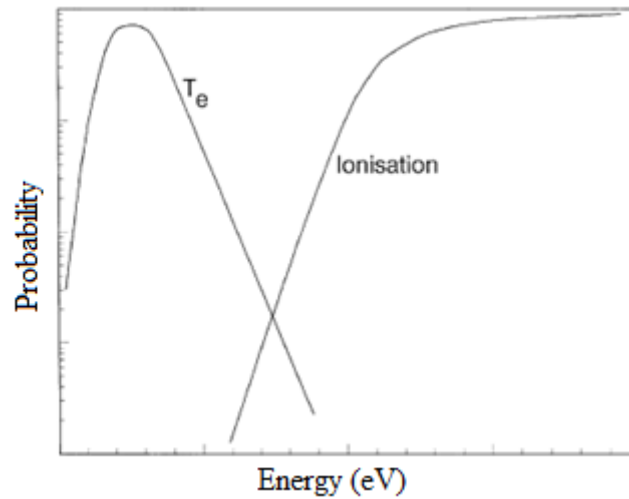
Fig. 4.1: Schematic diagram of electron temperature T_e and the ionization probability of a species.
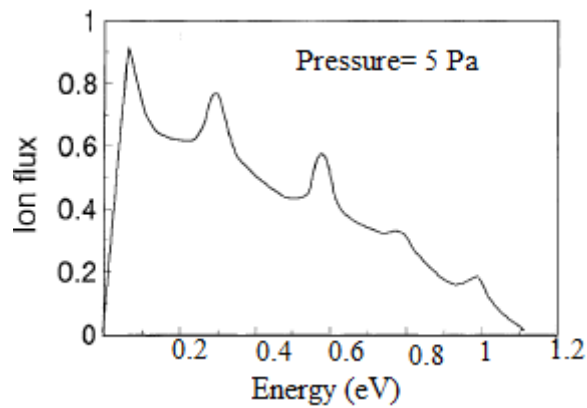
Fig. 4.2: An example of typical ion energy distribution in conventional plasma deposition at 5 Pa pressure. Reprinted from [174] with permission from 2002 Elsevier.

Ions being accelerated by the cathode sheath potential gain sufficient energy with the maximum energy impinging the cathode surface corresponding to the bias potential. Such ions striking a material can penetrate to a certain depth within a depth distribution [178]. The depth distribution depends on the nature of the ions, their energy and their atomic mass and on the density and the atomic mass of target atoms. During their travel through the material, energy is transferred to the near environment. Depending on the energy range, ions can transfer energy in a pure mechanical way through nuclear interaction (nuclear stopping power), but can also loose energy through electronic collisions (electronic stopping power). In the low energy range (below 50 eV) these mechanisms will cause rearrangement of the neighboring atoms, initiating an atomic collision cascade [179]. As a result, target atoms will be relocated from their original position. Ions (mass M_1) striking elastically

69

the atoms at the surface of the film transfer energy to the target atoms (mass M_2). The maximum energy transfer (E_T) from an ion of maximum energy, E_{max}, to an atom at rest is obtained from the laws of conservation of energy and momentum and is given by [180]

$$E_T = \frac{4M_1M_2}{(M_1+M_2)^2}E_{max} \tag{4.6}$$

There is some minimum energy that must be transferred in order to produce atomic displacement, called the displacement threshold energy, E_d. By definition of E_d, the probability of displacement for $E_T < E_d$ is zero. If E_d is a fixed value under all conditions then the probability of displacement for $E_T > E_d$ is one. The struck lattice atom with energy at least E_T is referred as primary knock-on atom. This atom moves through the lattice producing energy transfer to the neighboring atoms, resulting in a collision cascade mechanism [181]. The cohesive energy of a crystal is defined as the energy which must be added to the crystal in order to separate its components into neutral free atoms at rest, at infinite separation, with the same electronic configuration. It is known that the typical cohesive energy between atoms in a solid equals several eV (~4.6 eV for Si atoms) [182]. Whenever the impinging ions have sufficient energy, they can displace atoms in the lattice. The typical values for average surface atomic displacement threshold energy for Si (atomic mass = 28 amu) are roughly in the range of ~15 to 25 eV and ~20 to 40 eV for more bonded bulk atom displacement [183-186]. When the ions have higher kinetic energy, the target atoms are sputtered away. The sputtering energy threshold for Si is roughly >50 eV and sputter yield increases with the increasing incoming ion energy [180, 187]. The energy threshold values for N atoms are slightly larger than Si atoms, due to the lower energy transfer from the ions toward N atoms owing to its lower atomic mass (atomic mass = 14 amu) and to its higher cohesive energy. The ion bombardment on the surface must be such that it disrupts the atomic distribution to a few nm in depth, disturbing the continuity of a structural defect through this interface but it cannot significantly damage the interface.

The plasma treatment is carried out between each successive SiN_x:H single-layer deposition by moving the sample holder from HW-CVD chamber to the RF PE-CVD chamber through the gate valve without breaking the vacuum keeping the same substrate temperature (100 °C). The number of plasma treated single-layers (m) is increased by stacking the layers one after the other and thus increase the total thickness of the barrier. For the plasma treatment argon (atomic mass = 40 amu and first ionization potential = 15.75 eV) has been chosen as an ion source for bombarding the sample surface at normal incidence, because as being one of the rare gases, it is much less reactive than oxygen ions for example. Ar is a good compromise in terms of ionization energy (15.75 eV) between higher atomic number rare gases (like Kr and Xe) and lower atomic number rare gases (like He and Ne) for displacing Si atoms according to equation 4.6. Four different parameters are varied in order

to obtain an optimal treatment condition which can improve the barrier properties significantly. The following block diagram shows the variation of treatment parameters: treatment time (t); power density (P_w); working pressure (p_g) and number of layers (m). Here the thickness of each single-layer is fixed at the critical thickness (50 nm). The sub-script b stands for the 'best' parameter while others remain fixed, which gives rise to the 'best' barrier properties under such conditions. It should be reminded that the four parameters are not totally independent to each other. Thus, best parameter does not mean necessarily the optimum value versus variation of each parameter.

The treatment parameters are optimized using a double layer SiN$_x$:H structure (total thickness = 100 nm), in order to simplify the procedure. First, the treatment duration is optimized with a fixed power density and working pressure. This is followed by variation of power density and working pressure in order to find an optimum treatment parameter while the treatment duration remains constant. Whenever one parameter is varied, other parameters remain fixed. Finally, all the observations are taken into account to obtain good barrier properties by increasing the total number of layers.

In order to observe effects on the permeation barrier properties due to the different plasma treatment parameters, and to give a coherent physical interpretation of the experimental results, intermediate steps including extra analytical techniques have been mandatory through new specific samples prepared for this purpose. For example, morphological, compositional and structural data demanded extra samples deposited on c-Si substrates in order to be assessed through AFM, Fourier Transform Infrared Spectroscopy, Glow Discharge Optical Emission Spectroscopy, X- ray Photoelectron Spectroscopy and X-ray Reflectometry measurements. These intermediate steps have been possible with the help of INL at Braga; LPMC at Ecole Polytechnique; IRAMIS-CEA Saclay and HORIBA Jobin-Yvon at Palaiseau.

Figure content (flowchart):

Parameters
Treatment time (t)
Power density (P_w)
Working pressure (p_g)
Number of layer (m)

Increase of m (2-5)
Fixed P_w, p_g, t_{min} → Lag-time and WVTR

Variation of t
Fixed P_w, p_g, $m=2$ ↓

$t_{(b)}$

Increase of m (2-5)
Fixed P_w, p_g, $t_{(b)}$ → Lag-time and WVTR

Variation of P_w
Fixed $t_{(b)}$, p_g, $m=2$ ↓

Variation of p_g
Fixed $t_{(b)}$, P_w, $m=2$ ↓

$P_{w(b)}$ $p_{g(b)}$

Increase of m (2-5)
Fixed $P_{w(b)}$, $p_{g(b)}$, $t_{(b)}$ → Lag-time and WVTR
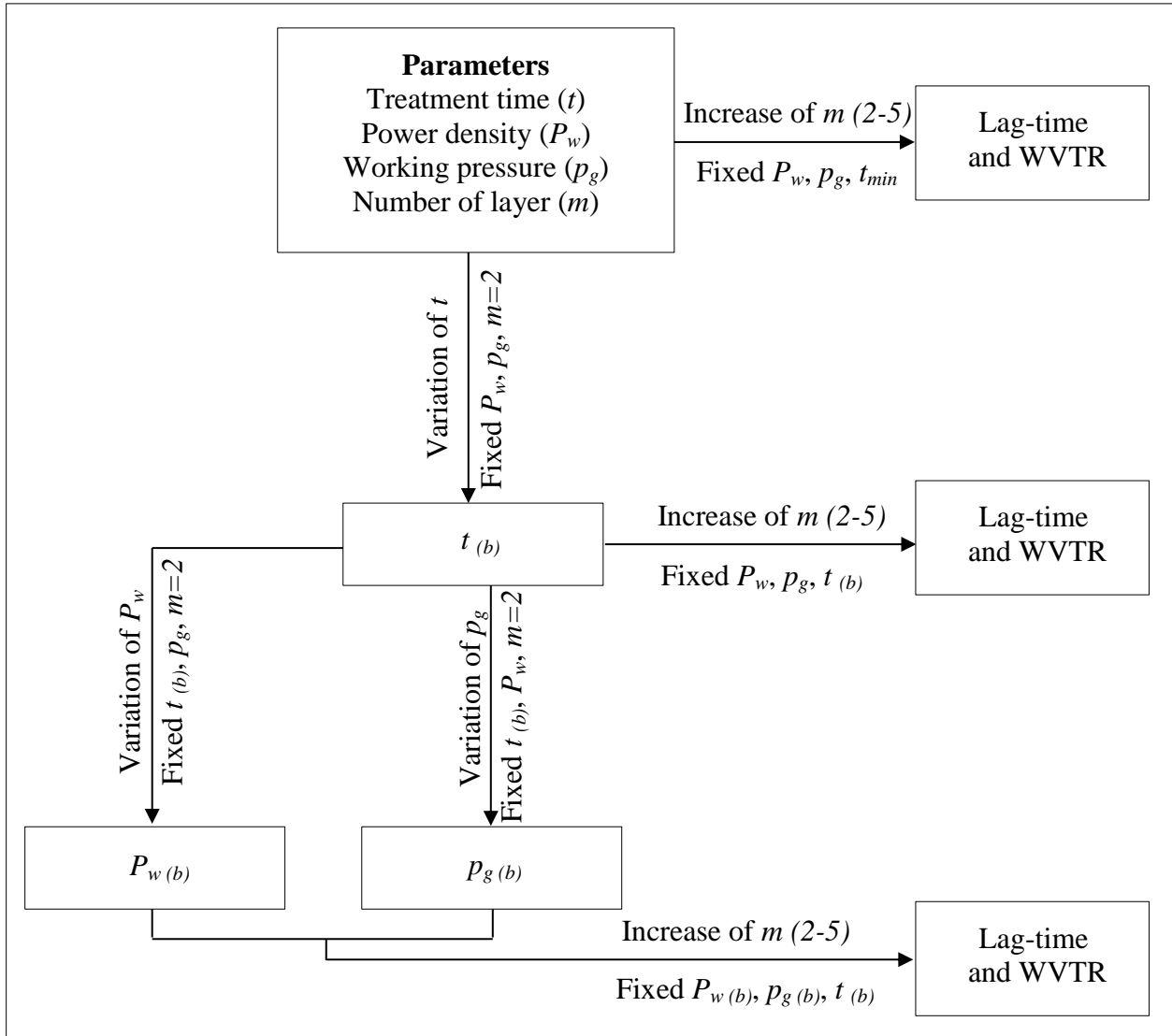
4.3 IMPACT OF ARGON TREATMENT DURATION

4.3.1 Treatment duration of 2 min

Initially the plasma treatment duration has been kept fixed at 2 min which can be considered as a short duration. The other plasma treatment parameters, such as power density and working pressure, have been kept fixed at 350 mW/cm^2 and 50 mTorr respectively. The effective measured bias voltage corresponds to $|V_{Bias}|$ =20 V, which gives rise to the mean ion energy of 8 eV and the maximum ion energy of 20 eV. The treatment has been performed on the surface of SiN$_x$:H single-layers deposited using the HW-CVD chamber. Then the sample is moved from the HW-CVD chamber to the PE-CVD chamber without breaking the vacuum. 4 different samples are developed on PET substrates at a substrate temperature of 100 °C by increasing the number of single-layers (m) and thus the total thickness of the barrier. The thickness of each single-layer has been fixed at the critical thickness (d_c)

of 50 nm and the developed samples are multiple of $m \times 50$ nm, where m varies from 2 to 5. The effect of plasma treatment is investigated by assessing their surface roughness by tapping mode AFM method and their barrier properties (lag-time and WVTR) by electrical calcium degradation tests.

4.3.1.1 Morphological effect

The three dimensional surface images of the multilayers are shown in Fig. 4.3 and summarized in Fig. 4.4. The high initial roughness of the samples corresponds to the very high initial roughness of the PET substrates when heat treated as discussed before. It should be reminded that the high initial roughness of PET is decreased drastically when it is coated by 50 nm SiN_x:H single-layer (see Chapter 3). The constant average surface roughness values of the multilayers shows that there is almost no significant effect of the plasma treatment on the surface of the SiN_x:H layers with such treatment conditions and short treatment time of 2 min.
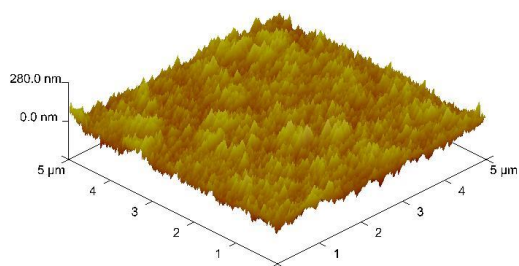
(a)
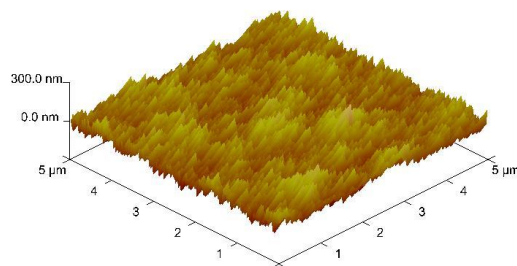
(b)
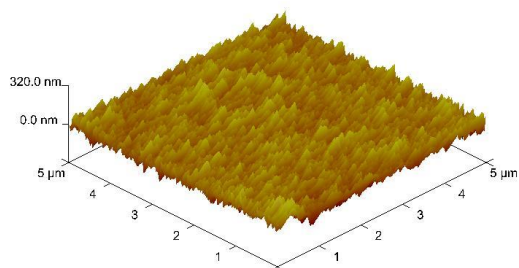
(c)
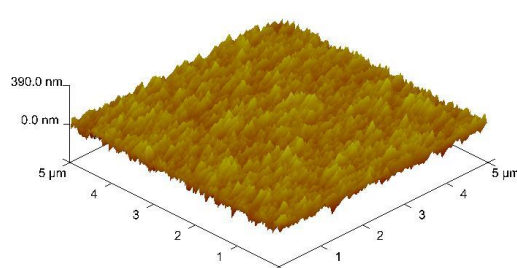
(d)

Fig. 4.3: Three dimensional AFM images of the surfaces of SiN_x:H multi-layers deposited on PET substrates with 2 min Ar plasma surface treatment time performed between each single-layer

deposition: (a) 50 nm + 50 nm, (b) 50 nm + 50 nm + 50 nm, (c) 50 nm + 50 nm + 50 nm + 50 nm, (d) 50 nm + 50 nm + 50 nm + 50 nm + 50 nm.
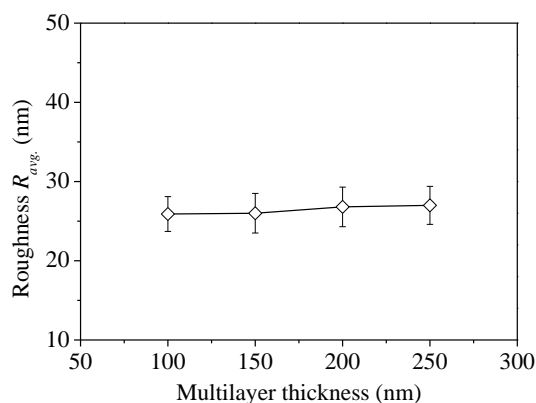
Fig. 4.4: Average surface roughness of SiN_x:H multi-layers deposited on PET substrates treated by Ar plasma during 2 min between each single-layer deposition.

4.3.1.2 Barrier effect

Fig. 4.5 (a) shows the evolutions of normalized conductance for the calcium sensors deposited on the barrier coated PET substrates. The number of layers (m) is increased from 2 to 5 and thus the total barrier thickness increases from 100 nm to 250 nm, where the thickness of each single-layer is fixed at 50 nm and the argon plasma treatment has been performed between each subsequent single-layer deposition with the above mentioned conditions. With the increase of the number of layers, the minimum time taken by the water molecules to penetrate through the whole thickness (barrier + substrate) increases, as seen from the lag-time variation with multilayer thickness in Fig. 4.5 (b). The lag-time variation for the multilayers without any argon treatment (discussed in previous chapter) is shown for comparison. It can be clearly observed that with the plasma treatment for a short duration, the lag-time increases and reaches a maximum value of 17 h for 5 stacked single-layers (total thickness =250 nm). The WVTR also varies with the number of layers as shown in Fig. 4.5 (c). There is a slight decrease of WVTR value (~11.4%) compared to the multilayers without any argon plasma treatment. The minimum WVTR value with such treatment conditions and using 5 stacked single-layers is 7×10^{-3} g/m^2.day. However, even though the plasma treatment reduces the effective WVTR slightly, the minimum WVTR value obtained with such conditions is not sufficient for the targeted value. In order to reduce the WVTR further, several other parameters should be varied. The argon plasma treatment duration will be increased in the next section using a minimum number of stacked single-layers (m =2, total thickness $\approx$ 100 nm).

(a)

(b)

(c)
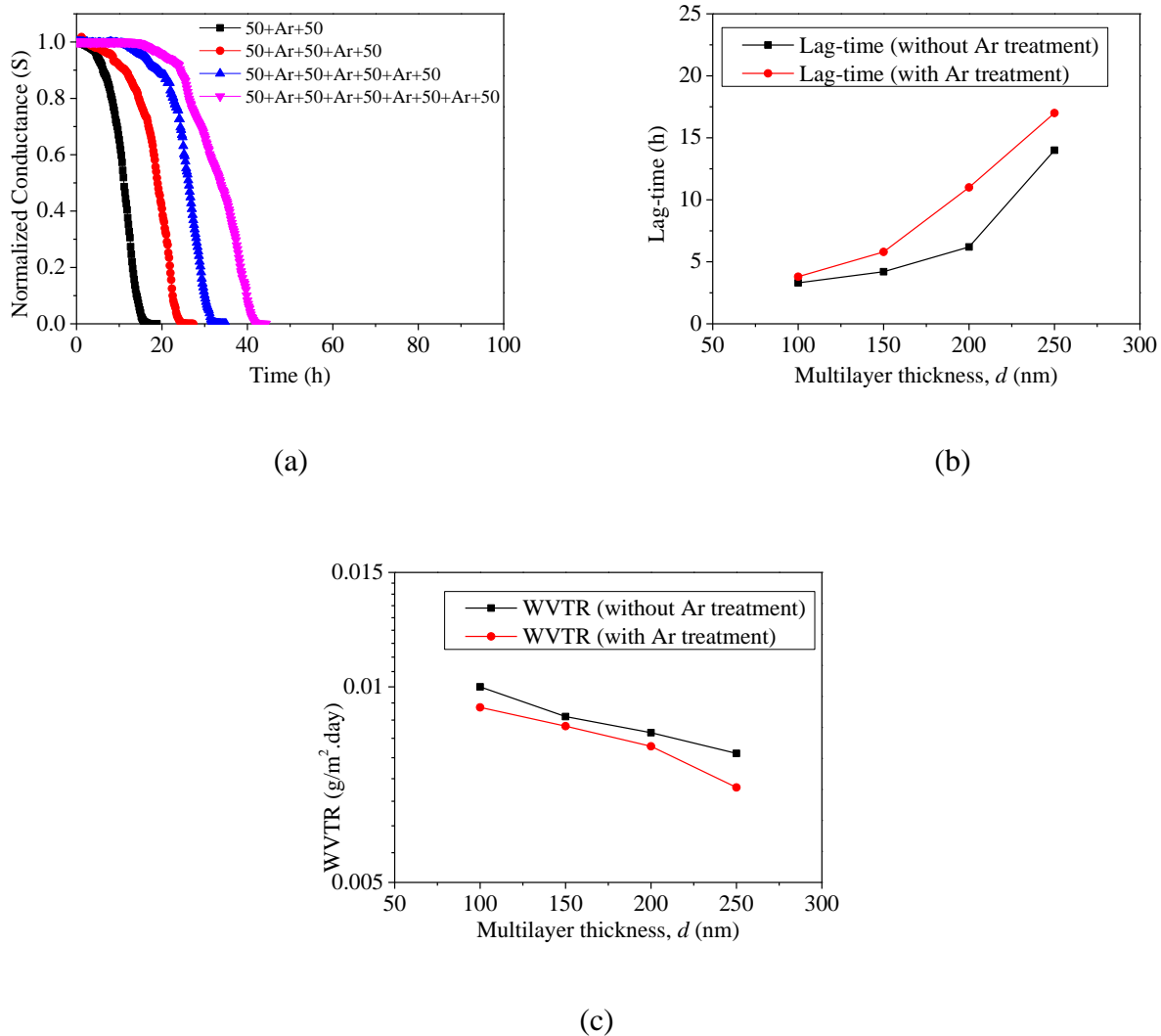
Fig. 4.5: (a) Normalised conductance of Ca sensors deposited on barrier coated PET substrates versus time for SiN$_x$:H multi-layers separated by 2 min Ar plasma surface treatment. (b) Evolution of the "lag-time" versus the SiN$_x$:H multi-layer thickness. (c) Evolution of WVTR values versus the SiN$_x$:H multi-layer thickness. The evolutions of lag-time and WVTR for the SiN$_x$:H multi-layers without any Ar plasma treatment are shown for comparison.

4.3.2 Variation of treatment duration for double-layer

The argon plasma treatment duration has been increased from 2 min until 15 min (2, 5, 8, 10 and 15 min) in order to investigate the impact on the overall barrier properties. The power density and working pressure have been kept fixed at 350 mW/cm^2 and 50 mTorr as mentioned above. The measurements have been carried out on double-layer structures in order to simplify both the deposition process for all the concerned samples and the subsequent interpretations. The total thickness of the double-layer structures being 100 nm (2 × 50 nm), the plasma treatment has been

carried out once after depositing the first single-layer. It should be noted that with the increase of the treatment duration, the ion fluence increases as well, as shown in Table 4.1.

Power density, P_w (mW/cm^2)	Pressure, p_g (mTorr)	V_{Bias} (V)	Maximum ion energy (eV)	Time, t (s)	Ion flux, F_i (cm^{-2}.s^{-1})	Ion fluence (cm^{-2})	Ion energy fluence (eV. cm^{-2})
350	50	-20	20	120	1.1×10^{17}	13×10^{18}	26×10^{19}
350	50	-20	20	300	1.1×10^{17}	33×10^{18}	66×10^{19}
350	50	-20	20	480	1.1×10^{17}	53×10^{18}	10×10^{20}
350	50	-20	20	600	1.1×10^{17}	66×10^{18}	13×10^{20}
350	50	-20	20	900	1.1×10^{17}	99×10^{18}	20×10^{20}

Table 4.1: Variations of ion fluences with the change in treatment times.

4.3.2.1 Morphological effect

Fig. 4.6 shows the three dimensional surface images and Fig. 4.7 shows evolution of the average roughness of the sample surface, obtained by atomic force microscopy, of the SiN$_x$:H double-layer without Ar plasma treatment and several double-layers separated by Ar-plasma surface treatment with increased plasma treatment time. It is clear from Fig. 4.7 that for the longer Ar treatment time, the roughness decreases (40 %) as compared to the shorter Ar treatment time of 2 min, corresponding to a smoothening of the surface. This particular effect is noticeably due to the impact of ion energy fluence. The maximum Ar ion energy (~ 20 eV) is around the threshold energy value for surface Si atomic displacement (15 to 25 eV) and therefore it is expected that at this energy the Ar ions can displace Si surface atoms.

Similar effect has been reported by Chason *et al*. [188, 189], where H ion induced smoothing effect of SiO$_2$ surface was shown. According to the authors, the surface smoothing depends considerably on the ion fluence for a fixed ion energy. The ion energy fluence (9×10^{19} eV.cm^{-2}) for a fixed 1000 eV H ion energy, required for similar reduction (40 %) of surface roughness, was around one order of magnitude lower compared to our present situation (19.8×10^{20} eV.cm^{-2}). This is due to the fact that, the transfer of kinetic energy (130 eV) from H ions to the Si atoms, according to equation 4.6, was considerably higher compared to the transfer of energy (19.2 eV) from Ar ions to the Si atoms in

our present case. This effect confirms that once the transfer of ion kinetic energy to the surface atoms becomes close to the maximum surface atom displacement threshold, the ion energy fluence required for surface smoothing becomes lower, which means lower treatment duration of plasma.
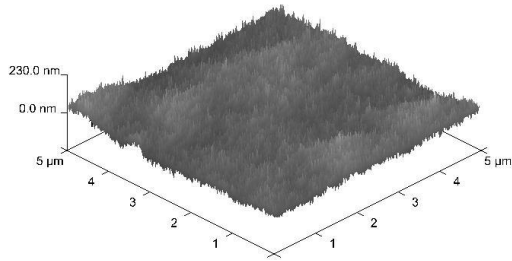
(a)
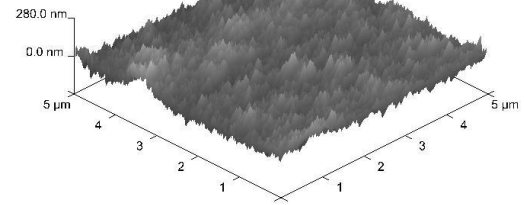
(b)
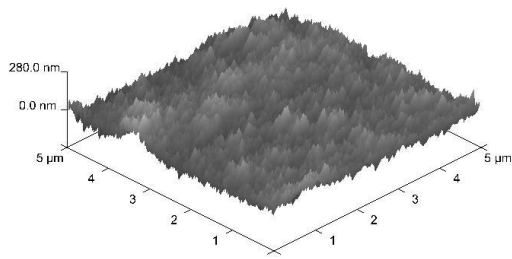
(c)
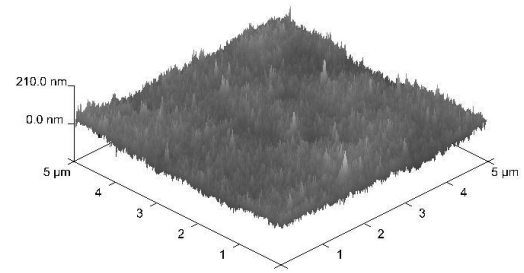
(d)
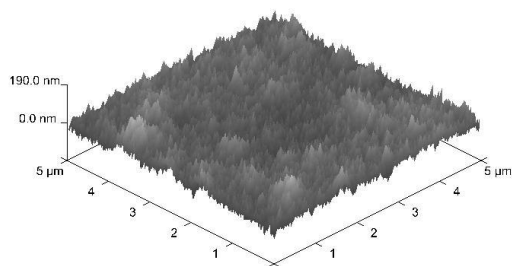
(e)
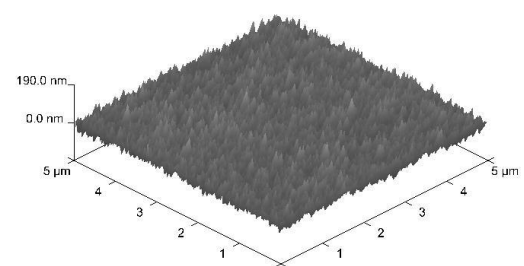
(f)

Fig. 4.6: Three dimensional AFM images of the surfaces of SiN$_x$:H double-layers deposited on PET substrates as a function of the Ar plasma surface treatment time performed between the two single-layer depositions: (a) Non treated, (b) 2 min Ar-treated, (c) 5 min Ar-treated, (d) 8 min Ar-treated, (e) 10 min Ar-treated and (f) 15 min Ar-treated.
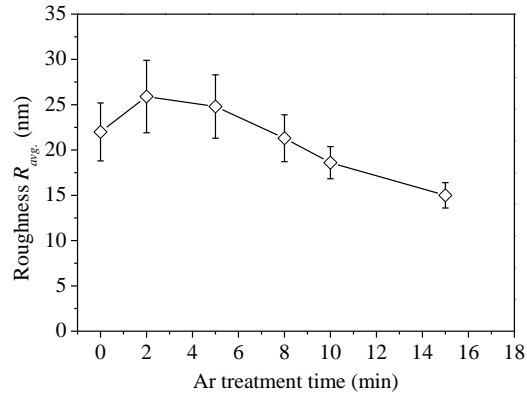
Fig. 4.7: Average surface roughness of SiN$_x$:H double-layers deposited on PET substrates as a function of the Ar plasma treatment time.

4.3.2.2 Barrier effect

Fig. 4.8 (a) shows the evolution of normalized conductance of Ca sensors, deposited on the double-layer barrier coated PET substrates with the variation of the plasma treatment duration. From the Fig. 4.8 (b) it can be seen that the lag-time of diffusion is increasing with the increase of plasma treatment time and is always higher than that of the double-layer without any plasma treatment. The evolution of the WVTR values for SiN$_x$:H double-layers (50 nm + 50 nm) with and without Ar plasma treatment is shown in Fig. 4.8 (c) as a function of the treatment time. With increasing treatment time in the range 2 to 8 min, the WVTR value strongly decreases down to $\sim 3 \times 10^{-3}$ g/m^2.day. For longer treatment times almost no variation on the WVTR value is observed. This is probably due to the fact that during the first minutes of treatment, the impinging Ar$^+$ ions are inducing atomic relocations on the surface of the SiN$_x$:H layer uniquely and 8 min can be sufficient time to get atomic rearrangements for the first few atomic layers at the surface of the film at this ion energy. Once the rearrangement of the single-layer for the first few atomic layers has been completed, the whole interface is stabilized and there is almost no effect on WVTR values for higher treatment times. From these first observations, it is expected that if the ion energy is increased much above the threshold energy for atomic displacements, the atomic displacements will be considerably severe using the same treatment duration.
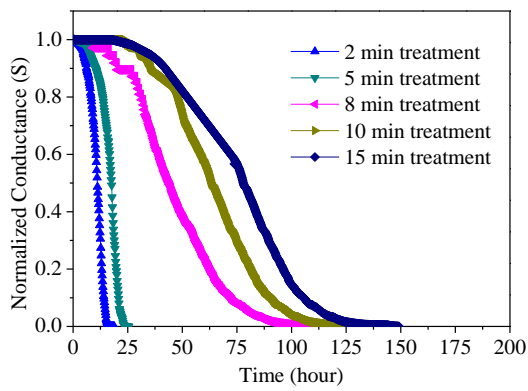
(a)
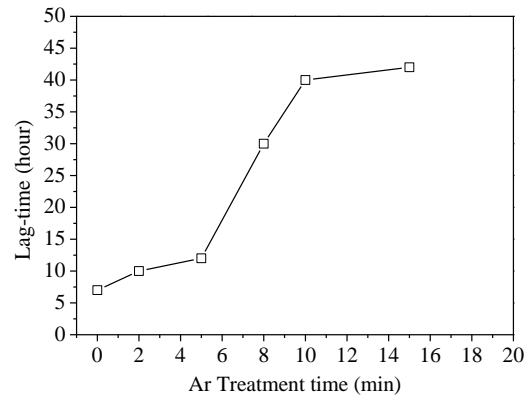
(b)
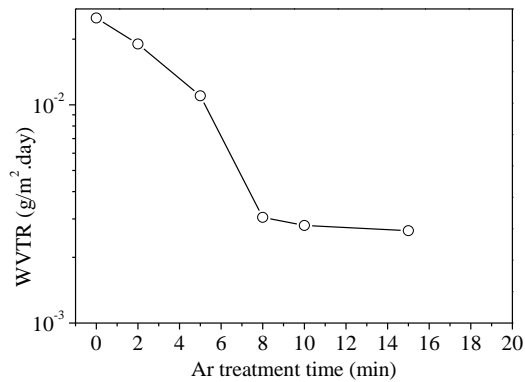
(c)

Fig. 4.8: (a) Normalised conductance of Ca sensors deposited on barrier coated PET substrates versus time for two 50 nm thick SiN_x:H single-layers separated by Ar plasma surface treatment for different plasma exposure times. (b) Evolution of the "lag-time" versus the Ar plasma treatment time of the SiN_x:H films as a function of the Ar plasma exposure time. (c) Evolution of WVTR values versus the Ar plasma treatment time of the SiN_x:H films as a function of the Ar plasma exposure time.

4.3.3 Effect of argon treatment on multilayers for 8 min duration

The best treatment time (8 min) obtained from the above discussions has been kept fixed to develop barrier layers with increasing number of stacked layers. The other parameters, such as power density and working pressure, remain fixed at 350 mW/cm^2 and 50 mTorr respectively. The number of layers (*m*) is varied from 2 to 5, in order to increase the total barrier thickness.

4.3.3.1 Morphological effect

Fig. 4.9 shows the three dimensional surface images of the multi-layer barriers versus the number of layers (*m*); the average roughness values are summarized in Fig. 4.10. It is clear that, the optimal treatment time has the effect of reducing overall surface roughness as compared to the treatment with 2 min, where no effect has been seen. From this initial indication of continuous reduction of surface roughness, it may be asserted that the three parameters which have been fixed during this experiment are well controlled, thus giving reproducible effects in which we should be confident. Therefore, it is expected that the final barrier properties of the multilayers will improve drastically compared to the short time treatment.

(a)   (b)

(c)   (d)
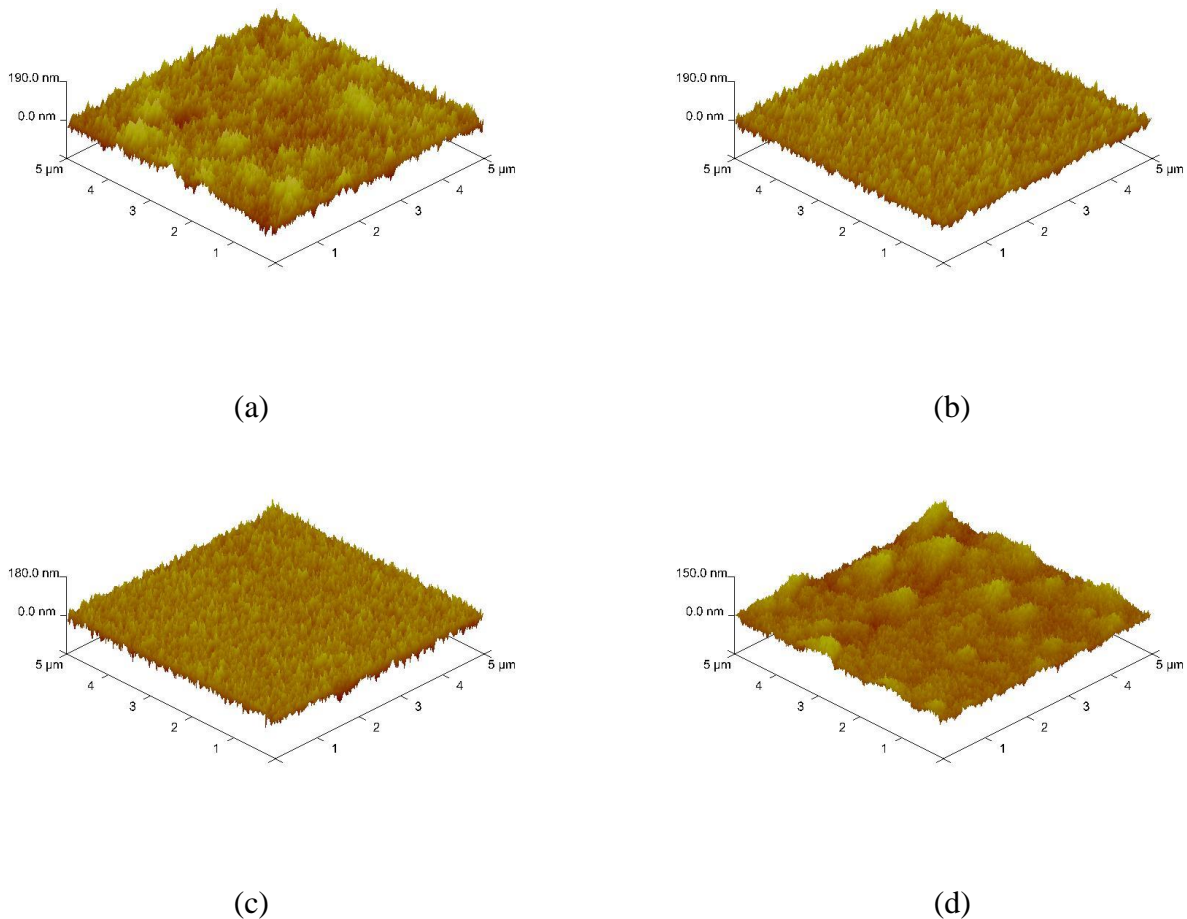
Fig. 4.9: Three dimensional AFM images of the surfaces of SiN_x:H multi-layers deposited on PET substrates with 8 min Ar plasma surface treatment time performed between each single-layer deposition: (a) 50 nm + 50 nm, (b) 50 nm + 50 nm + 50 nm, (c) 50 nm + 50 nm + 50 nm + 50 nm, (d) 50 nm + 50 nm + 50 nm + 50 nm + 50 nm.
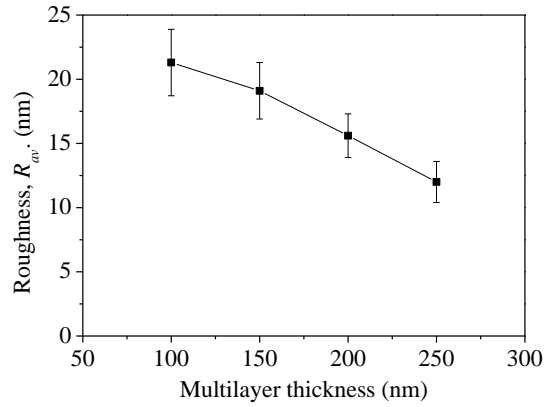
Fig. 4.10: Average surface roughness of SiN$_x$:H multi-layers deposited on PET substrates with 8 min Ar plasma surface treatment time performed between each single-layer deposition.

4.3.3.2 Optical effect

Figure 4.11 shows the optical data consisting of reflectance and the transmittance measurements of the multi-layer structure (stack of 5 SiN$_x$:H single-layers, each separated by 8 min of Ar$^+$ plasma treatment) deposited on PET substrates. The transmittance curve indicates that the multi-layer structure is highly transparent (~ 80%) in the visible region. It can also be seen from Fig. 4.11 that reflectance and transmittance of this multi-layer structure add to almost 100%, meaning that no absorption takes place in the layers and the barrier structure can be perfectly used as a window layer for organic electronic devices. Slight absorption below 450 nm wavelength is due to the plastic substrate itself.
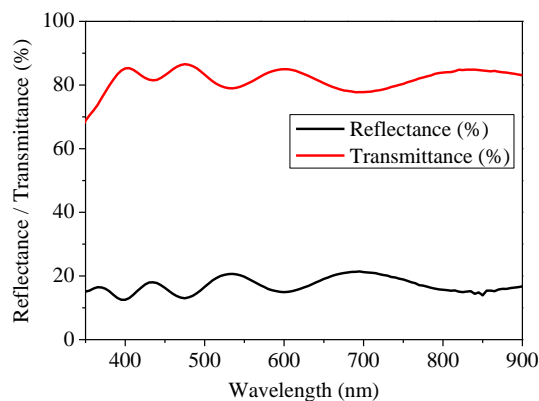
Fig. 4.11: Reflection and transmission spectra of SiN$_x$:H multilayer (stack of 5 SiN$_x$:H single-layers each separated by 8 min Ar-treatment) deposited on PET substrate.

4.3.3.3 Barrier effect

The evolutions of normalized conductance of the Ca sensors deposited on such multi-barrier coated PET substrates are shown in Fig. 4.12 (a). Slight kinks are observable in the traces, which are probably due to the inhomogeneous oxidation of the calcium surface. The reason of this inhomogeneous oxidation is the in-homogeneities inside the barrier layers and the PET substrate. When the number of SiN_x:H single layers increases, the number of interfaces between SiN_x:H films treated with argon plasma increases as well. The water molecules face a complex diffusion path when passing from one SiN_x:H single-layer to the other through the intermediate treated SiN_x:H interfaces. Due to that reason and to the increase in total thickness of the coating, the minimum time taken by the water molecules to reach the Ca sensor which is at the opposite side of the coated PET substrates (lag-time), increases with increasing number of stacked SiN_x:H single-layers (Fig. 4.12 (b)). A maximum lag-time of 77 hours is achieved with 5 stacked SiN_x:H single-layers, each layer being separated from the next one by the Ar^+-treatment. The WVTR values also decreases monotonically with increasing number of layers (see Fig. 4.12 (c)) reaching a minimum value of ~2 $\times 10^{-4}$ g/ m^2.day. This trend suggests that if the number of layers was further increased, then the barrier properties would be better. But the increased thickness would decrease the flexibility of the whole structure. Therefore, a trade-off should be found.
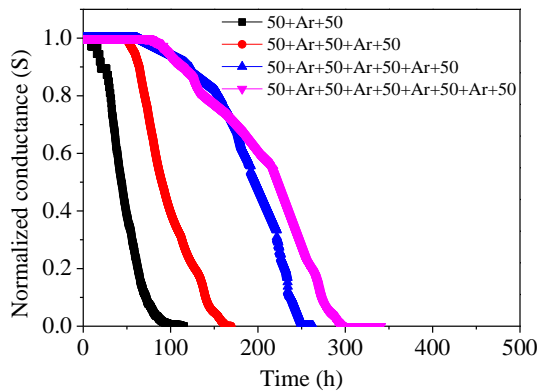
(a)
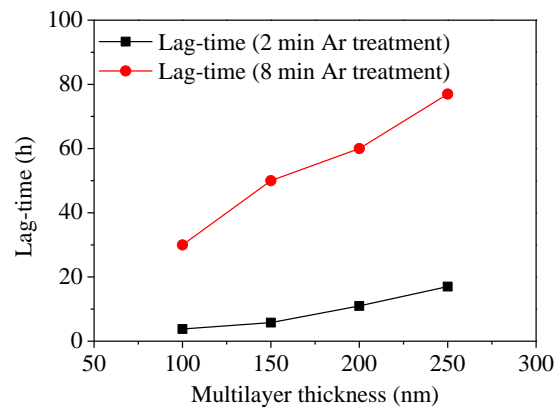
(b)
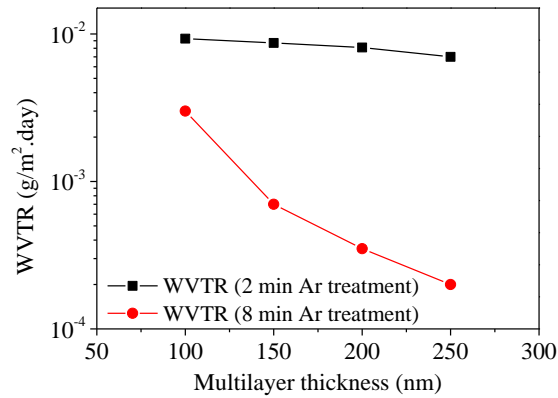
(c)

Fig. 4.12: (a) Normalised conductance of Ca sensors deposited on barrier coated PET substrates versus time for SiN$_x$:H multi-layers separated by 8 min Ar plasma surface treatment. (b) Evolution of the lag-time versus the SiN$_x$:H multi-layer thickness. (c) Evolution of WVTR values versus the SiN$_x$:H multi-layer thickness. The evolutions of lag-time and WVTR for the SiN$_x$:H multi-layers with 2 min Ar plasma treatment are shown for comparison.

4.4 IMPACT OF THE POWER DENSITY OF ARGON TREATMENT

The above measurements have been carried out using a fixed power density of 350 mW/cm^2. Power density has an important role to determine the kinetic energy of the impinging ions as well as the ion energy fluence [172]. In order to investigate the impact of power density on the overall barrier properties, the power density has been varied from a lower value of 85 mW/cm^2 to a higher value of 700 mW/cm^2. The treatment time is kept constant at the best treatment duration of 8 min and the working pressure remains same as above (50 mTorr). The investigations are performed using a double-layer structure (total thickness = 100 nm) in order to simplify both the deposition process for all the concerned samples and the subsequent interpretations.

Power density, P_w	Pressure, p_g	V_{Bias}	Maximum ion energy	Time, t	Ion flux, F_i	Ion fluence	Ion energy fluence
(mW/cm^2)	(mTorr)	(V)	(eV)	(s)	(cm^{-2}.s^{-1})	(cm^{-2})	(eV.cm^{-2})
85	50	-10	10	480	5.4×10^{16}	26×10^{18}	26×10^{19}
350	50	-20	20	480	1.1×10^{17}	53×10^{18}	11×10^{20}
400	50	-28	28	480	8×10^{16}	38×10^{18}	12×10^{20}
450	50	-38	38	480	7.6×10^{16}	36×10^{18}	14×10^{20}
700	50	-100	100	480	4.4×10^{16}	21×10^{18}	21×10^{20}

Table 4.2: Variations of maximum ion energy with the change of RF power density.

4.4.1 Morphological effect

Fig. 4.13 shows the variation of average surface roughness values for stack of two 50 nm thick SiN$_x$:H single-layers separated by Ar plasma surface treatment for different RF power densities. When the power density is low (85 mW/cm^2) which corresponds to the maximum Ar ion bombardment energy of 10 eV, there is no significant variation of roughness as compared to the double layer structure without any plasma treatment. This is due to the fact that the energy is quite low to rearrange the surface atoms and needs higher treatment time in order to attain sufficient ion energy fluence and smoothing effect. The change of surface roughness after this power density is significantly dominated by the energy of the impinging ions since the ion energy fluence is more or less similar for those power density values. With increasing power density values, the energy of ions increases as well and the effect on surfaces becomes more pronounced. The lowest average roughness (18 nm) is achieved for 400 mW/cm^2, which corresponds to the maximum ion energy of 28 eV. It should be noted here that this energy (28 eV) is just above the maximum surface atomic displacement threshold (25 eV for Si) and below the bulk atomic displacement threshold (40 eV for Si) and therefore, it is expected that at this energy there is sufficient surface atom rearrangement for few atomic layers which results in surface roughness reduction. The roughness values increases after that and reaches a maximum value of 22.8 nm for 700 mW/cm^2 which corresponds to the maximum energy of 100 eV, an energy higher enough for Si atomic sputtering threshold (50 eV) and induces damage of the surface.
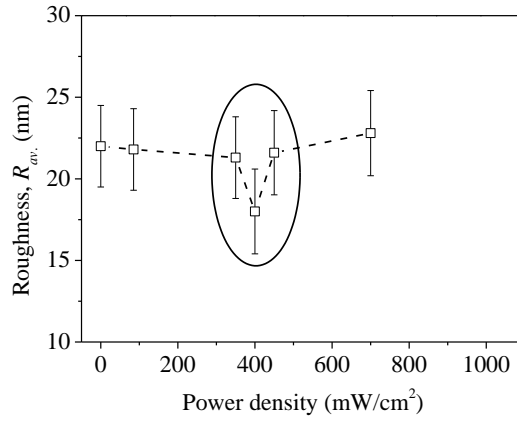
Fig. 4.13: Variation average surface roughness for two 50 nm thick SiN$_x$:H single-layers separated by Ar plasma surface treatment for different RF power densities.

4.4.2 Barrier effect

The evolutions of the normalized conductance of the calcium sensors are shown in Fig. 4.14 (a) and (b). The variations of lag-time and WVTR with increase of power-density are shown in Fig. 4.14 (c) and (d) respectively. Three separate regions are observed for the barrier properties and vary in a similar way of the variation of average surface roughness values (Fig. 4.13). In the first region, the power density is increased up to 85 mW/cm^2, which corresponds to maximum ion energy of ~10 eV impinging on the sample surface (see Table 4.2). Within the uncertainty of conductance decrease with time, no effect on the barrier properties can be observed. This is probably due to the fact that, the maximum ion energy is below the minimum surface atom displacement threshold for Si (~15 eV). When the power density is increased (350 mW/cm^2), the maximum ion energy also increases (see Table 4.2). For a fixed working pressure, when the maximum energy is around ~20 eV, there is a drastic change in the barrier properties. The lag-time is increased up to 30 h and the WVTR is decreased down to 3 × 10^{-3} g/m^2.day. This is probably due to the fact that, the ion kinetic energy approaches the maximum surface atom displacement threshold energy for Si (~25 eV). If the power density is increased again up to 400 mW/cm^2, then the maximum ion kinetic energy (28 eV) is above the maximum surface atom displacement threshold energy. The barrier properties are further improved. The lag-time is increased up to 35 h and the WVTR is decreased down to 9.2 × 10^{-4} g/m^2.day. An interesting feature occurs when the power density is increased again up to 450 mW/cm^2. Clearly the normalized conductance curve shows a net degradation compared to the conductance curve obtained for 400 mW/cm^2. The lag-time reduces and the WVTR increases. This is probably because of the fact that, the maximum ion energy (38 eV) is close to the maximum bulk displacement threshold energy for Si (~40 eV) and possibly some damage or sputtering of the film

begins to occur with very low sputtering yield. Thus, it can be concluded that with the increase of maximum ion kinetic energy to such a value (38 eV), the surface atoms and few atomic layers of the bulk have been rearranged and some other surface atoms have been sputtered away, damaging somewhat the uniquely treated interface. In other words, it seems that the optimum ion energy giving the minimum WVTR value has been overcome. Finally, when the power density is increased drastically up to 700 mW/cm^2, the maximum ion energy corresponds to ~100 eV. The barrier properties degrade considerably at this ionic treatment. The lag-time decreases sharply (3 h) and the WVTR increases above the value obtained for double-layer without any Ar treatment or with 85 mW/cm^2 treatment. This effect confirms that Ar ions with an energy of 100 eV (and perhaps below) degrade totally the uniquely treated interface between the two SiN$_x$:H single-layers.

(a)

(b)

(c)

(d)
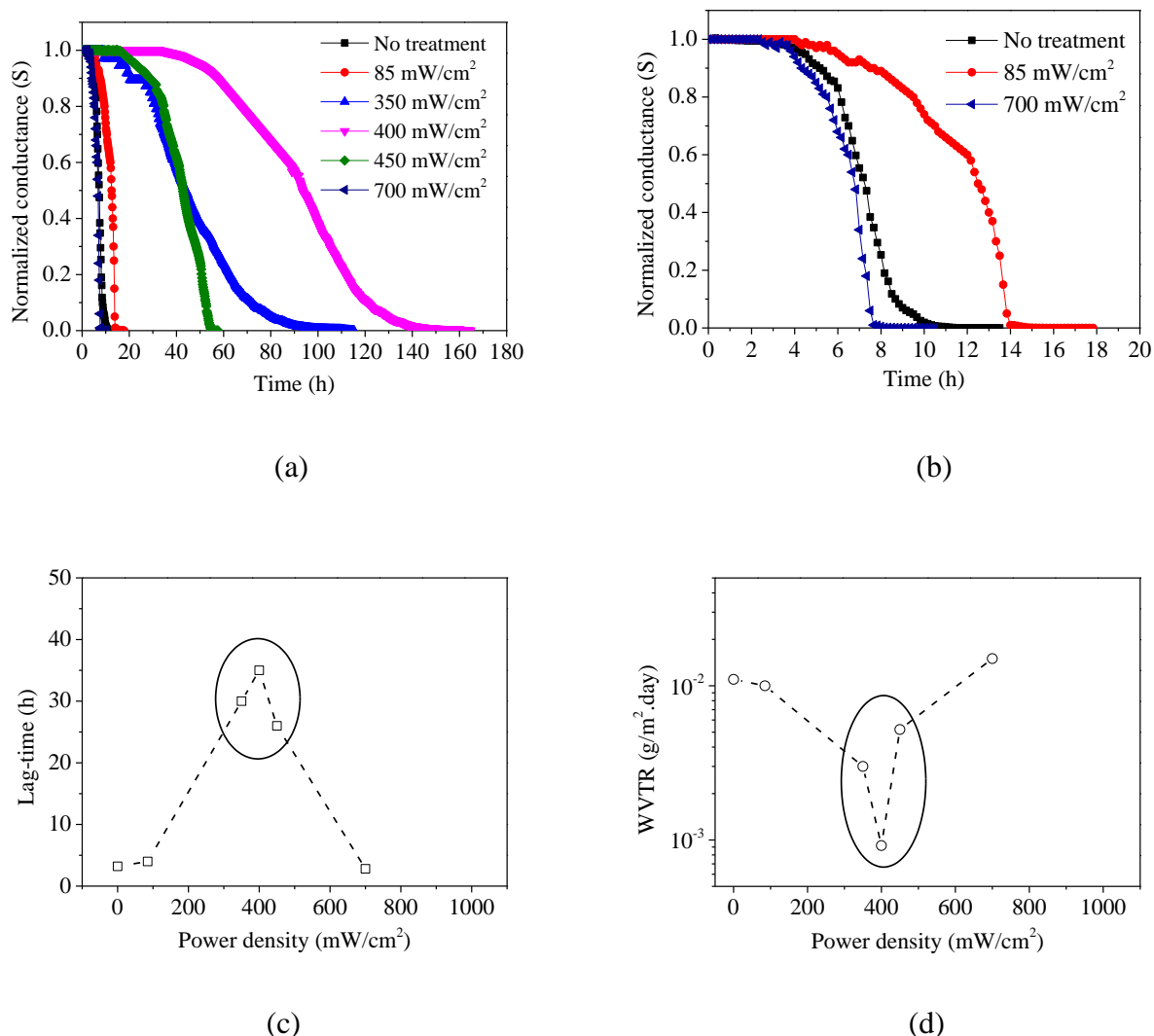
Fig. 4.14: (a) Normalized conductance of Ca sensors deposited on barrier coated PET substrates versus time for two 50 nm thick SiN$_x$:H single-layers separated by Ar plasma surface treatment for different RF power densities. (b) Zoom of the first region of conductances. (c) Evolution of the "lag-

time" versus the Ar plasma power density of the SiN$_x$:H films. (d) Evolution of WVTR values versus the Ar plasma power density of the SiN$_x$:H films.

4.5 EFFECT OF WORKING PRESSURE OF ARGON TREATMENT

The working pressure plays an important role in determining the maximum ion energy impinging on the film surface. The mean free path of the ions varies inversely with the working pressure. If the mean free path of the ions is larger than the width of the sheath of charge that forms close to the electrode, then the ions can gain the maximum energy corresponding to the bias voltage [174, 176, 177]. If conversely the ion mean free path is smaller than the space charge sheath, then the ions have a probability to collide with each other inside the sheath and the mean ion energy impinging on the cathode surface is a fraction of the bias voltage, with a broad ion energy distribution having as maximum energy the bias voltage multiplied by the ion charge. Therefore, a low pressure in the range of mTorrs is desirable in order to maximize the number of ions with the maximum energy colliding with the sample surface. However, it should not be drastically low as in this case the total number of ions in the chamber would be too low.

In order to investigate the effect of working pressure on the overall barrier properties, the pressure is varied between 25 to 75 mTorr. The power density (350 mW/cm^2) and the best treatment duration (8 min) remain fixed for this treatment. The measurements are performed using a double-layer structure (total thickness = 100 nm) in order to simplify the effort. Table 4.3 shows the variation of the maximum ion energy with the change of working pressures.

Power density, P_w	Pressure, p_g	V_{Bias}	Maximum ion energy	Time, t	Ion flux, F_i	Ion fluence	Ion energy fluence
(mW/cm^2)	(mTorr)	(V)	(eV)	(s)	(cm^{-2}.s^{-1})	(cm^{-2})	(eV.cm^{-2})
350	25	-22	22	480	1×10^{17}	48×10^{18}	11×10^{20}
350	50	-20	20	480	1.1×10^{17}	53×10^{18}	11×10^{20}
350	75	-18	18	480	1.2×10^{17}	58×10^{18}	10×10^{20}

Table 4.3: Variations of maximum ion energy with the change of working pressure.

4.5.1 Morphological effect

Fig. 4.15 shows the variation of average surface roughness values for stack of two 50 nm thick SiN$_x$:H single-layers separated by Ar plasma surface treatment for different working pressures. From the variation it is observed that there is no significant change of surface roughness with the variation of working pressures. This is due to the fact that the maximum Ar ion energies impinging on the sample surface varying slightly and they are around the Si surface atomic displacement threshold energy (15 to 25 eV). Also the ion energy fluence values are more or less similar and therefore the effect would be more pronounced with longer treatment duration. However, slight reduction of roughness (19.7 nm) is achieved for 25 mTorr, because the maximum energy value (22 eV) being close to the maximum surface atomic displacement threshold, has higher probability to rearrange the surface atoms compared to the other working pressures. Therefore, it can be concluded that in order to attain sufficient effect by the variation of working pressure, we need either longer treatment time (> 8 min) to achieve higher ion energy fluence or higher power density (400 mW/cm^2) to achieve higher energy value which is close to the surface and bulk atomic displacement thresholds as observed in Fig. 4.14.
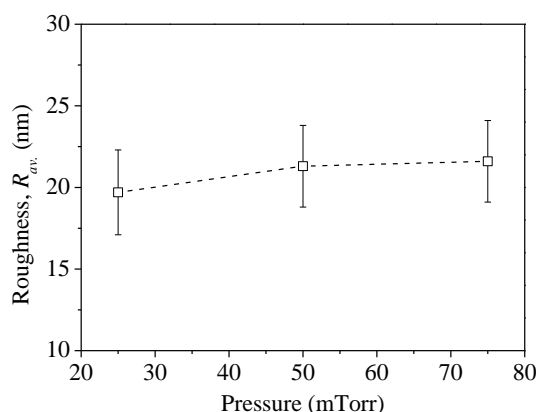
Fig. 4.15: Variation of average surface roughness for two 50 nm thick SiN$_x$:H single-layers separated by Ar plasma surface treatment for different working pressures.

4.5.2 Barrier effect

The evolutions of the normalized conductance of the calcium sensors are shown in Fig. 4.16 (a). The variations of lag-time and WVTR with increase of pressure are shown in Fig. 4.16 (b) and (c) respectively. A slight variation of both the lag-time and the WVTR is observed when the pressure is increased. The lag-time is decreasing slightly when the pressure is increased from 25 to 75 mTorr. The WVTR increases from 1×10^{-3} g/m^2.day (for 25 mTorr) to 4×10^{-3} g/m^2.day (for 75 mTorr). The

maximum ion energy varies between 18 to 22 eV, which is around the energy threshold for the Si surface atom displacement. The improvement of barrier properties at comparatively lower working pressure (25 mTorr) is probably due to the fact that when the pressure is lower than 50 mTorr, the ions have fewer collisions, but the number of ions impinging on the films surface can gain a higher maximum energy (22 eV). Thus, the effect on the surface is more pronounced and the barrier properties improve.

On the contrary, when pressure is higher than 50 mTorr, the maximum energy gained by the Ar ions is lower (18 eV). Therefore, the effect on the SiN$_x$:H surface is less pronounced as Si atomic displacement is more difficult to reach in these conditions. The barrier properties are slightly degraded compared with the 50 mTorr treatment.

(a)   (b)

(c)
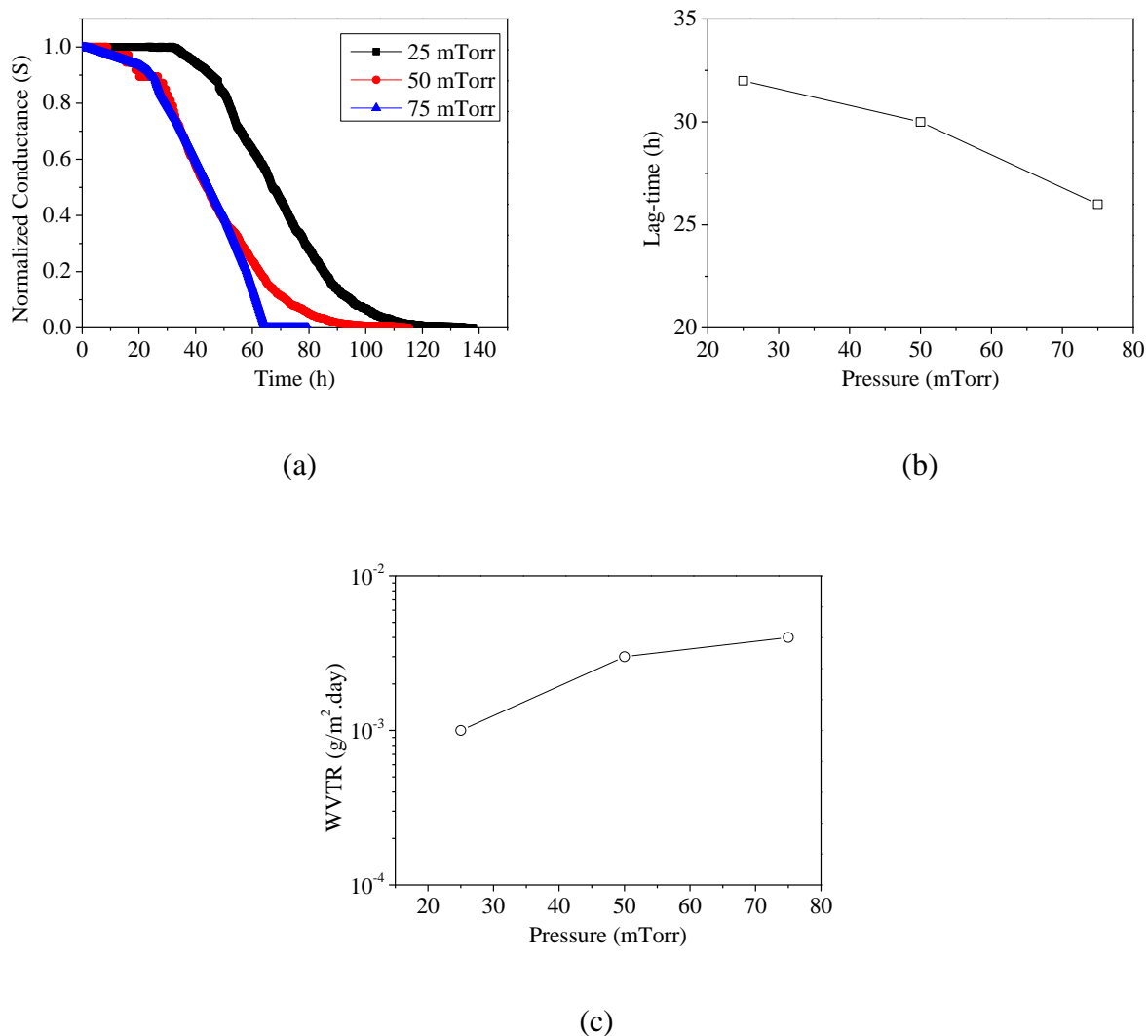
Fig. 4.16: (a) Normalized conductance of Ca sensors deposited on barrier coated PET substrates versus time for two 50 nm thick SiN$_x$:H single-layers separated by Ar plasma surface treatment for different working pressures. (b) Evolution of the "lag-time" versus the working pressure. (c)

Evolution of WVTR values versus the working pressure.

4.6 EFFECT OF BEST TREATMENT PARAMETERS ON THE MULTILAYERS

The above mentioned optimizations for the Ar treatment on SiN_x:H single-layers are considered to develop multilayers of SiN_x:H films in order to investigate their combined effect on the overall barrier properties. However, it should be noted that the above optimizations have been carried out independently and the combined effect of power density and pressure is controlling the bias voltage and thus the maximum ion energy. Therefore, when all the above mentioned optimized parameters are merged, we can consider that we are capable to control maximum ion energy compared to the Si atomic displacement threshold. So we are able to improve the barrier properties, even though we are convinced that the complete optimization of the four Ar treatment parameters should need further studies. The optimized parameters used in this study are: 400 mW/cm^2 power density, 25 mTorr working pressure and 8 min of treatment duration. We measured that these parameters give rise to an effective bias voltage of -30 V and thus the maximum ion energy impinging on the film surface is ~30 eV. The multilayers composed of 2 to 5 SiN_x:H single-layer films are analyzed in order to see the effect on morphological, optical and barrier properties.

4.6.1 Morphological effect

The surface topography of the multilayer SiN_x:H films treated with the above mentioned optimized parameters has been characterized using tapping mode AFM technique. Fig. 4.17 shows the surface topography and Fig. 4.18 shows the average surface roughness variation with increase of the number of layers. It is clear from the analysis that with the optimized Ar treatment parameters, the roughness decreases quite drastically. Compared to previous roughness results for double-layer structures we can notice that the roughness value (16 nm) obtained for 400 mW/cm^2, 25 mTorr and 8 min is smaller than that obtained (21.3 nm) for 350 mW/cm^2, 50 mTorr and 8 min (see Fig. 4.7). This example confirms the positive effect due to the optimization of power density and pressure together and confirms as well that evolution of roughness versus multilayer thickness is a good indication of the possible evolution of barrier properties versus multilayer thickness.
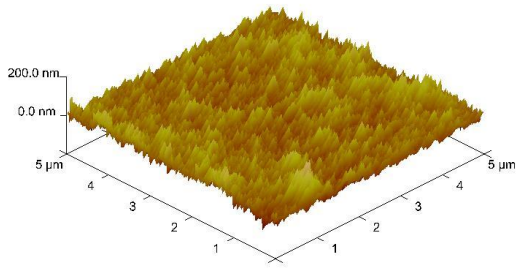
(a)
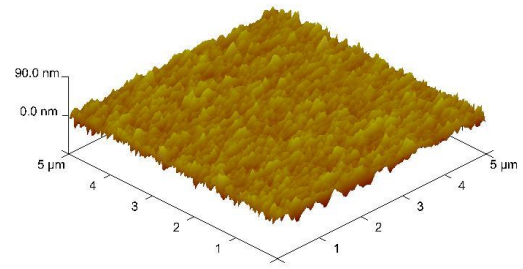
(b)
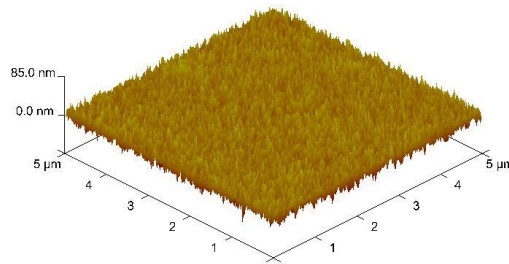
(c)

Fig. 4.17: Three dimensional AFM images of the surfaces of SiN$_x$:H multi-layers deposited on PET substrates with optimized Ar plasma surface treatment performed between each single-layer deposition: (a) 50 nm + 50 nm, (b) 50 nm + 50 nm + 50 nm + 50 nm, (d) 50 nm + 50 nm + 50 nm + 50 nm + 50 nm.
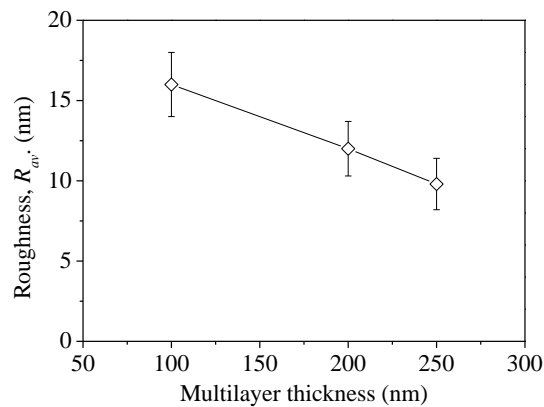
Fig. 4.18: Average surface roughness of SiN$_x$:H multi-layers deposited on PET substrates with optimized Ar plasma surface treatment performed between each single-layer deposition.

91

4.6.2 Optical effect

Figure 4.19 shows the optical data consisting of reflectance and the transmittance measurements of the multi-layer structure (stack of 5 SiN_x single-layers, each separated by Ar^+ plasma treatment) deposited on PET substrates. The transmittance curve indicates that the multi-layer structure is highly transparent (~ 80%) in the visible region. It can also be seen from Fig. 4.19 that reflectance and transmittance of this multi-layer structure add to almost 100% in the visible range.
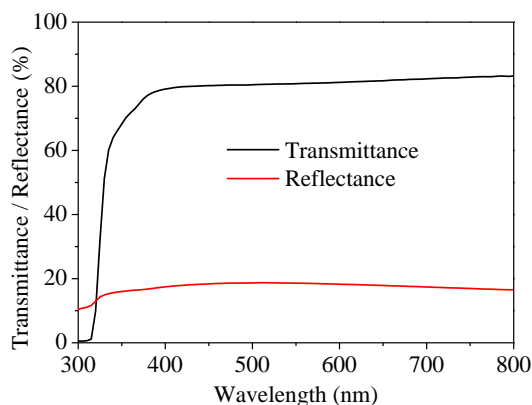
Fig. 4.19: Reflection and transmission spectra of SiN_x:H multilayer (stack of 5 SiN_x:H single-layers each separated by optimized Ar-treatment deposited on PET substrate).

4.6.3 Barrier effect

The normalized conductances of the Ca sensors deposited on such multi-layer barrier coated PET substrates are shown in Fig. 4.20 (a). Kinks are also observed in the traces for higher thickness barriers. These are due to slight in-homogeneities inside the barriers and PET substrates as discussed before. The lag-time and WVTR values are evaluated from the evolutions and are shown in Fig. 4.20 (b) and (c) respectively. When the number (m) of single-layers treated with the optimized Ar treatment conditions is increased from 2 to 5, the permeation path becomes considerably tortuous due to the treated interfaces and increase of total film thickness. Thus the minimum time taken by the water molecules to reach the Ca sensor surface increases and leads to an increased lag-time of permeation up to 125 h for 5 stacked SiN_x:H single-layers. Due to the same reason, the permeation rate (WVTR) decreases monotonically when the number of SiN_x:H single-layer increases. A minimum WVTR of 7×10^{-5} g/m^2.day is obtained for 5 stacked SiN_x:H single-layers. This result confirms the drastic effect of power density and pressure on the permeation barriers and roughness values.
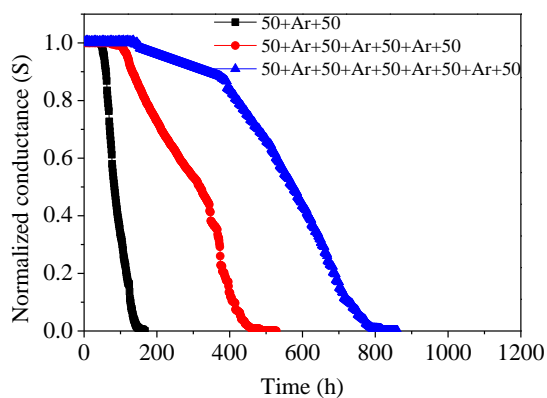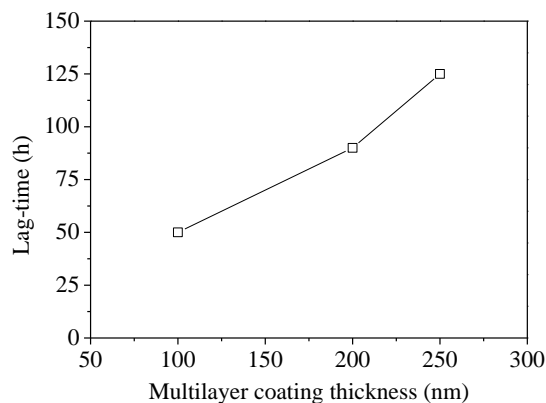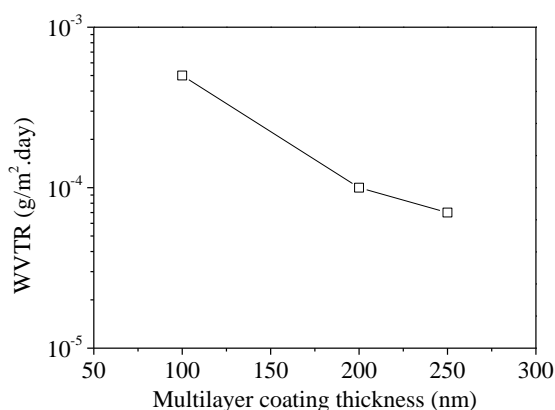
Fig. 4.20: (a) Evolution of normalized conductance of Ca sensor deposited on PET coated with multi-layers of SiN$_x$:H films treated by argon plasma. (b) Variation of "lag-time" with SiN$_x$:H multi-layer coating thickness (Ar treated). (c) Variation of WVTR values with SiN$_x$:H multi-layer coating thickness (Ar treated).

4.7 MECHANICAL PROPERTIES

Mechanical flexibility is an important property for the barrier layers for the utilization in flexible organic optoelectronic devices. In addition to their requisite barrier properties, the encapsulation layers should maintain their barrier performances during and after mechanical deformations. The inorganic materials used as a permeation barrier are brittle in nature and due to the mechanical deformation strain; stress is induced inside the films which develop cracks inside the inorganic films. Cracking of the inorganic films make the whole barrier ineffective. According to Yanaka *et al*. [190], onset strain for crack formation for thin oxide films is 1.3%, while Leterrier *et al*. [191] measured a

93

range of strains from 1.2% to 2.0% before the fracture. Suo *et al.* [192] have given a useful analysis of the thin film mechanics. Whenever, a brittle inorganic film is deposited on a flexible under layer (substrate) and the whole structure is bent with decreasing radius of curvature (*r*), the neutral axis, where no compressive or tensile strain exists, shifts towards the film, reducing stress inside the film. The strain inside the top film is given by

$$\varepsilon_{top} = \left(\frac{d_f+d_s}{2r}\right)\frac{(1+2\eta+\chi\eta^2)}{(1+\eta)(1+\chi\eta)} \qquad (4.7)$$

Where $\eta = (d_f / d_s)$ and $\chi = (Y_f / Y_s)$. d_f, d_s, Y_f and Y_s belong to the film thickness, substrate thickness, Young's modulus of film and Young's modulus of substrate respectively. Using moduli values of 5.53 [193] and 297 GPa for the PET substrate and the SiN$_x$:H film, respectively, and 175 μm and 100 nm (two 50 nm double layer) for the substrate and film thickness, respectively, the variation of strain with the radius of curvature is shown in Fig. 4.21. It is clear that the onset strain for crack formation (~ 1.3%) is around 5 to 7 mm of radius of curvature.

The mechanical flexibility of the barrier structure has been investigated by bending permeation barriers correspond to a double-layer (100 nm) [deposited using HW-CVD method and Ar treatment in the conditions: $P_w = 350$ mW/cm^2, $p_g = 50$ mTorr and $t = 8$ min (see sub-section 4.3.3)] structure with a radius of curvature of 5 mm for different cycles of bending. Ca degradation tests are performed on such bent samples in order to assess the impact of bending on the permeation barrier properties. It is obvious that at this curvature, some cracks are formed inside the films that should damage the permeation barriers. However, this is an indirect result as the defect density inside the films is not measured during this study.

Fig. 4.22 (a) shows the Ca degradation test results relative to different samples: one has not been bent. So the black curve describes its normalized conductance evolution. The other two samples have been bent for 100 (red curve) and 500 (blue curve) cycles respectively. The effect of bending on the lag-time is shown in Fig. 4.22 (b) which shows a sharp decrease in lag-time during the first 100 times of bending and whose magnitude of degradation continues after 100 cycles. The WVTR of the samples also increases sharply during the first 100 times of bending and whose magnitude of degradation continues after 100 cycles. The observations show that even-though the barrier properties of the inorganic films can be drastically improved using argon plasma treatment, the mechanical flexibility of the barriers is limited. After several cycles of bending, the barrier properties become progressively worse.
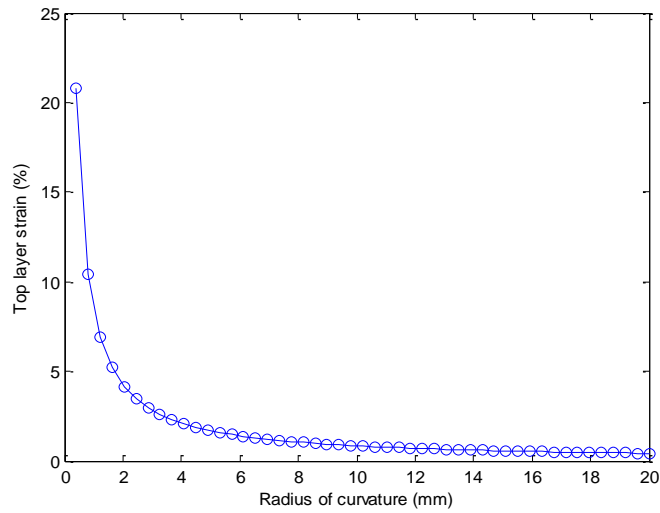
Fig. 4.21: The strain induced in the double barrier layer with the variation of radius of curvature (*r*).
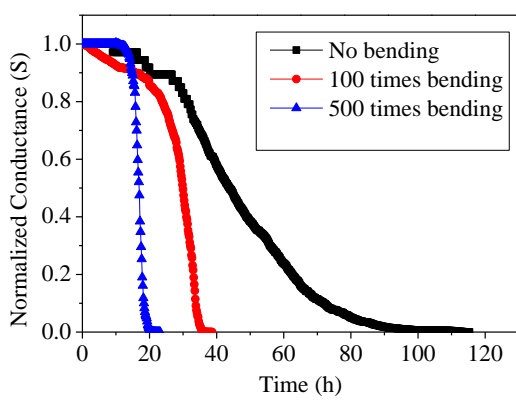
(a)
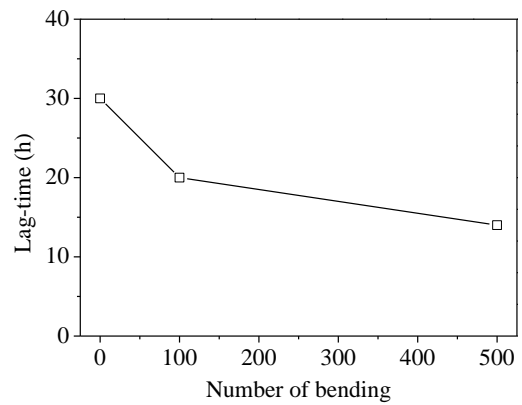
(b)
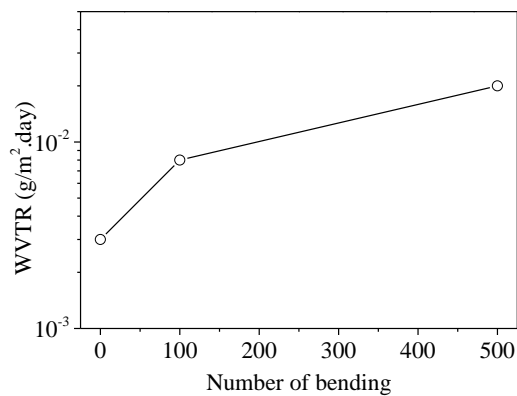
(c)

Fig. 4.22: (a) Normalized conductance of Ca sensors deposited on barrier coated PET substrates versus time for two 50 nm thick SiN$_x$:H single-layers separated by Ar plasma surface treatment for

different number of bendings (0, 100, 500). (b) Evolution of the "lag-time" versus the number of bendings. (c) Evolution of WVTR values versus the number of bendings.

4.8 INTERPRETATION

The Ar plasma treatment with the above mentioned optimized parameters improves the permeation barrier properties of SiN$_x$:H films drastically. In order to interpret the above observations, it has been necessary to analyze deeply the effect of plasma treatment on the SiN$_x$:H films. Several characterizations have been performed on two types of samples grown on c-Si wafers: as deposited SiN$_x$:H single-layer film (50 nm) and SiN$_x$:H single-layer film (50 nm) with plasma treated on the top surface. Two different plasma treatments have been carried out: plasma treated with optimized treatment parameters (400 mW/cm^2, 25 mTorr and 8 min) and plasma treated with 700 mW/cm^2, 50 mTorr and 8 min. For simplicity the samples are named as following (Table 4.4):

Sample	Films on c-Si wafer	Plasma treatment conditions
A	SiN$_x$:H single-layer film (50 nm)	No treatment
B	SiN$_x$:H single-layer film (50 nm)	400 mW/cm^2, 25 mTorr and 8 min (E_{max} = 30 eV)
C	SiN$_x$:H single-layer film (50 nm)	700 mW/cm^2, 50 mTorr and 8 min (E_{max} = 100 eV)

Table 4.4: Samples used for different characterizations.

Those three kinds of samples have been analyzed to observe the plasma treatment effect on the morphological, compositional and structural properties. The morphological analysis has been carried out by tapping mode AFM, the compositional analysis have been performed by FTIR, XPS and GDOES techniques and the morphological as well as structural characterization has been carried out by XRR method.

4.8.1 Morphological analysis and interpretation

The AFM measurements are performed on as-grown and plasma-treated SiN$_x$:H (50 nm) thin films deposited on crystalline silicon wafers, shown in Fig. 4.23, in order to verify the modification of the surface done by plasma treatment in different conditions. The as deposited SiN$_x$:H films (sample A) observed in Fig. 4.23 (a) exhibits a comparatively rough surface with 2.1 nanometer scale peaks on the surface. It should be noted that 2.1 nm peak on c-Si wafer based SiN$_x$:H is quite low value compared to 23 nm peak observed on PET substrate based SiN$_x$:H film (see Chapter 3). After

plasma treatment with the optimized treatment conditions (sample B) as shown in Fig. 4.23 (b)), the film shows a flat surface: root mean squared (rms) roughness = 0.7 nm, corresponding to a reduction of 67% compared to 2.1 nm. From this first result it is clear that ion treatment with 30 eV leads to a surface modification which corresponds to a smoothing [194]. On the contrary, after plasma treatment with 700 mW/cm^2, 50 mTorr and 8 min (sample C), the film becomes more rough (rms roughness = 2.7 nm).

The explanation for the decrease of surface roughness of SiN$_x$:H film under the exposition to the optimized plasma treatment with 400 mW/cm^2, 25 mTorr and 8 min (sample B) is related to the minimization of surface energy during the impact of the incident Ar ion flux on the first few atomic layers of the film. When the plasma is sustained, Ar ions issued from the quasi-neutral region and crossing the interface quasi-neutral region/cathode sheath can gain sufficient energy, depending on the working pressure, to kick on the surface atoms of the film. The total energy brought every second to this surface involves the ion flux directed towards the surface and the mean energy of these ions. Moreover, the maximum energy in the ion energy distribution, issued from the electron energy distribution function, is competing with the surface or bulk atomic displacement threshold in the solid. When maximum ion energy reaches or exceeds the surface displacement threshold (15 to 25 eV for Si), there is a statistical rearrangement of the surface atoms minimizing the effective surface area and thus the surface energy of the system under consideration. Minimization of the effective surface area is equivalent to the decrease of the surface roughness [195].

For the 400 mW/cm^2 power density used for the plasma treatment observed in Fig. 4.23 (b) the maximum ion energy has been assessed as 30 eV (see subsection 4.6), an energy higher than the energy needed for displacing Si atoms in the film surface (> 20 eV). This surface rearrangement (displacement of Si atoms relative to N atoms) can be the efficient way for inhibiting the diffusion of water molecules from one SiN$_x$:H layer to the next one, thus improving drastically the permeation barrier, what has been observed in Fig. 4.20 for five stacked SiN$_x$:H layers treated with such Ar plasma conditions.

For the 700 mW/cm^2 power density used for the plasma treatment observed in Fig. 4.23 (c), the maximum ion energy has been assessed as 100 eV (see Table 4.6). In that case this energy is much higher than the surface and bulk atomic displacement thresholds (15 to 40 eV) and higher than the sputtering threshold (~ 40 eV for Si). It is also slightly higher than the implantation energy of Ar in the solids (> 60 eV). The ion flux with such an energy is producing damage to the SiN$_x$:H surface.

This is the reason of the large structural degradation of the top layers giving rise to induced roughening, what has been observed in Fig. 4.23 (c). This large degradation effect has been also observed for the permeation barrier of the sample consisting of double-layer treated with this Ar plasma conditions (see Fig. 4.14).

It is known that for relatively low ion velocities, the main energy loss mechanism is through nuclear collisions which results in zig-zag path inside the solid (cascade collisions). For high energy ions (> 50 keV), the energy loss is through electronic collisions which result in straight forward path (projected range used in ion implantation).

(a)

(b)

(c)
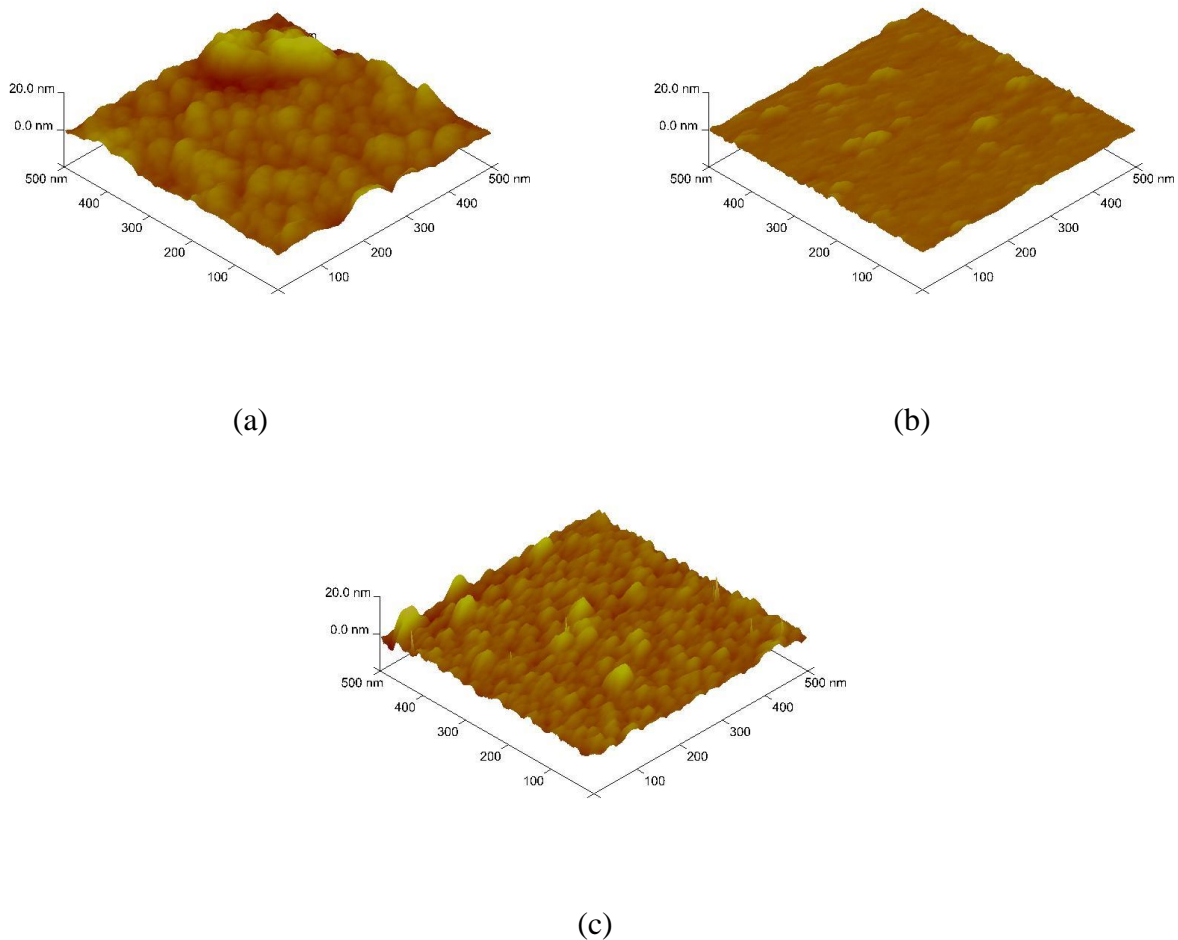
Fig. 4.23: Three-dimensional AFM images of the surface (500×500 nm^2) of SiN$_x$:H layer deposited on c-Si wafers (a) as deposited, (b) Ar$^+$-plasma treated with 30 eV and (c) Ar$^+$-plasma treated with 100 eV.

4.8.2 Compositional analysis and interpretation

4.8.2.1 FTIR analysis

FTIR absorption analysis has been carried out with the three above mentioned samples. The relative absorption intensities corresponding to the different band structures are shown in Fig. 4.24 (a) and (b). Four different bands are visible for the samples [84]: Si-N stretching mode (860 cm^{-1}), Si-H (630 cm^{-1}) bending mode and Si-H$_2$ stretching mode (2100 cm^{-1}), as well as N-H stretching mode (3340 cm^{-1}). Si-O stretching mode (1060 cm^{-1}) and N-H bending mode (1160 cm^{-1}) vibrations are not visible in the spectrum, probably due to the large amount of moisture inside the FTIR setup and insufficient N$_2$ purging. All the vibration peaks shows no difference for as-grown and Ar$^+$ treated samples, except the absorption region around 2100 cm^{-1} which is zoomed in Fig. 4.24 (a). The integrated absorption peaks corresponding to different bonds are summarized in Fig. 4.24 (c). Concentrations of chemical species can be calculated as [196]

$$N_{chemical\ species}(cm^{-3}) = \frac{A}{d(cm).S_{eff}(cm^2)} \qquad (4.8)$$

Where A is the height of integrated absorbance peak (dimensionless parameter), d is the film thickness and S_{eff} is the effective absorption cross-section. The values of S_{eff} for Si-N bonds is 1.6×10^{-19} cm^2 [197], for Si-H bonds is 0.57×10^{-19} cm^2 [198] and for N-H bonds is 0.8×10^{-19} cm^2 [199] respectively. Table 4.5 shows the concentrations of chemical species obtained from the above equation. It can be noted that the total concentration of Si-N bonds ($\sim 11.15 \times 10^{22}$ cm^{-3}) is close to the stoichiometric Si$_3$N$_4$, which is about 15.5×10^{22} cm^{-3} [200]. There is no significant change in chemical compositions corresponding to Si-N and N-H bonds for as-deposited and plasma treated samples, except slight modifications of Si-H$_2$ bonds.

The Si-H$_2$ chemical concentration is reduced when the SiN$_x$:H film is treated with Ar$^+$-plasma treated with optimized parameters (sample B). It was reported that SiH$_2$ bonds originating the absorption at ≈ 2100 cm^{-1} are grouped and situated on the surfaces of micro and nano-sized voids in amorphous phase. The minimization of the Si-H$_2$ chemical concentration with the optimized Ar$^+$ treatment conditions is possibly due to the reduction of micro-voids or nano-voids [201] in the SiN$_x$:H film and thus an indication of the SiN$_x$:H film densification [202]. The reduction of micro-voids or nano-voids could be related to the surface atom displacement by the energetic (~ 30 eV) Ar$^+$ ions, which relocate the surface atoms to another lattice sites or defect positions.

When the SiN$_x$:H film is treated with highly energetic (~ 100 eV) Ar$^+$ ions (sample C), noticeably the Si-H$_2$ chemical concentration at 2100 cm^{-1} increases as compared to the as deposited sample. This is because of the enlargement of the number of micro-voids at the surface or possibly inside the bulk,

due to the high bombardment damage of the film by highly energetic ions. The observations are coherent with the structural deterioration of the permeation barriers.
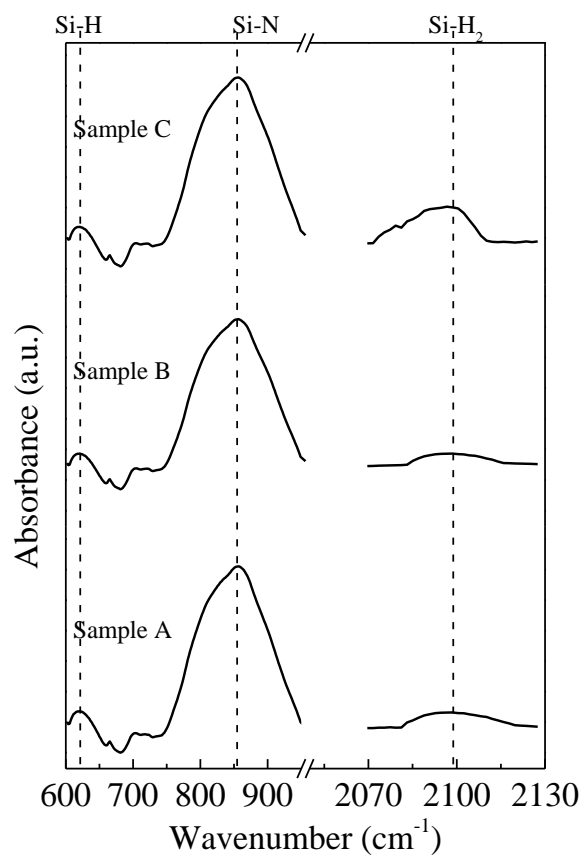
(a)
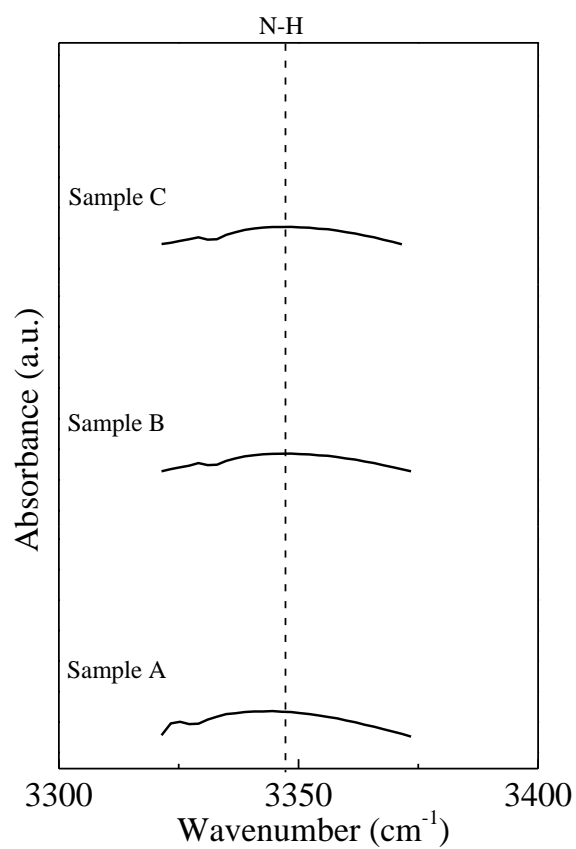
(b)
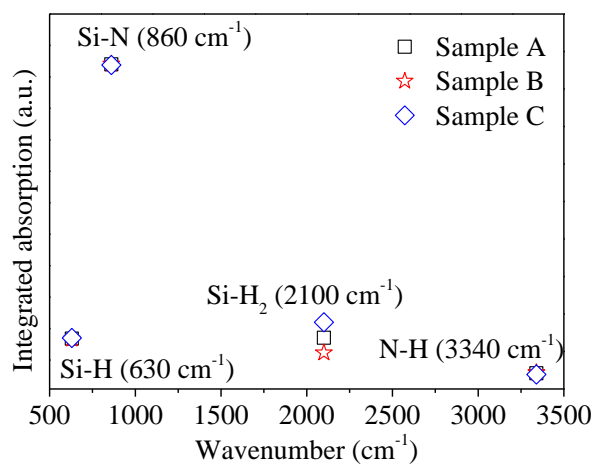
(c)

Fig. 4.24: (a) and (b) FTIR absorption of the different peaks corresponding to the different bond structures for as deposited and Ar$^+$ treated SiN$_x$:H (50 nm thick) grown on c-Si wafers. (c) Integrated absorption peaks for different bond structures.

SiN$_x$:H (50 nm thick) samples	Si-N (860 cm^{-1}) 10^{22} cm^{-3}	Si-H$_2$ (2100 cm^{-1}) 10^{22} cm^{-3}	N-H (3340 cm^{-1}) 10^{22} cm^{-3}
A	11.15	2	0.9
B	11.23	0.89	1.05
C	10.97	6	0.88

Table 4.5: Concentration of chemical species in SiN$_x$:H (50 nm thick) samples according to FTIR data.

4.8.2.2 GD-OES analysis

GD-OES analysis has been performed on all the above mentioned samples in order to investigate the atomic components through the depth profile. Fig. 4.25 shows the GD-OES depth profiles of selected elements (Si, N, H, O and Ar) for as deposited and Ar$^+$ treated SiN$_x$:H films. Since sputter rates depend upon the element, the density etc., they cannot be defined directly. So, the depth profiles are plotted against the sputter time. The relative intensities of the elemental components have been determined using their respective characteristics wavelengths corresponding to the emission of the excited atoms: Si (252 nm), N (149 nm), O (130 nm), H (121 nm) and Ar (404 nm). The intensity of the Si lines shows sinusoidal modulations corresponding to the SiN$_x$:H films and saturates at the interface SiN$_x$:H/c-Si substrate (10 s etch time). The light emitted from the glow discharge is reflected at the front and the back surface of the SiN$_x$:H film, which gives rise to the interferometric superposition of light and in turns the sinusoidal signal modulation. The modulation arises due to the continuous change of the film thickness during the sputtering process which in turn changes the optical path of the beams. The other signals show no modulation since SiN$_x$:H has a direct band gap of 5 eV (248 nm) and therefore absorbs UV light. The SiN$_x$:H film is transparent for those wavelengths [108]. Note that all the signals show a tendency of gradual increase near the surface that is most probably caused by higher reflectivity of the samples before the sputtering roughens the crater bottom.

Although in a commercial c-Si wafer the O-concentration is quite low (10^{15} - 5×10^{16} atoms/cm^3) [203], the O-signal shows some amount of oxygen inside the crystalline silicon wafer, which is probably due to the intrinsic atmosphere inside the glow discharge chamber. The same argument is valid for H content inside the c-Si wafer. However, if the concentrations of O and H are taken as a baseline of measurement, the respective concentrations inside the as deposited SiN$_x$:H film is very low compared to Si and N concentrations, which in turns confirms the comparatively higher density (2.83 g/cm^3) of the HW-CVD grown SiN$_x$:H film as discussed in Chapter 3. Slight bump of the O-line at the film-substrate interface is due to the oxide layer formed on the c-Si wafer owing to the imperfect cleaning procedure.

When the SiN$_x$:H film is Ar$^+$ plasma treated with the optimized treatment parameters (sample B), the depth profile shows almost no significant modifications for the atomic components, except slight reduction of the amount of H near the surface, which is probably due to reduction of nano-voids as already observed by FTIR analysis. This observation is consistent with the fact that at such treatment energy the bulk layer is not disturbed, while the modifications at the very top surface are not completely visible here.

The compositional change in SiN$_x$:H film is pronounced when the sample is treated by Ar$^+$ plasma with -100 V bias voltage (sample C). Due to this energetic ion bombardment causing atomic sputtering, structural damage induces some porosity in the film. This porosity is confirmed by the increase of H and O contents as shown in Fig. 4.25, probably due to the adsorption of moisture and oxygen inside the nano or micro voids. Some Ar atoms (1 ppm < C_{Ar} < 0.1 at %) are also observed implanted in first few layers of the film inside the film. Implantation of Ar atoms inside Si up to less than 2 nm from the surface at 60 eV ionic bombardments has been reported by Al-Bayati *et al* [204] and thus making our observation consistent.
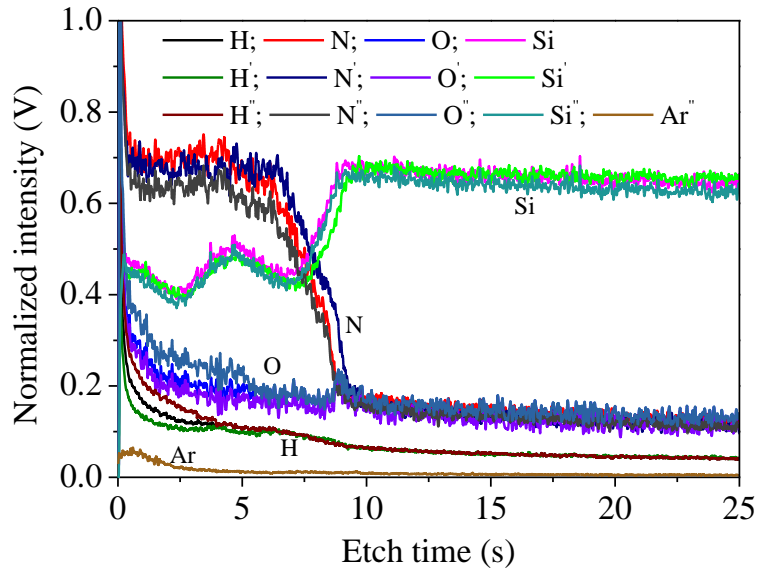
Fig. 4.25: Depth profile of the atomic compositions for as deposited and Ar^+ treated SiN_x:H (50 nm thick) grown on c-Si wafers. The single-prime compositions correspond to the sample B and double-prime compositions correspond to the sample C.

4.8.2.3 XPS analysis

The above mentioned samples have been analyzed using X-ray photoelectron spectroscopy at IRAMIS, CEA Saclay. The details of technical specifications are discussed in chapter 2. The XPS spectrums of different chemical components corresponding to the above samples are shown in Fig. 4.26. The peaks corresponding to Si, N and O are fitted by Gaussian fitting method to obtain the atomic concentrations of the elements. As observed from Fig. 4.26 (a) and (b), the as deposited SiNx:H and Ar plasma treated (30 eV) shows no variations of the peak heights for Si and N components. However, slight reduction (2 at %) of O is observed for 30 eV Ar treated sample (16 at %) compared to sample A (18 at %), which is possibly due to reduction of micro-or nano voids reducing the probability of adsorption of moisture from the atmosphere. Slight discrepancy of the N atomic concentration is also observed compared to the GD-OES measurements.

The sample treated with 100 eV Ar ions, shows a higher concentration of O (30 at %). This is due to increased porosity and increased roughness (see 4.8.1) inside the film due to the damage induced by the higher energy ionic bombardments, which increases the possibility of adsorption of moisture from the atmosphere. No Ar atom is detected for this sample which is in apparent contradiction to the GD-OES measurements. As the detection limit of typical XPS measurement is 0.1 at %, thus it

confirms the low (< 0.1 at %) atomic percentage of Ar atom implantation inside the film observed by GD-OES (see 4.8.2.2).

(a)

(b)

105
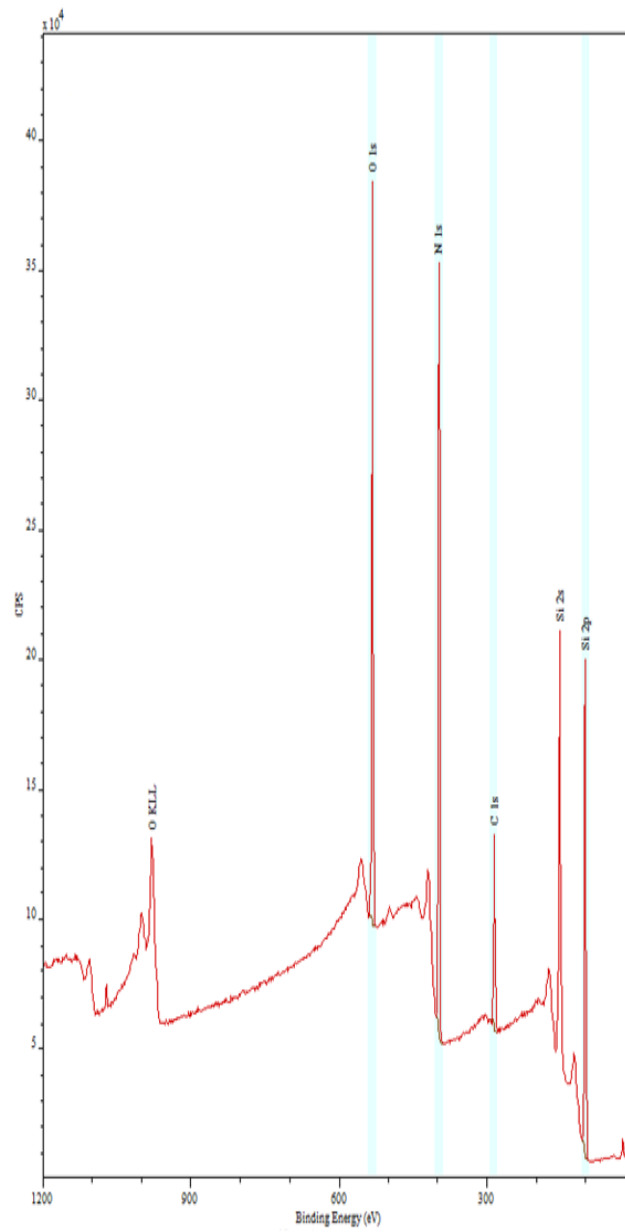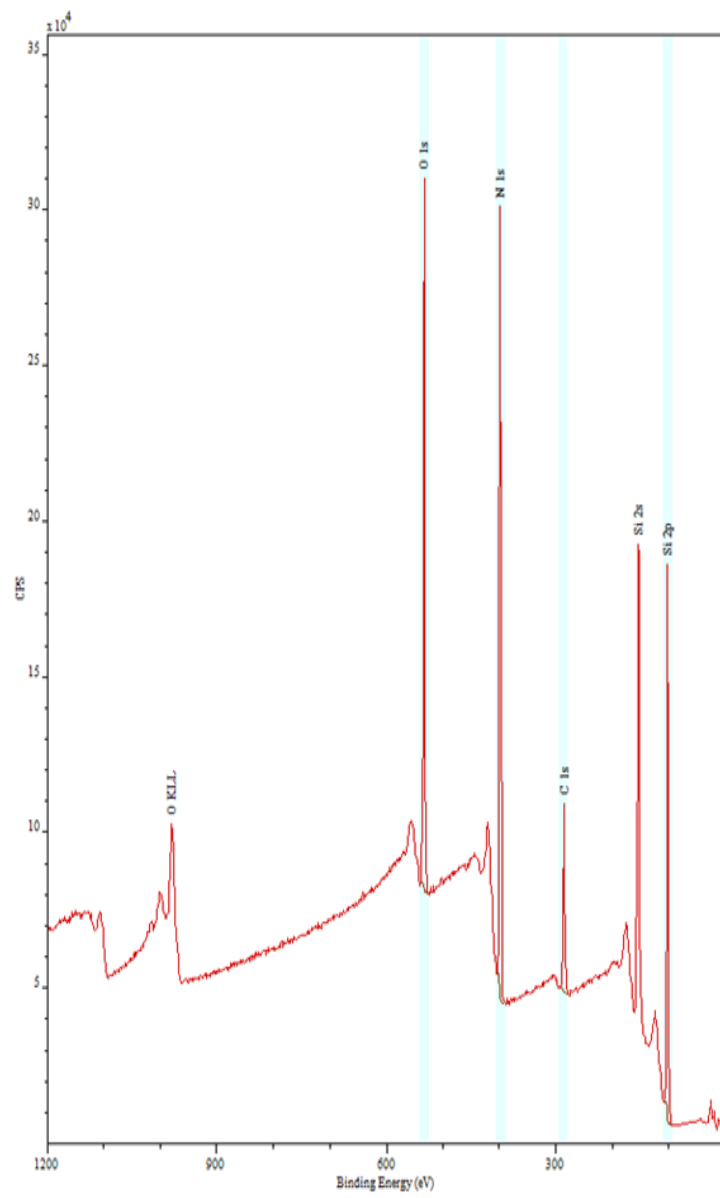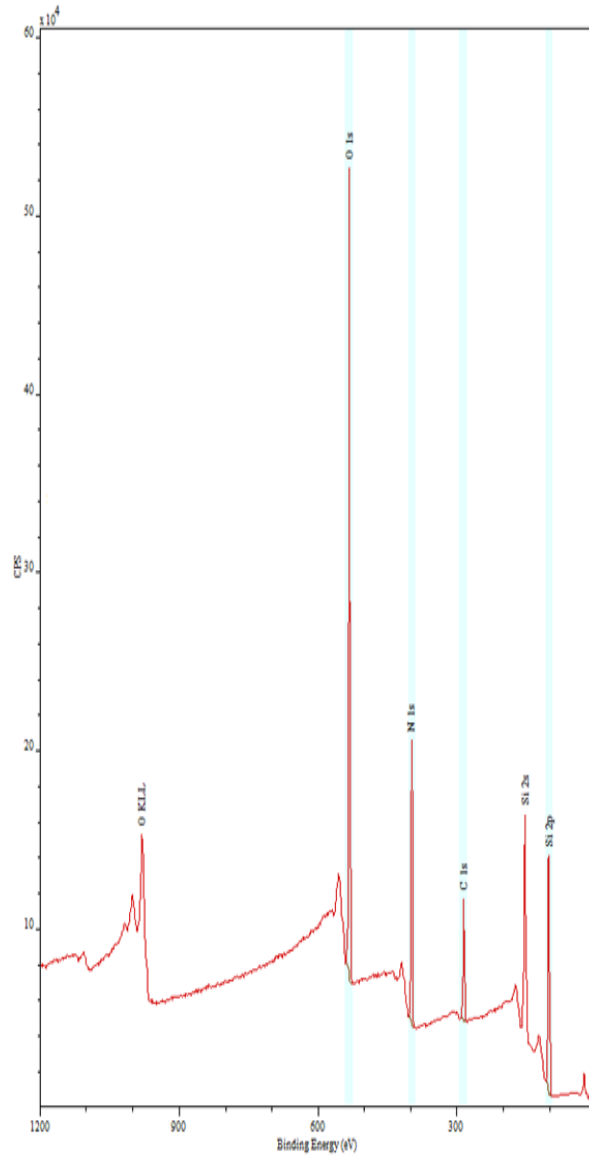
(c)

Fig. 4.26: XPS spectrum of different chemical components of: (a) Sample A, (b) sample B and (c) sample C.

4.8.3 Structural analysis and interpretation

Density profile measurements have been carried out by XRR on the above mentioned samples. Normalized reflectivity signals are shown in Fig. 4.27 (a). In general, roughness of the sample surface gives rise to diffuse scattering, resulting in a lower intensity in the specularly reflected beam [188]. The total reflectivity signal for the as-deposited SiN_x:H film (sample A) being observed lower than that for the Ar^+-plasma treated film with the optimized treatment parameters (sample B), indicates the decrease of roughness (0.9 nm) for the treated sample compared to that for the as-

deposited one (2 nm), thus confirming the above mentioned results using AFM. The third SiN$_x$:H sample treated with 100 V bias Ar$^+$-plasma (sample C) shows a lower reflectivity signal compared to the as-deposited sample, which gives rise to the roughness value of ~2.8 nm and consistent with the AFM analysis.

The density profiles in depth obtained from fitting of the reflectivity signals are shown in Fig. 4.27 (b). As mentioned in Chapter 3, the as deposited SiN$_x$:H film is well fitted with a density value of ~ 2.83 ± 0.02 g/cm^3 and a thickness of 50 ± 0.1 nm. When the film is treated with optimized Ar$^+$ treatment parameters (sample B), two different density regions can be observed: one region of density 2.83 ± 0.02 g/cm^3, corresponding to the usual bulk SiN$_x$:H layer (compared with sample A) with a thickness of 48.8 nm, and a "higher" density region (2.91 ± 0.02 g/cm^3) on top of this bulk density region, with a thickness of 1.2 nm. This increase in density (~3%) has been fitted with the lowest chi^2 value (~ 10^{-6}). The mechanism of ion assisted densification by low energy ion bombardment (30 eV) can be understood taking into account the mechanism suggested by Martin and Müller [205, 206]. The ions with sufficient kinetic energy (below the sputtering threshold) impinging on the surface of the SiN$_x$:H film can penetrate the surface to an average depth of few nanometers. This produces a collision cascade of knock-on atoms. The displacement of the target atoms occurring at the displacement energy threshold range, forward the recoiled atoms pushed into interstitial sites deeper from the surface. The depth depends on the kinetic energy of the ions and the relative exchange of energy between ions and the target atoms. The densification of the film is coherent with the decrease of surface roughness, reduction of nano-voids and reduction of H content near the surface as observed by AFM, FTIR and GD-OES measurements respectively. In other words, as said by Grigorov *et al*. [207], the displacement of surface atoms by the atomic bombardment into another energetically profitable lattice site explains the higher packing density of atoms.

With the increase of bias voltage, $\left| V_{Bias} \right|$ =100 V, the maximum kinetic energy of the ions impinging on the surface of the film increases as well. The exchange of energy is higher in this case. Ions can penetrate much deeper from the surface and induce more bulk atomic displacements (more collision cascades). Due to significant knock-on of the atoms, the recoiled atoms receive sufficient energy to be sputtered out of the sample. This mechanism creates large number of nano-voids and significant damage of the film, which in turns is deteriorating for the permeation barrier properties. As a result of the ion-induced damage of the film, the density of the film becomes lower for larger depth from the top surface and the top layer becomes porous; the rest of the layer keeping the bulk density (2.83 g/cm^3). As shown in Fig. 4.27 (b), the lower density (2.35 g/cm^3) extends to a depth of

~7 nm from the surface. This observation is coherent with the GD-OES measurement, where the Ar implantation depth is similar to the low density region.

(a)

(b)
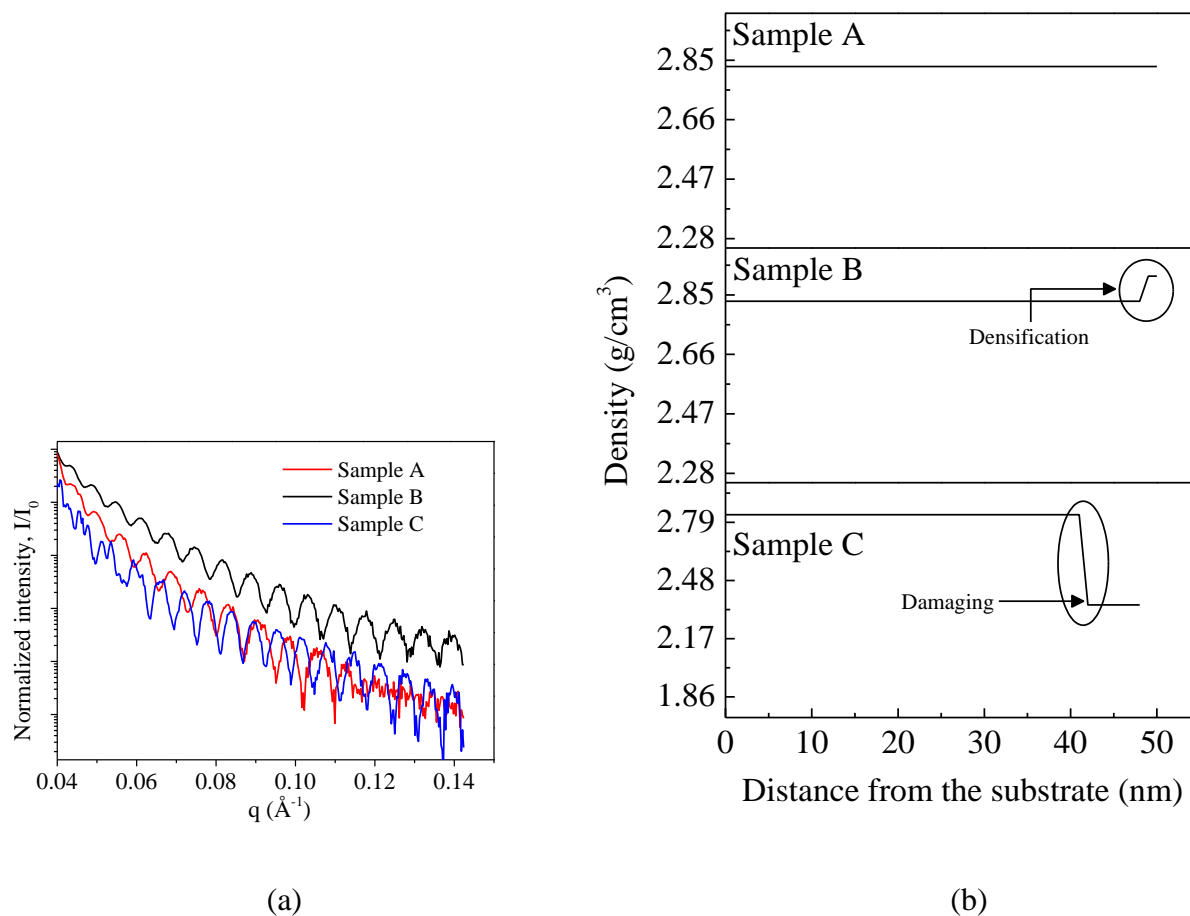
Fig. 4.27: (a) XRR normalized reflection of the different SiN$_x$:H samples (50 nm thick) grown on c-Si wafers: sample A (red), sample B (black) and sample C (blue).(b) Density profile of the films.

4.8.4 General discussion on barrier improvement

We summarize here what has been observed and explained in the previous sub-headings of this chapter. In Fig. 4.28 (a), the single-layers contain pin-holes through which water molecules can easily diffuse. The argon plasma treatment with optimized treatment parameters (30 eV) induces a denser top surface (1.2 nm thick) containing a lower number of micro-or-nano voids compared to the bulk SiN$_x$:H single-layer and hindering the native nucleation centers which were existing at the top of the first SiN$_x$:H layer (Fig. 4.28 (b)). This modified surface impedes the diffusion of water molecules from the outside to enter into the pinholes. We grow a second SiN$_x$:H layer on top of the Ar treated surface with low probability of alignment of pinholes with the first layer (Fig. 4.28 (c)). When these plasma treated SiN$_x$:H layers are stacked together, the water molecules face a tortuous diffusion path and the total time of diffusion throughout the whole barrier structures becomes longer.

Thus, the permeation barrier properties logically improve for this plasma treated barrier structures, as observed in this chapter. Therefore, without creating a real physical interlayer as proposed by the conventional barrier structures, this method provides a unique encapsulation procedure which is viable in terms of throughput compared to the conventional barrier structures.

<table>
<tr><td>(a)</td><td>(b)</td><td>(c)</td><td>(d)</td></tr>
</table>
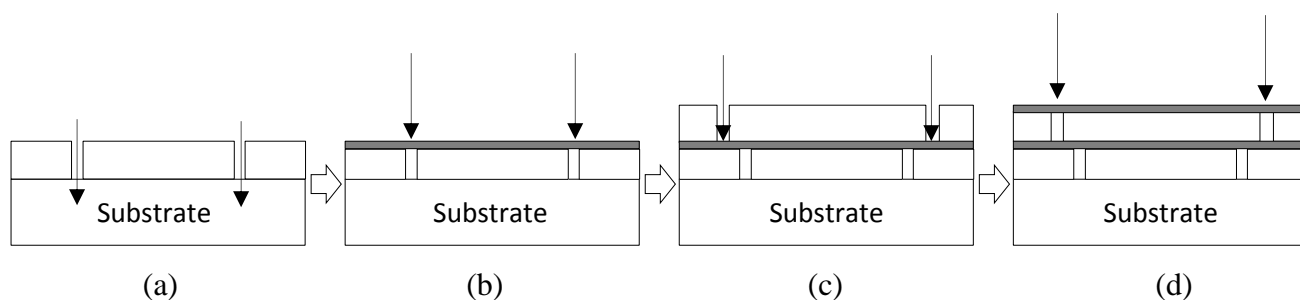
Fig. 4.28: Schematic diagrams of steady state permeation of water molecules through different structures of SiN$_x$:H thin films deposited on PET substrates (not to scale): (a) single-layer of SiN$_x$:H (50 nm), (b) single-layer with Ar treated at the top surface (dark color), (c) second single-layer on top of the Ar treated layer and (d) Ar treatment on top of the second single-layer.

4.9 SUMMARY OF CHAPTER 4

i.   This chapter is comprised of a unique method of developing permeation barrier layers consisting in multilayers of SiN$_x$:H thin films and low energy plasma treatment between each successive single-layer deposition.

ii. Several plasma treatment parameters (treatment duration, power density and working pressure) are varied in order to achieve an optimal plasma treatment condition, which gives rise to drastic reduction of the film surface roughness as well as a reduction of the WVTR values and increase of the lag-time.

iii. The minimum WVTR obtained (7×10^{-5} g/m^2.day) should be sufficient for the longer shelf-life-time of organic electronic devices.

iv. The mechanical property of the barrier structure is investigated in order for this permeation barrier to be utilized in real flexible organic electronic devices.

v. Several characterizations are performed to interpret both the improvement and the deterioration of barrier properties. Physical interpretations are given taking into account the different plasma treatment parameters. For relatively high energy Ar ions, some Ar atoms have been detected using glow discharge optical emission spectroscopy but not detected using X-ray photoelectron spectroscopy, confirming the low concentration of Ar (< 0.1 at %) implanted below the surface.

CHAPTER 5

INORGANIC / ORGANIC HYBRID-LAYER FILMS

5.1 INTRODUCTION

The improvement in barrier performance of inorganic single layers such as SiN_x:H films is limited mainly by pinholes or nanometer-to-micron sized structural defects, which can favor the diffusion of water molecules from the underlying SiN_x:H film. As mentioned in chapter 4, a technique which could make a break of the propagation of structural defects by decoupling the defects in consecutive single-layers is needed. The conventional approach of developing encapsulation structures is based on fabricating alternating inorganic and organic layers in order to minimize the propagation of structural defects throughout the barriers. This common strategy involves sandwiching a smooth organic layer between two inorganic layers [38, 69, 91-98] and thus creates a complex and tortuous diffusion path for the water molecules throughout the whole structure.

Organic materials (e.g., polymers) are often robust but highly permeable to moisture, while single-layers of inorganic materials (SiN_x:H) are comparatively less permeable to moisture but extremely fragile and contain structural defects. Thus, neither by itself is an effective permeation barrier for flexible electronics. Such a conception has led to the design of multilayer barrier coatings consisting of alternating thin films of inorganic and organic materials, with the hope to capitalize on both the impermeability of the inorganic layers and the robustness of the organic layers [119].

The primary goal of this chapter is to develop high performance encapsulation barriers layers applying alternating inorganic and organic layers on PET substrates. The particular interest of this chapter is to investigate the effect of number of inorganic-organic interfaces on the overall barrier performance. Two different deposition techniques (MDECR-PECVD and HW-CVD) for the growth of the inorganic layers (SiN_x:H) are utilized and the overall barrier properties are compared. The permeation barrier quality depends largely on the deposition techniques. The organic layer of PMMA [Poly (methyl methacrylate)] is deposited by the widely used spin–coating technique. Very recently, several researchers have developed high quality organic films with very precise thickness and optical properties. Initiated-CVD (i-CVD) is one of those techniques which could allow one to grow high quality organic layers [69]. However, this particular technique is not extensively used and requires years of research on this particular technique, which is out of the scope of this present thesis. Instead,

the particular attention is focussed on increasing the inorganic-organic interfaces to reduce the barrier properties.

In the first section of this chapter, the specific growth conditions and characteristics of the MDECR-PECVD grown SiN_x:H films obtained from the previous dedicated works are summarized. The barrier properties of the MDECR-PECVD grown SiN_x:H single-layer films are investigated in order to obtain the critical thickness parameter (d_c) and compared with the HW-CVD grown single-layer films which is described before in chapter 3. The structures of the hybrid layers are discussed after that taking into account the requirements of the thickness of the individual layers. The growth conditions of the organic layer are then introduced.

In the last section of this chapter, the impact of number of inorganic-organic interfaces for both MDECR-PECVD and HW-CVD grown SiN_x:H films are described in detail. Their optical properties are also introduced in order to show the compatibility of the structures with the utilization in real devices. Finally, the mechanical properties of the barrier structure are discussed taking into account different number of cyclic bending.

5.2 MDECR-PECVD GROWN SILICON NITRIDE FILMS

5.2.1 Growth of thin films

The silicon nitride films (SiN_x:H) are deposited in Matrix Distributed Electron Cyclotron Resonance (MDECR) PECVD reactor which is a high plasma density low-pressure deposition technology used for the fabrication of dielectric, functional and optical thin films for different applications. The detailed description and schematic diagram of the reactor has been described previously in chapter 2. The SiN_x:H thin films are deposited on cleaned PET substrates with previously optimized deposition conditions as listed below in table 5.1 [103-105].

Parameters	Value
SiH$_4$ flow rate F(SiH$_4$) (sccm)	10
N$_2$ flow rate F(N$_2$) (sccm)	80
Process gas pressure p_g (mTorr)	2
T_s (˚C)	Room temperature
Microwave power (W)	1000
Deposition rate (Å/s)	6

Table 5.1: Deposition conditions of SiN$_x$:H thin films using MDECR-PECVD system.

5.2.2 Film characteristics

The compositional analysis and structural properties of the MDECR-PECVD grown SiN$_x$:H films were characterized extensively in previous dedicated works [105]. Since the barrier properties depend on density and stoichiometry of the films; in the present study, these properties are investigated again. The density measurements of the films are carried out using X-ray reflectivity technique (BRUKER-D8) and analyzed using Parratt32 software. The optical constants (refractive index, n and thickness, d_f) are measured using the phase modulated spectroscopic ellipsometer Uvisel (Jobin-Yvon, Horiba Group) in the $1.5 - 5.0$ eV photon energy range on the films deposited on 510 µm thick crystalline silicon wafers and the measured data are fitted with classical Lorentz dielectric model.

From the fit of the spectroscopic ellipsometric data to the model, we obtained a refractive index (n) value of ~1.76 at 632.8 nm wavelength. From the fitting of the measured XRR data, the SiN$_x$:H mass density of ~2.43 g/cm^3 has been obtained. Compared to the stoichiometric value of amorphous Si$_3$N$_4$:H refractive index (2.05 at 632.8 nm wavelength) and mass density (3.1 g/cm^3) [158], MDECR-PECVD grown films have significantly lower density. The reason could be either oxygen contamination and/or relatively higher hydrogen content, which is always the case in room temperature deposition.

5.2.3 Determination of critical thickness:

The permeation barrier properties of the MDECR-PECVD grown SiN$_x$:H single-layers on PET substrates are analysed by electrical calcium degradation test method, where the thickness of the single-layers varies from 20 to 300 nm. It should be noted here that, compared to the HW-CVD

method, there is no thickness limitation in MDECR system due to the room temperature deposition and absence of filament radiation. The deposition rate (6 Å/s) for MDECR system is also higher than the HW-CVD system (1.1 Å/s).

As seen in Fig. 5.1 (a), the barrier performance assessed by the decrease of WVTR value, improves with the increase of SiN_x:H single-layer coating thickness (d_f). The curve can also be divided into three separate regions, as obtained for the HW-CVD grown films (see Fig. 5.1 (b) for comparison). The first one, from 0 to 30 nm, corresponds to the "threshold thickness (d_{th})" region, below which there is no barrier effect and over which ($d_f > d_{th}$) the permeation rate drops rapidly until it stabilizes at a critical thickness (d_c) value (about 120 to 150 nm in this case). For, $d_f > d_c$, no further significant decrease in WVTR is observed, the stabilized value being ~1.5×10^{-2} g/m^2.day.

The above observations can be interpreted taking into account the density and stoichiometry of the films deposited by two different techniques. As a result of the reduced amount of hydrogen inside the HW-CVD deposited films due to the abstraction reactions, the density of the SiN_x:H thin films are higher (2.83 g/cm^3) and films are close to the stoichiometry ($n \sim 2.01$ at 632.8 nm wavelength). Therefore, it is possible in the case of HW-CVD to deposit coatings on PET substrates that reduce the WVTR value one order of magnitude less than the PET substrates; at a thinner coating thickness of around 50 to 60 nm. Although both techniques seem viable in terms of throughput, the thinner critical thickness of HW-CVD films facilitates partly recovering lower deposition rate as compared to the MDECR system. Thinner coating thickness may have additional benefits, such as improved flexibility and thermo-mechanical properties.

Since the critical thickness is the minimum single-layer thickness that reduces the WVTR to its minimum value, in the rest of this chapter, the critical thickness for HW-CVD films is taken as a fixed parameter for the inorganic layer thickness to develop alternating inorganic-organic structures. In order to compare the barrier performance of the MDECR grown films, the thickness of the SiN_x:H films has also been fixed at 50 nm (d_c for HW-CVD system) to achieve comparable mechanical flexibility, even though the permeation barrier should not be as efficient.

(a)   (b)
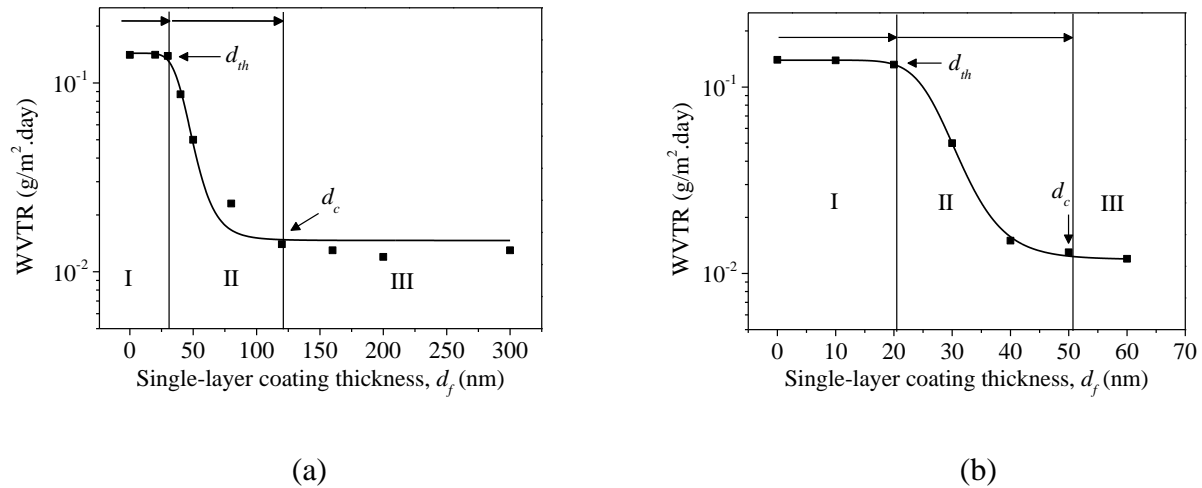
Fig. 5.1: Moisture permeation rates measured through: (a) MDECR-PECVD grown SiN$_x$:H single-layers coated on PET substrates; and (b) HW-CVD grown SiN$_x$:H single-layers coated on PET substrates.

5.3 HYBRID STRUCTURE

5.3.1 Choice of organic material

The organic material to be used as the interlayer between two inorganic layers should have some intrinsic properties in order to be compatible with the encapsulation process. The inorganic layers are deposited through either MDECR-PECVD or HW-CVD methods, and therefore the organic material should be stable during these deposition techniques. The organic material have low glass transition temperature, which should be slightly higher than 100 °C; since the SiN$_x$:H films deposited by HW-CVD method are grown at a substrate temperature of 100 °C. Furthermore, they should be stable with the radicals or plasma generated in HW-CVD and MDECR methods respectively. The organic layer should also have smoothing effect in order to enhance the growth of the next inorganic layer with better structural quality. Additionally, the organic material should have lower Young's modulus in order to enhance better flexibility (discussed later in this chapter). In the present thesis, PMMA [Poly (methyl methacrylate)] has been used as an organic material, because it is widely used and inexpensive compared to other organic polymers. The glass transition temperature (T_g) of 106 °C allows it to be stable during the inorganic film deposition. However, the impact of radicals or the plasma on PMMA material is not investigated extensively in this study.

5.3.2 Optimization of thickness

The permeation barrier properties of the whole hybrid structure depend largely on the organic layer thickness. The organic layer thickness must be such that it can decouple the defects between two

115

consecutive inorganic layers and thus create a tortuous diffusion path for the permeating water molecules. According to Schaepkens *et al*. [102], the organic layer thickness is quite critical in reducing the overall permeation barrier property. As shown in Fig. 5.2, whenever the interlayer thickness is smaller than the average lateral distance between two consecutive defects, the permeation rate reduces drastically. This is due to the fact that in this regime the permeation is no longer Fickian diffusion, but one enters into the conduction limited diffusion. The ultrahigh barriers should be in this regime. Although, in our present inorganic films, the exact defect density and defect spacing are not extensively investigated, if realistic values are considered with a defect density of 100 defects/mm^2 and consecutive defect spacing of 100 μm [102], it would be logical to have an idea of the interlayer thickness.
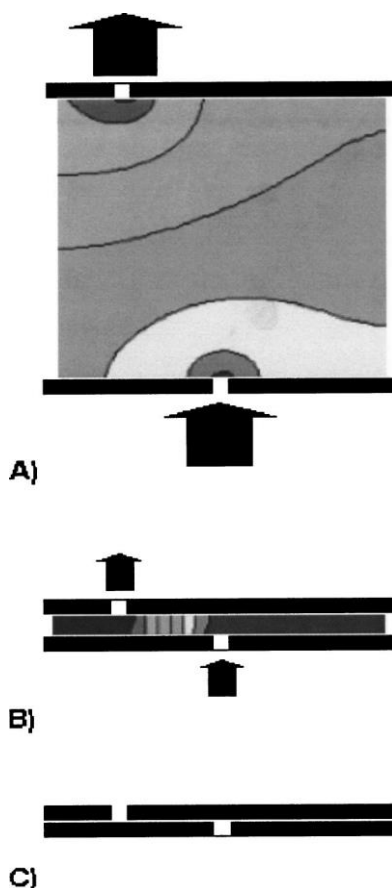
Fig. 5.2: Dependence of interlayer thickness on overall permeation: (a) the interlayer thickness is larger than the lateral distance between two consecutive defects; (b) the interlayer thickness is smaller than the lateral distance between two consecutive defects and (c) ideal structure for ultrahigh barrier coatings (note: the last structure is impossible to fabricate in practice, since the defect of the underlying layer would propagate into the top layer). Reprinted with permission from [102]. Copyright 2004 American Vacuum Society.

To make alternating hard / soft structure, 300 nm polymer layers (PMMA) are deposited by spin-coating technique inside the glove-box between two SiN_x:H single-layers. The commercially available PMMA is dissolved in chloroform (5 wt. %) and the solution is spin-coated on the already grown SiN_x:H film at 5000 rpm for 50 s followed by an annealing treatment at 100 °C for 30 min. The thickness of the layer is measured by the Dektak 150 profilometer using the films coated on Corning glass substrates. At least ten thickness measurements are taken on the film along the centerline of the substrate. Fig. 5.3 shows the variation of PMMA layer thickness with spin-coater speed.
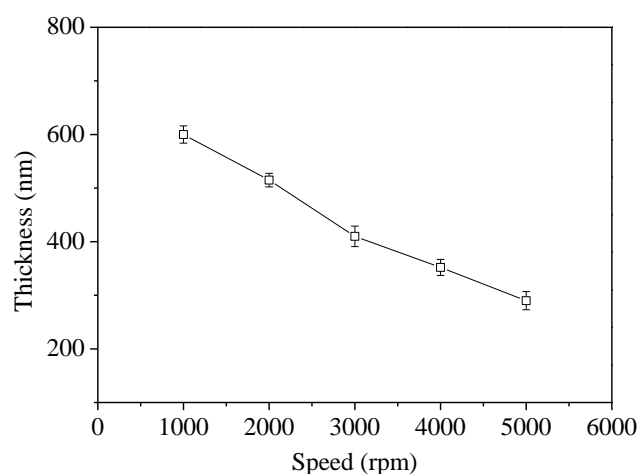
Fig. 5.3: Variation of PMMA film thickness with speed of the spin coater.

5.3.3 Surface morphology

The surface morphology of the as deposited and annealed PMMA films is analyzed by tapping mode AFM technique. PMMA can be crystallized and become smoother when annealed near its glass transition temperature (T_g) of 106 °C, as shown in Fig. 5.4. The average roughness of the PMMA layer decreases 80% when it is annealed. The observed change in the morphology at the annealing temperature of around 100 °C may be assigned to the reasons such as intensified thermal oscillations of molecules at higher temperatures leading to the diminished order of their orientation, the improved stoichiometry, reduction of defects and faster structural relaxation [208]. The surface topography of the as deposited PMMA layer also shows some 50 nm diameter scale holes (in average) throughout the surface. However, with the annealing of the layer the holes disappeared. This could be probably due to the faster evaporation of the solvent when the sample is annealed. Structural modification of the PMMA layer could help in hindering the propagation of any structural defects and producing the subsequent inorganic layer with high quality.

<center>(a)</center>

<center>(b)</center>
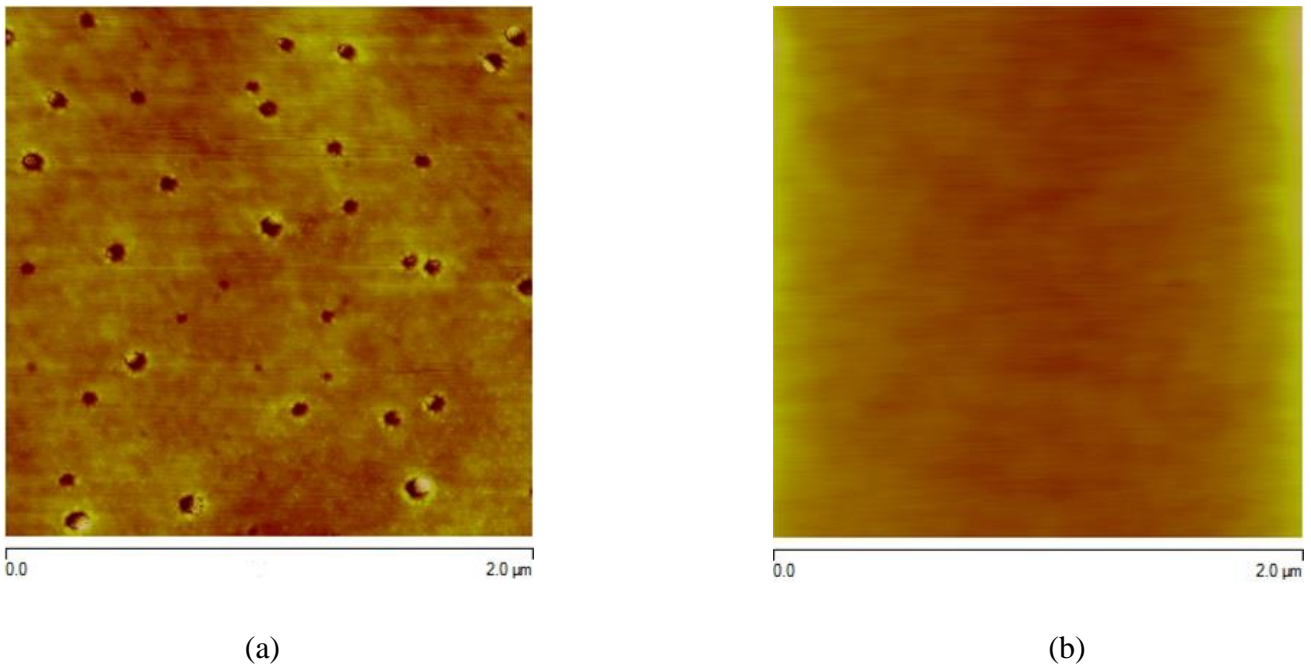
Fig. 5.4: The surface topography of the (a) as deposited PMMA film ($R_{avg.}$ = 1.57 nm); (b) PMMA film annealed at 100 °C ($R_{avg.}$ = 0.31 nm).

5.3.4 Development of hybrid structure

An alternating layer structure is created consisting of an organic layer (PMMA) sandwiched between two inorganic layers (SiN$_x$:H), where the critical thickness (d_c) is taken as a fixed parameter for inorganic films, by making the moisture penetration path through the organic/inorganic interfaces much longer and tortuous in order to improve the barrier performance. We prepared four different structures of alternating barriers, as shown in Fig. 5.5, with increasing number of interfaces. The interface between the first SiN$_x$:H layer and the PET substrate is also counted. To check the compatibility of both MDECR-PECVD and HW-CVD grown SiN$_x$:H films and the spin-coated PMMA films with the utilization in real optoelectronic devices, the optical transparency of the layers is measured using the films grown on PET substrates. The reflectance and the transmittance spectra are measured using Perkin Elmer Integrating Sphere.
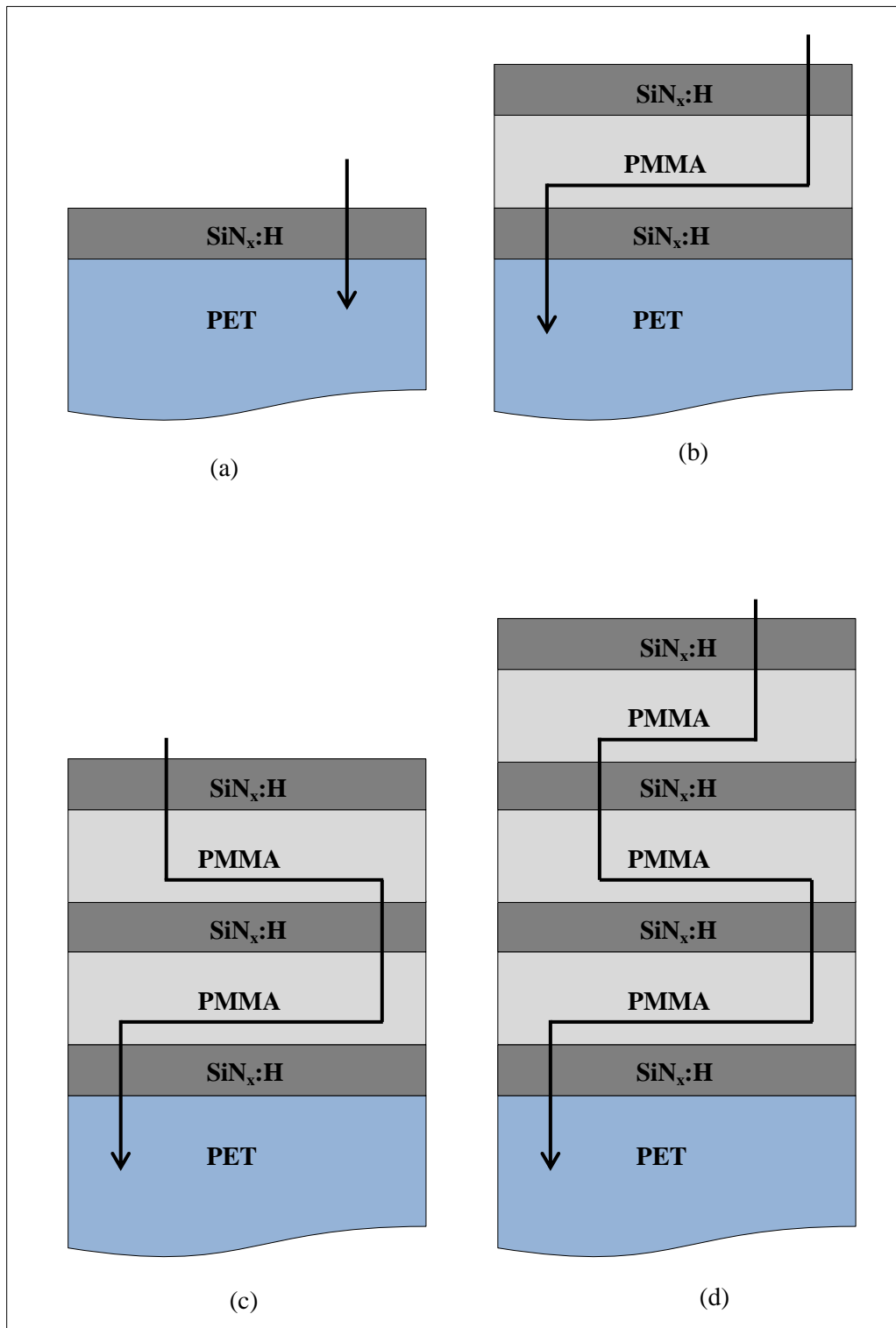
Fig. 5.5: Schematic diagrams (not to scale) of 4 different permeation barrier hybrid structures with different number of inorganic-organic interfaces. Here the thickness of SiN$_x$:H layers is fixed at 50 nm. (a) 1 interface; (b) 3 interfaces; (c) 5 interfaces and (d) 7 interfaces.

5.4 HYBRID STRUCTURE WITH MDECR-PECVD GROWN SiN$_x$:H

5.4.1 Optical properties of the hybrid structure

Figure 5.6 shows the reflectance and the transmittance measurement of the alternating layer structure (stack of four 50 nm SiN$_x$:H single-layers each separated by a 300 nm PMMA layer). The transmittance curve indicates that the alternating layer structure is highly transparent ($\sim$ 80%) in one part of the visible region (450 to 800 nm). It can also be seen from Fig. 5.6 that reflectance and transmittance of this hybrid layer structure together are almost 100% in the range between 450 to 800 nm, meaning that some absorption takes place in the layers below 450 nm. In can be concluded that even-though the increase of interfaces should logically improve the barrier properties, a trade-off should be found between the permeation barrier properties and optical transparency taking into account the number of interfaces.
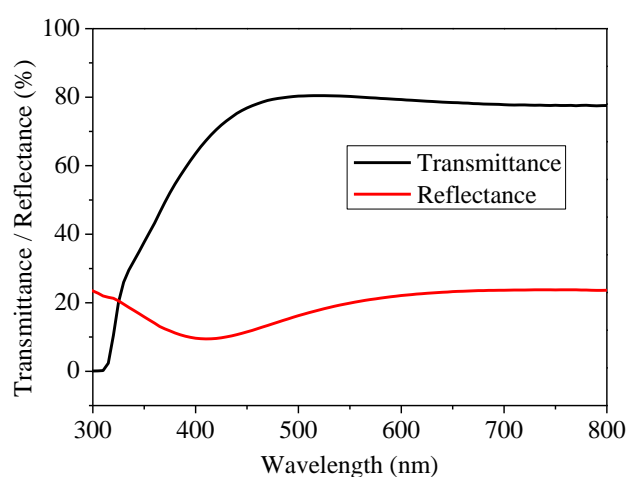
Fig. 5.6: Reflection and transmission spectra of hybrid structure with 7 interfaces (stack of 4 SiN$_x$:H single-layers each separated by a PMMA layer).

5.4.2 Barrier properties of the hybrid structures

The evolutions of normalized conductance of the Ca sensors deposited on such hybrid-barrier coated PET substrates are shown in Fig. 5.7 (a). When the number of SiN$_x$:H / PMMA layers increases, the number of interfaces between the organic and inorganic films increases as well. The water molecules face a complex diffusion path when passing from one SiN$_x$:H single-layer to the other through the intermediate polymer layer (see Fig. 5.5). Due to that reason and to the increase in total thickness of the coating, the minimum time taken by the water molecules to reach the Ca surface which is at the opposite side of the coated PET substrates, increases with increasing number of interfaces. The variation of "lag-time" with the increasing number of interfaces is shown in Fig. 5.7 (b) and a maximum lag-time of 85 hours is achieved with 7 interfaces. The WVTR values also decreases with

increasing number of interfaces (see Fig. 5.7 (c)) and there is a significant drop of WVTR value when the first PMMA layer is inserted between two 50 nm SiN$_x$:H single-layers (3 hard/soft interfaces), reaching down to 8×10^{-4} g/m^2.day. This confirms the efficiency of the PMMA layer to impede water vapour molecule diffusion. After that WVTR values decreases monotonically with increasing number of interfaces reaching a minimum value of 2×10^{-4} g/m^2.day for 7 interfaces, which is quite sufficient for the requirement for the encapsulation of organic solar cells. However, the barrier improvement factor (BIF) shown in Fig. 5.7 (d), clearly reveals that the impact of additional interfaces beyond 3 interfaces of inorganic-organic is not quite efficient. Therefore, in order to improve the barrier performance, either the quality of the inorganic/organic materials should be improved, or a higher thickness of the inorganic layer (> critical thickness for MDECR) should be used.
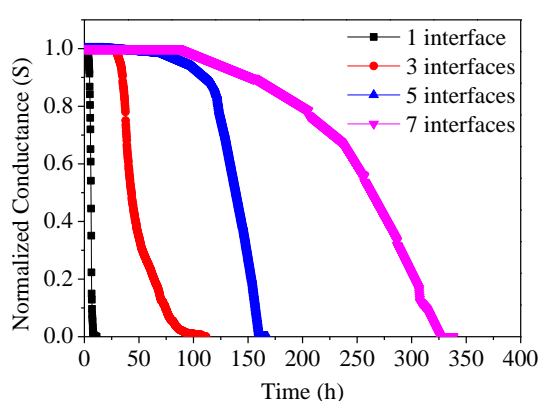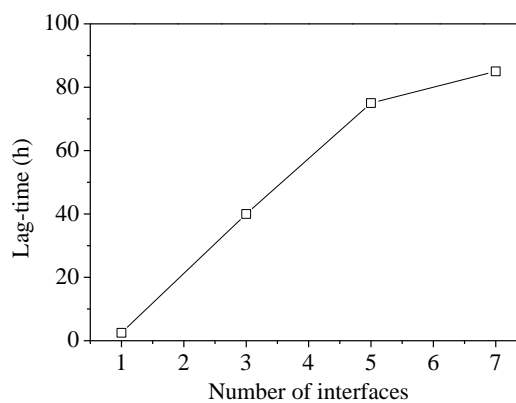
(a)   (b)
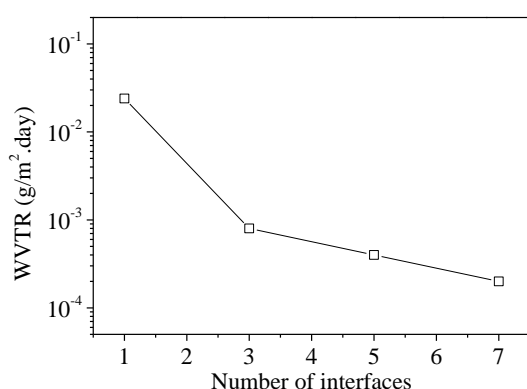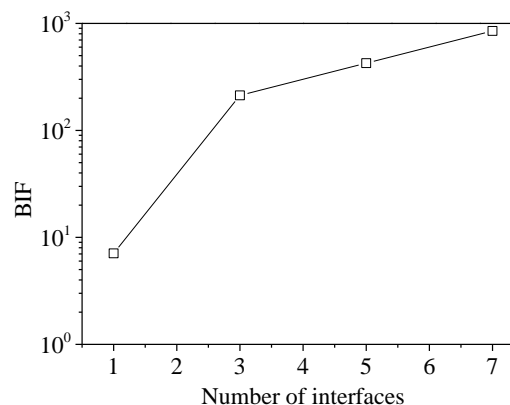
(c)   (d)

Fig. 5.7: (a) Evolution of normalized conductance of the Ca sensor with time for different hybrid structures deposited on PET with increasing number of interfaces. (b) Variation of lag-time with

121

number of interfaces. (c) Variation of WVTR with number of interfaces. (d) Variation of barrier improvement factor with number of interfaces.

5.5 HYBRID STRUCTURE WITH HW-CVD GROWN SiN$_x$:H

5.5.1 Optical properties of the hybrid structure:

Figure 5.8 shows the reflectance and the transmittance measurement of the alternating layer structure. The transmittance curve indicates that all the alternating layer structures are highly transparent (~ 80%) in the range between 350 to 800 nm. It can also be seen from Fig. 5.8 that reflectance and transmittance of this hybrid layer structure together are almost 100% in that range, meaning that no absorption takes place in the layers and the barrier structures can be perfectly used as a window layers for optoelectronic devices. Slight absorption below 400 nm wavelength is due to the plastic substrate itself. It should be noted that in comparison with hybrid layer structure developed by MDECR system, the optical transparency is higher for the whole range of wavelength for HW-CVD grown samples and therefore, the number of interfaces could be increased beyond 7 until the transparency begins to decrease.
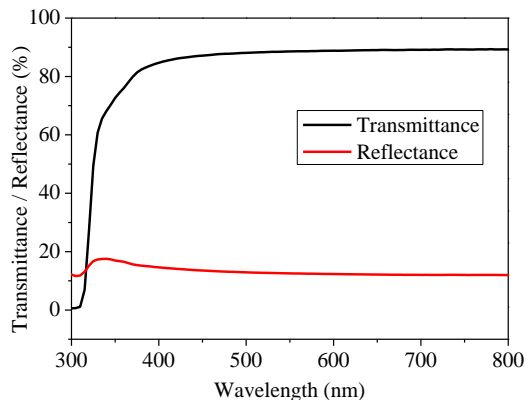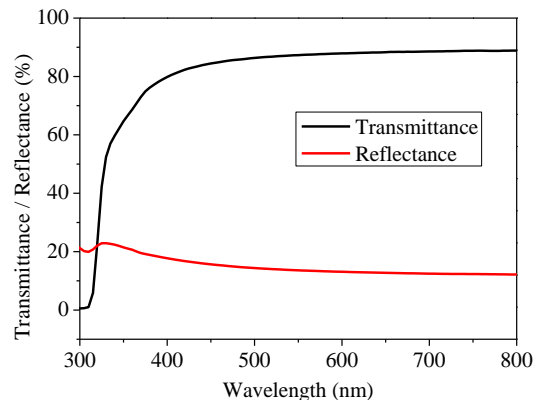
(a)   (b)
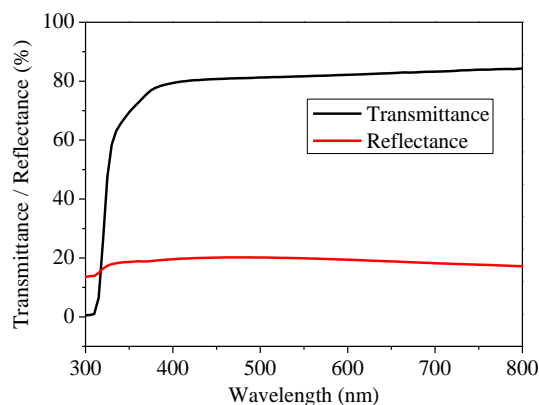
(c)

Fig. 5.8: Reflection and transmission spectra of hybrid structures: (a) 3 interfaces; (b) 5 interfaces; (c) 7 interfaces.

5.5.2 Barrier properties of the hybrid structures:

The evolutions of normalized conductance of the Ca sensors deposited on such hybrid-barrier coated PET substrates are shown in Fig. 5.9 (a). The lag-time and WVTR values are assessed from the evolution of the conductance and are shown in Fig. 5.9 (b) and (c). The results show a clear trend of barrier improvement with an increasing number of interfaces. A maximum lag-time of 155 hours is achieved with 7 interfaces. The WVTR value decreases with increasing number of interfaces and there is a significant drop of WVTR value when the first PMMA layer is inserted between two 50 nm SiN$_x$:H single-layers (3 hard/soft interfaces), reaching down to 9.2×10^{-5} g/m^2.day, confirming the quality of PMMA as before. After that WVTR values decreases monotonically with increasing number of interfaces reaching a minimum value of 4.5×10^{-5} g/m^2.day for 7 interfaces. The barrier improvement factor is one order of magnitude higher compared to the MDECR grown samples. As the same organic layer (PMMA) is used to build the hybrid structures, therefore, the quality (the deposition technique in other words) of the inorganic layers (SiN$_x$:H) is quite critical in order to improve the overall barrier performance.
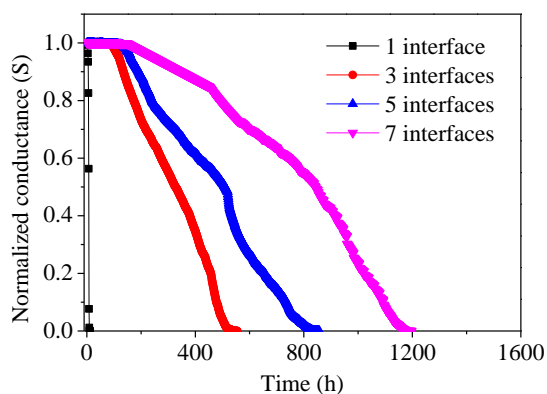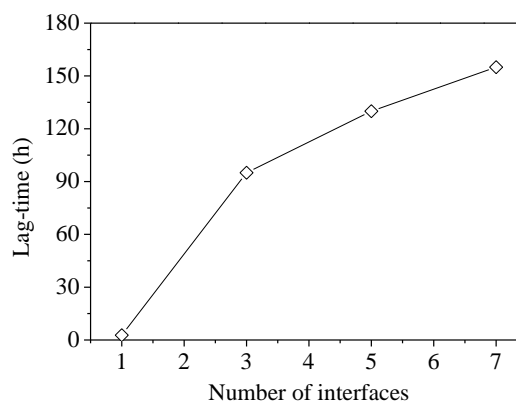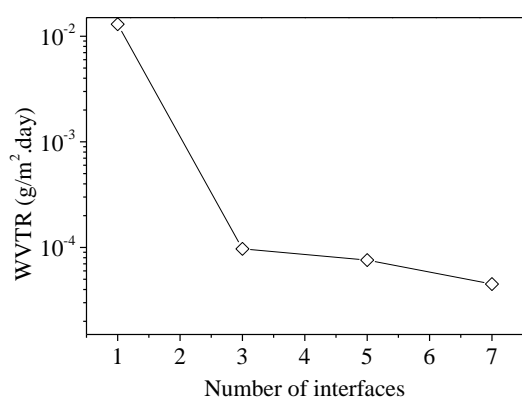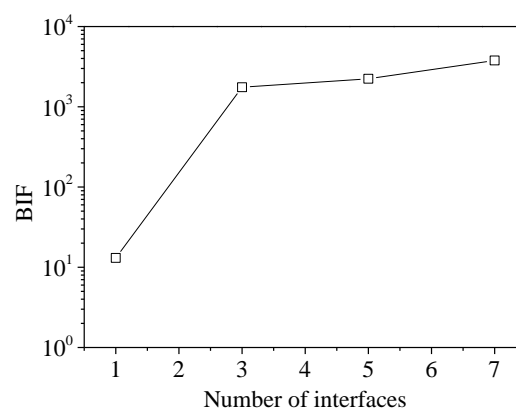
Fig. 5.9: (a) Evolution of normalized conductance of the Ca sensor with time for different hybrid structures deposited on PET with increasing number of interfaces. (b) Variation of lag-time with number of interfaces. (c) Variation of WVTR with number of interfaces. (d) Variation of barrier improvement factor with number of interfaces.

5.5.3 Mechanical property of the hybrid structures

The mechanical flexibility of the hybrid structure is investigated by bending a 3 interface structure with a radius of curvature of 5 mm for different cycles of bending. Ca degradation tests are performed on such deformed samples in order to assess the impact of bending on the permeation barrier properties. It is quite obvious that when the samples are bent, due to the tensile stress channel cracks are formed inside the inorganic films as shown in Fig. 2.12 in chapter 2. A good barrier property of a structure depends on the ability of retaining the initial barrier properties even after certain number of bending. In this section, such ability of the hybrid structure is discussed.

As discussed in chapter 4, when an inorganic film (in this case SiN$_x$:H) is deposited on a pliable under-layer (in this case PMMA), during deformation a tensile strain is induced inside the inorganic layer. According to Yanaka *et al.* [190], onset strain for crack formation for thin inorganic films is 1.3%. In order to investigate the impact of bending on the induced strain inside the top inorganic layer, the calculated variations of induced strains with radius of curvature, inter-layer (PMMA) thickness and inter-layer's Young's modulus are shown in Fig. 5.10. When one parameter is changed, other two parameters remain fixed. As shown in Fig. 5.10 (a), with the decrease of radius of curvature (*r*); the induced strain inside the top inorganic SiN$_x$:H layer increases. However, with very serious bending (< 2 mm), the onset strain (1.3%) for cracking never reached. This is probably due to the fact that during deformation, the soft under-layer (with lower Young's modulus) of PMMA absorbs the stress. The variation of the induced strain with increasing PMMA thickness is shown in Fig. 5.10 (b): when the inter-layer thickness is increased, more strain is induced inside the top SiN$_x$:H layer. Therefore, the inter-layer thickness should be as small as possible. In the present study, a PMMA thickness of 300 nm is used, which is a good approximation in order not to increase the induced strain intensively. With the decrease of the inter-layer (PMMA) modulus, the induced strain also decreases. This shows that the inter-layer material should be soft compared to the inorganic barrier materials in order to develop a good barrier. In this case, the inter-layer material PMMA has a modulus of 3.1 GPa, which is considerably small compared to the SiN$_x$:H (297 GPa).

Fig. 5.11 (a) shows the Ca degradation test results after different number of bending cycles. The black curve corresponds to the initial Ca test result without any bending. After that, the samples are bent for 100 and 500 cycles respectively. The effect of bending on the lag-time is shown in Fig. 5.11 (b), which shows almost no change in lag-time even after 500 times of bending. Correspondingly, the WVTR of the samples shows no change after 500 times of bending (Fig. 5.11 (c)). The observations show that the hybrid structure can keep its moisture barrier properties even it is bent for several times. It is worth mentioning that, the mechanical flexibility of the inorganic-organic hybrid structure is much better compared to our other barrier structure (inorganic films with plasma surface treatment).
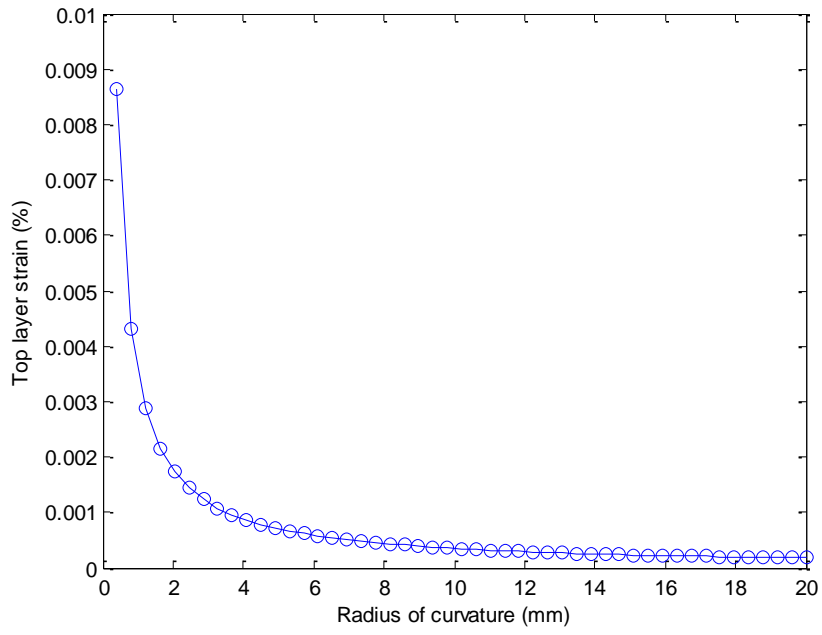
(a)
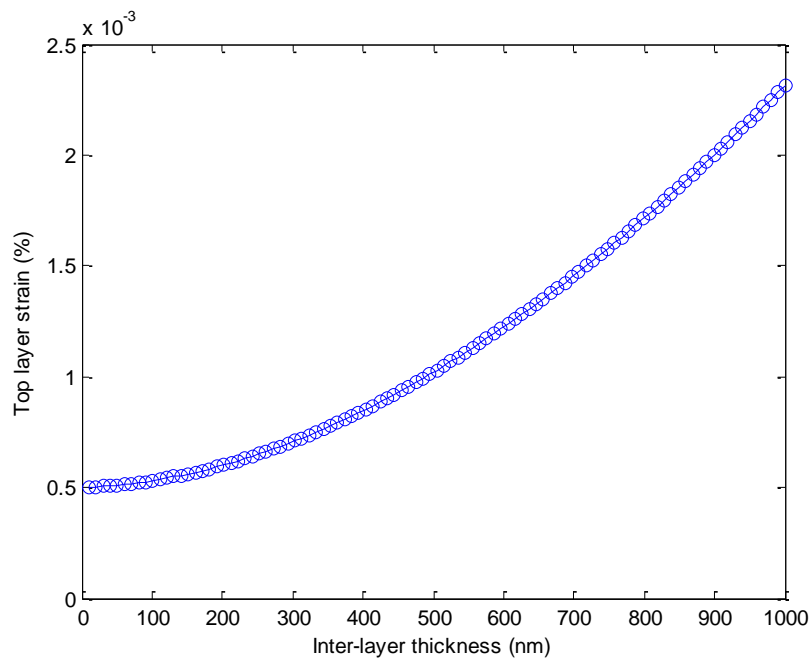
(b)
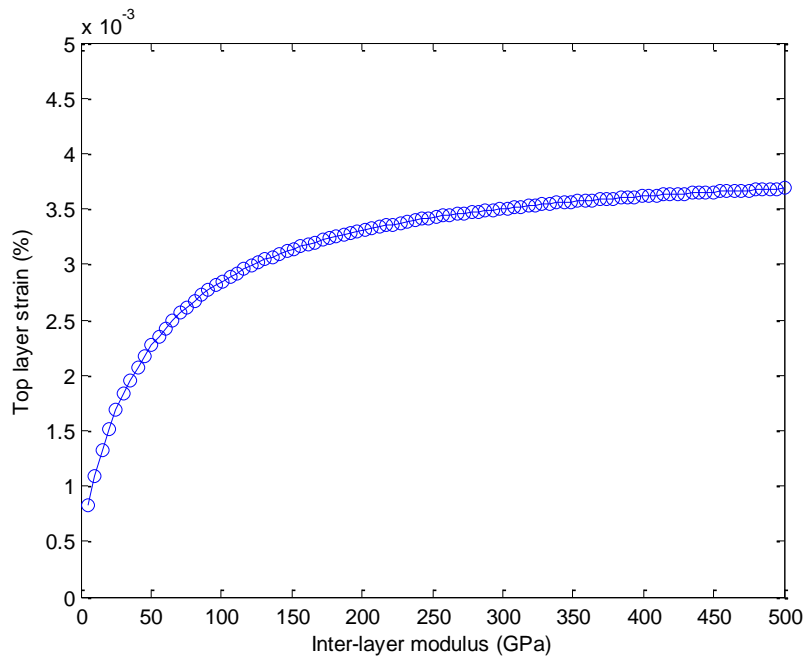
(c)

Fig. 5.10: Induced strain inside the top inorganic SiN$_x$:H layer with the variation of (a) the radius of curvature for a fixed inter-layer thickness and modulus; (b) inter-layer PMMA thickness for a fixed inter-layer thickness and radius of curvature and (c) inter-layer modulus for a fixed thickness and radius of curvature.
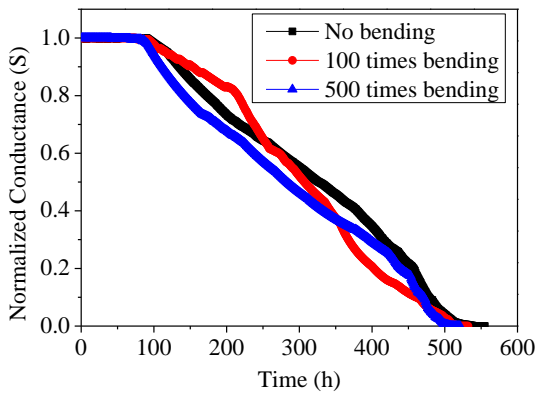

(a)
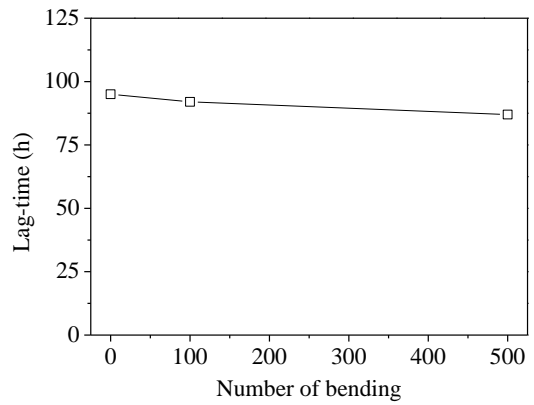
(b)
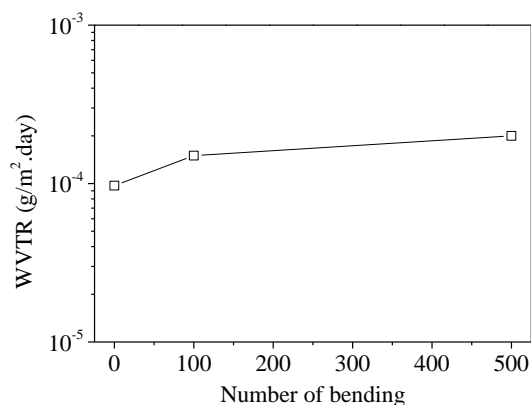
(c)

Fig. 5.11: (a) Evolution of normalized conductance of the Ca sensor with time for hybrid structure deposited on PET with different bending cycles. (b) Variation of lag-time with number of bending. (c) Variation of WVTR with number of bending.

5.6 DISCUSSIONS ON BARRIER IMPROVEMENT

The above observed results can be interpreted qualitatively considering the different permeation mechanisms and also processing conditions of hybrid structures. This conventional approach is a well-established barrier structure which is already commercialized. Usually the permeation barrier properties of the multilayer structures are explained by Ideal Laminate Theory (ILT) [209], which actually corresponds to a series resistance model. The tortuous path model is also often used to explain the permeation mechanism qualitatively. However, the impact of individual layers and the quality of individual materials are not well understood.

The defect density of the inorganic layers and the defect size are probably the most important factor which controls the water molecule permeation. In the present study, the impact of film quality in terms of its density and stoichiometry on the overall barrier property is well demonstrated. However, the lower barrier properties of MDECR grown films compared to HW-CVD films may not solely depend on the quality of the films, but depend also on the defects created by the inner wall flakes or dust particles, which is always the case for face-down deposition system. Since the MDECR is a face-down deposition system, it is expected that the films grown have larger defect density compared to face-up HW-CVD deposition system. Another technical problem arises from the sample handling. Since the samples had to be transferred between reactor and the spin-coater system, there is a large probability of dust particle contamination.

5.7 SUMMARY OF CHAPTER 5

i) The basic aim of this chapter is to fabricate ultrahigh barrier films using the conventional inorganic-organic hybrid structures. Two different deposition techniques (MDECR-PECVD and HW-CVD) are used to deposit the inorganic films, whereas the organic films are deposited by spin-coating technique.

ii) The quality of the inorganic film is quite critical in order to achieve high barrier performance. The density and the stoichiometry of the films affects largely on the overall permeation. Due to the higher density and stoichiometry of the HW-CVD deposited films, the barrier properties are better compared to MDECR-PECVD grown samples.

iii) The morphological property of the interlayer affects the overall barrier properties. The annealing of the organic layer helps to develop a smoother layer which in turns helps to deposit the subsequent inorganic layer with high structural quality.

iv) A minimum WVTR of 4.5×10^{-5} g/m^2.day is achieved for 7 interfaces combining 4 HW-CVD grown SiN$_x$:H films and 3 spin-coated PMMA films. This value is one order of magnitude higher than the requirement for organic LED devices. However, it can be utilized for the encapsulation of organic solar cells.

v) Mechanical property of the hybrid structure is investigated thoroughly in order for their utilization in flexible devices.

CHAPTER 6

ULTRA-BARRIER AND APPLICATION

6.1 INTRODUCTION

A perfect flexible encapsulation barrier should protect the degradable sensitive devices to attain a shelf-lifetime of thousands of hours in operation, as well as provide flexibility to the whole device system. The term ultra-barrier can be defined as a perfect barrier which has the lowest WVTR value providing flexibility to the system. In the present thesis, two separate encapsulation strategies have been developed and discussed which provided effective moisture barrier properties. Both strategies gave rise to an effective WVTR of $(4 - 7) \times 10^{-5}$ g/m^2.day. Although, the flexibility of the plasma treated multi-barrier was not efficient, the other strategy consisting of hybrid organic-inorganic layers showed excellent flexibility. The basic aim of this chapter is to combine the two strategies in order to achieve improved barrier properties as well as higher flexibility of the whole system. The last part of this chapter is devoted in fabricating real organic opto-electronic devices with the encapsulation barriers to extend their shelf life-times.

6.2 COMBINED BARRIER STRUCTURE

The two different strategies discussed in the thesis, have been merged to develop an ultra-barrier structure with the hope to reduce the water vapor diffusion drastically and capitalize the flexibility of the soft organic layer between two inorganic layers. The ultra-barrier structure is shown in Fig. 6.1. The structure consists of two 50 nm thick SiN$_x$:H single-layers deposited by HW-CVD system with the optimized growth conditions and both treated at the top surface by argon plasma with the optimized treatment conditions (400 mW/cm^2 power density, 25 mTorr pressure and 8 min duration). The single-layers are separated by a spin-coated 300 nm thick PMMA layer as a soft interlayer. The sample is deposited on clean PET substrate.
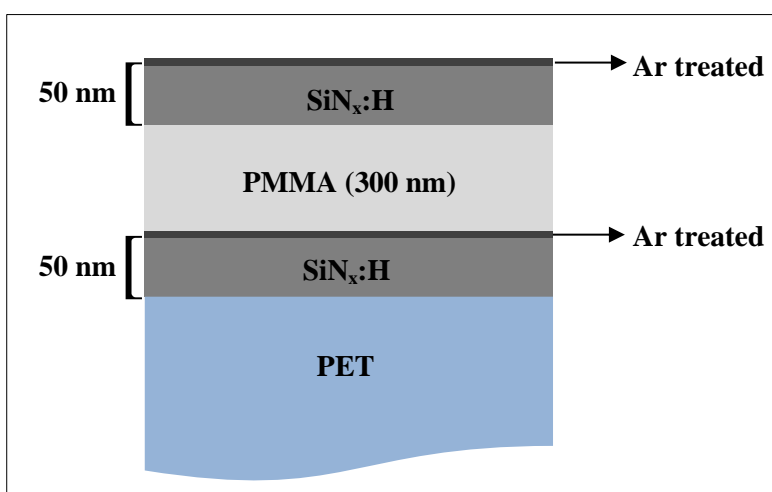
Fig. 6.1: Ultra-barrier structure (not to scale) consisting of two Ar plasma treated (30 eV) SiN$_x$:H single-layers (50 nm) separated by a soft PMMA (300 nm) layer deposited on PET substrate.

6.3 OPTICAL PROPERTIES

Optical transparency is an important parameter that defines the utilization of the barrier structure in real electronic devices. The transparency of the barrier structure has been evaluated using the integrating-sphere measurement. The transmittance (T) and the reflectance (R) of the sample are shown in Fig. 6.2. The sample is highly transparent (> 80%) in the visible region. Slight absorption below 400 nm is due to the plastic substrate itself as discussed before. This three layer barrier structure can be perfectly used as window layer for organic electronic device, because almost no absorption takes place in the visible region.
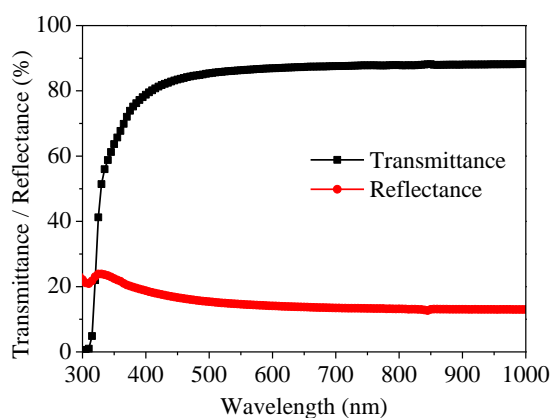
Fig. 6.2: Transmittance and reflectance of the barrier structure in the visible region.

6.4 BARRIER PROPERTIES

The barrier properties have been assessed with the electrical calcium degradation test method. The normalized conductance of the Ca sensor deposited on the other side of the barrier coated PET substrate is shown in Fig. 6.3. The usual kinks can be observed in the traces, which arise due to inhomogeneity inside the barrier as well as the substrate itself. The stable region of the evolution which defines the minimum time taken by the water molecules to reach the calcium sensor (lag-time) extends to ~420 h. This is the maximum lag-time value obtained in the present thesis. The degradation of the calcium sensor extends to more than 3 months period. From a linear slope of the degradation (just after the lag-time until the null value) the WVTR is assessed. A minimum WVTR of ~6 $\times$ 10^{-6} g/m^2.day has been obtained which is the lowest WVTR value achieved during the present thesis. This result confirms the positive effect of the combination of the two different encapsulation strategies and this tendency shows that if the number of layers is further increased, the barrier properties will be possibly improved further.
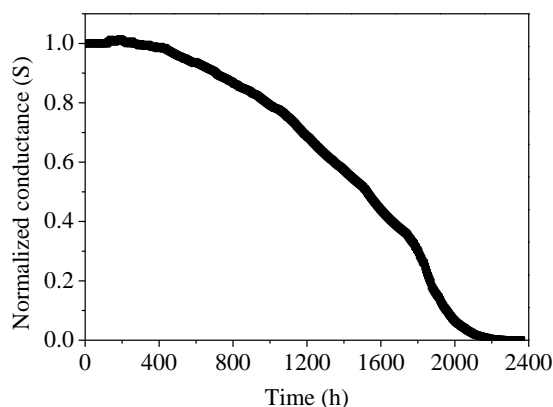
Fig. 6.3: Normalized conductance of the Ca sensor deposited on the barrier coated PET substrate.

6.5 MECHANICAL PROPERTIES

The mechanical flexibility of the barrier structure has been investigated by bending the permeation barrier with a radius of curvature of 5 mm for different cycles of bending. Ca degradation tests are performed on such bent samples in order to assess the impact of bending on the permeation barrier properties. Fig. 6.4 shows the Ca degradation test results relative to different bent samples after several bending cycles. Both the barrier properties (lag-time and WVTR) show almost no degradation even after 1000 bending cycles and thus confirming the viability of such barrier in real flexible applications.
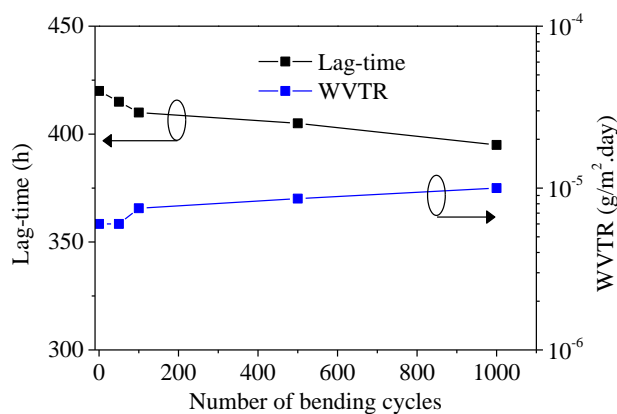
Fig. 6.4: Variation of lag-time and WVTR with number of bending cycles.

6.6 DISCUSSIONS

There are two different strategies that affect the permeation of water molecules through the whole barrier system. As discussed in chapter 4, the ionic bombardment with an energy of 30 eV impinging on the SiN_x:H film surface, rearrange the surface atoms locally and densify the surface up to few nanometer (1.2 nm) in depth. The rearrangement of surface atoms also makes the SiN_x:H surface smoother and possibly reduces the number of micro or nano-voids. This rearrangement of atoms blocks the propagation of water molecules through the SiN_x:H single-layers hindering the native nucleation centers which were existing at the top of the SiN_x:H layers. The organic (PMMA) interlayer in between two SiN_x:H single-layers provides a planarization effect and decouples the pinholes between two consecutive SiN_x:H layers. The combination of those two strategies makes the penetration path for water molecules much more complex and tortuous. Thus the effective diffusion path of water molecules becomes longer which in turn is responsible for the excellent permeation barrier properties.

6.7 APPLICATION

The encapsulation barrier structures used in this thesis have been used to test the encapsulation performance in real OLED devices. The OLED devices have been fabricated at the OLAE facility of LPICM and their shelf life-times have been assessed using the barriers. The two best encapsulation barriers obtained from the two different encapsulation strategies used in this thesis have been used here. Encapsulation with a glass cover has been used as a reference.

6.7.1 OLED DEVICE FABRICATION:

Glass cover or barrier
LiF (1.2 nm) / Al (100 nm)
TPBi (40 nm)
EML (20 nm)
TCTA (10 nm)
NPB (40 nm)
CuPc (10 nm)
ITO (100 nm)
Glass substrate

(a)

Glass cover or barrier
Epoxy resin
OLED

Glass substrate

(b)
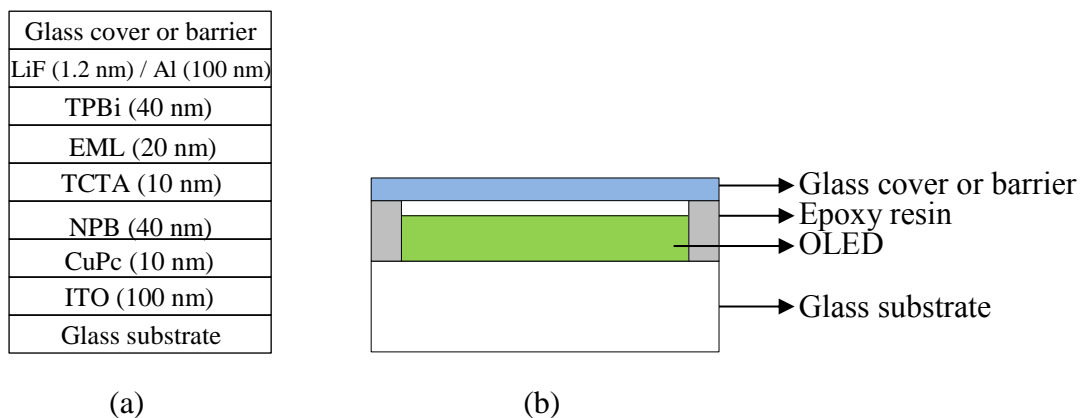
Fig. 6.5: (a) Typical OLED device structure used for testing the shelf life-time (dimensions not to scale). (b) Side view of the test structure.

The OLED devices used for testing the shelf life time are based on a multilayer structure and have been fabricated onto ITO coated glass substrates. The organic materials are deposited onto the ITO anode by sublimation under high vacuum ($< 10^{-6}$ Torr) at a rate of 0.2 – 0.3 nm/s. The structure of the device is shown in Fig. 6.5. In this device, ITO is used as the anode, CuPc (copper phtalocyanine) is the hole injecting layer, NPB (N, N'-di(1-naphtyl)-N,N'-diphenyl-[1,1'-biphenyl]-4,4'-diamine) is the hole-transporting layer, TCTA (4,4',4''-Tris(carbazol-9-yl)-triphenylamine) is the electron/exciton blocking layer, EML is the green light emissive layer host matrix doped by [Ir(ppy)3] (*fac*-tris(2-phenylpyridine)iridium), TPBI (1,3,5-Tris(1-phenyl- 1H-benzimidazol-2-yl)benzene) is both the electron transporting layer and the hole blocking layer and a thin film of lithium fluoride (electron injecting layer) covered with aluminum is the cathode. The entire devices are fabricated in the same run without breaking the vacuum. In order to test the encapsulation performance, the top surface has been covered with either glass cover or encapsulating barrier coated PET using UV curable epoxy resin.

6.7.2 TESTING METHOD:

Three types of samples have been prepared to test the encapsulation performance. The as grown OLED sample (sample A) covered with a glass cover has been used as a reference sample since glass is supposed to be a perfect barrier. The other two samples (sample B and sample C) have been covered with the thin film barrier coated PET substrates.

Sample B   Stack of 5 SiN$_x$: H single layers each separated by Ar plasma treatment (30 eV), which gave rise to WVTR of 7×10^{-5} g/m^2.day (see chapter 4).

Sample C   Stack of 4 SiN$_x$: H single layers each separated by 300 nm PMMA layer, which gave rise to WVTR of 4×10^{-5} g/m^2.day (see chapter 5).

The luminance-current-voltage (*L-I-V*) characteristics of the devices have been measured with a regulated power supply combined with a multimeter and a 1 cm^2 area silicon calibrated photodiode. The spectral emissions have been recorded with a Spectra Scan PR650 spectrophotometer. All the measurements have been performed at room temperature and at ambient atmospheric conditions. The bias current was set prior to the data collection in order to fix the OLED intensity at around 1000 cd/m^2.

6.7.3 RESULTS AND DISCUSSIONS

The *L-I-V* characteristics of the as grown and the encapsulated OLED devices measured directly after preparation are shown in Fig. 6.6. There are no significant differences in the electro-optical device characteristics of the as grown and the encapsulated OLED devices. From this initial result, we can conclude that there is no deterioration of the OLED characteristics even with encapsulation.

To verify the quality of the encapsulation layers, lifetime tests are carried out in constant current mode at a starting luminance of 1000 cd/m^2. We set the current density at 3 mA/cm^2 to measure the luminance and the bias voltage at a regular time interval.
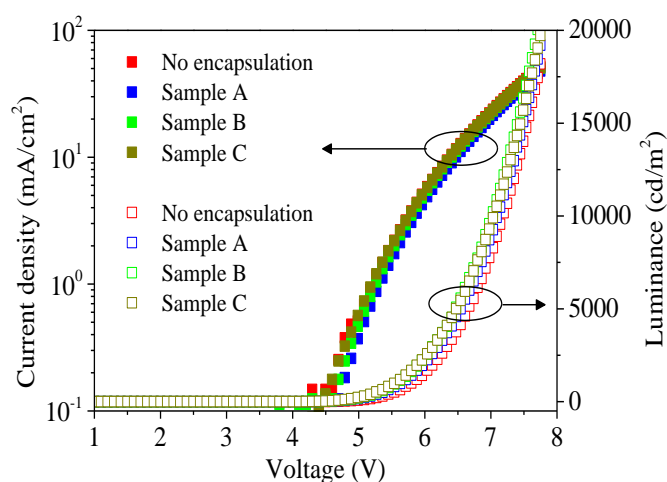
Fig. 6.6: *L-I-V* characteristics of as grown and encapsulated OLEDs measured directly after fabrication.
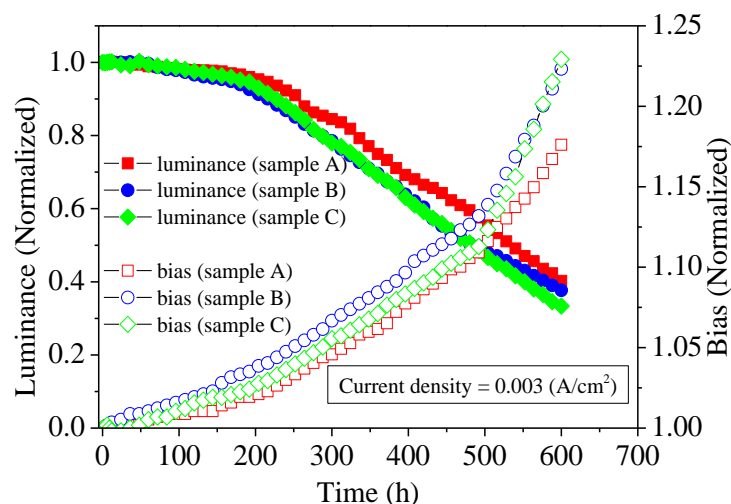
Fig. 6.7: Lifetime characteristics (luminance and bias voltage) of the encapsulated OLED devices (constant current mode).

The normalized luminance and the normalized bias voltage characteristics of the encapsulated OLED devices are shown in Fig. 6.7. The OLED device without any encapsulation degraded very rapidly (not shown in figure). Both characteristics show a constant luminance and bias values until 150 h which is similar to the lag-time values obtained for those encapsulation barriers. The sample with glass encapsulation also degrades after 150 h which is probably due to the residual gas volume in the test structures. This is the drawback of this test set-up. In actual situations, the barriers should be directly deposited on the OLED devices inside the vacuum chamber. The evolutions of the normalized luminance values for all the above mentioned samples vary in a similar manner until the lag-time value (150 h). Compared to the glass encapsulation, the OLEDs sealed with thin-film barriers show a pronounced degradation after 150 h. The half-lifetime of all the OLED devices are measured to be > 500 h, where the normalized luminance values degrade down to 0.5. From this test results, we can conclude that our barriers imposed from the two different encapsulation strategies show barrier properties nearly similar to hermetic sealing with glass encapsulation. This result is in coherence with the Ca test result. In order to improve the shelf-lifetime of the OLEDs, the barriers should be deposited directly on the OLED inside the vacuum chamber.

6.8 SUMMARY OF CHAPTER 6

i) An ultra-barrier layer structure has been developed combing two separate strategies as discussed in chapter 4 and in chapter 5.

ii) The two strategies being compatible to each other provided excellent moisture permeation barrier properties.

iii) A minimum WVTR of ~6×10^{-6} g/m^2.day and an extended lag-time of ~420 h have been obtained with this barrier structure.

iv) The barrier structure shows excellent flexibility even after 1000 bending cycles and thus confirming the viability of this barrier in flexible applications.

v) We demonstrated the encapsulation barrier properties of the thin-film barriers fabricated by two separate encapsulation strategies discussed in this thesis by utilizing the barriers on real OLED devices.

vi) The thin-film barriers show good encapsulation behavior which evolves, in the first approximation, in a similar way as the glass encapsulation. All the OLED samples showed an extrapolated shelf-lifetime of > 500 h under ambient atmospheric conditions.

CHAPTER 7

CONCLUSIONS AND PERSPECTIVES

Several constraints must be addressed before successful commercialization of flexible organic electronic devices like organic light emitting diode (OLED) and organic solar cells (OPV). The requirement of an effective flexible encapsulation barrier is a critical one. The objective of the research in this thesis has been the development of effective flexible encapsulation barrier layers for organic electronic devices. A variety of challenges prevail for the development of effective encapsulation barrier films such as, high optical transparency, low stress and low temperature deposition in order to be compatible with the underlying polymer substrates. The appropriate choice of the inorganic material as well as the deposition technique is critical in order to be congruent with all the above mentioned limitations. SiN_x:H film deposited by HW-CVD method was selected as the inorganic permeation barrier material. The HW-CVD deposition method is advantageous compared to the conventional plasma enhanced CVD deposition method because a lower concentration of H is incorporated inside the films, leading to higher density films. ALD is an attractive method for depositing barrier layers, even though the deposition rate is quite low. In order to synthesize the permeation barriers, two separate ways have been adopted: either fabricating inorganic / inorganic multilayer barriers separated by a plasma treated interface or fabricating inorganic / organic hybrid multilayer moisture barriers.

The efforts of the present work have been focused on two main items: Firstly, the development of a novel concept of encapsulation films other than the conventional approach of organic/inorganic hybrid layer structures was imperative: this concept has consisted of deposition of insulating multilayers separated by a plasma treatment. Secondly, the implementation of an accurate assessment of the quality of the deposited permeation barrier layers: the measurement of permeation through the use of the electrical calcium degradation test developed in our laboratory. This method is highly sensitive and it has allowed measuring the WVTR rate below 10^{-6} g/ m^2.day which is the requirement for highly sensitive OLED devices. The WVTR results obtained from various measurements shows the reproducibility and sensitivity (10^{-6} g/ m^2.day with a standard deviation of 3.7%) of this tool.

Transparent and quasi-stoichiometric silicon nitride thin films have been deposited by HW-CVD using silane and ammonia gaseous precursors, diluted in hydrogen, at a substrate temperature of 100 °C and with optimized growth parameters (filament current, flow rates, pressure). The evolution of

the lag-time and WVTR values with the increasing SiN$_x$:H single-layer thickness have been observed using the Ca degradation test in order to define the critical thickness of 50 nm. The critical thickness is the optimal thickness above which both quantities do not improve anymore. This experimental work has been followed by the development of multilayer stacks of SiN$_x$:H single-layers, where the thickness of each single-layer has been fixed at the critical thickness. Although the multilayer stack of SiN$_x$:H single-layers showed a slight improvement of the permeation barrier properties, the WVTR improvement was clearly insufficient. Thus, a supplementary process was absolutely necessary to reduce the diffusion of moisture drastically.

This process has been based on the combination of multilayer of SiN$_x$:H, separated by intermediate plasma treatments between the successive single-layers. The choices of Ar as species for the plasma, treatment parameters and their optimizations have been crucial. The arduous part of the plasma treatment was to modify the surface atom arrangement without disturbing the bulk. In order to accurately reach this goal, several energy threshold values were taken into consideration, like surface atomic displacement threshold, bulk atomic displacement threshold, sputtering energy threshold and implantation threshold, which collectively determines the maximum ion bombardment energy permissible for obtaining surface atomic rearrangement. The treatment power density, working pressure and treatment duration were varied independently keeping the other parameters constant for the combined effect of controlling the maximum ion bombardment energy on the film surface. The treatment parameters were carefully chosen so that the maximum ion bombardment energy slightly exceeded the bulk atomic displacement energy threshold, without damaging the barrier properties. Two extreme treatment conditions were shown: a low energy treatment which had no significant effect on the barrier properties and a high energy treatment which had deleterious effect on the barrier properties. It has been shown in this dissertation that the accurate choice of the energy range is noticeably limited in order to improve the performance.

Utilizing the optimized Ar treatment parameters between successive HW-CVD grown SiN$_x$:H single-layers, we reported extremely low WVTR values (7×10^{-5} g/m^2.day). Compared to the conventional procedures based on either hybrid structures of two different inorganic materials [84] or hybrid structures of organic/inorganic materials [69], our encapsulation method has the merit of reducing the efforts needed to get the permeation barrier quality of the same level as those obtained by hybrid structures. Several intermediate characterizations have been performed to qualify and quantify the results due to the ion induced surface modifications. Densification of the film up to few nanometers in depth, reduction of micro-voids and smoothening of the surface explain indirectly the improvement of barrier properties. Although, the measurement of the actual porosity of the films

without and with plasma treatment could make the explanation much more illuminating, it can be a future characterization work continuing this dissertation. The dissertation shows that the improvement of permeation barrier properties depends strongly on the precise range of low kinetic energy (< 40 eV) of the bombarding ions. Therefore, a future research direction of this work could be focused on studying the plasma treatment with tailored voltage waveform with a fixed maximum energy, without applying a large distribution of ion energy used in the present study. Further optimizations could be performed varying the bombarding energy step by step within the limit shown in the thesis. Moreover few experiments have been carried out during the thesis with a plasma treatment using low frequency plasma (100 kHz) and the permeation barrier properties improved slightly compared to RF plasma used in this study (see Appendix A). However, due to some technical issues, the optimizations were not performed thoroughly. Thus, it will be also interesting to study the plasma treatment effects using low frequency (100 kHz) plasma, a frequency low enough for the Ar^+ ions to follow the variations of the electric field of the wave, so that the ions can gain higher kinetic energy, thus decreasing the treatment duration.

The second part of this dissertation has been devoted to fabricating inorganic/organic hybrid layer structure which is the conventional approach of developing encapsulation films. The quality of the organic layer material is quite important in order to fabricate high quality barriers. The contribution of the present thesis was based on improving the barrier properties by improving the organic-inorganic interfaces, using simple deposition method (spin-coating) for the organic layer. Two different techniques, MDECR-PECVD and HW-CVD, were used to deposit the SiN_x:H single-layers and their performances were compared. It was concluded that density and stoichiometry of the inorganic material is critical to obtain efficient barrier layers. As a future research direction of this approach, the processing steps could be minimized and the quality of the organic layer as well as ability to deposit precise organic layer thickness should be taken into account. Spin-coating process with reduced annealing time, initiated CVD method, ink-jet printing and spraying methods can be some deposition solutions to process large area substrates.

Finally, it should be noted that the plasma treated inorganic multilayer structures or the organic-inorganic hybrid barrier structures are not distinctive encapsulation fabrication solutions. Efforts have been devoted to combine these two separate processes, which have drastic effect on the overall barrier performance (WVTR = 6×10^{-6} g/m^2.day) and showed better mechanical flexibility. However, the processing steps should be minimized in order to be attractive for successful commercialization.

Recently, graphene has shown permeation barrier properties towards atmospheric gases and this idea has led to some basic studies performed during this dissertation to fabricate hybrid barrier layers by combining commercially available monolayers of graphene and SiN_x:H single-layers (thickness < 50 nm). The barrier performance improved slightly and further studies are required to develop this method successfully (see Appendix B). Transparent hydrophobic clay can also be used as effective permeation barrier layers, which will be an unusual process other than the conventional approaches.

The performance of the encapsulation techniques have been evaluated on real organic electronic devices (OLEDs), which showed an extended shelf life-times for those devices. However for the successful commercialization, integration of encapsulation films on real devices is one of the major issues that should be solved in future research. When economically viable encapsulation solutions is integrated on highly efficient organic electronic devices, the flexible electronics is expected to overcome all the present device technologies.

REFERENCES

[1] (www.iea.org).

[2] N. Grossiord, J. M. Kroon, R. Andriessen, P. W.M. Blom, "Degradation mechanisms in organic photovoltaic devices", *Organic Electronics*, **13** (2012) 432-456.

[3] R. W. Bentley, "Global oil & gas depletion: an overview", *Energy Policy*, 30 (2002) 189-205.

[4] R. A. Kerr, "How Urgent Is Climate Change", *Science*, **318** (2007) 1230.

[5] A. Jäger-Waldau, *PV Status Report* 2003, European Commission (2003), EUR 20850 EN.

[6] W. A. Hermann, "Quantifying global energy resources, *Energy*, **31** (2006) 1685.

[7] J. Kalowekamo, E. Baker, "Estimating the manufacturing cost of purely organic solar cells", *Solar Energy*, **83** (2009) 1224-1231.

[8] G. Dennler, C. J. Brabec, Socio-economic I"mpact of Low Cost PV Technologies, in: C. J. Brabec, V. Dyakonov, U. Scherf (Eds.), Organic Photovoltaics: Materials, Device Physics and Manufacturing, Wiley VCH Verlag GmbH & Co., Weinheim, 2008.

[9] J. Schmidtke, "Commercial status of thin-film photovoltaic devices and materials", *Optics Express*, **18** (2010) A477-A486.

[10] C. K. Chiang, C. R. Fincher, Y. W. Park, A. J. Heeger, H. Shirakawa, E. J. Louis, S. C. Gau, A. G. MacDiarmid, "Electrical Conductivity in Doped Polyacetylene", *Phys. Rev. Lett*., **39** (1977) 1098.

[11] C. J. Brabec, J. A. Hauch, P. Schilinsky, C. Waldauf, "Production Aspects of Organic Photovoltaics and Their Impact on the Commercialization of Devices", *MRS Bulletin*, **30** (2005) 50-52.

[12] M. Stolka, "Organic Light Emitting Diodes (OLEDs) for General Illumination Update 2002", *Optoelectronics Industry Development Association*, Washington, DC 20036-4380, 2002.

[13] C. W. Tang, S. A. Vanslyke, "Organic electroluminescent diodes", *Appl. Phys. Lett*., **51** (1987) 913-915.

[14] B. Geffroy, P. le Roy, C. Prat, "Organic light-emitting diode (OLED) technology: materials, devices and display technologies", *Polym. Int*., **55** (2006) 572-582.

[15] J. H. Burroughes, D. D. C. Bradley, A. R. Brown, R. N. Marks, K. Mackey, R. H. Friend, P. L. Burns, A. B. Holmes, "Light emitting diodes based on conjugated polymers", *Nature*, **347** (1990) 539-541.

[16] (http://www.clubic.com/actualite-74135-sony-ecran-oled-flexible-16-couleurs.html).

[17] (http://newenergyandfuel.com/http:/newenergyandfuel/com/2011/05/24/new-record-set-for-flexible-solar-cells/).

[18]   J. S. Lewis, M. S. Weaver, "Thin-Film Permeation-Barrier Technology for Flexible Organic Light-Emitting Devices", *IEEE Journal of Selected Topics in Quantum Electronics*, **10** (January/February 2004) No.1.

[19]   D. Letian, Y. Jingbi, Y. Jun, C. Chun-Chao, H. Youjun, M. Seiichiro, M. Tom, E. Keith, L. Gang, Y. Yang, "Tandem polymer solar cells featuring a spectrally matched low-band gap polymer". *Nature Photonics*, **6** (3) (2012) 180.

[20]   J. Zhou, Y. Zuo, X. Wan, G. Long, Q. Zhang, W. Ni, Y. Liu, Z. Li, G. He, C. Li, B. Kan, M. Li, Y. Chen, "Solution processed and high performance organic solar cells using small molecules with a Benzodithiophene unit", *J. Am. Chem. Soc.*, **135** (2013) 8484.

[21]   Y. Liu, C. –C. Chen, Z. Hong, J. Gao, Y. (Michael) Yang, H. Zhou, L. Dou, G. Li, Y. Yang, "Solution processed small molecule solar cells : breaking the 10% power conversion efficiency", *Scientific Reports*, **3** (2013) 3356.

[22]   J. Morgado, R. H. Friend, F.Cacialli, "Environmental aging of poly (p-phenylenevinylene) based light emitting diodes", *Synt. Met.*, **114** (2000) 189-196.

[23]   D. G. J. Sutherland, J. A. Carlisle, P. Elliker, G. Fox, T. W. Hagler, I. Jimenez, H. W. Lee, K. Pakbaz, L. J. Terminello, S. C. Williams, F. J. Himpsel, D. K. Shuh, W. M. Tong, J. J. Jia, T. A. Callcott, D. L. Ederer, "Photo-oxidation of electro-luminescent polymers studied by core-level photoabsorption spectroscopy", *App. Phys. Lett.*, **68** (1996) 2046-2048.

[24]   R. Scurlock, B. Wang, P. Ogilby, J. Sheats, R.Clough, "Singlet oxygen as a reactive intermediate in the photo-degradation of an electroluminescent polymer", *J. Am. Chem. Soc.* **117** (1995) 10194.

[25]   S. Kumar, A. Biswas, V. Shukla, A. Awasthi, R. Anand, J. Narain, "Application of spectroscopic ellipsometry to probe the environmental and photo-oxidative degradation of poly(p-phenylene vinylene) (PPV)", *Synth. Met.*, **139** (2003) 751.

[26]   H. Neugebauer, C. Brabec, J. Hummelen, N. Sariciftci, "Stability and photo-degradation mechanisms of conjugated polymer/fullerene plastic solar cells", *Sol. Energy. Mat. Sol. Cells.*, **61** (2000) 35.

[27]   F. Padinger, T. Fromherz, P. Denk, C.J. Brabec, J. Zettner, T. Hierl, N.S. Sariciftci, "Degradation of bulk heterojunction solar cells operated in an inert gas atmosphere: a systematic study", *Synth. Met.*, **121** (2001) 1605-1606.

[28]   Y. C. Han, C. Jang, K. J. Kim, K. C. Choi, K. H. Jung, B. S. Bae, "The encapsulation of an organic light emitting diode using organic-inorganic hybrid materials and MgO", *Organic Electronics*, **12** (2011), 609-613.

[29]   S. Y. Kim, K. Y. Kim, Y. H. Tak, J. L. Lee, "Dark spot formation mechanism in organic light emitting diode", *Appl. Phys. Lett.*, **89** (2006), 132108.

[30]   P. Melpignano, A. Baron-Toaldo, V. Biondo, S. Priante, R. Zamboni, M. Murgia, S. Caria, L. Gregoratti, A. Barinov, M. Kiskinova, "Mechanism of dark-spot degradation of organic light emitting devices", *Appl. Phys. Lett*., **86** (2005) 041105.

[31]   Y. F. Liew, H. Aziz, N. X. Hu, H. S. O. Chan, G. Xu, Z. Popovic, "Investigation of the sites of dark spots in organic light emitting devices", *Appl. Phys. Lett*., **77** (2000) 2650.

[32]   Jay Lewis, "Material challenges for flexible organic devices", *Materials Today*, **9** (2006) 4.

[33]   F. Papadimitrakopoulos, X. –M. Zhang, K. A. Higginson, "Chemical and Morphological Stability of Aluminum Tris (8-Hydroxyquinoline) (Alq_3): Effects in Light-Emitting Devices", *IEEE J. Sel. Topics in Quantum Electronics*, **4** (1998) 1.

[34]   P. E. Burrows, G. L. Graff, M. E. Gross, P. M. Martin, M. Hall, E. Mast, C. C. Bonham, W. D. Bennett, L. A. Michalski, M. S. Weaver, J. J. Brown, D. Fogarty, L. S. Sapochak, "Gas permeation and lifetime tests on polymer-based barrier coatings", *Proc. SPIE*, **4105** (2001) 75-83.

[35]   M. S. Weaver, L. A. Michalski, K. Rajan, M. A. Rothman, J. A. Silvernail, J. J. Brown, P. E. Burrows, G. L. Graff, M. E. Gross, P. M. Martin, M. Hall, E. Mast, C. Bonham, W. Bennett, M. Zumhoff, "Organic light emitting devices with extended operating lifetimes on plastic substrates", *Appl. Phys. Lett*., **81** (2002) 2929-2931.

[36]   E. Guenther, R. S. Kumar, F. Zhu, H. Y. Low, K. S. Ong, M. D. Auch, K. Zhang, S. –J. Chua, "Building blocks for ultra-thin, flexible organic electroluminescent devices", *Proc. SPIE*, **4464** (2002) 23-33.

[37]   G. Nisato, P. C. P. Bouten, P. J. Slikkerveer, W. D. Bennett, G. L. Graff, N. Rutherford, L. Wiese, "Evaluating high performance diffusion barriers: The calcium test", *Proc. Int. Display workshop/Asia Display*, (2001) 1435-1438.

[38]   G. Nisato, M. Kuilder, P. Bouten, "Thin film encapsulation for OLEDs: Evaluation of multilayer barriers using the Ca test", *Proc. Soc. Inform. Display Symp. Dig. Tech. Papers*, **34** (2003) 550-553.

[39]   L. C. Olsen, S. N. Kundu, C. C. Bonham, M.Gross, "Barrier coatings for CIGSS and CdTe cells", *Photovoltaics Specialists Conference*, January 3–7, 2005, *Conference Record of the Thirty-First IEEE* (2005) 327.

[40]   J. Fahlteich, M. Fahland, W. Schönberger, N. Schiller, "Permeation barrier properties of thin oxide films on flexible polymer substrates", *Thin Solid Films*, **517** (2009) 3075-3080.

[41]   International Electrotechnical Commission, IEC-61646- Thin film terrestrial photovoltaic (PV) modules- design qualification and type approval (1997).

[42] G. Dennler, C. Lungenschmied, H. Neugebauer, N.S. Sariciftci, M. Latrèche, G. Czeremuszkin, M.R. Wertheimer, "A new encapsulation solution for flexible organic solar cells", *Thin Solid Films*, **511-512** (2006) 349-353.

[43] J. A. Hauch, P. Schilinsky, S. A. Choulis, S. Rajoelson, C. J. Brabec, "The impact of water vapor transmission rate on the lifetime of flexible polymer solar cells", *Appl. Phys. Lett*., **93** (2008) 103306.

[44] S. Cros, R. de Bettignies, S. Berson, S. Bailly, P. Maisse, N. Lemaitre, S. Guillerez, "Definition of encapsulation barrier requirements: A method applied to organic solar cells", *Sol. Energy Mater. Sol. Cells*, **95** (2011) S65.

[45] K. Zhang, F. R. Zhu, C. H. A. Huan, A. T. S. Wee, "Indium tin oxide films prepared by radio frequency magnetron sputtering method at a low processing temperature", *Thin Solid Films*, **376** (2000) 255-263.

[46] S. Angiolini, M. Avidano, C. Bracco, C. Barlocco, R. Bracco, J. Bacskay, J. –H. Lipian, P. S. Neal, L. S. Rhodes, R. A. Shick, X. –M. Zhao, G. Freeman, "High performance plastic substrates for flexible flat panel display", *Society For Information Display, Digest of Technical Papers*, 1-4, 2000.

[47] AQUATRAN Model 1, Mocon, Minneapolis MN 55428, 2006.

[48] C. Charton, N. Schiller, M. Fahland, A. Hollander, A. Wedel, K. Noller, "Development of high barrier films on flexible polymer substrates", *Thin Solid Films*, **502** (2006) 99-103.

[49] J. –S. Park, H. Chae, H. K. Chung, S. I. Lee, "Thin film encapsulation for flexible AM-OLED: a review", *Semicond. Sci. Technol*., **26** (2011) 034001.

[50] R. S. Kumar, M. Auch, E. Ou, E. Guenther, S. –J. Chua, "Low moisture permeation measurement through polymer substrates for organic light emitting devices", *Thin Solid Films*, **417** (2002) 120-126.

[51] R. Paetzold, A. Winnacker, D. Henseler, V. Cesari, K. Heuser, "Permeation rate measurements by electrical analysis of calcium corrosion", *Rev. Sci. Instrum*., **74** (2003) 5147.

[52] P. F. Carcia, R. S. McLean, M. H. Reilly, M. D. Groner, S. M. George, "Ca test of Al_2O_3 gas diffusion barriers grown by atomic layer deposition on polymers", *Appl. Phys. Lett*., **89** (2006) 031915.

[53] S. Cros, M. Firon, S. Lenfant, P. Trouslard, L. Beck, "Study of thin calcium electrode degradation by ion beam analysis", *Nuclear Instruments and Methods in Physics Research B*, **251** (2006) 257.

[54] J. H. Choi, Y. M. Kim, Y. W. Park, J. W. Huh, B. K. Ju, I. S. Kim, H. N. Hwang, "Evaluation of gas permeation barrier properties using electrical measurements of calcium degradation", *Rev. Sci. Instrum*., **78** (2007) 064701.

[55]   P. F. Carcia, R. S. McLean, M. H. Reilly, "Permeation measurements and modeling of highly defective Al_2O_3 thin films grown by atomic layer deposition on polymers", *Appl. Phys. Lett*., **97** (2010) 221901.

[56]   M. O. Reese, A. A. Dameron, M. D. Kempe, "Quantitative calcium resistivity based method for accurate and scalable water vapor transmission rate measurement", *Rev. Sci. Instrum.*, **82** (2011) 085101.

[57]   S. Schubert, H. Klumbies, L. Muller-Meskamp, K. Leo, "Electrical calcium test for moisture barrier evaluation for organic devices ", *Rev. Sci. Instrum*., **82** (2011) 094101.

[58]   E. H. Song, Y. W. Park, J. H. Choi, T. H. Park, J. W. Jeong, H. Ju. Choi, B. K. Ju, "The flexible Ca-test: An improved performance in a gas permeability measurement system", *Rev. Sci. Instrum.*, **82** (2011) 054702.

[59]   M. D. Kempe, M. O. Reese, A. A. Dameron, "Evaluation of the sensitivity limits of water vapor transmission rate measurements using electrical calcium test", *Rev. Sci. Instrum*., **84** (2013) 025109.

[60]   S. Majee, M. F. Cerqueira, D. Tondelier, B. Geffroy, Y. Bonnassieux, P. Alpuim, J. E. Bourée, "The Effect of Argon Plasma Treatment on the Permeation Barrier Properties of Silicon Nitride Layers", *Surf. Coatings Technol*., **235** (2013) 361.

[61]   S. Majee, M. F. Cerqueira, D. Tondelier, B. Geffroy, Y. Bonnassieux, P. Alpuim, J. E. Bourée, "Influence of Low Energy Ar Plasma Treatment on the Moisture Barrier Performance of Hot Wire -CVD Grown SiN_x Multilayers", *Japaneese Journal of Applied Physics*, **53** (2014) 05FM05.

[62]   S. Majee, M. F. Cerqueira, D. Tondelier, B. Geffroy, Y. Bonnassieux, P. Alpuim, J. E. Bourée, "Permeation barrier performance of HW-CVD grown silicon nitride films treated by argon plasma", *Thin Solid Films*, (accepted).

[63]   M. D. Groner, S. M. George, R. S. McLean, P. F. Carcia, "Gas diffusion barriers on polymers using Al_2O_3 atomic layer deposition", *Appl. Phys. Lett*., **88** (2006) 051907.

[64]   A. R. Coulter, R. A. Deeken, G. M. Zentner, "Water permeability in poly(ortho ester)s", *J. Membrane Sci*., **65**, 269.

[65]   C. M. Hansen, L. Just, "Water transport and condensation in fluoro-polymer films", *Prog. Org. Coat*., **142** (2001) 167–178.

[66]   W. Prins, J. J. Hermans, "Theory of Permeation through Metal Coated Polymer Films", *J. Phys. Chem*., **63** (1959) 716.

[67]   T. A. Beu, P.-V. Mercea, D. Silipas, "Gas transport through metallized polymer membranes", *Mater. Chem. Phys*., **26** (1990) 309.

[68]   S. da Silva Sobrinho, G. Czeremuszkin, M. Latrèche, M. R. Wertheimer, "Defect-permeation correlation for ultrathin transparent barrier coatings on polymers", *J. Vac. Sci. Technol. A*, **18** (2000) 149.

[69]   D. Spee, K. van der Werf, J. Rath, R. Schropp, "Excellent organic/inorganic transparent thin film moisture barrier entirely made by hot wire CVD at 100 °C", *Phys. Status Solidi: Rapid Res. Lett.*, **6** (2012) 151–153.

[70]   A. P. Roberts, B. M. Henry, A. P. Sutton, C. R. M. Grovenor, G. A. D. Briggs, T. Miyamoto, M. Kano, Y. Tsukahara, M. Yanaka, "Gas permeation in silicon-oxide / polymer (SiO_x / PET) barrier films: role of the oxide lattice, nano-defects and macro-defects", *Journal of Membrane Science*, **208** (2002) 75-88.

[71]   Yves Leterrier, "Durability of nanosized oxygen-barrier coatings on polymers", *Progress in Materials Science*, **48** (1) (2003) 1-55.

[72]   A. S. da Silva Sobrinho, M. Latrèche, G. Czeremuszkin, J. E. Klemberg-Sapieha, and M. R. Wertheimer, "Transparent barrier coatings on polyethylene terephthalate by single and dual frequency plasma enhanced chemical vapour deposition", *J. Vac. Sci. Technol. A*, **16** (1998) 3190.

[73]   W. Huang, X. Wang, M. Sheng, L. Xu, F. Stubhan, L. Luo, T. Feng, X. Wang, F. Zhang, S. Zou, "Low temperature PECVD SiN_x films applied in OLED packaging", *Materials Science and Engineering: B*, **98** (2003) 248-254.

[74]   P. Mandlik, J. Gartside, L. Han, I-C. Cheng, S. Wagner, J. A. Silvernail, R. –Q. Ma, M. Hack, J. J. Brown, "A single layer permeation barrier for organic light emitting displays", *Appl. Phys. Lett.*, **92** (2008) 103309.

[75]   S. –H. K. Park, J. Oh, C. –S. Hwang, J. –I. Lee, Y. S. Yang, H. Y. Chu, K. –Y. Kang., "Ultra-thin film encapsulation of organic light emitting diode on a plastic substrate", *ETRI Journal*, **27** (2005) 545-550.

[76]   W. J. Potscavage, S. Yoo, B. Domercq, B. Kippelen, "Encapsulation of pentacene/ C_{60} organic solar cells with Al_2O_3 deposited by atomic layer deposition", *Appl. Phys. Lett.*, **90** (2007) 253511.

[77]   A. P. Ghosh, L. J. Gerenser, C. M. Jarman, and J. E. Fornalik, "Thin film encapsulation of organic light emitting devices", *Appl. Phys. Lett.*, **86** (2005) 223503.

[78]   Y. –Q. Yang, Y. Duan, P. Chen, F. –B. Sun, Y. –H. Duan, X. Wang, D. Yang, "Realization of Thin Film Encapsulation by Atomic Layer Deposition Al_2O_3 at Low Temperature", *J. Phys. Chem. C*, **117**(39) (2013) 20308-20312.

[79]   S. –W. Seo, E. Jung, C. Lim, H. Chae, S. M. Cho, "Moisture permeation through ultrathin TiO_2 films grown by atomic layer deposition", *Appl. Phys. Exp.*, **5** (2012) 035701.

[80]   H. Matsumura, "Silicon nitride produced by catalytic chemical vapor deposition method", *J. Appl. Phys.*, **66** (1989) 3612.

[81]   H. Matsumura, H. Umemoto, A. Izumi, A. Masuda, "Recent progress of Cat-CVD research in Japan—bridging between the first and second Cat-CVD conferences", *Thin Solid Films*, **430** (2003) 7.

[82]   A. Masuda, M. Totsuka, T. Oku, R. Hattori, H. Matsumura, "Highly moisture-resistive silicon nitride films prepared by catalytic chemical vapor deposition and application to gallium arsenide field-effect transistors", *Vacuum*, **74** (2004) 525.

[83]   A. Heya, T. Niki, Y. Yonezawa, T. Minamikawa, S. Muroi, A. Izumi, A. Masuda, H. Umemoto, H. Matsumura, "Highly Moisture-Resistive SiN_x Films Prepared by Catalytic Chemical Vapor Deposition", *Jpn. J. Appl. Phys.*, **43** (2004) 1362.

[84]   Y. Ogawa, K. Ohdaira, T. Oyaidu, H. Matsumura, "Protection of organic light-emitting diodes over 50 000 hours by Cat-CVD SiN_x/SiO_xN_y stacked thin films", *Thin Solid Films*, **516** (2008) 611.

[85]   A. Heya, T. Minamikawa, T. Niki, S. Minami, A. Masuda, H. Umemoto, N. Matsuo, H. Matsumura, "Cat-CVD SiN passivation films for OLEDs and packaging", *Thin Solid Films*, **516** (5) (2008) 553-557.

[86]   P. Alpuim, L. M. Gonçalves, E. S. Marins, T .M. R. Viseu, S. Ferdov, J. E. Bourée, "Deposition of silicon nitride thin films by hot-wire CVD at 100 °C and 250 °C", *Thin Solid Films*, **517** (2009) 3503.

[87]   H. –K. Kim, M. S. Kim, J. –W. Kang, J. –J. Kim, M. –S. Yi, "High-quality thin-film passivation by catalyser-enhanced chemical vapour deposition for organic light-emitting diodes", *Appl. Phys. Lett.*, **90** (2007) 013502.

[88]   K. Saitih, R. S. Kumar, S. Chua, A. Masuda, H. Matsumura, "Estimation of moisture barrier ability of thin SiN_x single layer on polymer substrates prepared by Cat-CVD method", *Thin Solid Films*, **516** (2008) 607-610.

[89]   H. Nakayama, M. Ito, "Super H_2O-barrier film using Cat-CVD (HWCVD)-grown SiCN for film based electronics", *Thin Solid Films*, **519** (2011) 4483-4486.

[90]   C.C. Chiang, D.S. Wuu, H.B. Lin, Y.P. Chen, T.N. Chen, Y.C. Lin, C.C. Wu, W.C. Chen, T.H. Jaw, R.H. Horng, "Deposition and permeation properties of SiN_X/parylene multilayers on polymeric substrates", *Surface and Coatings Technology*, **200** (2006) 5843-5848.

[91]   T. –N. Chen, D. –S. Wuu, C. –C. Wu, C. –C. Chiang, Y. –P. Chen, R. –H. Horng, "Improvements of Permeation Barrier Coatings Using Encapsulated Parylene Interlayers for Flexible Electronic Applications", *Plasma Processes and Polymers*, **4** (2007) 180.

[92]   A. B. Chwang, M. A. Rothman, S. Y. Mao, R. H. Hewitt, M. S. Weaver, J. A. Silvernail, K. Rajan, M. Hack, J. J. Brown, X. Chu, L. Moro, T. Krajewski, N. Rutherford, "Thin film encapsulated flexible organic electroluminescent displays", *Appl. Phys. Lett.*, **83** (2003) 413.

[93]   T. W. Kim, M. Yan, A. G. Erlat, P. A. McConnelee, M. Pellow, J. Deluca, T. P. Feist, A. R. Duggal, M. Schaepkens, "Transparent hybrid inorganic/organic barrier coatings for plastic organic light emitting diode substrates", *J. Vac. Sci. Technol. A*, **23** (2005) 971.

[94]   M. Yan, T. Wonkim, A. G. Erlat, M. Pellow, D. F. Foust, J. Liu, M. Schaepkens, C. M. Heller, P. A. McConnelee, T. P. Feist, A. R. Duggal, "A transparent, high barrier and high heat substrate for organic electronics", *Proc. IEEE*, **93** (2005) 1468.

[95]   S. Ramadas, "Ultra-High-Barrier Films for Solar, Display and Plastic Electronics Applications", *Future Photovoltaics*, August 2011.

[96]   K. Akedo, A. Miura, H. Fujikawa, Y. Taga, "Plasma-CVD SiN_x / plasma-polymerized CN_x:H multi-layer passivation films for organic light emitting diodes", *Proc. Soc. Inform. Display Symp., Dig. Tech. Papers*, **34** (2003) 559-561.

[97]   C. Lungenschmied, G. Dennler, H. Neugebauer, S. N. Sariciftci, M. Glatthaar, T. Meyer, A. Meyer, "Flexible, long-lived, large-area, organic solar cells", *Solar Energy Materials and Solar Cells*, **91** (2007) 379-384.

[98]   A. Yoshida, A. Sugimoto, T. Miyadera, S. Miyaguchi, "Organic light emitting devices on polymer substrates", *J. Photopolymer Sci. Technol.*, **14** (2001) 327-332.

[99]   S. –W. Seo, E. Jung, H. Chae, S. M. Cho, "Optimization of Al_2O_3/ZrO_2 nanolaminate structure for thin film encapsulation of OLEDs", *Organic Electronics*, **13** (2012) 2436-2441.

[100] S. –W. Seo, H. Chae, S. J. Seo, H. K. Chung, S. M. Cho, "Extremely bendable thin-film encapsulation of organic light emitting diodes", *Appl. Phys. Lett.*, **102** (2013) 161908.

[101] E. Kim, Y. Han, W. Kim, K. C. Choi, H. –G. Im, B. –S. Bae, "Thin film encapsulation for organic light emitting diodes using a multi-barrier composed of MgO prepared by atomic layer deposition and hybrid materials", *Organic Electronics*, **14** (2013) 1737-1743.

[102] M. Schaepkens, T. W. Kim, A. G. Erlat, M. Yan, K. W. Flanagan, C. M. Heller, P. A. McConnelee, "Ultrahigh barrier coating deposition on polycarbonate substrates", *J. Vac. Sci. Technol. A*, **22** (2004) 1716.

[103] A. Hofrichter, P. Bulkin, B. Drévillon, "Plasma enhanced chemical vapour deposition of SiO_xN_y in an integrated distributed electron cyclotron resonance reactor", *Appl. Surf. Sci.*, **142** (1999) 447.

[104] R. Botha, B. Haj Ibrahim, P. Bulkin, B. Drévillon, "Deposition of dielectrics using a matrix distributed electron cyclotron resonance plasma enhanced chemical vapor deposition system", *Thin Solid Films*, **515** (2007) 7594–7597.

[105] R. Botha, *Ph.D. thesis*, Ecole Polytechnique, France, 2008. (http://tel.archives-ouvertes.fr/docs/00/50/37/45/PDF/Botha.pdf).

[106] M. Yasaka, "X-ray thin film measurement techniques", *The Rigaku Journal*, **26** (2010) 2.

[107] L. G. Parratt, "Surface studies of solids by total reflection of X-rays", *Phys. Rev.*, **95** (1954) 2.

[108] S. W. Schmitt, G. Gamez, V. Sivakov, M. Schubert, S. H. Christiansen, J. Michler, "Chemical and optical characterisation of atomic layer deposition aluminium doped ZnO films for photovoltaics by glow discharge optical emission spectrometry", *J. Anal. At. Spectrom.*, **26** (2011) 822-827.

[109] B. Ber, P. Bábor, P.N. Brunkov, P. Chapon, M.N. Drozdov, R. Duda, D. Kazantsev, V.N. Polkovnikov, P. Yunin, A. Tolstogouzov, "Sputter depth profiling of Mo/B4C/Si and Mo/Si multilayer nanostructures: A round-robin characterization by different techniques", *Thin Solid Films,* **540** (2013) 96–105.

[110] B. Drévillon, "Phase modulated ellipsometry from the ultraviolet to the infrared: In situ application to the growth of semiconductors", *Prog. Cryst. Growth Char. Mat.*, **27** (1993) 1.

[111] R. Azzam, N. Bashara, "Ellipsometry and polarized light", North Holland Personal Library (1970).

[112] S.N. Jasperson, D.K. Burge, R.C. O'Handley, "A modulated ellipsometer for studying thin film optical properties and surface dynamics", *Surface Science*, **27** (1973) 548.

[113] F. Abelès, "Recherches sur la propagation des ondes électromagnétiques sinusoïdales dans les milieux stratifiés. Application aux couches minces", *Annales de Physique*, **5** (1950) 596 (706).

[114] D.A.G. Bruggeman, "Berechnung verschiedener physikalischer Konstanten von heterogenen Substanzen", *Ann. Physik*, Leipzig, Germany, **24** (1935) 636.

[115] M. Stchakovsky, C. Caillaud, M. Foldyna, R. Ossikovski, E. Garcia-Caurel, "Polarimetric characterization of optically anisotropic flexible substrates", *Thin Solid Films*, **516** (2008) 1414-1418.

[116] S. W. Rutherford, D. D. Do, "Review of time lag permeation technique as a method for characterization of porous media and membranes", *Adsorption*, **3** (1997) 283-312.

[117] G. L. Graff, R. E. Williford, P. E. Burrows, "Mechanics of vapor permeation through multilayer barrier films: Lag time versus equilibrium permeation", *Journal of Applied Physics*, **96** (2004) 4.

[118] F.M.Smits, "Measurement of Sheet Resistivities with the Four-Point Probe," *The Bell System Technical Journal*, **37** (1958) 711-718.

[119] Z. Jia, M. B. Tucker, T. Li, "Failure mechanics of organic-inorganic multilayer permeation barriers in flexible electronics", *Composites Science and Technology*, **71** (2011) 365-372.

[120]   A. Masuda, H. Umemoto, H. Matsumura, "Various applications of silicon nitride by catalytic chemical vapor deposition for coating, passivation and insulating films", *Thin Solid Films*, **501** (2006) 149-153.

[121]   A. Shah, "Thin-film silicon solar cells", EPFL Press, Lausanne, Switzerland, 2010.

[122]   H. Matsumura, K. Ohdaira, "Recent situation of industrial implementation of Cat-CVD technology in Japan", *Thin Solid Films*, **516** (2008) 537-540.

[123]   S. Asari, T. Fujinaga, M. Takagi, M. Hashimoto, K. Saito, M. Harada, M. Ishikawa, "ULVAC research and development of Cat-CVD applications", *Thin Solid Films*, **516** (2008) 541-544.

[124]   T. Oku, Y. Kamo, M. Totsuka, "AlGaN/GaN HEMTs passivated by Cat-CVD SiN Film", *Thin Solid Films*, **516** (2008) 545-547.

[125]   T. Osono, A. Heya, T. Niki, M. Takano, T. Minamikawa, S. Muroi, A. Masuda, H. Umemoto, H. Matsumura, "High-rate deposition of SiN$_x$ films over 100 nm/min by Cat-CVD method at low temperatures below 80 °C", *Thin Solid Films*, **501** (2006) 55-57.

[126]   V. Verlaan, Z. S. Houweling, C. H. M. van der Werf, I. G. Romijn, A. W. Weeber, H. D. Goldbach, R. E. I. Schropp, "Deposition of device quality silicon nitride with ultra-high deposition rate (>7 nm/s) using hot-wire CVD", *Thin Solid Films*, **516** (2008) 533-536.

[127] C. Niikura, "Microcrystalline silicon films prepared by hot–wire assisted catalytic chemical vapor deposition: from analysis of film properties to realization of solar cells", *PhD thesis*, Ecole Polytechnique, Palaiseau Cedex, France (2002).

[128] K. Honda, K. Ohdaira, H. Matsumura, "Study of silicidation process of Tungsten catalyzer during silicon film deposition in catalytic chemical vapor deposition", *Jpn. J. Appl. Phys.*, **47** (2008) 3692-3698.

[129] J. E. Bourée, J. Guillet, C. Grattepain, J. Chaumont, "Quantitative analysis of tungsten, oxygen and carbon concentrations in the microcrystalline silicon films deposited by hot wire CVD", *Thin Solid Films*, **430** (2003) 110-115.

[130] P. A. T. T. van Veenendaal, O. L. J. Gijzeman, J. K. Rath, R. E. I. Schropp, "The influence of different catalyzers in hot-wire CVD for the deposition of polycrystalline silicon thin films", *Thin Solid Films*, **395** (2001) 194-197.

[131] A. Pflüger, C. Mukherjee, B. Schröder, "Optimization of process parameters in a large-area hot-wire CVD reactor for the deposition of amorphous silicon (a-Si:H) for solar cell application with highly uniform material quality", *Solar Energy Materials and Solar Cells*, **73** (2002) 321-337.

[132] A. Heya, *PhD Thesis*, Japan Advanced Institute of Science and Technology, Japan (2000).

[133] K. F. Feenstra, R. E. I. Schropp, W. F. van der Weg, "Deposition of amorphous silicon films by hot-wire chemical vapour deposition", *Journal of Applied Physics*, **85** (1999) 6843.

[134] E. C. Molenbroek, A. H. Mahan, A. Gallagher, "Mechanisms influencing "hot-wire" deposition of hydrogenated amorphous silicon", *J. Appl. Phys.*, **82** (1997) 1909.

[135] J. E. Bourée, S. R. Jadkar, S. Kasouit, R. Vanderhaghen, "Transport in microcrystalline silicon thin films deposited at low temperature by hot-wire chemical vapour deposition", *Thin Solid Films*, **501** (2006) 133-136.

[136] K. Yasui, H. Katoh, K. Komaki, S. Kaneda, "Amorphous SiN films grown by hot-filament chemical vapor deposition using monomethylamine", *Appl. Phys. Lett.*, **56** (1990) 898.

[137] J. L. Dupuie, E. Gulari, F. Terry, "The Low Temperature Catalyzed Chemical Vapor Deposition and Characterization of Silicon Nitride Thin Films", *J. Electrochem. Soc.,* **139(4)** (1992) 1151-1159.

[138] S. Okada, H. Matsumura, "Improved properties of silicon nitride films prepared by the catalytic chemical vapor deposition method", *Jpn. J. Appl. Phys.*, 36 (1997) 7035-7040.

[139] B. P. Nelson, Q. Wang, E. Iwaniczko, A. H. Mahan, R. S. Crandall, "The Influence of Electrons From the Filament on the Material Properties of Hydrogenated Amorphous Silicon Grown by the Hot-Wire Chemical Vapor Deposition Technique", *Mater. Res. Soc. Symp. Proc.*, **507** (1998) 927.

[140] Q. Wang, S. Ward, L. Gedvilas, B. Keyes, E. Sanchez, S. Wang, "Conformal thin-film silicon nitride deposited by hot-wire chemical vapor deposition", *Appl. Phys. Lett.*, **84** (2004) 338.

[141] D. Spee, "Thin film organic / inorganic multilayer gas barriers by hot wire and initiated CVD", *PhD thesis*, Utrecht University, The Netherlands, 2013.

[142] J. Doyle, R. Robertson, G. H. Lin, M. Z. He, A. Gallagher, "Production of high-quality amorphous silicon films by evaporative silane surface decomposition", *J. Appl. Phys.*, 64 (1988) 3215.

[143] A. Gallagher, "Some physics and chemistry of hot-wire deposition", *Thin Solid Films*, **395** (2001) 25.

[144] S. Tange, K. Inoue, K. Tonokura, M. Koshi, "Catalytic decomposition of SiH$_4$ on a hot filament", *Thin Solid Films*, **395** (2001) 42-46.

[145] Y. Nozaki, K. Kongo, T. Miyazaki, M. Kitazoe, K. Horii, H. Umemoto, A. Masuda, H. Matsumura, "Identification of Si and SiH in catalytic chemical vapor deposition of SiH$_4$ by laser induced fluorescence spectroscopy", *J. Appl. Phys.*, **88** (2000) 5437.

[146] W. Zheng, A. Gallagher, "Radical species involved in hotwire (catalytic) deposition of hydrogenated amorphous silicon", *Thin Solid Films*, **516** (2008) 929-939.

[147] H. L. Duan, S. F. Bent, "The influence of filament material on radical production in hot wire chemical vapor deposition of a-Si:H", *Thin Solid Films*, **485** (2005) 126-134.

[148] S. M. Gates, S. K. Kulkarni, "Kinetics of surface reactions in very low-pressure chemical vapor deposition of Si from SiH$_4$", *Appl. Phys. Lett*., **58** (1991) 2963.

[149] J. K. Holt, M. Swiatek, D. G. Goodwin, H. A. Atwater, "The aging of tungsten filaments and its effect on wire surface kinetics in hot-wire chemical vapor deposition", *J. Appl. Phys.*, **92** (2002) 4803-4808.

[150] H. L. Duan, G. A. Zaharias, S. F. Bent, "Probing radicals in hot wire decomposition of silane using single photon ionization", *Appl. Phys. Lett*., **78** (2001) 1784-1786.

[151] H. Umemoto, K. Ohara, D. Morita, T. Morimoto, M. Yamawaki, A. Masuda, H. Matsumura, "Radical species formed by the catalytic decomposition of NH$_3$ on heated W surfaces", *Jpn. J. Appl. Phys*., **42** (2003) 5315-5321.

[152] H. Umemoto, Y. Kashiwagi, K. Ohdaira, H. Kobayashi, K. Yasui, "Catalytic decomposition of NH$_3$ on heated Ru and W surfaces", *Thin Solid Films*, **519** (2011) 4429-4431.

[153] I. Langmuir, "The dissociation of hydrogen into atoms", *J. Am. Chem. Soc.*, *34 (7),* (1912) 860–877.

[154] H. Umemoto, K. Ohara, D. Morita, Y. Nozaki, A. Masuda, H. Matsumura, "Direct detection of H atoms in the catalytic chemical vapor deposition of the SiH$_4$/H$_2$ system", *J. Appl. Phys.*, **91** (2002) 1650.

[155] M. Heintze, R. Zedlitz, H. N. Wanka, M. B. Schubert, "Amorphous and microcrystalline silicon by hot wire chemical vapor deposition", *J. Appl. Phys*., **79** (1996) 2699.

[156] Q. Wang, "Hot-wire CVD amorphous Si materials for solar cell application", *Thin Solid Films*, **517** (2009) 3570-3574.

[157] N. Honda, A. Masuda, H. Matsumura, "Transport mechanism of deposition precursors in catalytic chemical vapor deposition studied using a reactor tube", *J. Non-Cryst. Solids*, **266-269** (2000) 100-104.

[158] S. M. Sze, K. K. Ng, "Physics of Semiconductor Devices", Third edition Wiley-Interscience, 2007, p. 791.

[159] H. C. Cheng, in: C.Y. Chang, S.M. Sze (Eds.), "ULSI Technology", International editions, McGraw-Hill, Singapore, 1996, p. 205, (Chapter 5).

[160] A. C. Diebold, "Handbook of Silicon Semiconductor Metrology", Marcel Dekker Inc., 2001, p. 758.

[161] J. W. Klaus, A. W. Ott, A. C. Dillon, S. M. George, "Atomic layer controlled growth of Si$_3$N$_4$ films using sequential surface reactions", *Surf. Sci*., **418** (1998) L14–L19.

[162] D. S. Katzer, D. J. Meyer, D. F. Storm, J. A. Mittereder, V. M. Bermudez, S. F. Cheng, G. G. Jernigan, S. C. Binari, "Ultra-high vacuum deposition and characterization of silicon nitride thin films", *J. Vac. Sci. Technol. B*, 30 (2012) 02B129.

[163] D. A. Minkov, "Method for determining the optical constants of a thin film on a transparent substrate", *J. Phys. D. Appl. Phys.*, **22** (1989) 199.

[164] V. Verlaan, A. D. Verkerk, W. M. Arnoldbik, C. H. M. van der Werf, R. Bakker, Z. S. Houweling, I. G. Romjin, D. M. Borsa, A. W. Weeber, S. L. Luxembourg, M. Zeman, H. F. W. Dekkers, R. E. I. Schropp, "The effect of composition on the bond structure and refractive index of silicon nitride deposited by HWCVD and PECVD", *Thin Solid Films*, **517** (2009) 3499-3502.

[165] A. G. Erlat, R. J. Spontak, R. P. Clarke, T. C. Robinson, P. D. Haaland, Y. Tropsha, N. G. Harvey, E. A. Vogler, "SiO$_x$ gas barrier coatings on polymer substrates: morphology and gas transport considerations", *J. Phys. Chem. B*, **103** (1999) 6047-6055.

[166] H. Chatham, "Oxygen diffusion barrier properties of transparent oxide coatings on polymeric substrates", *Surf. Coat. Technol.*, **78** (1996) 1-9.

[167] M. Yanaka, T. Miyamoto, Y. Tsukahara, N. Takeda, "In-situ observation and analysis of multiple cracking phenomena in thin glass layers deposited on polymer-films", *Compos Interfaces*, **6** (1999) 409.

[168] JT Felts, "Transparent gas barrier technologies", *J. Plast. Film Sheet*, **9** (1993) 201.

[169] P. Schrenk, T. Alfrey, "Some physical properties of multilayered films", *J. Polym. Eng. Sci.*, **9** (1969) 393.

[170] B. M. Henry, A. P. Roberts, C. R. M. Grovenor, A. P. Sutton, G. A. D. Briggs, Y. Tsukahara et al., "Microstructural characterization of transparent silicon oxide permeation barrier coatings on PET", *Proc. 41st Society of Vacuum Coaters Annual Conference*, Boston, April 18-23, SVC, **434** (1998).

[171] M. Yanaka, Y. Tsukahara, N. Nasako, N. Takeda, "Cracking phenomena of brittle films in nanostructure composites analysed by a modified shear lag model with residual strain", *J. Mater. Sci.*, **33** (1998) 2111.

[172] J Reece Roth, "Industrial Plasma Engineering, Volume 2: Applications to Nonthermal Plasma Processing", IOP publishing, Bristol & Philadelphia, 2001, p. 336.

[173] M. A. Lieberman, A. J. Lichtenberg, "Principles of plasma discharges and materials processing", Wiley-Interscience, New York, 1994.

[174] J. Robertson, "Diamond-like amorphous carbon", *Materials Science and Engineering R*, **37** (2002) 129-281.

[175] A. Metze, D. W. Ernie, H. J. Oskam, "The energy distribution of ions bombarding electrode surfaces in rf plasma reactors", *J. Appl. Phys.*, **65** (1989) 993.

[176] Ch. Wild, P. Koidl, "Structured ion energy distribution in radio frequency glowdischarge systems", *Appl. Phys. Lett.*, **54** (1989) 505.

[177] Ch. Wild, P. Koidl, "Ion and electron dynamics in the sheath of radiofrequency glow discharges", *J. Appl. Phys.*, **69** (1991) 2909.

[178] E. Spiller, "Smoothing of multilayer x-ray mirrors by ion polishing", *Appl. Phys. Lett.* **54** (1989) 2293.

[179] P. Sigmund, "Radiation Damage Processes in Materials", edited by C. H. S. Dupuy (Noordhoff, Leyden, 1975).

[180] E. Hotston, "Threshold energies for sputtering", *Nucl. Fusion*, **15** (1975) 544.

[181] G. S. Was, "Fundamentals of Radiation Materials Science", Springer, 2007.

[182] A. H. M. Smets, W. M. M. Kessels, M. C. M. van de Sanden, "The effect of ion-surface and ion-bulk interactions during hydrogenated amorphous silicon deposition", *J. Appl. Phys.*, **102** (2007) 073523.

[183] K. J. Boyd, D. Marton, J. W. Rabalais, S. Uhlmann, Th. Frauenheim, "Semiquantitative subplantation model for low energy ion interactions with solid surfaces. III. Ion beam homoepitaxy of Si", *J. Vac. Sci. Technol. A*, **16** (1998) 463.

[184] S. T. Picraux, E. Chason, T. M. Mayer, "Ion-assisted surface processing of electronic materials", *MRS Bulletin*, (June 1992) 52.

[185] L. A. Miller, D. K. Brice, A. K. Prinja, S. T. Picraux, "Molecular dynamics simulations of bulk displacement threshold energies in Si", *Radiation Effects and Defects in Solids*, **129** (1994) 127-131.

[186] Z. Q. Ma, Y. F. Zheng, B. X. Liu, "Ion-induced surface and bulk displacement threshold for epitaxial growth", *Phys. Stat. Sol. (a)*, **169** (1998) 239.

[187] K. Wittmaack, "Analytical description of the sputtering yields of silicon bombarded with normally incident ions", *Phys. Rev. B.*, **68** (2003) 235211.

[188] E. Chason, T. M. Mayer, "Low energy ion bombardment induced roughening and smoothing of SiO_2 surfaces", *Appl. Phys. Lett.*, **62** (1993) 363.

[189] T. M. Mayer, E. Chason, A. J. Howard, "Roughening instability and ion induced viscous relaxation of SiO_2 surfaces", *J. Appl. Phys.*, **76** (1994) 1633.

[190] M. A. Yanaka, Y. Kato, Y. Tsukahara, N. Takeda, "Effects of temperature on the multiple cracking progress of sub-micron thick glass films deposited on a polymer substrate", *Thin Solid Films*, **355-356** (1999) 337-342.

[191] Y. Leterrier, J. Andersons, Y. Pitton, J. A. E. Manson, "Adhesion of silicon oxide layers on poly(ethylene terephthalate). II: Effect of coating thickness on adhesive and cohesive strengths", *J. Polymer Sci. B: Polymer Phys.*, **35** (1997) 1463-1471.

[192] Z. Suo, E. Y. Ma, H. Gleskova, S. Wagner, "Mechanics of rollable and foldable film-on-foil electronics", *Appl. Phys. Lett.*, **74** (1999) 1177-1179.

[193] S. K. Park, J. I. Han, D. G. Moon, W. K. Kim, "Mechanical stability of externally deformed indium-tin-oxide films on polymer substrates", *Jpn. J. Appl. Phys.*, **42** (2003) 624-629.

[194] R. Vernhes, A. Amassian, J. E. Klemberg-Sapieha, L. Martinu, "Plasma treatment of porous SiN$_x$:H films for the fabrication of porous-dense multilayer optical filters with tailored interfaces", *J. Appl. Phys.*, **99** (2006) 114315.

[195] M. C. Desjonquères, D. Spanjaard, "Concepts in surface physics", Springer, Berlin Heidelberg, 1993.

[196] K. O. Bugaev, A. A. Zelenina, V. A. Volodin, "Vibrational spectroscopy of chemical species in silicon and silicon-rich nitride thin films", *International Journal of Spectroscopy*, (2012) doi: 10.1155/2012/281851.

[197] V. I. Belyi, L. L. Vasilyeva, A. S. Ginkover, et al., "Silicon Nitride in Electronics", Elsevier, New York, NY, USA, 1988.

[198] W. A. Lanford, M. J. Rand, "The hydrogen content of plasma-deposited silicon nitride," *Journal of Applied Physics*, **9**(4) (1978) 2473–2477.

[199] H. J. Stein, H. A. R. Wegener, "Chemically bound hydrogen in CVD Si3N4: dependence on NH /SiH ratio and on annealing," *Journal of the Electrochemical Society*, **124**(6) (1977) 908–912.

[200] V. A. Gritsenko, "Atomic structure of the amorphous nonstoichiometric silicon oxides and nitrides," *Physics-Uspekhi*, **51**(7) (2008) 699–711.

[201] J. C. Knights, "Characterization of plasma-deposited amorphous Si:H thin films", *Jpn. J. Appl. Phys.*, **18** (1979) Supplement 18-1, 101-108.

[202] A. C. Bronneberg, N. Cankoy, M. C. M. van de Sanden, M. Creatore, "Ion induced effects on grain boundaries and a-Si:H tissue quality in microcrystalline silicon films", *J. Vac. Sci. Technol. A*, **30** (2012) 061512.

[203] A. Borghesi, B. Pivac, A. Sassella, A. Stella, "Oxygen precipitation in silicon", *J. Appl. Phys.*, **77** (1995) 4169.

[204] A. H. Al-Bayati, K. G. Orrman-Rossiter, R. Badheka, D. G. Armour, "Radiation damage in silicon (001) due to low energy (60-510 eV) argon ion bombardment", *Surface Science*, **237** (1990) 213-231.

[205] P. J. Martin, "Ion assisted thin film deposition and applications", *Vacuum*, **36** (1986) 585-590.

[206] K. H. Müller, "Model for ion assisted thin film densification", *J. Appl. Phys*., **59** (1986) 2803.

[207] G. I. Grigorov, K. G. Grigorov, R. Sporken, R. Caudano, "Ion-induced densification of pvd films-a choice of the optimum density of ion bombardment", *Appl. Phys. A*, **63** (1996) 399-401.

[208] M. Na, S-W. Rhee, "Electronic characterization of Al/PMMA [poly(methyl methacrylate)]/p-Si and Al/CEP(cyanoethyl pullulan)/p-Si structures", *Organic Electronics*, **7** (2006) 205-212.

[209] C. Jang, Y. R. Cho, B. Han, "Ideal laminate theory for water transport analysis of metal-coated polymer films", *Appl. Phys. Lett.*, 93 (2008) 133307.

APPENDIX A

PLASMA TREATMENT WITH 100 kHz

Some basic studies have been performed using 100 kHz plasma treatment effect on the permeation barrier properties. However, due to some technical issues this study has not been performed thoroughly. Fig. A (a) shows the normalized conductance of Ca sensors deposited on barrier coated PET substrates versus time for SiN_x:H multi-layers separated by 2 min Ar plasma surface treatment with 100 kHz. The lag-time and WVTR values shows some drastic improvement compared to the 13.56 MHz plasma treated samples as shown in Fig. A (b) and (c). We achieved a minimum WVTR of 1.2×10^{-3} g/m^2.day for 100 kHz plasma treated sample even at lower SiN_x:H thickness (200 nm), as compared to 7×10^{-3} g/m^2.day obtained by using 13.56 MHz plasma with a higher SiN_x:H thickness (250 nm), treated for the same duration (2 min).

This effect is certainly due to frequency at which the Ar^+ plasma was excited. In 100 kHz plasma treated samples, made at the University of Minho, Portugal, we used 100 kHz plasma generator, a frequency low enough for the Ar^+ ions to follow. At INL, Braga we used 13.56 MHz which is too high, and therefore probably less effective in driving the Ar^+ ions which pick much less kinetic energy from the field.
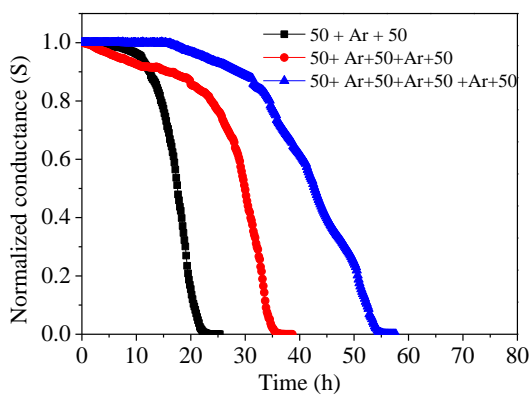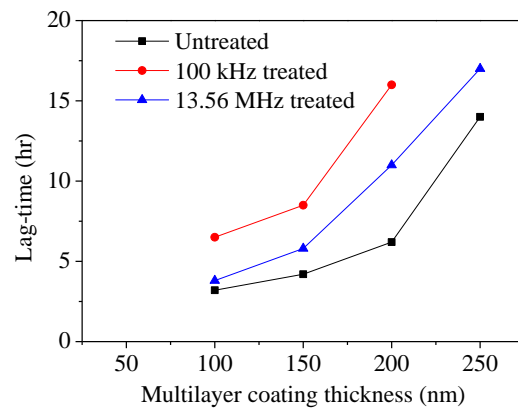
(a)   (b)
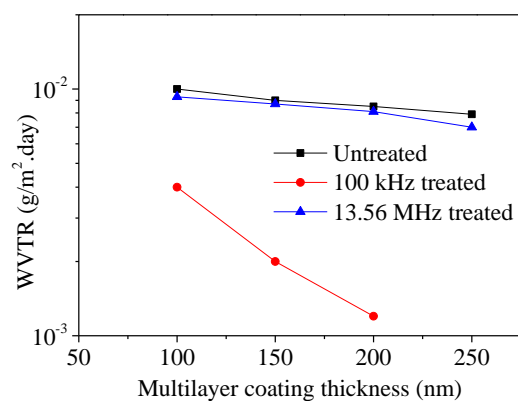
(c)

Fig. A: (a) Normalized conductance of Ca sensors deposited on barrier coated PET substrates versus time for SiN$_x$:H multi-layers separated by 2 min Ar plasma surface treatment with 100 kHz. (b) Evolution of the "lag-time" versus the SiN$_x$:H multi-layer thickness. (c) Evolution of WVTR values versus the SiN$_x$:H multi-layer thickness. The evolutions of lag-time and WVTR for the SiN$_x$:H multi-layers without any Ar plasma treatment and with 13.56 MHz plasma treatment are shown for comparison.

APPENDIX B

HYBRID LAYER OF GRAPHENE AND SILICON NITRIDE

Transparent monolayers of graphene on PET substrates were studied as the permeation barrier layers. We have deposited SiN_x:H single-layers using HW-CVD chamber on the commercially available graphene monolayers. Two different thicknesses of SiN_x:H single-layers have been studied. The monolayer of graphene without any SiN_x:H single-layer shows a reduction of WVTR as compared to the bare PET substrates. The WVTR of monolayer of graphene is 0.01 g/m^2.day. When the hybrid structures are developed, the structure shows an effective WVTR of 0.005 g/m^2.day for 40 nm SiN_x:H single-layer deposited on graphene. However, this is very basic study performed during the course of this thesis and this study needs further optimizations and developments in order to qualify the permeation barrier properties.
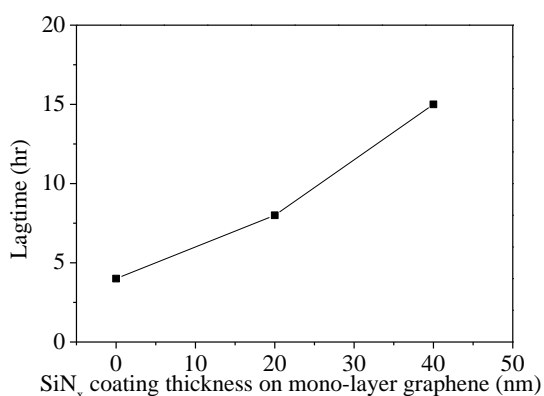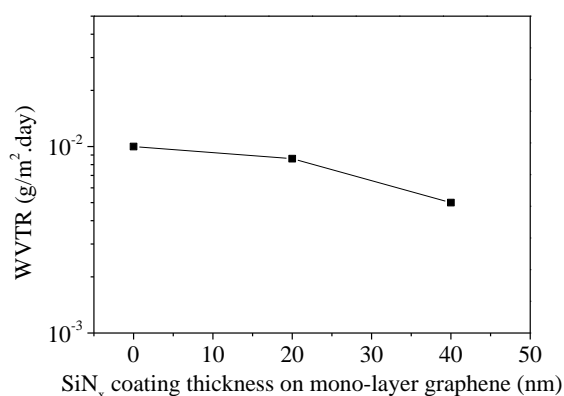
(a)   (b)

Fig. B (a) Lag-time variation of the hybrid structures with increase of SiN_x:H layer thickness and (b) Variation of WVTR of the hybrid structures.

LIST OF PUBLICATIONS

This thesis is based on following journal and conference contributions:

Publications in Journals:

[1] **S. Majee**, M.F. Cerqueira, D. Tondelier, B. Geffroy, Y. Bonnassieux, P. Alpuim, J.E. Bourée, "The Effect of Argon Plasma Treatment on the Permeation Barrier Properties of Silicon Nitride Layers", Surface & Coatings Technology, 235 (2013) 361-366. [**Featured article in** *Advances in Engineering*]

[2] **S. Majee**, M. F. Cerqueira, D. Tondelier, J. C. Vanel, B. Geffroy, Y. Bonnassieux, P. Alpuim, J. E. Bourée, "Influence of Low Energy Ar Plasma Treatment on the Moisture Barrier Performance of Hot Wire -CVD Grown SiN_x Multilayers", Japanese Journal of Applied Physics, 53 (2014) 05FM05.

[3] **S. Majee**, M. F. Cerqueira, D. Tondelier, J. C. Vanel, B. Geffroy, Y. Bonnassieux, P. Alpuim, J. E. Bourée, "Permeation barrier performance of HW-CVD grown silicon nitride films treated by argon plasma", Special Issue of Thin Solid Films (accepted, under process).

Conferences contributions:

[1] **S. Majee**, M.F. Cerqueira, D. Tondelier, B. Geffroy, Y. Bonnassieux, P. Alpuim, J.E. Bourée, "Encapsulation for organic devices deposited on polymer substrates", IONS conference, February 2012, Paris.

[2] **S. Majee**, M.F. Cerqueira, D. Tondelier, B. Geffroy, Y. Bonnassieux, P. Alpuim, J.E. Bourée, "Silicon nitride multilayers as permeation barrier for OLEDs. Effect of Argon plasma treatment", E-MRS Spring meeting, May 2012, Strasburg.

[3] **S. Majee**, M.F. Cerqueira, D. Tondelier, B. Geffroy, Y. Bonnassieux, P. Alpuim, J.E. Bourée, "Effect of argon plasma surface treatment on the permeation barrier performance of silicon-nitride thin films", HWCVD7 conference, October 2012, Japan.

[4] **S. Majee**, M.F. Cerqueira, D. Tondelier, B. Geffroy, Y. Bonnassieux, P. Alpuim, J.E. Bourée, "Multilayers of Silicon nitride thin films as an encapsulation barrier for flexible organic electronic devices", DIELOR conference, November 2012, Limoges, France.

[5] **S. Majee**, "Silicon Nitride multilayers as a permeation barrier for PET based organic devices", JAIST International School on Cat-CVD, March 2013, Japan.

[6] **S. Majee**, M.F. Cerqueira, D. Tondelier, B. Geffroy, Y. Bonnassieux, P. Alpuim, J.E. Bourée, "The Effect of Argon Plasma Treatment on the Performance of Silicon Nitride Permeation Barrier Multilayers for Organic Photovoltaics", E-MRS Spring meeting, May 2013, Strasburg.

[7] **S. Majee**, M.F. Cerqueira, D. Tondelier, B. Geffroy, Y. Bonnassieux, P. Alpuim, J.E. Bourée, "Effect of Argon Plasma Treatment on Silicon Nitride Barrier films for OPV cells", MRS-JSAP Joint Symposium, September 2013, Japan.

[8] **S. Majee**, M.F. Cerqueira, D. Tondelier, B. Geffroy, Y. Bonnassieux, P. Alpuim, J.E. Bourée, "Permeation barrier performance of inorganic / organic / inorganic hybrid structure for organic photovoltaic devices", Matériaux et Nanostructures π-Conjugués (MNPC) conference, October 2013, Annecy, France.

[9] **S. Majee**, M.F. Cerqueira, D. Tondelier, B. Geffroy, Y. Bonnassieux, P. Alpuim, J.E. Bourée, "Effect of Low Energy Ar Plasma Treatment on the Morphology of Hot-Wire CVD Grown SiN_x Interface and on the Permeation Barrier of Stacked SiN_x Single-layers", JNPV2013 conference (French meeting on photovoltaics), December 2013, Dourdan, France.

[10] **S.Majee**, "Encapsulation for flexible organic electronics: Protection from environment", International Displays Research Workshop 2014 (10th French-Korean Joint Workshop), January 2014, Palaiseau, France.

CURRICULUM VITAE

Subimal Majee

Date of birth: 01-03-1984

Citizen of: India

2010-2014:   Doctoral studies at the Laboratoire de Physique des Interfaces et Couches Minces, Ecole Polytechnique, CNRS (UMR 7647), Palaiseau, 91128, France

2009-2010:   Master of Science (Material Science & Nano Objects) from Ecole Polytechnique, France

2008-2010:   Master of Technology (Radio Physics and Electronics) from University of Calcutta, India

2005-2008:   Bachelor of Technology (Radio Physics and Electronics) from University of Calcutta, India

2002-2005:   Bachelor of Science (Physics) from University of Calcutta, India

2000-2002:   Higher Secondary (10+2) in Science, STP High (H.S.) School, West Bengal, India